UNIVERSITÉ FRANÇOIS RABELAIS DE TOURS

École Doctorale [SST]

Laboratoire d'Électrodynamique des Matériaux Avancés

THÈSE présentée par :

Francesco M. VITUCCI

soutenance prévue le 17 Décembre 2010

pour obtenir le grade de : Docteur de l'Université François - Rabelais

Discipline / Spécialité : Physique des Solides

PROPRIÉTÉS OPTIQUES ET MAGNÉTIQUES DE MATÉRIAUX MULTIFERROÏQUES : $GaFeO_3$ ET $LuFe_2O_4$

THÈSE DIRIGÉE PAR :

CALVANI Paolo	Professeur, Université La Sapienza – Rome
SORET Jean-Claude	Professeur, Université François-Rabelais – Tours

RAPPORTEURS :

DEGIORGI Leonardo	Professeur, ETH – Zurich
LOBO Ricardo	Chargé de Recherche HDR, CNRS-ESPCI – Paris

JURY :

BALESTRINO Giuseppe	Professeur, Université Tor Vergata – Rome
CALVANI Paolo	Professeur, Université La Sapienza – Rome
DE SOUSA MENESES Domingos	Maître de Conférence, Université d'Orléans
SORET Jean-Claude	Professeur, Université François-Rabelais – Tours

Remerciements

The work has been presented here, has involved a large number of people that I really want to thank for supporting and for the kindness they have shown. First of all I want to thank Paolo Calvani, my supervisor, for being a great guide and a strong chief, never forgetting to be a "magister". Beside him, I really want to thank all the staff of the IRS laboratory in Rome : Stefano Lupi, Alessandro Nucara, Paola Maselli. Everything I know about being a researcher came from them.

This experience would not have been as pleasant as it was without my collegues of the IRS group : Daniele Nicoletti, Chiara Mirri, Odeta Limaj, Gihan Kamel and Paola Di Pietro. The wonderful net of friendships we have created made the IRS lab a warm and comfortable house. A special thank goes to Matteo Valentini, for everything we shared, for everything we are going to share.

For the French part, I want to thank Jean-Claude Soret, my co-supervisor from the LEMA laboratory in Tours, for teaching me as a student, for working with me as a colleague. I want to thank also Gisele Gruener and Rodolphe Sopracase, which have been nice colleagues and kind friends. I am gratefully indebted to Francois Gervais, which allowed me to work in the LEMA Laboratory and to all the members of the lab for their kind and warm welcome. I am also grateful to the members of the CEMHTI-CNRS Laboratory in Orleans for the fruitful scientific collaboration.

I want to thank Ullrich Schade for helping us in our hard work in the IRIS beamline @Bessy II synchrotron in Berlin and for all the nice moments spent in Berlin. A great thank also goes to Michele Ortolani and all the staff of the IFN which helped opening a new path for our laboratory.

I also thank infinitely all the new friends that this amazing journey has allowed me to meet : they made red something which could have rest pale blue.

Ringrazio gli amici di sempre, per esserci stati, per esserci ora, con un po' di rimpianto per non aver avuto troppo tempo per dimostrare loro quanto siano radicati in me. Ringrazio tutta la mia famiglia, per aver sempre creduto in me, per la stima che mi ha sempre preventivamente donato, una dose di serenità che mi ha permesso di affrontare tante difficili prove. Ringrazio profondamente i miei genitori : il nostro rapporto in perenne evoluzione non smette mai di affascinarmi e di guidarmi verso maturità e felicità. Ringrazio Michela : travagliata è stata la strada del cammino comune, ma ciò che mi risplende dentro è la meraviglia con cui guardiamo all'orizzonte. Grazie di cuore a tutti.

Résumé

Nous présentons une contribution à l'étude des propriétés structurale, électronique et magnétique de composés multiferroïques – c'est ï¿½ dire de matériaux dans lesquels ordre magnétique et ordre ferroélectrique coexistent, les deux aspects étant couplés via des interactions et des mécanisme qui ne sont pas encore bien compris.

C'est dans ce contexte que nous avons étudié les deux composés $GaFeO_3$ et $LuFe_2O_4$, synthétisés sous forme de céramiques pour le premier et sous forme de monocristaux pour le second. L'étude a nécessité l'utilisation de plusieurs techniques : la résonance magnétique électronique (RPE), les mesures magnétiques par magnétométrie (susceptibilité AC et aimantation DC), la spectroscopie infra rouge (IR) dans le domaine de l'IR lointain au visible et dans le domaine sub-terahertz au synchrotron Bessy-II.

Du point de vue du magnétisme de $GaFeO_3$, les mesures par magnétométrie confirment un ordre ferrimagnétique à basse température ($T \leq T_C \approx 206\,\mathrm{K}$) correspondant à $0,77$ magnéton de Borh par atome de fer, et révèlent une phase paramagnétique anormale sur un large intervalle de température $T_C < T \leq 240\,\mathrm{K}$. Cette anomalie – également observées par RPE – est attribuée à l'effet de corrélations magnétiques de courte portée. D'autre part, l'analyse des spectres de phonon IR en fonction de la température ($10 \leq T \leq 1000\,\mathrm{K}$) montre que la mise en ordre des moments magnétiques n'affecte pas les propriétés structurales de $GaFeO_3$.

Le cas de $LuFe_2O_4$ est très différent puisque les degrés de liberté magnétiques semblent couplés aux propriétés structurales au travers de l'ordre de charge des ions Fe^{3+}/Fe^{2+} comme le suggèrent les mesures RPE et de spectroscopie IR dans le domaine sub-terahertz.

Mots clés : Multiferroics, EPR, Infrared spectroscopy, Magnetism

Abstract

We present a contribution to the study of structural, electronic and magnetic properties of multiferroic compounds, materials in which magnetic and ferroelectric order coexist, coupled together via interaction mechanisms that are not yet well understood.

In this context we have studied the two compounds : a ceramics sample of $GaFeO_3$, and a single crystal $LuFe_2O_4$. The study involved the use of several techniques : Electronic paramagnetic resonance (EPR), magnetic measurements by magnetometry (AC susceptibility and DC magnetization), infrared spectroscopy (IR) from the sub-TeraHertz to the visible range.

From the point of view of magnetism, $GaFeO_3$, measurements by magnetometry confirm a ferrimagnetic order at low temperature ($T \simeq 206K \leq T_C$), which corresponds to a 0.77 μ_B per Fe ion, and show a paramagnetic phase in an abnormal wide temperature range $T_C < T \leq 240$ K. This anomaly is also observed by EPR and it has been attributed to a short-range magnetic correlations. On the other hand, the analysis of the infrared phonon spectra as a function of temperature ($10 \leq T \leq 1000$ K) shows that the ordering of magnetic moments does not affect the structural properties of GaFeO3.

For $LuFe_2O_4$, conversely, the magnetic degrees of freedom are coupled to the magnetic structural properties, through the charge ordering of Fe^{3+} / Fe^{2+} ions, as suggested by EPR and IR spectroscopy.

Keywords : Multiferroics, EPR, Infrared spectroscopy, Magnetism

Table des matières

Introduction **23**

1 General properties of multiferroic and magnetoelectric materials **29**
1.1 The magnetoelectric effect 30
1.2 Multiferroics 32
1.2.1 The problem of incompatibility between ferroelectricity and magnetism 34
1.3 Mechanisms for ferroelectric and magnetic integration 37
1.3.1 Independent systems 37
1.3.2 Ferroelectricity induced by lone-pair electrons 38
1.3.3 Geometric ferroelectricity in hexagonal manganites 41
1.3.4 Spiral spin-order-induced ferroelectricity 45
1.3.5 Ferroelectricity in charge-ordered systems 57
1.3.6 Ferrotoroidic systems 62
1.4 Potential applications 65
1.4.1 Magnetic field sensors using multiferroics 65
1.4.2 Electric field control of the exchange bias by multiferroics 68
1.4.3 Multiferroic/semiconductor structures as spin filters 69
1.4.4 Logical states in a tunneling junction by use of multiferroics 70
1.4.5 Negative refractive-index materials 71

2 The experimental techniques **79**
2.1 Reflectivity measurements with FT-IR Spectroscopy 79
2.1.1 Optical conductivity function 81
2.1.2 The Drude-Lorentz model 82
2.1.3 Fourier-Transform Infrared Spectroscopy 87
2.1.4 FT-IR Spectroscopy Experimental apparatus 87
2.1.5 Terahertz spectroscopy with Coherent Synchrotron Radiation 95
2.1.6 Reflectivity measurements in electric field 103

2.2 Electron Paramagnetic Resonance Spectroscopy . . . 104
2.2.1 Bulk magnetic properties . . . 104
2.2.2 Interaction of magnetic dipoles with electromagnetic radiation : bases of EPR spectroscopy . . . 105
2.2.3 Interactions between magnetic moments . . . 108
2.2.4 The EPR experimental apparatus : the spectrometer . . . 112

3 Structural, electronic and ferroic properties of the investigated systems 121
3.1 $LuFe_2O_4$ . . . 121
3.1.1 Sample characterization . . . 121
3.1.2 Magnetoelectric coupling : Magnetic-field control of the dielectric properties and of the charge structure . . . 129
3.1.3 Magnetoelectric coupling : electric-field control of dielectric and magnetic properties . . . 132
3.2 $GaFeO_3$ . . . 135
3.2.1 Sample characterization . . . 135
3.2.2 Magnetoelectric coupling . . . 137

4 Experimental results and discussion : magnetic and optical properties of $LuFe_2O_4$ and $GaFeO_3$ 145
4.1 Sample preparation . . . 146
4.2 Magnetic measurements and Electron Paramagnetic Resonance. . . . 146
4.2.1 Magnetic susceptibility and magnetization of $GaFeO_3$ . . . 146
4.2.2 Electron Paramagnetic Resonance on $GaFeO_3$ . . . 154
4.2.3 Magnetic measurements and EPR on $LuFe_2O_4$ . . . 162
4.3 Infrared spectroscopy of $GaFeO_3$ and $LuFe_2O_4$ . . . 163
4.3.1 Reflectivity measurements on $GaFeO_3$ . . . 163
4.3.2 Reflectivity measurements on $LuFe_2O_4$ . . . 168
4.3.3 Infrared response of $LuFe_2O_4$ under an electric field . . . 173

Conclusions 183

Index 187

Liste des tableaux

4.1 Physical quantities for $GaFeO_3$ deduced from magnetization and EPR measurements. 157

4.2 Parameters obtained by fitting Eq. 4.3 to the phonon spectrum of $LuFe_2O_4$, as measured with the radiation field polarized in the *ab*-plane and along the *c*-axis. The calculated values are those reported in Ref. [26]. All figures are in cm^{-1}. 173

Table des figures

1.1 Classification of insulating oxides (see text) [1]. 30

1.2 (a) Lattice structures of the high-temperature PE phase (left) and low-temperature ferroelectric phase (right) of perovskite $BaTiO_3$. In the ferroelectric phase, the B-site Ti ions shift from the centrosymmetric positions, generating a net polarization and thus ferroelectricity ; (b) Orbital configuration of O-TM-O chain unit in perovskite cell 36

1.3 A summary of experimental results on BiMnO3. (a) X-ray diffraction spectra at various temperatures ; (b)-(d) lattice parameters, thermal analysis YG and DTA, and resistivity as a function of temperature, respectively ; (e) magnetic M-H hysteresis and (f) hysteresis of magnetodielectric effect $\Delta\varepsilon(\mu_0 H)/\varepsilon(0)$ against magnetic field at various temperatures [31]. 39

1.4 (a) Lattice structure of $BiFeO_3$, with the Bi ion shifting along the [111] direction and the distorted FeO_6 octahedra surrounding the [111] axis. Polarization P points along the [111] direction, as indicated by the arrow [35]. (b) Measured P-E loop for a $BiFeO_3$ single crystal [34]. (c), (d) Spin configuration of $BiFeO_3$. The spiral spin propagation wave vector q is along the $[10\bar{1}]$ direction and the polarization is along the [111] direction. These two directions define the $(\bar{1}2\bar{1})$ cycloidal plane on which the spin rotation proceeds, as shown by the shaded region in (c) and (d)[36]. 40

1.5 (a) Lattice structure of ferroelectric $YMnO_3$, with the arrows indicating the direction of ion shift from the centrosymmetry positions [43]. (b) Electronic configuration of Mn ions in the MnO_5 pyramid of $YMnO_3$ [35] 42

1.6 Crystal structures of (a) PE phase and (b) ferroelectric phase of $YMnO_3$. The spheres and pyramids represent Y ions and MnO_3 pyramids, respectively. The arrows indicate the direction of ion shift from the centrosymmetry positions, and the numbers are the bond lengths [43]. 43

1.7 a) Spin configurations and lattice symmetry of $HoMnO_3$ in different temperature ranges with and without electric field. The red arrows represent the Ho spins and the yellow arrows for the Mn spins (see the text for details)[48]. (b) Dielectric constant as a function of temperature for $HoMnO_3$, indicating three anomalies [35]. (c) Dielectric constant as a function of temperature for $HoMnO_3$ under different magnetic fields [49]. 45

1.8 (a) Sinusoidal (upper) and spiral (lower) spin order for a one-dimensional spin chain with competing exchange interactions. (b) Geometric spin frustration in a two-dimensional triangular lattice. The DM interaction in La_2CuO_4 and $RMnO_3$ are illustrated in (c) and (d). The open arrow in (d) for La_2CuO_4 denotes the direction of weak ferromagnetism and the open arrow in (d) for $RMnO_3$ denotes the direction of the generated polarization [32]. 47

1.9 (a) Crystal structure of $LiCu_2O_2$ and (b) its spin-ordered configuration. The blue lines indicate the quasi-1D spin ladders consisting of Cu ions. The red spheres represent the oxygen ions and grey spheres denote the Li ions. Spiral arrangements of the Cu spin ladders and corresponding polarization under (c) zero magnetic field and (d) 9.0T applied along the b-axis [56]. 50

1.10 (a) Lattice structure and three spin arrangements in Ni sublattice for $Ni_3V_2O_8$. The LTI (low-temperature insulator) phase exhibits a spin spiral structure which can induce ferroelectric polarization P along the *b*-axis, while the spins in the HTI (high- temperature insulator) and CAF (canted antiferromagnetic) phases are collinear. (b) Phase diagram of magnetic field against temperature for $Ni_3V_2O_8$ under magnetic field along the *a*-axis and *c*-axis, respectively. (c) Polarization along the b-axis as a function of temperature and magnetic field applied along the *a*-axis and *c*-axis, respectively [57]. . . 51

1.11 Crystal lattice structure (a) and 120°spin-ordered state (b) in triangular-lattice $RbFe(MoO_4)_2$[58]. 52

1.12 (a) Spin configuration of the ICM collinear sinusoidal spin-ordered state at T = 35K (upper) and the spiral spin-ordered state at 15K (middle : the bc-plane, lower : 3D view) in $TbMnO_3$. The measured magnetization and specific heat, modulation wave number, dielectric constant and polarization along the a-axis, b-axis and c-axis, respectively, are shown in (b), (c), (d) and (e) [59]. 53

1.13 Dielectric constants (a) and (b) and polarizations (c) and (d) along the *c*-axis and *a*-axis as functions of temperature under different magnetic fields for $TbMnO_3$ [59]. 54

1.14 Phase diagram of temperature against Mn-O-Mn bonding angle ϕ (corresponding to different rare-earth ionic radii) for manganites $RMnO_3$. The inset shows the wave numbers of spiral spin order for these manganites [60]. . . . 55

1.15 Reversal of electric polarization Pc and spiral spin order induced by external electric field along the *c*-axis in $TbMnO_3$. (a) Scattering intensities and (b) spin configurations of the spin-order states with different polarization P_c. See the text for details [61]. 56

1.16 CO-OO structure of $Pr_{0.5}Ca_{0.5}MnO_3$ at low temperature [70]. 58

1.17 Atomic configuration of the charge-order state of $LuFe_2O_4$ (a) on the ab-plane and (c) in 3D space (c). The red arrow in (c) indicates the direction of polarization. (b) Transmission electron diffraction pattern of $LuFe_2O_4$ along the $[1\bar{1}0]$ direction at T = 20 K. (d) Electric polarization of $LuFe_2O_4$ as a function of temperature under two different cooling field modes. (see Ref.[71] for (a) and (b), Ref.[32] for (c) and Ref.[72] for (d). 59

1.18 Synchrotron X-ray oscillation photographs (upper row), and schematic CO-OO configurations (middle row) as well as lattice structures (lower row) of $Pr(Sr_{0.1}Ca_{0.9})_2Mn_2O_7$ at three different temperatures [76]. 61

1.19 Magnetic toroidic moment in a simple system : (a) a ring-shaped torus with an even number of current windings exhibits a toroidic moment T (the green arrow) ; (b) a magnetic field along the ring plane induces the current loops in one direction and eventually an electric polarization along this direction [78]. 62

1.20 Crystal lattice structure and (b) schematic magnetic toroidic moments of $GaFeO_3$; (c) four kinds of magneto- optical effects [79]. 64

1.21 Relations between the ferroic orders and the space-/time-reversal [78]. . . . 65

1.22 Relations between electric polarization along the z-direction and magnetic field along the x-direction at different temperatures adjacent to the magnetic transition point of $LiNiPO_4$ [83]. 66

1.23 (a) Multiferroic as a probe of the magnetic field. The middle (white) layer is multiferroic, while both the upper and lower layers (grey) are ferromagnetic metals. An external magnetic field H will induce an electric polarization perpendicular to the magnetic field direction, and then a voltage V. (b) The read-head device uses the probe in (a). The blue layer is the magnetic media (magnetic disk) and the black arrows in it indicate two opposite bits [35]. . 67

1.24 Schematic view of a soft ferromagnetic layer deposited on multiferroic antiferromagnetic film. The external electric field induces a variation in the magnetization of the antiferromagnetic multiferroic film, and results in the reversal of magnetization in the soft ferromagnetic layer due to the magnetic pinning effect [84]. 68

1.25 Exchange bias in the $CoFe/BiFeO_3$ system. Magnetic field dependence of magnetization of $CoFeB/BiFeO_3/SrTiO_3(001)$ multilayer (upper left), CoFeB/ $BiFeO_3/SrTiO_3(111)$ (upper right), $CoFeB/BiFeO_3/La_{0.7}Sr_{0.3}MnO_3/SrTiO_3(001)$ (lower left), and $CoFeB/BiFeO_3/La_{0.7}Sr_{0.3}MnO_3/SrTiO_3(111)$ (lower right) [87]. 69

1.26 Measured (a) M-H loops and (b) magnetization of the exchange-biased $Pt/YMnO_3/Py$ structure under different external electric fields V_e. The inset in (a) shows the relation between magnetization and temperature, and the inset in (b) is the multilayered structure [89]. 70

1.27 Structure and energy scheme for a new magnetic tunneling junction (MTJ). Multiferroic $La_{0.1}Bi_{0.9}MnO_3$ (LBMO) was used as the insulating barrier and ferromagnetic half-metal $La_{2/3}Sr_{1/3}MnO_3$ (LSMO), while Au were used as the bottom and top electrodes, respectively [1]. 71

1.28 Measured TMR effect in a $La_{2/3}Sr_{1/3}MnO_3/La_{0.1}Bi_{0.9}MnO_3/Au$ multilayer structure. The red curve represents the resistivity and the black curve the magnetoresistance ratio [1]. 72

1.29 Influence of the external electric field on the tunneling current in $La_{2/3}Sr_{1/3}MnO_3/La_{0.1}Bi_{0.9}MnO_3/Au$ junctions. The arrows denote the sequence for electric field application. (b) Dependence of the tunneling electroresistance effect (TER) and tunneling magnetoresistance (TMR) on the external electric field V_{dc}. (c) Measured TMR upon an electric bias of $+2V$ and $-2V$. (d)-(g) Four-state resistance in the junction [1]. 73

2.1 Sketch of a density of states N(ε) (grey : occupied, white : unoccupied). The optical conductivity at a given frequency ω is the sum of all the transitions from an occupied to an empty state separated by an energy $\hbar\omega$. 82

2.2 Displaced Fermi sphere in the presence of an applied electric field E. Electrons are moved from region B to A. The Figure applies to a metal with a spherical Fermi surface of radius k_F, or to a circular Fermi surface in two dimensions. 83

2.3 Frequency-dependent reflectivity and optical conductivity calculated using the Drude model (see text) : values for plasma frequency ω_p and scattering rate γ_D are typical for metals (ω_p = 14000 cm^{-1}, γ_D = 100 cm^{-1}). 84

2.4 Frequency dependent reflectivity and optical conductivity calculated using the Lorentz model (see text) with parameter values typical for an insulator. A phonon absorption in the far infrared (ω_0 = 400 cm^{-1}, S = 1000 cm^{-1}, γ = 20 cm^{-1}) and an optical electronic transition in the visible range (ω_0 = 30000 cm^{-1}, S = 100000 cm^{-1}, γ = 20000 cm^{-1}) are shown. 85

2.5 Sketch of a Michelson interferometer. From a point source S, using collimating mirrors, electromagnetic radiation is sent to a beam splitter BS that separates it in two components. One of them is sent to a static mirror SM, while the other one to a moving mirror MM. Thereafter the signals are recombined and sent to the detector D. 88

2.6 Interferogram I(x) and the corresponding power spectrum B(ω), obtained through a Fast Fourier Transform (FFT) algorithm 89

2.7 Scheme of BOMEM DA-3 : side and front view. The source location and the beamsplitter are shown, as well as the moving mirror. 90

2.8 Experimental setup for different optical ranges. Note that many far-IR ranges overlap to get independent determinations of the IR reflectivity. 91

2.9 Schematic top view of the interferometer BOMEM DA-3. The optical path within the reflectivity setup is indicated by a red line. 92

2.10 Reflectivity setup in the sample compartment of BOMEM DA-3. The optical path from the Michelson interferometer to the detector is indicated by a red line. 92

2.11 Scheme of the Leybold cryopump with the sample holder on top. Two vacuum environments are present : LV (low vacuum, for the interferometer optics) and HV (high vacuum, in the cryostat). An IR window separates the two environments. 93

2.12 Schematic representation of heating system. As for the closed-cycle cryogenerator there are two vacuum environments : LV (low vacuum, for the interferometer optics) and HV (high vacuum, for the cryostat). An IR window separates the two environments. 94

2.13 Scheme of the evaporator. The filament is in position 1 while measuring, where it allows the passage of the light beam. When the spectra on the sample have been acquired at all temperatures, the sample is re-heated to room temperature ; the filament is displaced to position 2, a current of about 3 A is applied to evaporate metal. Filament is then moved back to position 1 to acquire reference spectra. 94

2.14 (a) Long bunches emit incoherent waves with random phase relation. Short bunches behave as a macroparticle and emit coherent waves at equal phase. (b) The resulting power grows linearly with the number of electrons for the incoherent case, while the coherent intensity grows with the square of the charges involved. (c) The synchrotron radiation spectrum shows a dramatic increase of photon flux in the long-wavelength range, if the coherent radiation is no longer shielded by the vacuum chamber. This additional increase is proportional to the number N of electrons involved [13] 96

2.15 (a) Radiation frequency spectra measured with a Fourier-transform spectrometer. (b) The intensity is normalized by the square of the bunch current : the intensity enhancement is more than square of the bunch current, indicating bunch deformation effects. (c) The amplification factor AF is the ratio between the coherent and the incoherent intensity. The amplification due to the coherent superposition of the waves becomes 10^5 times grater. 98

2.16 Optical and mechanical draft of the BESSY II infrared beamline IRIS. The beamline provides highly-brilliant synchrotron radiation from the far-IR or THz up to the near-IR region. Experiments are mounted on the roof of the 0.7 m thick monolithic radiation shielding tunnel in the experimental hall, providing an almost vibration-free environment necessary for Fourier-transform spectroscopy [4]. 100

2.17 Optical functions in low-α and normal operation mode. The low-α optics changes the dispersion function (green) inside the dipoles in an appropriate way. α is defined as the change of the orbit length L per momentum p change $\alpha = (\delta L/L)/(\delta p/p)$ [20] 101

2.18 Sketch of the optical setup for terahertz reflection spectroscopy with coherent synchrotron radiation at the storage ring BESSY. The optical setup is placed in the sample compartment of a Bruker 66/v interferometer. The sample is placed and oriented into a cryostat chamber. By using two remotely controlled mirrors (a), the beam can be either sent to the sample (upper panel) or directly transmitted to the detector (lower panel). A tight, diffraction-limited focusing of radiation is obtained through an ellipsoidal mirror (b). the specular reflection is collected by a symmetric mirror and sent to the detector [4]. 102

2.19 Sketch of the geometry of the electrical contacts (grey in the figure) on the sample for electric field reflectivity measurements. 103

2.20 Zeeman Energy-level scheme for a simple system (free electron) as a function of the applied magnetic field B, showing the EPR absorption. Uα and Uβ represent the energies of the M=$\pm$1/2 states. g and μ_B are defined in text. . 107

2.21 Superexchange in magnetic oxides. Examples of superexchange interaction between the localized 3d electrons of a transition metal (M) and the p-orbitals of the oxygen (O). For simplicity, we consider only one electron at the magnetic ion site on a single orbital. 111

2.22 Resonance fields for a g = 2 signal at microwave frequencies commonly available in EPR spectrometers. 112

2.23 Schematic view of an electron paramagnetic resonance (EPR) spectrometer (see text). 113

2.24 The EPR experimental apparatus used in this work : on the left the BRUKER Elaxsys EMX 6/1 spectrometer, on the right the console for signal processing and electronic controls. 114

2.25 Components of the EMX spectrometer. 115

2.26 Block diagram of a microwave bridge. 116

2.27 Magnetic and electric field patterns in a standard EPR cavity. 117

2.28 A block diagram of the field controller and associated components. 117

3.1 Schematic description of the crystal structure of $LuFe_2O_4$. Fe ions form the hexagonal double layers (A,B) which are packed between (Lu, O) blocks and stacked along the rhombohedral axis in (AB), (CA), (BC).... [9] (b) Spin frustration and charge frustration on a 2D hexagonal lattice. The common nearest-neighbor site for the ($\uparrow - \downarrow$) pair (black and white pair) has no preference for $\uparrow$ or $\downarrow$ (black or white) since the energy is completely degenerate. This situation is expressed by the gray site in the case of charge frustration [1]. 122

3.2 Scheme of the superstructure of the CO phase of $LuFe_2O_4$. The solid lines show the chemical unit cell. The dotted lines show the charge superlattice cell. The Fe ions in the upper and lower layers are indicated by large and small circles, respectively. Fe^{2+} and Fe^{3+} are represented by open and filled circles, respectively. The polarization P is represented with a short, black arrow. A charge density wave vector Q is drawn as a long, grey arrow [1]. . 123

3.3 Measured $\rho\ vs$ T curve in $LuFe_2O_4$. Two different activation energies for the CO (T<320 K) and the disordered phase (T>320 K) are detected [8]. . . . 124

3.4 Thermo-magnetization curves of $LuFe_2O_4$ in 300 Oe. The solid and dotted lines show the $H \parallel c$ and $H \perp c$ configuration, respectively. 124

3.5 High field magnetization curves in the parallel configuration $H \parallel c$ of $LuFe_2O_4$. (a) Solid and broken lines refer to ZFC and FC data at 4.2 K, respectively . (b) Isothermal magnetization curves above 77 K. 125

3.6 Magnetic structure of $LuFe_2O_4$ at T = 220 K. The three magnetic domains correspond to the three symmetry equivalent magnetic propagation vectors [2]. 126

3.7 The a.c. dielectric dispersion in $LuFe_2O_4$ polycrystalline samples. The in-phase component of the a.c. dielectric constant has been measured in the frequency range from 1 kHz to 1 MHz [4]. 126

3.8 Integration of a pyroelectric current measurement. The current flow from the sample was recorded on heating after electric field cooling along the *c*-axis. The direction of the electric polarization depends on the direction of electric field, which indicates the macroscopic electric polarization [4]. 127

3.9 Frequency dependence of (a) real part ε' and (b) imaginary part ε'' of the dielectric constant of $LuFe_2O_4$ at various T by THz-TDS [8] 128

3.10 Scheme of main phase transitions of $LuFe_2O_4$. Inspired by [1]. 128

3.11 Real part of the dielectric constant (k) versus temperature measured at various frequencies for $LuFe_2O_4$ under zero magnetic field. The inset shows the variation of k with magnetic field at room temperature at 20 kHz [5]. . . 129

3.12 Magnetic and charge order in $LuFe_2O_4$. (a) The magnetic and charge Bragg-peak intensities as a function of temperature. (b) (c) Linear intensity profiles of the charge superlattice peak (2/3,2/3,3.5) along the (110) and (001) directions, respectively. The horizontal bars indicate the instrument resolution along the measured directions. The lines are fits to the data using a Lorentzian function. The inset denotes the direction of the performed scans [9]. . . 130

3.13 Magnetic-field response on the charge superlattice peak (2/3,2/3,3.5). Charge peak intensity measured at 300 K with FC from 350 K at different magnetic-field strengths. The lines are guides to the eyes [9]. 131

3.14 Temperature dependence of relative tunability n_r under a 50 V/cm dc bias field at various frequencies between 10 and 200 kHz [10]. 132

3.15 Temperature dependence of the relative tunability n_r under a 50 V/cm dc bias field at various frequencies between 10 and 200 kHz [10]. 133

3.16 (a)Current and magnetization measurements vs. time. (b) I-V curves in the *ab* plane at 200 K. The inset shows the simple experimental setup. (c) The c-axis magnetization as a function of applied voltage. The curve marked with 0 T is the remanent magnetization measured after cooling in a field of 5 T and removing the field at 200 K. The curve marked with 0.1 T was measured in a constant 0.1 T field after a ZFC process[11]. 134

3.17 (a) Crystal structure of $GaFeO_3$. Ga1, Ga2, Fe1, and Fe2 sublattices and O atoms are presented in different colors. (b) The Ga2 and Fe2 sublattice layer structure [15]. 136

3.18 Magnetization curves as functions of temperature (M vs T) and an applied magnetic field (M vs H)[15]. 136

3.19 Temperature dependence of the resistivity ρ of $GaFeO_3$ in the temperature interval 265-360 K. The inset shows the linear behavior of the logarithm of the resistivity vs $1/T$ [17]. 137

3.20 Temperature dependence of (a) the dielectric constant (ε) and (b) the dissipation factor (D = $tan\ \delta$) for f = 100 kHz, 500 kHz, and 1 MHz. The insets show the temperature dependences of ε and D (left scale) in μ_0H=0 and 60 mT for f =1 MHz. The inset in the figure (a) shows the MD coefficient (right scale) as a function of temperature for f =1 MHz. [17]. 138

3.21 Dependence of magnetoelectric polarization on magnetic field, δP_b versus H_c (solid lines) and δP_c versus H_b (dashed lines). Measurements were performed for the crystals immersed in liquid helium, i.e., at 4.2 K. [20]. 139

3.22 (a) Magnetic structure of $GaFeO_3$. Arrows indicate Fe moments. Note that the positions of Fe1 and Fe2 are shifted to +b and -b, respectively, from the center of the two adjacent oxygen layers. (b), (c) Qualitative explanation of a large difference between the α_{bc} and α_{cb} values. $\mathbf{u}_i$ is the local displacement from the center of the octahedron and $\boldsymbol{\mu}_i$ the magnetic moments on Fe_i site (i=1,2) in zero (black lines) and strong (red and blue) magnetic fields H (see text). [20]. 140

3.23 (a) Absorption spectra, $\alpha(\omega)t$, and (b) magnetoelectric effect spectra, $\Delta\alpha(\omega)t$ for $E \parallel b$ (solid lines) and $E \parallel c$ (dashed lines) in $GaFeO_3$ (t $\sim$ 50 μm) at 10 K. In (b), open squares represent the second harmonic signal. Solid and open circles in the inset of (b) represent the $\Delta\alpha(\omega)t$ for the light propagation vector (k) being parallel and antiparallel to the outer product of spontaneous polarization and magnetization ($P \times M$), respectively, through the reversal of P, namely, the 180°rotation of the b axis of the sample [21]. 141

4.1 (a) Temperature dependence of the ac magnetic susceptibility of polycrystalline $GaFeO_3$ measured by Quantum Design-Physical Properties Measurement System (QD-PPMS) with an ac field modulation up to 1.7 mT. The divergence at 207 K suggest the onset of a magnetic transition. (b) Temperature dependence of the inverse susceptibility. 147

4.2 Temperature dependence of the magnetization under different magnetic fields, from 500 Oe to 90 kOe in both ZFC and FC for polycrystalline $GaFeO_3$. No difference between the ZFC and FC curve is detected above 5 kOe. . . 148

4.3 Magnetic field dependence of the magnetization at 2 K up to 9 kOe in ZFC for polycrystalline $GaFeO_3$. In the inset, the magnetization is plotted vs, the reciprocal of the magnetic field applied. 149

4.4 Magnetic field dependence of the magnetization in FC procedure at selected temperatures down to 5 K, as calculated from data in Fig.4.2. 150

4.5 Arrott plot at selected temperatures calculated from data in Fig.4.2 for polycrystalline $GaFeO_3$. 151

4.6 Comparison between the magnetic susceptibility data reported in Fig.4.1 (blu circles) and the magnetic susceptibility calculated from the Arrott plots (black circles) χ_{Arrott} (see text). In the inset the temperature dependence of χ_{Arrott} is plotted in the paramagnetic region. The red dashed line is the Curie-Weiss fit. 152

4.7 Temperature dependence of the product $m \times T$ deduced from the Arrott plot : it suggests a crossover from a simple paramagnetic to a ferrimagnetic phase occurring at 240 K. The dashed lines are only a guide for the eyes. . 153

4.8 Temperature dependence of the EPR spectra for polycrystalline $GaFeO_3$. In the inset the intensity of the signal is enlarged 20 times. 158

4.9 Comparison between EPR experimental data (solid lines) and Lorentzian fit (dashed lines) for $T > T_C$. The fit has been performed with one and two Lorentzian contributions in (a) and (b), respectively. 159

4.10 Temperature dependence of EPR spectra parameters calculated from Lorentzian fit shown in Fig.4.9. g is the Landé factor related to the center of the absorption line through the Eq.4.1, ΔH and I_{EPR} are the HWHM and the Intensity of the Lorentzian functions, respectively. 160

4.11 Temperature dependence for $T > T_C$ of the inverse magnetic susceptibility $\chi^{-1}_{EPR}(T)$ calculated from the double integration (DIN) of EPR spectra, compared with the susceptibility measurements and χ_{Arrott}. In the inset, $\chi^{-1}_{EPR}(T)$ is plotted with a Curie-Weiss fit (red solid line). 161

4.12 Magnetic susceptibility of the single crystal of $LuFe_2O_4$, as measured in zero-field cooling. 162

4.13 Reflectivity of $GaFeO_3$ between 10 K and 1000 K in the MIR and FIR ranges (6 meV - 1 eV) in logarithmic scale. 164

4.14 (a) Optical conductivity of $GaFeO_3$ between 10 K and 1000 K in the phonon region. (b) Comparison of experimental (line) data with the fitting function (dashed lines). The zero of the curves measured at 500 K and 1000 K has been shifted by 150 and 300 $\Omega^{-1}\text{cm}^{-1}$ respectively, for sake of clarity. 166

4.15 Temperature dependence of the phonon frequencies for polycrystalline $GaFeO_3$. 167

4.16 Reflectivity of $LuFe_2O_4$ between 10 K and 500 K, as measured with the radiation field polarized along the $a(b)$-axis (above) and along the c-axis (below). The phonon region is reported in the inset on a linear frequency scale. 168

4.17 Optical conductivity of $LuFe_2O_4$ at 10 K in the whole energy range, as measured with the radiation field $\mathbf{E} \perp \mathbf{c}$ or $\mathbf{E} \parallel \mathbf{c}$. The fitting curves are reported by dashed lines. The zero of the upper curves has been shifted by 200 $\Omega^{-1}\text{cm}^{-1}$ for sake of clarity. 169

4.18 Optical conductivity of $LuFe_2O_4$ between 10 K and 500 K in the phonon region, as measured with the radiation field $\mathbf{E} \perp \mathbf{c}$ and $\mathbf{E} \parallel \mathbf{c}$. 171

4.19 Optical conductivity at 10 K and 500 K, for both $\mathbf{E} \perp \mathbf{c}$ and $\mathbf{E} \parallel \mathbf{c}$, with the fitting curves which provide the parameters listed in Table 4.2. The zero of the upper curves has been shifted by 200 $\Omega^{-1}\text{cm}^{-1}$ for sake of clarity. . . 172

4.20 Temperature dependence of the phonon frequencies for $\mathbf{E} \perp \mathbf{c}$ (left) and $\mathbf{E} \parallel \mathbf{c}$ (right) in $LuFe_2O_4$. 174

4.21 Optical conductivity for $\mathbf{E} \perp \mathbf{c}$ of $LuFe_2O_4$ in the sub-THz region at different temperatures. The arrows mark the frequencies of the peaks in ϵ_2 extracted from a time-domain experiment [17]. 175

4.22 Current vs. voltage (above) and resistance vs. voltage (below) of the $LuFe_2O_4$ crystal, showing the transition to a more conducting state at a threshold voltage which is higher for increasing field than for decreasing field. The contact geometry is also shown. The light impinges on the ac plane of the crystal. . 177

4.23 a) Infrared spectra at 300 K with applied electric field. The current limiter was set at 100 mA. At the value of 4.64 V the current reaches the limit of 100m A, the intensity starts to decrease and the temperature start to increase. b) Spectra as a function of temperature when no electric field is applied. c) Infrared spectra with no electric field (solid lines) and after transition (dashed lines) spectra are shifted for clarity. 178

4.24 Evolution of infrared spectra as a function of current in the a- a configuration (both light polarization and electric field are parallel to a axis respectively). In the inset in shown integration of intensity for all configurations. 179

Introduction

In materials science many efforts have been devoted in the last decades to synthesize and investigate new compounds with unusual and interesting properties. Among all, both high temperature superconductivity (HTSC) and colossal magneto-resistance (CMR) have been largely explored. Beside their interest for the theoretical interpretations, these fields have been explored also for the possibility to produce the so called "functional materials", which present some physical properties which are promising for technical applications. Moreover, a considerable amount of research is presently focused on "multifunctional" materials in which several physical properties could potentially be used simultaneously. In this work we explore two systems which belong to multifunctional materials : they are multiferroic (MF) or, more precisely, magnetoelectric (ME). The multiferroics - according to the original definition - are materials which present, in a common range of temperatures, two or more kinds of fundamental ferroicities : ferromagnetism, ferroelectricity and ferroelasticity. Within them, the magnetoelectric materials are systems where the electric and magnetic orders are coupled with each other : this mutual dependence, in fact, defines the magnetoelectric effect.

Since the 19th century, electricity and magnetism were reported to be naturally coupled together in the Maxwell equations, but the electric and magnetic ordering in solids were most often considered separately. The situation has changed when Dzyaloshinskii predicted [1], and Astrov observed [2], this coupling in matter, which is now known as the linear magnetoelectric effect. This led to the discovery of many other compounds of this class and to a classification of possible symmetry groups allowing for this effect. A new approach to this problem was the idea that beside the existence of the strong cross-coupling of magnetoelectric responses in solids, there may exist systems in which both types of ordering can coexist in the absence of external electric and magnetic fields. According to the definition proposed by Schmid [3], these are the materials now called multiferroics.

Magnetism and ferroelectricity are essential to many forms of technological devices. The search for multiferroic materials is driven by the mutual expectations of controlling charges by applied magnetic fields and spins by applied voltages. At present day, it is commonly accepted that ferroelectricity and magnetism tend to be mutually exclusive in matter, and when they coexist they interact weakly with each other [3] [4]. An exciting recent development is the discovery that even a weak magnetoelectric interaction can lead to spectacular cross-coupling effects, for example when it induces electric polarization in a magnetically ordered state. Such phenomenon is called magnetic ferroelectricity, and shows an extraordinary sensitivity to magnetic fields. A confluence of electronic, magnetic and elastic factors determine the properties of magnetoelectrics and multiferroics. There-

fore, different techniques are needed in order to achieve a complete understanding of their complex phenomena, arising from the interactions among several degrees of freedom.

In this work we used two complementary experimental techniques : Infrared (IR) Spectroscopy and the Electron Paramagnetic Resonance (EPR) spectroscopy. The IR techniques provide an experimental access to the optical response in the frequency range which is critical for understanding the properties of strongly correlated systems in solid state physics. Moreover, it allows one to study both the electronic and vibrational low-energy excitations, providing useful information on the microscopic mechanisms that build up to the electronic ground state. Indeed, optical spectroscopy of metals and semiconductors has provided invaluable insight into their low-energy electrodynamics. On the other hand, EPR is a spectroscopic method used to determine the structure, the dynamics and the spatial distribution of the electron spins in a paramagnetic phase. It can be used in several research fields, *e.g.* biology, physics, chemistry, medical science. Therein, it provided detailed information on many topics of scientific interest like chemical kinetics, electron exchange, crystal structure, fundamental quantum theory as well as catalysis and polymerization. As these capabilities of EPR are a result of the unpaired electron's spin magnetic moment, this technique is very sensitive to probe local magnetic fields within the sample. In this work, we completed the optical study by performing measurements in the Terahertz (THz) range, and the results of EPR spectroscopy with macroscopic magnetization measurements.

The purpose of this study is to investigate if and how the structural, magnetic and electronic properties are linked together in two iron-based multiferroics : $LuFe_2O_4$ and $GaFeO_3$. In both systems there is magnetoelectric coupling. $LuFe_2O_4$ exhibits simultaneous ferrimagnetic and ferroelectric order under $T = 240\ K$. It has been proposed that the ferroelectric order arises from an unconventional, electronic ferroelectricity, where the electric dipole arises from the electron correlations, rather than from covalency [5]. Coupled to the ferroelectric transition, $LuFe_2O_4$ exhibits a charge ordering process which can be described within a charge density wave (CDW) scenario. Moreover, recent experimental results suggest the presence of an electric-field-driven metal-to-insulator transition [6]. Finally, one of the most interesting feature reported for this compound is the possible influence of the magnetic field on the charge order even in the non-magnetic phase [7]. IR spectroscopy is a suitable tool to investigate the metal-to insulator-transition, and coupled with the magnetic study is able to provide informations onto the mutual interactions between the structural electronic and magnetic degrees of freedom involved in the several phase transitions found in this system.

$GaFeO_3$, in turn, presents a polar structure up to 1000 K and a ferrimagnetic transition at about 200 K. If for the former compound much interest has been directed toward the ferroelectric order, in $GaFeO_3$ an intriguing origin for the ferrimagnetic order has been proposed. Arima *et al.* [8] have proposed that Fe substituted at the Ga site may be at the origin of the observed magnetic moment : this is a special case where the net moment is derived from the site disorder. In this system the EPR measurements are of crucial importance. Indeed, the information of EPR can provide a detailed investigation of the local arrangement of the magnetic moments. Both optical and magnetization measurements, furthermore, allow for a comparison between the macroscopic behavior and the microscopic dynamics.

The first chapter of this thesis is devoted to a general overview of the characteristics of the MF and ME materials : structural, electronic, magnetic and transport properties are described and special attention is devoted to cross-coupling phenomena. A brief description of the theoretical models that have been developed over the years to interpret the phenomenology of these systems is also reported. In Chapter 2, the experimental techniques, i.e., the Fourier-Transform IR spectroscopy and EPR spectroscopy are introduced, the theory of linear response functions as well as the basic principles of magnetic measurements are reviewed. Moreover, the models for analyzing optical conductivity spectra and magnetic properties are presented. The third Chapter is an exhaustive review of the experimental results reported up to date on $LuFe_2O_4$ and $GaFeO_3$. In the last Chapter we discuss our experimental results and their analysis, in order to improve our knowledge of the $LuFe_2O_4$ and $GaFeO_3$ multiferroics.

This thesis arises from an European PhD Label collaboration between the University La Sapienza of Rome (Italy) and the University François-Rabelais of Tours (France). The measurements presented in this work have been performed in both the named institutions, as well as at the IRS beamline of the BESSY-II storage ring (Berlin) and at the CEMHTI-CNRS in Orleans (France).

Bibliographie

[1] I. E. Dzyaloshinskii, Sov. Phys. JETP **10**, 628 (1959).

[2] D. N. Astrov, Sov. Phys. JETP **11**, 708 (1609).

[3] H. Schmid, Ferroelectrics, **162**, 317 (1994)

[4] N.A. Hill, J. Phys. Chem. B **104**, 6694 (2000).

[5] N. Ikeda, H. Ohsumi, K. Ohwada, K. Ishi, T. Inami, K. Kakurai, Y. Murakami, K. Yoshii, S. Mori, Y. Horibe, and H. Kito, Nature **436**, 1136 (2005).

[6] C. Li, X.-Q. Zhang, Z.-H. Cheng, and Y. Sun, Appl. Phys. Lett. **92**, 152103 (2008).

[7] J. Wen, G. Xu, G. Gu, and S. M. Shapiro, Phys. Rev. B **80**, 020403(R) (2009).

[8] T. Arima, D. Higashiyama, Y. Kaneko, J. P. He, T. Goto, S. Mi- yasaka, T. Kimura, K. Oikawa, T. Kamiyama, R. Kumai, and Y. Tokura, Phys. Rev. B **70**, 064426 (2004).

Chapitre 1

General properties of multiferroic and magnetoelectric materials

The original definition of ferroics was aimed to categorize materials and effects that allow the formation of switchable domains. Since domains can be formed in the case of ferroelectric, ferromagnetic, ferrotoroidic or ferroelastic ordering, primary multiferroics are compounds exhibiting forms of ordering from this group. However, recently this definition has been enlarged to those systems presenting also *anti*ferroic properties. Thus we can now address a multiferroic material if it presents also ferrimagnetism, antiferromagnetism, antiferroelectricity ; the principle is to include all systems which present at least two order parameters. On the other hand, the magnetoelectric materials, are defined by the presence of coupling between electric and magnetic order, namely the magnetoelectric effect. The taxonomy in this research field is rich and often complex : the map in Fig.1.1 may help us to orient ourselves in the universe of multiferroics. The extern circle represents all insulating oxides in which electrically polarizable materials (green ellipse) and magnetically polarizable materials (orange ellipse) are included. Within each ellipse, the circle represents materials with a spontaneous finite polarization (ferroelectrics) and/or a magnetization (ferro- and ferrimagnets). The multiferroic group corresponds to the intersection between the two circles. The small blue circle in the middle denotes systems exhibiting a magnetoelectric coupling. As we can see from the scheme, between magnetoelectrics and multiferroics compounds there may be an intersection but in principle magnetoelectric effect and multiferroelectricity could be two independent effects.

Despite all the efforts which have been devoted to synthesize such multifunctional material, one should notice that among oxides there are really few MF and ME compounds if we compare this fields with CMR manganites or HTCS. This is especially because it has been shown that the presence of ferromagnetism and ferroelectricity in the same system is strongly structurally and energetically suppressed. In what follows we will describe the principal properties of MF and ME materials, giving at the same time some reasonable explanations to the incompatibility between ferromagnetism and ferroelectricity. We will also describe some approaches to overcome this mutual exclusion.

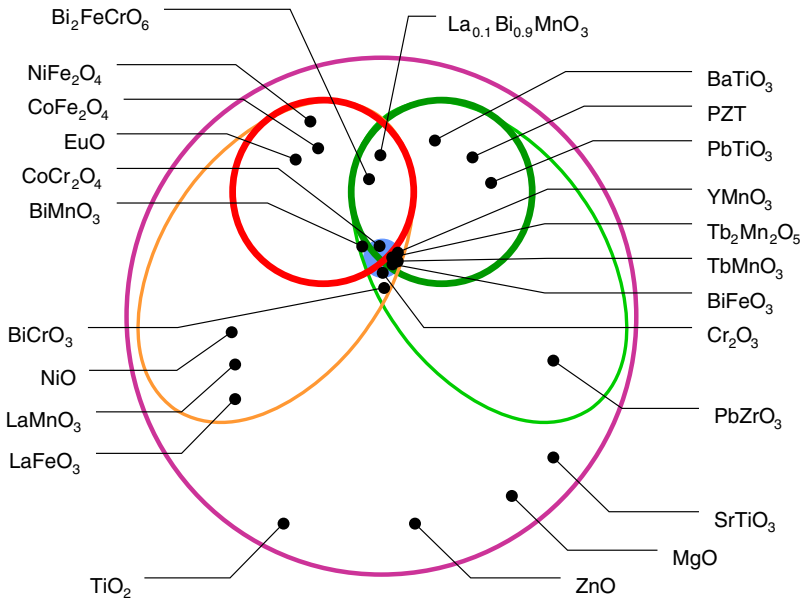

FIGURE 1.1 – Classification of insulating oxides (see text) [1].

1.1 The magnetoelectric effect

The magnetoelectric effect, in its original definition, describes the coupling between electric and magnetic fields in matter (i.e., induction of magnetization (M) by an electric field (E) or of polarization (P) by a magnetic field (H)). In 1894, by studying the crystal symmetry, Curie predicted an intrinsic magnetoelectric effect in some crystals [2] and subsequently, Debye called this kind of effect as a "magnetoelectric effect" [3]. The first successful observation of the magnetoelectric effect was obtained in Cr_2O_2 [4] and led to a big excitement because of the obvious potential of the cross-correlation between the magnetic and electric properties of matter for technical applications. However, the general weakness of the ME effect and the restricted number of available compounds determined a decline of research activities for about two decades. Only recently we assist to a renewed interest for the ME effect, which reflects into an impressive number of publications on this subject .

Thermodynamically, the magnetoelectric effect can be understood within the Landau theory framework : the expansion of the free energy for a magnetoelectric system [5] can be written

$$\begin{aligned} F(E,H) &= F_0 - P_i^S E_i - M_i^S H_i \\ &\quad -\frac{1}{2}\varepsilon_0\varepsilon_{ij}E_iE_j - \frac{1}{2}\mu_0\mu_{ij}H_iH_j - \alpha_{ij}E_iH_j \\ &\quad -\frac{1}{2}\beta_{ijk}E_iH_jH_k - \frac{1}{2}\gamma_{ijk}H_iE_jE_k - ... \end{aligned} \tag{1.1}$$

Differentiation of Eq.1.1 leads to the polarization

$$P_i(E,H) = -\frac{\partial F}{\partial E_i} = P_i^S + \varepsilon_0 \varepsilon_{ij} E_j + \alpha_{ij} H_j + \frac{1}{2}\beta_{ijk} H_j H_k + \gamma_{ijk} H_i E_j + ... \qquad (1.2)$$

and to the magnetization

$$M_i(E,H) = -\frac{\partial F}{\partial H_i} = M_i^S + \mu_0 \mu_{ij} H_j + \alpha_{ij} E_j + \beta_{ijk} H_j E_i + \frac{1}{2}\gamma_{ijk} E_j E_k + ... \qquad (1.3)$$

where E and H are the electric and magnetic field, respectively. F_0 is the ground state free energy, subscripts (i,j,k) refer to the three components of a variable in spatial coordinates, E_i and H_i are the components of the electric field E and of the magnetic field H, respectively, P_i^S and M_i^S are the components of the spontaneous polarization P^S and of the magnetization M^S. ε_0 and μ_0 are the dielectric and magnetic susceptibilities of vacuum, ε_{ij} and μ_{ij} are the second-order tensors of dielectric and magnetic susceptibilities, β_{ijk} and γ_{ijk} are the third-order tensor coefficients and, mostly, α_{ij} is the components of tensor $\boldsymbol{\alpha}$ which is designated as the ***linear magnetoelectric*** coefficient and corresponds to the induction of polarization by a magnetic field or a magnetization by an electric field. Most research on the ME effect is focused to the linear ME effect and it is generally accepted that the prefix "linear" is omitted.

The time-asymmetric nature of the ME effect requires a treatment within the 122 magnetic point groups (Shubnikov groups) [6]. The Shubnikov groups are formed from symmetry operations combining the 1-, 2-, 3-, 4- and 6-fold rotations with spatial inversion $\bar{1}$ and time reversal $\underline{1}$. The tensors are classified with respect to the eigenvalues of the parity operations as axial or polar ($\sim \bar{1}$) and i-type or c-type ($\sim \underline{1}$). The c tensors represent time asymmetric phenomena which become allowed when time reversal symmetry is broken by magnetic long-range ordering, while i tensors refer to phenomena that are already allowed in the dia- or paramagnetic state [7]. The ME point groups and the corresponding tensor elements are tabulated and described in Ref.[8]. By definition the ME effect involves both electric and magnetic fields, so that neither time reversal $\underline{1}$ nor inversion $\bar{1}$ can be a symmetry operation. One finds this property in 69 magnetic point groups, out of which only 58 allow for the ME effect because of additional restrictions.

Group theory is a very effective tool which can distinguish between systems that could or could not present ME effect. However these criteria are not sufficient to determine the magnitude and, thus, the detectability of the ME response. In order to estimate the magnitude of the coupling coefficients α, it is necessary to understand the microscopic mechanism driving the ME effect. Hornreich and Shtrikman presented a model which can explain the temperature dependence of ME effects in Cr_2O_3 [9]. From this model, a generalized approach which includes several magnetic interaction mechanisms was derived [10]. We will not describe in details this theory because is far from our scope, but we can summarize the relevant magnetic interactions which appear therein. In what follows i, j are index for lattice sites, $\vec{r}_{ij}$ is the distance between ions at sites i and j ; α,$\beta \in$ {x,y,z}, $\vec{m}$ is the magnetic dipole moment, and $\vec{B}$ is the local or applied magnetic field (see section 2.2.3 for details regarding the exchange processes) :

- Single-ion anisotropy $\propto (S_i^\alpha)^2$:
  the electric field moves the ions with respect to its ligands. This can change the magnitude and/or the local symmetry of the ligand field.
- Symmetric superexchange $\propto \mathrm{r}_{ij}$ $(S_i^\alpha S_j^\beta + S_i^\beta S_j^\alpha)$:
  opposite movement of differently charged ions in the electric field changes the electron wave functions of the ions because it modifies the orbital overlap. This, in turn, changes the values of the exchange integrals and energies.
- Antisymmetric superexchange $\propto \mathrm{r}_{ij}$ $(S_i^\alpha S_j^\beta - S_i^\beta S_j^\alpha)$:
  is the so-called Dzyaloshinskii-Moriya interaction. In many cases the spin canting is a common manifestation of this contribution and although its magnitude is usually small, this interaction is responsible of many interesting phenomena in MF and ME materials.
- Dipolar interactions $\propto m_i m_j / r_{ij}^3 - 3(m_i r_{ij})(m_j r_{ij})/r_{ij}^5$:
  A nonuniform movement (e.g. because of piezoelectric distortion) of the ions that carries a magnetic moment changes the dipolar fields and, thereby, the magnetic anisotropy.
- Zeeman energy $\propto \vec{B}^\alpha g_i^{\alpha\beta} \vec{S}_i^\beta$:
  The value of the Landé factor $\hat{g}$ can be changed by an electric field either by modifying the wave function or by inducing local distortions which change the crystal field. The modification of the wave function can be due to changes in electronic polarization (shift of the electrons away from the equilibrium position). This changes the orbital contribution to the magnetic moment and, hence, the $\hat{g}$ factor.

The experiments on Cr_2O_3 were the first big step in the research on the ME effect. Nevertheless it became immediately clear that technical applications were limited by the small magnitude of the induced polarization or magnetization. The ME effect in Cr_2O_3 was found to be $\alpha = 4.13$ ps m^{-1}. With an electric field of 10^6 V cm^{-1} this corresponds to the magnetization obtained after reversal of only five of every 10^6 spins in an antiferromagnetic lattice [11]. The largest ME coefficients have been observed for $LiCoPO_4$ ($\alpha = 30.6$ ps m^{-1} [12]), yttrium iron garnet (YIG) films ($\sim$30 ps m^{-1} [13]) and $TbPO_4$ ($\alpha = 36.7$ ps m^{-1} [14]). The weakness of the ME effect follows from the perturbative nature of the microscopic mechanisms driving ME behavior and it was further shown that the ME response is limited by the relation [15] :

$$\alpha_{ij}^2 =< \chi_{ii}^e \chi_{jj}^m > \tag{1.4}$$

where χ_{ii}^e and χ_{ii}^m are the electric and magnetic susceptibilities. Thus, according to equation Eq. 1.4, the ME can be large in ferroelectric and/or ferromagnetic materials only.

1.2 Multiferroics

As we have mentioned before, originally, crystals were defined multiferroic when two or more of the primary ferroic properties were united in the same phase [16]. The *ferroic* definition was motivated to categorize materials (and effects) which allow for the formation of switchable domains. Since domains can be formed in the case of ferroelectric, ferromagnetic, ferrotoroidic or ferroelastic ordering, primary ferroics are compounds exhibiting a form of ordering included in this group. It is to be noted that, in case of antiferroic com-

pounds, straightforward switching of antiferroic domains is in general not possible (because of macroscopic compensation), so that antiferroics were not considered at this stage. The definition may be generalized to include antiferroics, but because there is no proper analogy between the definitions of the antiferro-electric, -magnetic and -elastic states, the extension is to some extent arbitrary. One possible approach is to define antiferroics as being made up by equivalent ferroic sublattices whose arrangement leads to macroscopic compensation [5].

From the crystallographic point of view, four major types of multiferroics can be distinguished :

- ***Compounds with perovskite structure*** :
  This category is the most numerous and was the first to be explored. The general chemical formula of most of these compounds is either ABO_3 or $A_2B'B''O_6$. Many are synthesized by chemical substitution from these parent compounds (mostly $AB'_{1-x}B''_xO_3$). Usually the unit cell of the multiferroic perovskites does not possess the ideal cubic point symmetry, $m3m$ but is slightly rhombohedrally distorted. The most extensively studied compound is $BiFeO_3$, which is ferroelectric, ferroelastic and weakly ferromagnetic [17]. The interest in this compound is due to the high electric and magnetic ordering temperatures of, respectively, ∼1100 and ∼650 K, which can lead to the developing of multiferroic-based, room-temperature, multifunctional materials.
- ***Compounds with hexagonal structure*** :
  Compounds with the general formula ABO_3 or $A_2B'B''O_6$ can crystallize in a hexagonal rather than in the typical perovskite structure in the case of sufficiently small cationic radii. The largest and best known group of hexagonal multiferroics is formed by the ferroelectric antiferromagnetic manganites $RMnO_3$ with R = Sc, Y, In, Ho, Er, Tm, Yb, Lu. Their crystallographic point symmetry is $6mm$ and they possess up to four long-range ordered subsystems : the ferroelectric lattice, the antiferromagnetic Mn^{3+} lattice and two rare-earth sublattices. In contrast to the case of perovskite multiferroics, relatively few examples of element substitution have been reported.
- ***Boracites*** :
  Boracite compounds have as general formula $M_3B_7O_{13}X$ and are ferroelectric, ferroelastic, antiferromagnets (in some cases accompanied by a weak ferromagnetic moment). The M site is occupied by Cr, Mn, Fe, Co, Cu, Ni as divalent ion, while X = Cl, Br, I. This category presents a large variety of compounds, many of which possess a ferroelectric Curie temperature above room temperature, whereas the magnetic ordering temperature never exceeds 100 K [18]. At high temperatures the compounds are cubic with, $\bar{4}$3m, and in several cases a ferroelectric transition into the orthorhombic $mm2$ phase follows with subsequent phase transitions to m and $3m$ point symmetry at lower temperatures.
- ***$BaMF_4$ compounds*** :
  Multiferroics of composition $BaMF_4$ with M = Mg, Mn, Fe, Co, Ni, Zn were introduced and studied in detail by Guggenheim and Scott [19] [20]. The compounds possess an orthorhombic structure with $2mm$ point symmetry at high temperatures with an extrapolated Curie temperature above the melting point. At 25-70 K the ferroelastic ferroelectric structure displays either purely antiferromagnetic or weak ferromagnetic

ordering [18].

1.2.1 The problem of incompatibility between ferroelectricity and magnetism

In spite of the big research effort in the field, a general difficulty in uniting electric and magnetic long-range ordering in one compound cannot be denied : not many multiferroic compounds are known thus far. Most of them are antiferromagnetic ferroelectrics, and the preferred combination of ferromagnetism and ferroelectricity is only achieved in the form of weak ferromagnetism or weak ferroelectricity. Further, symmetry restrictions cannot explain the low number of magnetic ferroelectrics because even in compounds that allow for that coexistence, this is usually absent. Given such considerations, we shall try to address the incompatibility between ferroelectricity and magnetism.

From the point of view of symmetry considerations, ferroelectricity needs the broken spatial inverse symmetry while time reverse symmetry can be present. A spontaneous polarization appears if a structural distortion of the high-symmetry paraelectric (PE) phase breaks the inversion symmetry. In contrast, the broken time-reversal symmetry is the prerequisite for magnetism and spin order. Among the Shubnikov magnetic point groups, only 13 point groups allow for the simultaneous appearance of spontaneous polarization and magnetization (i.e. 1, 2, 2′, m, m′, 3, 3m′, 4, 4m′m′, m′m2′,m′m′2′, 6 and 6m′m′).

Most technologically important ferroelectrics such as $BaTiO_3$ and $(Pb,Zr)TiO_3$ are transition-metal oxides with perovskite structure (ABO_3). Attempts to search for or synthesize multiferroics have been mostly concentrated on this class of compounds and we can take this category as a good example to explain the incompatibility between ferroelectricity and magnetism. These compounds exhibit a cubic structure at high temperatures, with a small B-site cation at the centre of an octahedral coordination of oxygen ions and a large A-site cation at the unit cell corners. In most ferroelectric perovskites, the transition metal (TM) ion has a formal configuration d^0 at the B-site (i.e., the d-shell is empty). Although not all perovskite oxides with empty d-shell TM ions exhibit ferroelectricity, this seems to be a prerequisite. Magnetism, in contrast, requires TM ions at the B-site with partially filled shells because the spins of electrons occupying the filled shell completely add to zero and do not participate in magnetic ordering. The difference in filling the TM ion d-shells at the B-site, which is required for ferroelectricity and magnetism, makes these two ordered states mutually exclusive. However, an accurate analysis reveals some details that should be analyzed. In particular, multiferroic perovskites usually undergo a phase transition from a high-temperature, high- symmetry PE phase, into a low-symmetry polarized phase at low temperature, accompanied by an off-centre shift of the B-site TM ions. This is surprising because completely ionic-bond perovskite oxides are always centrosymmetric : in this structure, the short-range Coulomb repulsions between electron clouds on adjacent ions are minimized. The ferroelectric stability is therefore determined by a balance between these short-range repulsions and additional bonding, which stabilizes the ferroelectric phase. Presently, two different chemical mechanisms for stabilizing the distorted structures in ferroelectric oxides have been proposed : both can be described by means of the second-order Jahn-Teller effect (SOJT).

The transition-metal ion in perovskite compounds can be responsible for two types

of Jahn-Teller distortion : i) a first-order distortion which does not change the centre of symmetry, e.g. by elongation of the octahedron of ligands, in the case of partially filled $3d$ orbitals ; ii) a second-order distortion (second order Jahn-Teller effect (SOJT)) which breaks the centrosymmetry by an off-centre movement of the transition-metal ion. Since the intensity of this process is lower than that of the first mechanism, it requires an empty $3d$ shell, which prevents the first-order Jahn-Teller distortion. Since only a partially filled $3d$ orbital can lead to magnetic ordering, whereas the breaking of centrosymmetry is a necessary condition for the formation of a spontaneous polarization, the conditions for ferroelectricity and (anti-)ferromagnetism are mutually exclusive [43].

Quantitatively, the tendency of a material towards a ferroelectric instability appears as a second-order term in the perturbative expansion of the total energy with respect to distortion, from a high symmetry reference phase [21] [22] : this is the origin of the SOJT effect. Using the standard perturbation theory, the energy can be expanded as a function of the normal coordinate Q, referred to the high-symmetry reference structure with energy $E^{(0)}$, as

$$E(Q) = E(0) + \langle 0|(\partial H/\partial Q)_0|0\rangle Q + \tag{1.5}$$

$$\frac{1}{2}\left(\langle 0|(\partial^2 H/\partial Q^2)_0|0\rangle - 2\sum_n \frac{|\langle 0|(\partial H/\partial Q)_0|n\rangle|^2}{E_n - E(0)}\right) Q^2 + ...$$

Here $|0\rangle$ is the lowest energy solution of $H^{(0)}$ and the $|n\rangle$ are the excited states with energies $E^{(n)}$. The first-order term describes the usual first-order Jahn-Teller theorem. This term is nonzero only for orbitally degenerate states, and in the case of d orbitals it always leads to centrosymmetric distortions. Therefore it does not give rise to ferroelectricity. Note, however, that when it is non-zero, it dominates over any non-centrosymmetric second-order distortion. In the orbitally non-degenerate systems (unaffected by the first JT effect), the competition between the two second-order terms, which are of opposite sign, determines if a non-centrosymmetric distortion is favored or not. The first term describes the short-range repulsive forces between ions if they are displaced with the electrons frozen in their high-symmetry configuration. By definition it is always positive, thus it raises up the energy of the system : polar distortions are more likely to be favored if this term is small ; this tends to be the case for closed-shell d^0 cations without valence electrons. The second one of the second-order terms describes the relaxation of the electronic system in response to the ionic displacements which follow the formation of a covalent bond. It is always negative unless it is zero by symmetry, so that it favors ferroelectricity when its magnitude is large thus showing a non-centrosymmetric distortion. This occurs when the products of the ground and lowest excited states are of odd parity, so that the matrix elements are non-zero in the cases when $E^{(n)}$ - $E^{(0)}$ is small. In case of Mott-Hubbard insulators with partially filled d shells, the top of the valence band and bottom of the conduction band are both composed primarily of transition-metal d states. Therefore the ground ($|0\rangle$) and low-lying excited states ($|n\rangle$) have the same symmetry, the product $(\partial^2 H/\partial Q^2)_0|0\rangle$ is odd, and the matrix element $\langle 0|(\partial H/\partial Q)_0|n\rangle$ is zero. Conversely, for d^0 perovskites, the top of the valence band is made up largely of O 2p states, and the bottom of the conduction band of transition-metal 3d states, thus the product of the ground and low-lying excited states with $(\partial H/\partial Q)_0$ is even, and the matrix element $\langle 0|(\partial H/\partial Q)_0|n\rangle$ is nonzero. Consequently,

the balance between the positive and negative second-order terms usually results in off-centering for d^0 cations. Conversely, the balance between the second-order terms usually disfavors off-centering in transition metals with partially filled d shells, since in this case the repulsive Coulomb interactions are stronger than any energy gain from chemical-bond formation.

Another way to look at this effect is to consider the ligand-field hybridization of a TM cation with its surrounding anions. A textbook example is $BaTiO_3$, where a strong increase in O 2p-Ti 3d hybridization accompanies the distortion from the high symmetry to the polar structure. This is because, as the Ti ion moves toward an oxygen carrying its positive charge, negative electronic charge flows toward it from the oxygen ion, leading to a polarization larger than that would arise from the ionic component alone.

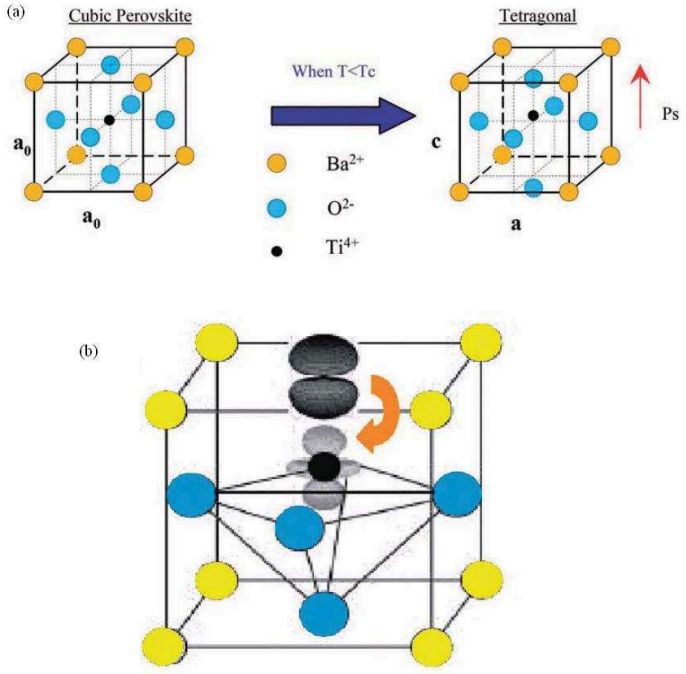

FIGURE 1.2 – (a) Lattice structures of the high-temperature PE phase (left) and low-temperature ferroelectric phase (right) of perovskite $BaTiO_3$. In the ferroelectric phase, the B-site Ti ions shift from the centrosymmetric positions, generating a net polarization and thus ferroelectricity ; (b) Orbital configuration of O-TM-O chain unit in perovskite cell

In Fig.1.2 the structure of $BaTiO_3$ is shown. The empty d-states of Ti^{4+} ions can be used to establish strong covalency with the surrounding oxygen anions which soften the Ti-O repulsion : it is favorable to shift the TM ions from the centre of O_6 octahedra towards one oxygen to form a covalent bond, as shown in Fig.1.2(b).

1.3 Mechanisms for ferroelectric and magnetic integration

In the last section we have shown as perovskite oxides need B-site TM ions with an empty *d*-shell to present ferroelectricity and how this type of electronic structure likely excludes magnetism. However, not all experimental and theoretical results support the argument that ferroelectricity and magnetism are absolutely incompatible. In principle there are two possible ways to combine these two properties. One is to synthesize materials which contain separate functional units, usually mixing the non-centrosymmetric units together with units with magnetic ions (independent multiferroicity). The second is to look for materials that present unconventional mechanisms for either ferroelectricity or magnetism. In the next sections we will describe in details the independent multiferroicity mechanism and the unconventional ferroelectricity, leaving apart the largely unexplored field of the unconventional magnetism.

1.3.1 Independent systems

Some good examples to explain the mechanism of independent multiferroicity can be found by analyzing perovskite oxides once more. We can imagine a system where the A-sites are occupied by cations of a $(ns)^2$ valence electron configuration, such as Bi^{3+}, Pb^{3+}, which favor the stability of ferroelectrically distorted structures and, at the same time, the B-sites are occupied by magnetic ions providing magnetism. This approach may avoid the exclusion rule of ferroelectricity and magnetism at the same sites.

The first experimental attempt towards perovskite multiferroics was performed by mixing magnetic TM ions (with d electrons) and ferroelectrically active TM ions with d^0 configurations at the same site (B-sites, i.e. by partially substituting the d^0-shell TM ions by magnetically active $3d$ ions). One of the most studied such compounds is $PbFe_{1/2}{}^{3+}Nb_{1/2}{}^{5+}O_3$ (PFN) [18][24] where Nb^{5+} and Fe^{3+} ions are ferroelectrically active and magnetic, respectively. A ferroelectric Curie temperature of $\sim$ 385 K and a Néel point of $\sim$143K were found. It is worth noting that the two ordering temperatures are far from each other : this is an indication that this rather simple approach does allow for ferroelectricity and magnetism, but not necessarily offers strong magnetoelectric coupling. In most cases, in fact, the coupling between magnetic order and ferroelectric order in this kind of multiferroics is very weak, mostly because the two orders arise from different kinds of ions.

In addition to PFN, other multiferroics in the category of $AB_{1-x}B'_xO_3$, such as $PbFe_{1/2}{}^{3+}Ta_{1/2}{}^{5+}O_3$ [23] and $PbFe_{1/2}{}^{3+}W_{1/2}{}^{5+}O_3$ [25], were synthesized. Similar investigations performed on these materials also revealed a weak magnetoelectric coupling between the ferroelectric and spin order. Again, it was shown that the weak magnetoelectric coupling exists because of the different and independent origins in the two types of orders.

As already mentioned, another way to combine magnetism and ferroelectricity is to search for unconventional ferroelectricity, e.g., that intrinsically generated by special spin orders. Such a mechanism not only could enable an effective combination of the two orders but also a spontaneous mutual control of both of them.

1.3.2 Ferroelectricity induced by lone-pair electrons

In addition to the ligand-field hybridization, another mechanism can be responsible for the ferroelectric order : the existence of $(ns)^2$ "lone- pair" ions, which also may break the inversion symmetry thus inducing the ferroelectric order. In general, a lone-pair is made of two valence electrons that do not participate in chemical bonds by means of (sp)-hybridized states (such as sp^2 or sp^3). For example the ions Bi^{3+} and Pb^{3+} have two valence electrons in an *s*-orbit, which form to the lone pair. These ions are always locate at A-sites in an ABO_3 perovskite structure and this allows one to locate magnetic TM ions at B-sites : again, the incompatibility for TM ions to induce both magnetism and ferroelectricity is thus partially avoided.

The lone-pair state is unstable and needs a mixing between the $(ns)^2$ ground state and a low-lying $(ns)^1(np)^1$ excited state, which eventually leads these ions to break the inversion symmetry. This so called "stereochemical activity of the lone pair" helps to stabilize the off-centre distortion and, in turn, the ferroelectricity [26]. It is worth nothing that, in typical ferroelectrics, the lone-pair mechanism and the ligand-field hybridization take place simultaneously [27]. Typical examples are $BiFeO_3$ and $BiMnO_3$, where the B-site ions contribute to the magnetism and the A-site ions via the lone-pair mechanism lead to the ferroelectricity. In both $BiMnO_3$ and $BiFeO_3$, Bi^{3+} ions with two electrons in a 6s orbit (lone pair) shift away from the centrosymmetric positions with respect to the surrounding oxygen ions, favoring the ferroelectricity, the magnetism comes out, of course, from Fe^{3+} and or Mn^{3+} ions. Physically, this approach shows no essential difference from that which leads to independent multiferroic materials.

1.3.2.1 $BiMnO_3$

$BiMnO_3$ is the unique system in which both M and P are reasonably large. In fact, it is one of the few multiferroics offering both ferroelectric and ferromagnetic orders. It has a monoclinic perovskite structure (space group $C2$) [28] [29], and shows a ferroelectric transition at $T_C \sim 800$ K accompanied by a structure transition shown in Fig.1.3(a)-(d) with the remnant polarization of $\sim$16 μC cm^{-2}, and a ferromagnetic transition at $T_{FM} \sim$ 110 K shown in Fig.1.3(e) [30] below which the two orders coexist.

A study of the electron localization functions (ELFs), obtained by a first principle study, provide evidence for the "lone-pair" mechanism in $BiMnO_3$. Further calculations reveal that the localized lone pair in the distorted structure includes a contribution from the 2p states on the oxygen ligands [33]. These predictions suggest that the lone pairs on the Bi ions are stereochemically active and are the primary driving force for the highly distorted monoclinic structure and, thus, for ferroelectricity in $BiMnO_3$.

The magnetoelectric coupling between ferroelectricity and magnetism in $BiMnO_3$ would be weak, as argued above and confirmed experimentally. The observed dielectric constant shows only a weak anomaly at T_{FM} and is fairly insensitive to external magnetic fields. The maximum decrease of dielectric constant upon a field of 9T appearing around T_{FM} is around 0.6%, as shown in Fig.1.3 [31].

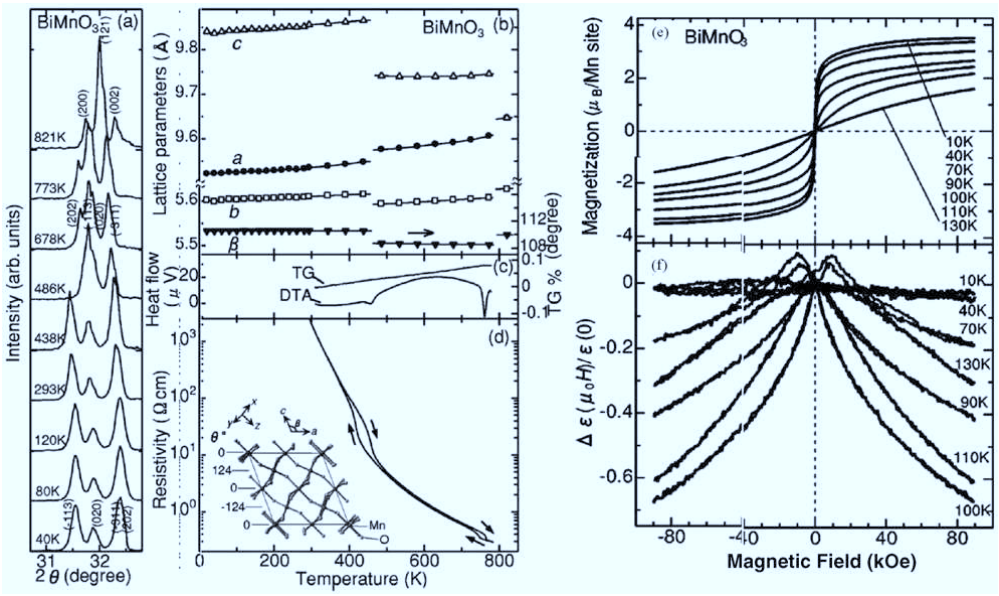

FIGURE 1.3 – A summary of experimental results on BiMnO3. (a) X-ray diffraction spectra at various temperatures ; (b)-(d) lattice parameters, thermal analysis YG and DTA, and resistivity as a function of temperature, respectively ; (e) magnetic M-H hysteresis and (f) hysteresis of magnetodielectric effect $\Delta\varepsilon(\mu_0 H)/\varepsilon(0)$ against magnetic field at various temperatures [31].

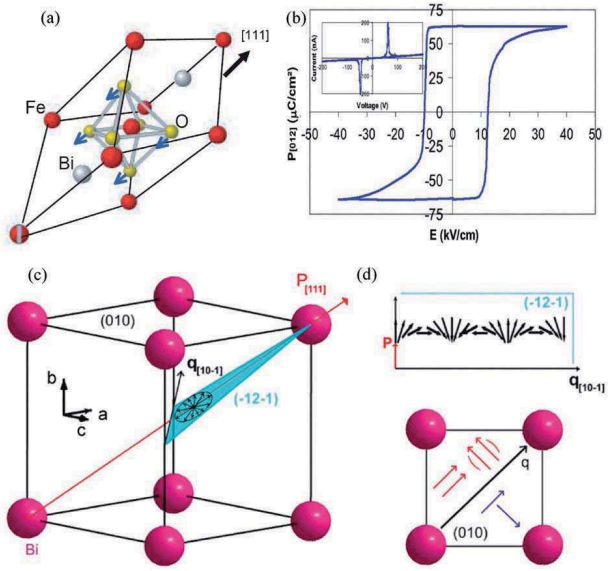

FIGURE 1.4 – (a) Lattice structure of $BiFeO_3$, with the Bi ion shifting along the [111] direction and the distorted FeO_6 octahedra surrounding the [111] axis. Polarization P points along the [111] direction, as indicated by the arrow [35]. (b) Measured P-E loop for a $BiFeO_3$ single crystal [34]. (c), (d) Spin configuration of $BiFeO_3$. The spiral spin propagation wave vector q is along the $[10\bar{1}]$ direction and the polarization is along the [111] direction. These two directions define the $(\bar{1}2\bar{1})$ cycloidal plane on which the spin rotation proceeds, as shown by the shaded region in (c) and (d)[36].

1.3.2.2 $BiFeO_3$

$BiFeO_3$ is also well known, as it is one of the few multiferroics with both ferroelectricity and magnetism above room temperature. The rhombohedrally distorted perovskite structure can be described with $a = b = c = 5.633$ and $\alpha = \beta = \gamma = 59.4^{\circ}$and space group $R3c$ at room temperature. The structure allows for the shift of Bi ions along the [111] direction as shown in Fig.1.4(a) and consequently the electric polarization prefers to align along the [111] direction, as shown by the arrow. The ferroelectric Curie point is $T_C = 1103$ K and the antiferromagnetic Néel point is $T_N = 643$ K, while weak ferromagnetism at room temperature can be observed due to a residual moment in a canted spin structure [37]. Usually a high ferroelectric Curie point leads to a large polarization, since other typical ferroelectrics with such Curie points have a polarization up to about 100 μC cm^{-2}. However, for $BiFeO_3$ single crystals, the measured P along the [001] direction at 77 K was 3.5 μC cm^{-2}, indicate a possible P of only 6.1 μC cm^{-2} along the [111] direction. For polycrystalline samples, the expected value of P should be smaller. The reason for this small polarization is possibly due to the high leakage current as a result of defects and the non-stoichiometry of the test materials.

$BiFeO_3$ has a complicated magnetic configuration. Neutron scattering experiments have revealed that the antiferromagnetic spin order is not spatially homogenous. It rather has a

spatially modulated structure [37], manifested by an incommensurate (ICM) cycloid structure of wavelength λ∼62nm, as shown in Fig. 1.4(c) and (d). The spiral spin propagation wave vector q is along the $[10\bar{1}]$ directions and the polarization is along the [111] directions. These two directions define the $(\bar{1}2\bar{1})$ cycloidal plane where the spin rotation occurs, as shown by Fig.1.4(d) and the shaded region in Fig.1.4(c). The antiferromagnetic vector is locked within the cycloid, averaged to zero over a scale of approximately λ, and responsible for the very weak magnetization. It is expected that this cycloid structure may be partially destroyed if the sample size is as small as the cycloid wavelength (∼62nm), predicting enhanced magnetization and even weak ferromagnetism in nanoscale samples. This mechanism is responsible for the enhanced magnetization observed in thin-film samples. Indeed, for practical applications high-quality thin films in heteroepitaxial form are preferred and a large amount of effort was devoted to produce thin films of $BiFeO_3$. Therein, the crystal structure is monoclinic rather than rhombohedral, due to the strain by the substrate [38] [87] [40]. High-quality $BiFeO_3$ epitaxial films with room-temperature polarization close to the theoretical value, about 60-80μC cm^{-2}, are available [41]. Further investigations have revealed that the in-plane strains in the thin films could drive a rotation of the spontaneous polarization on the (110) plane ; this result allows for a strain tunablity of the out-of-plane polarization in (001)-oriented $BiFeO_3$ films.

Because of the two almost independent mechanisms which originate magnetism and electrical polarization, one may postulate that the magneto-electric coupling in $BiFeO_3$ would also be very weak. However, some recent studies show that the ferroelectric polarization is closely tied to the ICM cycloid spin structure and a significant magnetoelectric effect was observed. This situation is very similar to the ferroelectricity induced by spiral spin order, that we will discuss later in detail.

For those ferroelectrics addressed in the last two sections, the main driving force for the ferroelectric transition comes from a structural instability mostly induced by electronic pairing processes. They were identified as "proper" ferroelectrics. If, on the other hand, polarization is part of a more complex lattice distortion or it appears as a product of some other configurations, the ferroelectricity is called "improper", as we will describe in the next sections.

1.3.3 Geometric ferroelectricity in hexagonal manganites

Hexagonal manganites $RMnO_3$, where R is a rare-earth element (Ho-Lu, or Y), fall into the improper ferroelectrics category, and they are often cited as typical examples of "d^0-ness" rule violation. In these compounds of this group, R is a relatively small ion, so that they have different crystal structures from the orthorhombic manganites which instead present large R ions such as La, Pr, Nd, etc. We will describe the hexagonal manganites by means of two examples : $YMnO_3$ and $HoMnO_3$. The analysis of the former compound will help us to discuss some details of this new kind of ferroelectricity. The description of the latter system will allow us to analyze the most fascinating effect concerning the hexagonal $RMnO_3$: the control of the magnetic phases by means of an electric field.

1.3.3.1 $YMnO_3$

$YMnO_3$ is a well-known multiferroic system with a ferroelectric Curie temperature T_C = 950 K and an antiferromagnetic Néel temperature T_N = 77 K. The hexagonal structure adopted by $YMnO_3$ and other manganites with small R ions consists of non-connected layers of MnO_5 trigonal bi-pyramids, corner-linked by in-plane oxygen ions (O_P). The apical oxygen ions (O_T) form close-packed planes separated by a layer of Y^{3+} ions. A schematic view of the crystal structure is given in Fig.1.5(a).

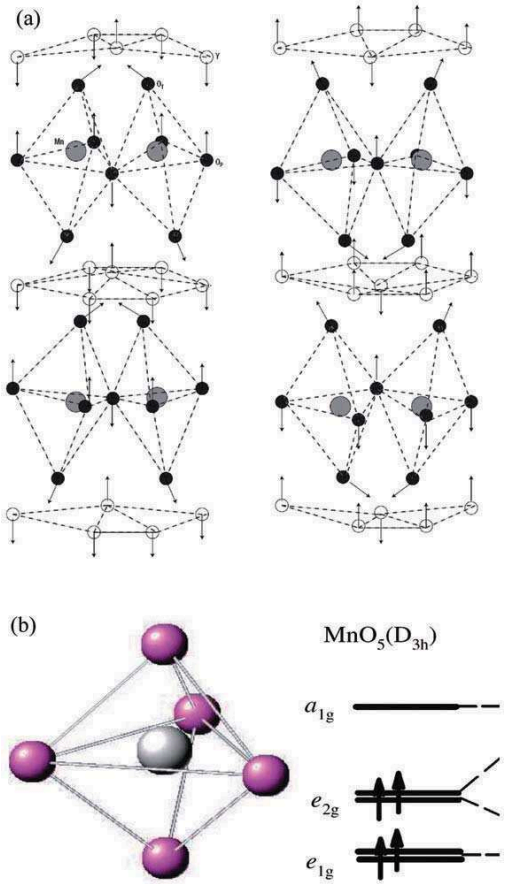

FIGURE 1.5 – (a) Lattice structure of ferroelectric $YMnO_3$, with the arrows indicating the direction of ion shift from the centrosymmetry positions [43]. (b) Electronic configuration of Mn ions in the MnO_5 pyramid of $YMnO_3$ [35]

Different crystal structures are related to different electronic configurations. In contrast to conventional perovskites, in $YMnO_3$ the Mn^{3+} ion is not inside the O_6 octahedra but in the centre of O_5 trigonal bi-pyramids (five-fold coordination). Similarly, R-ions (e.g. Y ions) are not in a 12-fold but a 7-fold coordination. Consequently, the crystal field level scheme of Mn ions is different from the usual scheme of manganites. The *d*-levels are split into two doublets and an upper singlet, instead of a triplet t_{2g} and a doublet e_g as in

orthorhombic perovskites (Fig.1.5(b)). Therefore, the four d electrons of Mn^{3+} ions occupy the two lowest doublets, leaving no orbital degeneracy. Consequently, Mn^{3+} ions in these compounds are not Jahn-Teller active.

Early work in the 1960s established $YMnO_3$ to be ferroelectric with space group $P6_3cm$, and revealed an A-type antiferromagnetic order with non-collinear Mn spins oriented in a triangular arrangement [44]. In this view the ferroelectric polarization should arise from an off-centre distortion of Mn ions towards one of the apical oxygen ions. However, structural analysis revealed that Mn ions remain very close to the centre of the oxygen bi-pyramids and, thus, are definitely not producing the ferroelectric distortion [43].

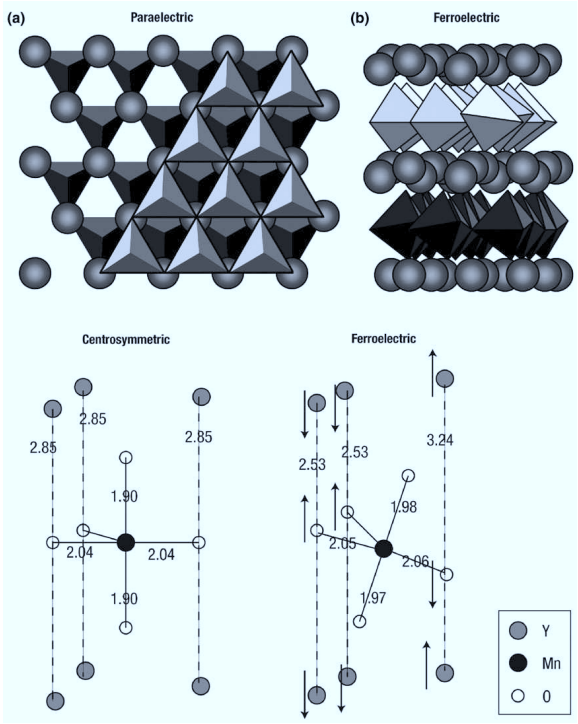

FIGURE 1.6 – Crystal structures of (a) PE phase and (b) ferroelectric phase of $YMnO_3$. The spheres and pyramids represent Y ions and MnO_3 pyramids, respectively. The arrows indicate the direction of ion shift from the centrosymmetry positions, and the numbers are the bond lengths [43].

New first-principle calculations also predict that the off-centre distortion of Mn ions is energetically unfavourable. The main difference between the PE $P63/mmc$ structure and ferroelectric $P6_3cm$ structure is that all ions in the PE phase are restricted in the ab plane, whereas in the ferroelectric phase, the mirror planes perpendicular to the hexagonal c-axis are lost (Fig.1.5(a) and Fig.1.6). The structural transition from the centrosymmetric $P63/mmc$ to the ferroelectric $P6_3cm$ is mainly facilitated by two types of atomic displacements (see Ref. [43] for details) and the result is that one of the two Y-O_P bonds of length $\sim$ 2.8 is reduced down to $\sim$2.3, and the other is elongated to 3.4, leading to a net elec-

tric polarization (Fig.1.6). Polarization-dependent X-ray absorption spectroscopy (XAS) indeed demonstrated that the Y 4*d* states are strongly hybridized with the O 2*p* states.

This picture suggests that the main dipole moments are contributed by the Y-O pairs instead of the Mn-O pairs previously inferred. This is also an additional example for the A-site ion-induced ferroelectricity, but the details of the mechanism for such distortion remain puzzling. In fact, the huge Y-O_P off-centre displacements are quite distinct from the small displacements induced by chemical activity in conventional ferroelectric perovskite oxides. In contrast, the induced electric polarization remains much smaller. Thus, one may argue that a different mechanism is responsible for the ferroelectric distortion.

The spin configuration of hexagonal $YMnO_3$ is frustrated, and the easy plane anisotropy of Mn spins restricts the moments on the *ab* plane, which are thus dominated by the strong in-plane antiferromagnetic superexchange interaction. The inter-plane exchange between the Mn spins is by two orders of magnitude lower. Therefore, $YMnO_3$ is an excellent example of a quasi-two-dimensional Heisenberg magnet on a triangular lattice with a spin frustration generated by geometric constraint. Accordingly, the Mn spins undergo long-range order at T_N with the magnetic moments developed into a non-collinear configuration with a 120°angle between neighboring spins [45].

1.3.3.2 $HoMnO_3$

$HoMnO_3$ is an interesting compound because it has been demonstrated that an external electric field may drive the system into a different magnetic state, thereby modulating the magnetic order of the Mn^{3+} sublattice. The ferroelectric phase of $HoMnO_3$ appears at the Curie point T_C = 875 K, and possesses $P6_3cm$ symmetry with a polarization P = 5.6 μC cm^{-2} along the hexagonal c-axis [47]. In addition to the Mn^{3+} ions, Ho^{3+} ions with *f* electrons also contribute to a non-zero magnetic moment with the easy axis anisotropy along the c-axis. The as-induced frustration favors a magnetic-ordered state composed of three magnetic sublattices with Mn^{3+} ($3d^3$) ions at the 6*c* positions and Ho^{3+} ($4f^{10}$) ions at the 2*a* and 4*b* positions, respectively, as shown in Fig.1.7(a) (see also Ref [48]). Below $T_N \sim$ 76 K, the Mn spins favor non-collinear antiferromagnetic ordering. The coupling between the Mn spins and Ho spins drives an in-plane rotation of the Mn spins at T_{SR}∼33K. Correspondingly, the Ho spins become magnetically polarized and a small magnetization from the antiferromagnetic sublattice was detected and enhanced as temperature fell. In fact, the measured *c*-axis magnetic susceptibility has an abrupt decrease at T_{SR}, although the change is small, indicating the onset of the antiferromagnetic Ho spin order with magnetic moments aligned along the hexagonal c-axis. At an even lower temperature, $T_{Ho} \sim 5$ K, another spin reorientation transition associated with the Ho spins takes place, leading to a low-temperature phase with $P6_3cm$ magnetic symmetry and a remarkable enhancement of Ho spin moment. This configuration remains antiferromagnetic. The two Ho^{3+} sublattices are assumed to be Ising-like ordered along the z(c)-axis, exhibiting antiferromagnetism or ferri-/ferromagnetism.

The most interesting feature in $HoMnO_3$ is that the dielectric property is very sensitive in response to the variation of the magnetic order. The dielectric constant as a function of temperature, ε(T), under zero magnetic field, exhibits three distinct anomalies, as shown in Fig.1.7(b) and (c). At the Néel point, ε(T) shows a clear decrease due to the onset of an

antiferromagnetic order with the Mn spins. This feature was confirmed in other hexagonal manganites or multiferroics and is usually viewed as a symbol of antiferromagnetic ordering. The transition into the $P6_3cm$ magnetic structure at $T_{Ho} \sim 5.2$ K is accompanied by a sharp increase of ε(T). The most notable anomaly is the sharpest peak at T_{SR}~32.8K. In addition, the dielectric constant exhibits an evident dependence on the magnetic field. A magnetic field H, imposed along the c-axis, shifts the sharpest peak at T_{SR} toward a lower temperature, and the peak at T_{Ho} toward a higher temperature. These additional anomalies mark the generation of a field-induced phase raising from the indirect coupling between the ferroelectric and antiferromagnetic orders.

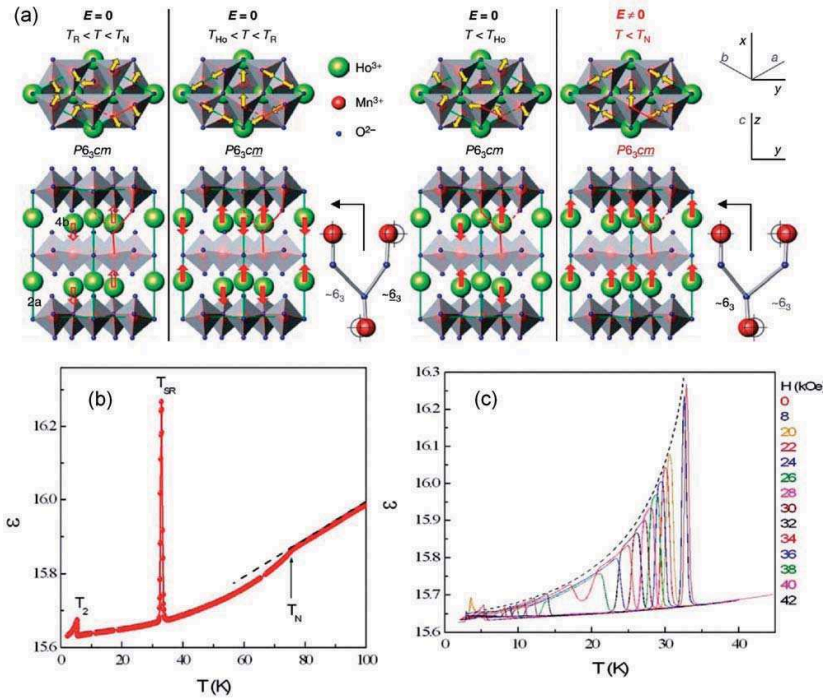

FIGURE 1.7 – a) Spin configurations and lattice symmetry of $HoMnO_3$ in different temperature ranges with and without electric field. The red arrows represent the Ho spins and the yellow arrows for the Mn spins (see the text for details)[48]. (b) Dielectric constant as a function of temperature for $HoMnO_3$, indicating three anomalies [35]. (c) Dielectric constant as a function of temperature for $HoMnO_3$ under different magnetic fields [49].

1.3.4 Spiral spin-order-induced ferroelectricity

It should be noted that the perspectives of the so far reviewed mechanisms for multiferroicity are in some ways disappointing, because the ferroelectricity and magnetism basically originate from different ions or subsystems. From a macroscopic point of view one may not expect a very strong magnetoelectric coupling in these multiferroics, as confirmed by the experiments. In the next section we will describe an alternative mechanism for ferroelec-

tricity, induced directly by the spin order, in which an intrinsic magnetoelectric coupling occurs between the ferroelectric and magnetic order parameters.

1.3.4.1 Symmetry considerations

We have already shown that a multiferroic system, that is both ferromagnetic and ferroelectric, requires the simultaneous breaking of the spatial-inversion and time-reversal symmetries. Moreover, time reversal $\mathbf{t} \rightarrow -\mathbf{t}$ must leave the magnetoelectric coupling invariant. As this operation transforms $\mathbf{M} \rightarrow -\mathbf{M}$, and leaves $\mathbf{P}$ invariant, the lowest order magnetoelectric coupling term has to be quadratic in $\mathbf{M}$. However, the fourth-order term $-P^2M^2$ does not contribute to any ferroelectricity because it is compensated by the energy cost for a polar lattice distortion proportional to $-P^2$ In presence of spatially inhomogeneous spin configuration, the above symmetry argument allows for the third-order magnetoelectric coupling, which describes the coupling between a homogeneous polarization and an inhomogeneous magnetization : this term is linear in P and contains the gradient of M [50]. This simple symmetry argument immediately leads to the following magneto- electric coupling term in the Landau free energy [51] :

$$\Phi_{ME}(\mathbf{r}) = P \cdot \left\{ \gamma \cdot \nabla(M^2) + \gamma' \left[M(\nabla \cdot M) - (M \cdot \nabla)M \right] + ... \right\} \tag{1.6}$$

where r is the vectorized spatial coordinate, $\mathbf{P}$ and $\mathbf{M}$ are the polarization and magnetization, and γ and γ' are the coupling coefficients. The first term on the right-hand side is proportional to the total derivative of the square of the magnetization and would not give contribution unless P is assumed to be independent of the spatial coordinate $\mathbf{r}$. By including the energy term associated with P, *i.e.* $P^2/2\chi_e$ (χ_e is the dielectric susceptibility) into the free energy, a minimization of the free energy with respect to P produces

$$P = \gamma' \chi_e \left[M(\nabla \cdot M) - (M \cdot \nabla)M \right] \tag{1.7}$$

This simple symmetry argument predicts the possible multiferroicity in spin-frustrated systems, which always prefer to have spatially inhomogeneous magnetization due to the competing interactions. For example, a one-dimensional spin chain with a ferromagnetic nearest-neighbour interaction $J < 0$ has a uniform ground state with parallel-aligned spins. An additional antiferromagnetic next-nearest-neighbour interaction $J' > 0$, which meets $J'/|J| > 1/4$, frustrates this simple spin order, as shown in Fig.1.8(a). This situation can be expressed as a Heisenberg model $\mathcal{H} = \sum_n \left[J \cdot \mathbf{S}_n \cdot \mathbf{S}_{n+1} + J' \cdot \mathbf{S}_n \cdot \mathbf{S}_{n+2} \right]$, where $\mathbf{S}_i$ is the Heisenberg spin moment at site i referring to a spin chain. The frustrated ground state is characterized by a spiral spin order (spiral spin-density wave (SDW)) and can be expressed as

$$\mathbf{S}_n = \mathbf{S}_1 \mathbf{e}_1 cos\mathbf{Q} \cdot \mathbf{r} + \mathbf{S}_2 \mathbf{e}_2 sin\mathbf{Q} \cdot \mathbf{r} \tag{1.8}$$

where the unit vectors $\mathbf{e}_i$ (i=1, 2, 3) form an orthogonal basis, $\mathbf{e}_3$ is the axis around which spins rotate and vector $\mathbf{Q}$ is given by $cos(Q/2) = -J'/(4J)$. If $\mathbf{S}_1$ and $\mathbf{S}_2$ are both non-zero, Eq.1.8 describes a spiral SDW with the $\mathbf{e}_3$ spin rotation axis. Like any other magnetic order, the spiral spin order spontaneously breaks the time-reversal symmetry. In addition, it also breaks the spatial inversion symmetry because the sign reversal of all

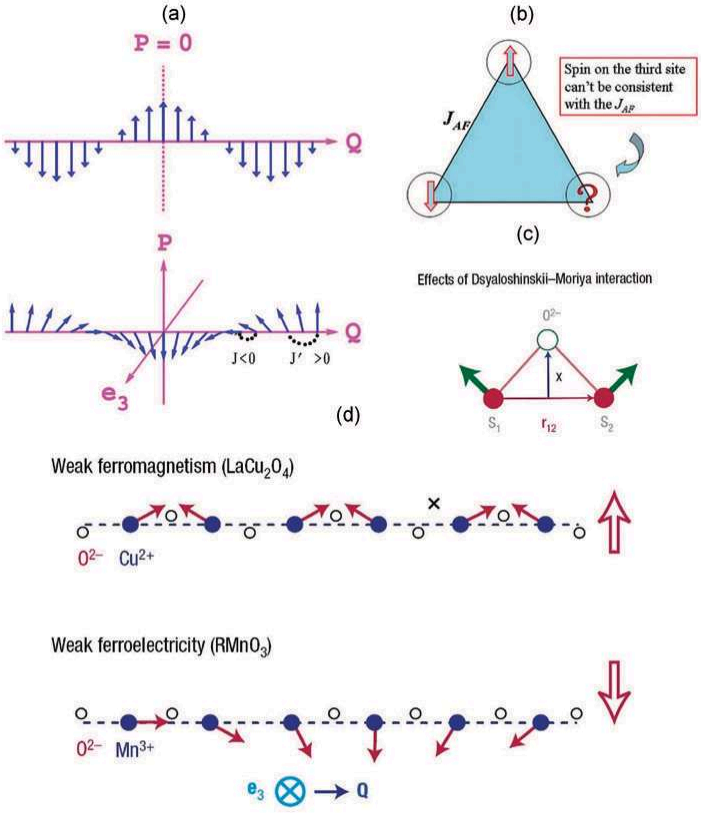

FIGURE 1.8 – (a) Sinusoidal (upper) and spiral (lower) spin order for a one-dimensional spin chain with competing exchange interactions. (b) Geometric spin frustration in a two-dimensional triangular lattice. The DM interaction in La_2CuO_4 and $RMnO_3$ are illustrated in (c) and (d). The open arrow in (d) for La_2CuO_4 denotes the direction of weak ferromagnetism and the open arrow in (d) for $RMnO_3$ denotes the direction of the generated polarization [32].

coordinates inverts the direction of the spin rotation in the spiral. Therefore, the symmetry of the spiral spin state allows for multiferroicity.

The above simple model can be extended to two or three-dimensional spin systems. In general, two or more competing magnetic interactions can induce the spin frustration and the spiral (helical) spin order which, in turn, breaks the spatial-inversion and time-reversal symmetries simultaneously, thus establishing the ferroelectric order.

1.3.4.2 Microscopic mechanism

In addition to the symmetry argument presented above, three microscopic mechanisms responsible for ferroelectricity in magnetic spiral systems have been proposed : the Inverse Dzyaloshinskii-Moriya (DM) model, the spin current model (KNB model), and the Electric current cancellation model. A complete description of this three models is far from the aim of this work. Therefore we will only present the overall idea behind those theoretical models.

The **Inverse DM model** consider the displacement of the oxygen ions in the spin spiral system as a plausible microscopic mechanism for ferrroelectricity [52]. According to this theory the oxygen ions displacement is driven by the antisymmetric DM interaction, that is a relativistic correction to the usual superexchange interaction. Qualitatively, the idea of the DM interaction is that if the symmetry of a pure antiferromagnetic state is such that the appearance of a small magnetization does not lead to further symmetry lowering, any microscopic mechanism favors a non-zero magnetization, even if it is rather weak. The result is that the DM interaction could drive the oxygen ions to shift in one direction perpendicular to the spin chain, thus resulting in an electric polarization, as shown in the lower panel of Fig.1.8(d). A detailed discussion for the typical multiferroic $TbMnO_3$ can be found in Ref. [53].

The **KNB** model was proposed by Katasura, Nagaosa and Balatsky, hence the name. This well known model has been widely utilized to explain a number of experimentally observed facts due to its clear physics and simple picture. It gives an expression for the spin current from site n to site $n+1$ which describes the precession of a spin S_n in the exchange field created by the spin S_{n+1} [54]. Although the model may be oversimplified, it is physically equivalent to the DM approach.

The **Electric current cancellation model** is derived from fundamental electromagnetic principles. The current operator of electrons is defined as the change in Hamiltonian with respect to the variance of the vector potential A of the electromagnetic field

$$J = -c\delta\mathcal{H}/\delta A \tag{1.9}$$

where c is the light velocity [55].

From this model we can obtain an important result on ferroelectric system : if there is an internal electric field E which is spontaneously generated, the electric field must satisfy $e|E|h/\sqrt{2m^*\Delta_g} < \Delta_g$ in order to maintain the validity of the insulator. A semi-quantitative estimation gives a polarization of only approximately $100\mu Cm^2$ for typical manganites, a disappointing prediction from the point of view of technological applications.

In spite of different microscopic origins, the three models outlined above give a similar

prediction

$$\mathbf{P}_{n,n+1} \propto \mathbf{r}_{n,n+1} \times (\mathbf{S}_n \times \mathbf{S}_{n+1}). \tag{1.10}$$

It has to be noted that all these models are based on the transverse spiral spin-ordered state in which the spin spiral plane contains the propagation vector of spin modulation. This postulation may not be always true. Some other spiral spin-ordered states, which are not reachable by the three models, can indeed induce ferroelectricity.

1.3.4.3 Experimental evidence

- **One-dimensional spiral spin chain systems. Example : $LiCu_2O_2$**
  We first describe systems which present one-dimensional (1D) spin systems, as 1D chain magnet with competing nearest-neighbour ferromagnetic interaction (J) and next-nearest-neighbour antiferromagnetic interaction (J'). Such a system will develop its magnetic configuration into a frustrated spiral spin order as long as $|J'/J| < 1/4$, as already theoretically predicted (Fig.1.8(a)). Experimentally, the spin configuration of $LiCu_2O_2$ can be approximately considered as a quasi-1D spin chain system. The crystal structure is shown in Fig.1.9(a), where magnetic Cu^{2+} ions are blue and non-magnetic copper ions are green with red dots for oxygen ions. The picture of a quasi-1D spin spiral has been verified since the equivalent nearest-neighbour exchange interactions and frustration ratio were estimated experimentally to be J_1=5.8 meV and $|J_2/J_1| = 0.29 > 1/4$ [56]. Indeed, a non-collinear spiral spin order was identified for these quasi-1D spin ladders with a spiral propagation vector (0.5, ξ, 0) and ξ = 0.174 was determined. A ferroelectric polarization along the c-axis (P_C) would be expected, and was experimentally evident in $LiCu_2O_2$, as shown in Fig.1.9(c).
  The most interesting characteristic of this system is the intrinsic magnetoelectric coupling which is evident in the response of the polarization : by applying an external magnetic field along the b-axis, a rotation of spins within the bc plane (Fig.1.9(c)) toward the ab plane is observed, which induces a switch of the polarization orientation from the c-axis to the a-axis.
- **Two-dimensional spiral spin systems : $Ni_3V_2O_8$ and $RbFe(MoO_4)_2$**
  $Ni_3V_2O_8$ is an example of a quasi-2D spin structure with a frustrated spin order. The electric polarization together with the spin structure and phase diagram are shown in Fig.1.10 It is well-known that in spin systems with 2D triangular lattices an antiferromagnetic interaction leads to a frustrated spin structure, as shown in Fig.1.8(b). While the second spin can easily align antiparallel with respect to the first spin due to the antiferromagnetic interaction, the third cannot align in any stable way, leading to a frustrated spin structure. However, real systems seem far more complicated than this simple picture. Given the classical Heisenberg spins, the 2D triangular lattice generally favors the 120°spiral spin order at the ground state.
  Another compound exhibiting a quasi-2D frustrated system is $RbFe(MoO_4)_2$ (RFMO), which presents at room temperature the typical easy-plane triangular lattice, described by space group $P\bar{3}m1$. At T_0 = 180 K, the symmetry is lowered to $P3$ by a lattice distortion, as shown in Fig.1.11(a), in which the out-of-plane ions lead to two types of triangles : the "up triangles" with a green oxygen tetrahedron above the plane and the "down triangles" with a tetrahedron below the plane [58]. For $T < T_0$, RFMO

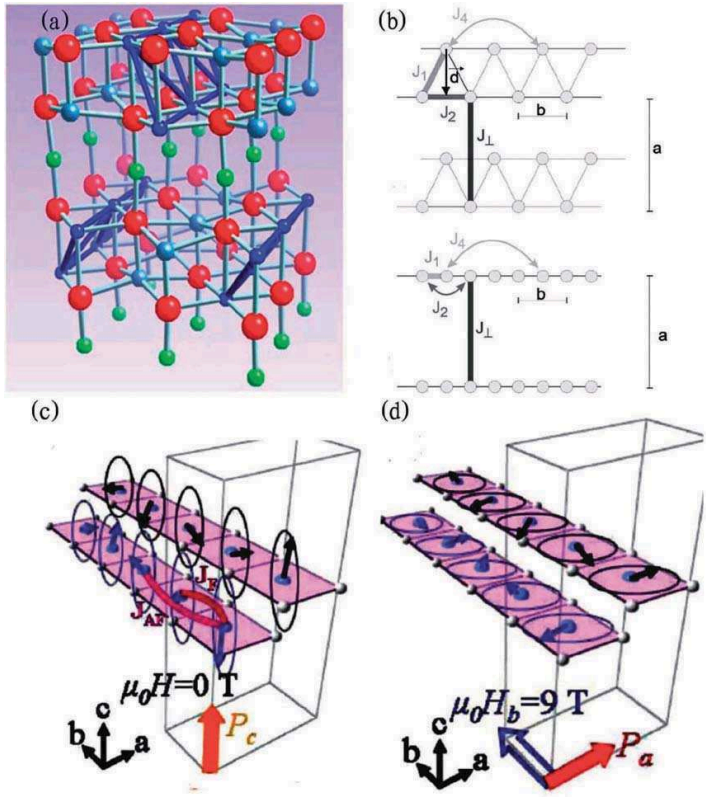

FIGURE 1.9 – (a) Crystal structure of $LiCu_2O_2$ and (b) its spin-ordered configuration. The blue lines indicate the quasi-1D spin ladders consisting of Cu ions. The red spheres represent the oxygen ions and grey spheres denote the Li ions. Spiral arrangements of the Cu spin ladders and corresponding polarization under (c) zero magnetic field and (d) 9.0T applied along the b-axis [56].

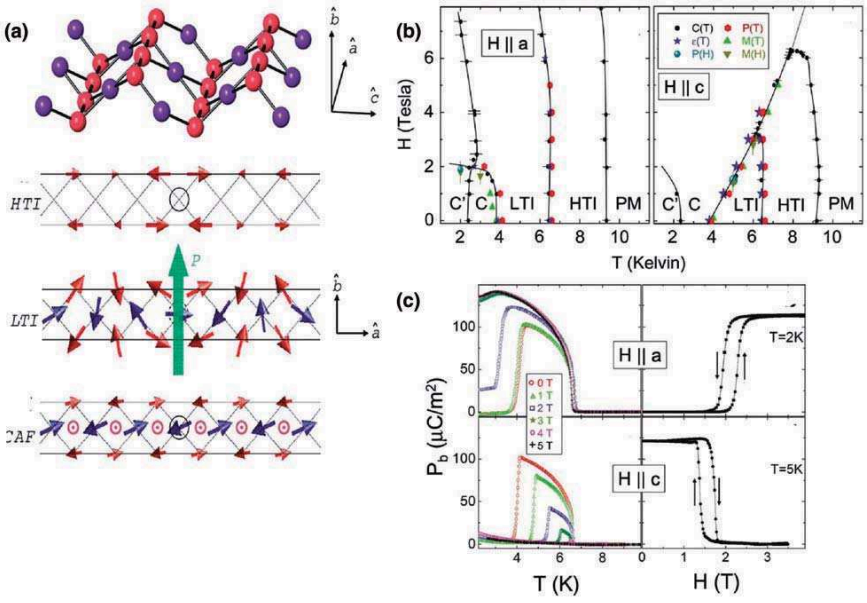

FIGURE 1.10 – (a) Lattice structure and three spin arrangements in Ni sublattice for $Ni_3V_2O_8$. The LTI (low-temperature insulator) phase exhibits a spin spiral structure which can induce ferroelectric polarization P along the *b*-axis, while the spins in the HTI (high-temperature insulator) and CAF (canted antiferromagnetic) phases are collinear. (b) Phase diagram of magnetic field against temperature for $Ni_3V_2O_8$ under magnetic field along the *a*-axis and *c*-axis, respectively. (c) Polarization along the b-axis as a function of temperature and magnetic field applied along the *a*-axis and *c*-axis, respectively [57].

contains perfect Fe^{3+} triangular lattice planes in which spins S = 5/2 are coupled through antiferromagnetic superexchange interactions. Magnetism is dominated by the intra-plane interactions of an energy scale of approximately 1.0 meV and by the inter-plane interaction at least 25 times weaker. Therefore, RFMO is essentially a XY antiferromagnet on a triangular lattice with a long-range magnetic ordering at T_N = 3.8 K. The magnetic ground state is shown in Fig.1.11(b). Experimental measurements revealed an electric polarization of approximately 5.5 μC cm^{-2} along the c-axis. According to the KBN model or the inverse DM model, the generated local polarization should lie in the basal plane but in view of the three-fold rotation axis, the macroscopic polarization $P = \sum_n P_{n,n+1}$ should vanish. This means that neither the KNB model nor the inverse DM model can explain the origin of ferroelectricity in RFMO.

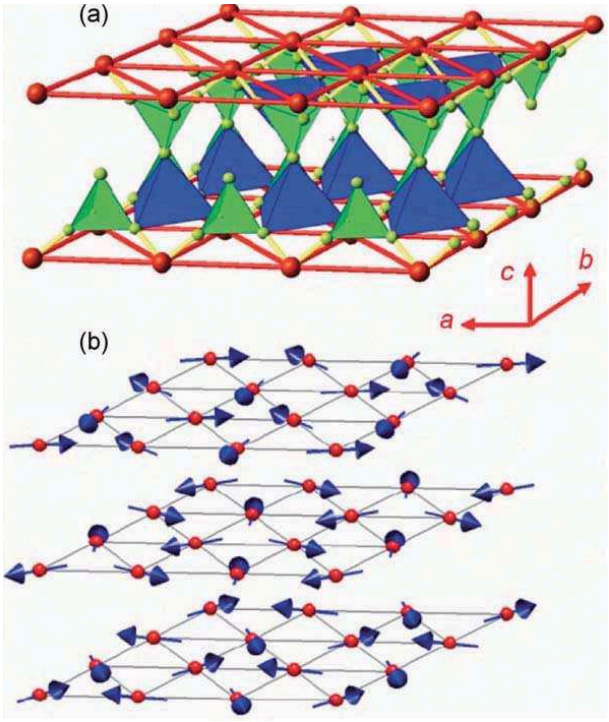

FIGURE 1.11 – Crystal lattice structure (a) and 120°spin-ordered state (b) in triangular-lattice $RbFe(MoO_4)_2$[58].

– **Three-dimensional spiral spin systems. Example : $TbMnO_3$**
We finally report some recent investigations on three-dimensional (3D) frustrated spin systems. The typical examples are perovskite manganites as $TbMnO_3$ or $DyMnO_3$. We pay special attention to $TbMnO_3$ which has been extensively investigated. At room temperature it has an orthorhombically distorted perovskite structure (space group *Pbnm*), unlike the antiferromagnetic-ferroelectric hexagonal rare-earth manganites $RMnO_3$ (R = Ho, Y, see section 1.3.3). The $t_{2g}^3 e_g^1$ electronic configuration of the Mn^{3+} site is identical to the parent compound of CMR manganites $LaMnO_3$ where the orbital order favors the ferromagnetic spin order in the ab-plane and anti-

ferromagnetic order along the c-axis. The replacement of La by smaller ions, such as Tb and Dy, enhances the structural distortion (*i.e.* enhances the strength of the next-nearest-neighbour antiferromagnetic exchange with respect to the nearest-neighbour ferromagnetic interaction in the ab-plane). Consequently, the competition between the two types of interactions frustrates the spin configuration within the ab-plane and induces magnetic phase transitions at low temperature.
At room temperature, the crystal symmetry of $TbMnO_3$ has an inversion centre, and the system is non-polar. Magnetic and neutron scattering experiments showed that the spin structure favors an ICM collinear sinusoidal antiferromagnetic ordering of Mn^{3+} spins along the *b*-axis, taking place at $T_N = 41$ K with a wave vector $q = (0, k_s \sim 0.29, 1)$ in the *Pbnm* orthorhombic cell, as shown in Fig.1.12(a), (b) and (c) [59]. It is easily understood that the collinear sinusoidal antiferromagnetic state is PE and the ferroelectric phase may not appear unless the spin order is spiral or helicoidal-like. The polar structure appears only below approximately 30 K (T_{lock}) where an ICM-CM (or lock-in) transition occurs, generating a helicoidal structure with the magnetic modulation wave vector k_s which is nearly temperature-independent and locked at a constant value of about 0.28.

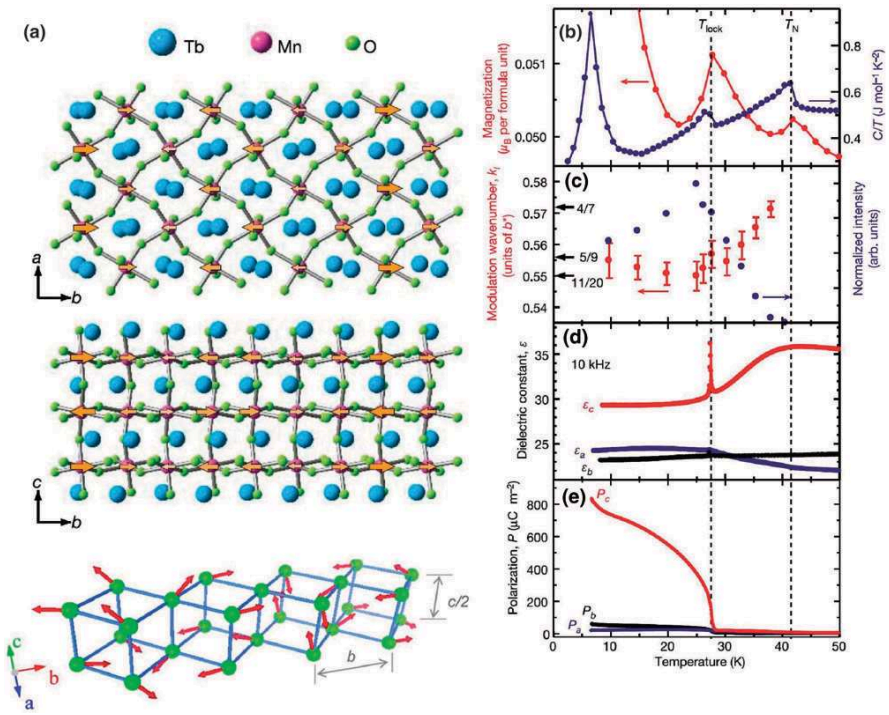

FIGURE 1.12 – (a) Spin configuration of the ICM collinear sinusoidal spin-ordered state at T = 35K (upper) and the spiral spin-ordered state at 15K (middle : the bc-plane, lower : 3D view) in $TbMnO_3$. The measured magnetization and specific heat, modulation wave number, dielectric constant and polarization along the a-axis, b-axis and c-axis, respectively, are shown in (b), (c), (d) and (e) [59].

The generated electric polarization $P \sim e \times k_s$, where e is the unit vector connecting

two neighboring spins, should parallel to the c-axis, because vector k_s is along the b-axis and the spin helicoidal points to the a-axis. This prediction is consistent with experiments, as shown in Fig.1.12(d) and (e). The dielectric constant along the c-axis exhibits a sharp peak at the lock-in point (T_{lock}), below which only the polarization along the c-axis is observable under a zero magnetic field. Further decrease of the temperature leads to a third anomaly in both the magnetization and the specific heat at approximately 7K, where the Tb^{3+} spins set the long-range ordering (propagation vector (0, ∼0.42, 1)).

As the lattice distortion is accompanied by spin order, an intrinsic magnetoelectric coupling between spin and polarization may be expected. In fact, experiments confirmed the realignment of polarization by an external magnetic field. A magnetic field over approximately 5 T applied along the b-axis suppresses the polarization along the c-axis (P_c) below a temperature T_{flop}. T_{flop} increases with increasing magnetic field, as shown in Fig.1.13(c). In turn, a finite polarization along the a-axis (P_a), is generated and the onset point is coherent with T_{flop} (Fig.1.13(d)). These experiments demonstrate convincingly the intrinsic magnetoelectric coupling effect characterized by a spontaneous switching of polarization from one alignment to another one.

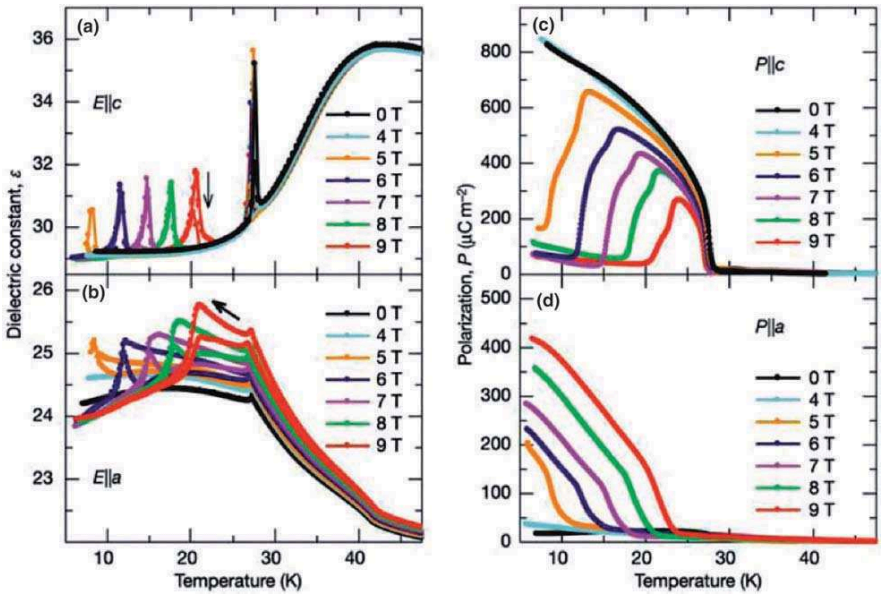

FIGURE 1.13 – Dielectric constants (a) and (b) and polarizations (c) and (d) along the c-axis and a-axis as functions of temperature under different magnetic fields for $TbMnO_3$ [59].

The multiferroicity in systems with spiral spin order was also found in several other perovskite manganites. Fig.1.14 summarizes the phase diagram by plotting T against the Mn-O-Mn bond angle ϕ which scales the rare-earth ionic radius. The shaded region corresponds to the spiral spin order and, thus, the multiferroicity [60]. Those manganites with even smaller rare-earth ions may exhibit geometrical ferroelectricity, as already discussed in Section 1.3.3.

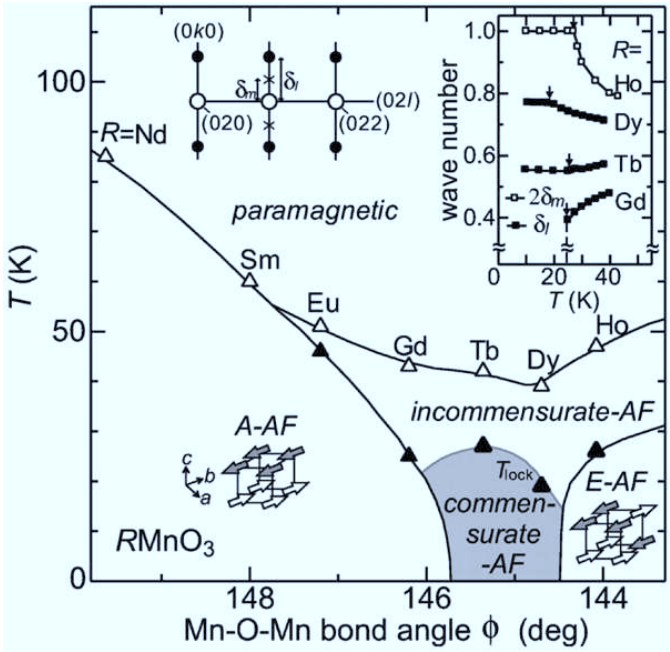

FIGURE 1.14 – Phase diagram of temperature against Mn-O-Mn bonding angle ϕ (corresponding to different rare-earth ionic radii) for manganites $RMnO_3$. The inset shows the wave numbers of spiral spin order for these manganites [60].

– **Electric field control of magnetism in spin spiral multiferroics : $TbMnO_3$ and $BiFeO_3$**

The control of polarization by the magnetic field in multiferroic frustrated oxides was demonstrated extensively. Starting from the intrinsic magnetoelectric coupling in those materials, one may also expect an effective control of the magnetization by an electric field. Nevertheless, so far no macroscopic evidence of this control has been presented, while the microscopic identification in some multiferroics was reported only very recently. An example is $TbMnO_3$, where the magnetization switching associated with the polarization reversal was observed using spin-polarized neutron scattering [61]. This seems to be the first evidence to demonstrate that the helical spin order can be modulated by an electric field or by polarization switching. In Fig.1.15(a) we show the recorded two satellite scattering peaks at position (4,±q,L=1) with the neutron spins parallel (mode $I_\uparrow$) and antiparallel (mode $I_\downarrow$), respectively, to the scattering vector in the ferroelectric phase. The intensities of the two peaks are reversed by switching the polarization between the two states along the ±c-axis. This suggests that the spin helicity, in clockwise or counterclockwise mode, can be controlled by reversing the polarization, as schematically shown in Fig.1.15(b). Although this effect is very weak and the spin helicity reversal might not be realized at a temperature above T_C, a reversible magnetoelectric coupling between magnetization and polarization in $TbMnO_3$ was identified.

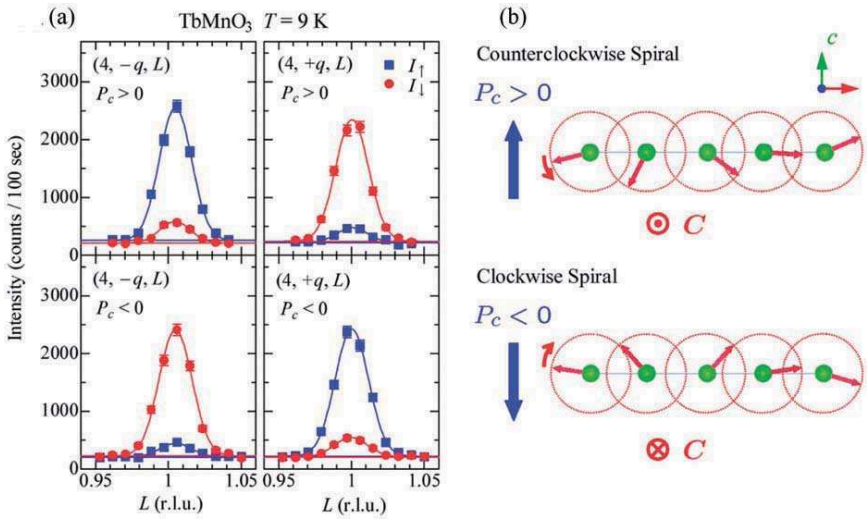

FIGURE 1.15 – Reversal of electric polarization Pc and spiral spin order induced by external electric field along the c-axis in $TbMnO_3$. (a) Scattering intensities and (b) spin configurations of the spin-order states with different polarization P_c. See the text for details [61].

Furthermore, this effect was recently demonstrated also in $BiFeO_3$. Although the ferroelectricity in this compound is commonly believed to originate from the lone-pair electrons of Bi ion (see Section 1.3.2), it has been shown that the Fe^{3+} ions are ordered antiferromagnetically (G-type) leading to a cycloidal spin structure, with a period

of approximately 62nm [62]. If such a structure contributes to the ferroelectricity in $BiFeO_3$ one may expect an intrinsic ME coupling. This idea was indirectly confirmed experimentally by a successful observation of the intimate link between the cycloidal magnetic structure of Fe^{3+} ions and the polarization vector [62]. The coupling between ferroelectric domains and antiferromagnetic domains in $BiFeO_3$ provides direct evidence of the above argument. Experimentally, piezo-force microscopy (PFM) or in-plane piezo-force microscopy (IPPFM) allows researchers to observe the ferroelectric domains under different electric fields, while X-ray photoemission electron microscopy (PEEM) can be used to monitor the antiferromagnetic domains simultaneously [63], [64].

Although there has been extensive research on this kind of multiferroics and several models have been developed, so far no quantitative agreement has been reached with experimental data in spiral spin-ordered materials. For example, first principle calculations on $LiCu_2O2_2$ [66] and $TbMnO_3$ [65] predict that all of these models are inadequate. Careful calculation on $TbMnO_3$ reveals that both the electronic and lattice effects contribute to the electric polarization and the latter one can be even dominant [65]. It is surprising that the displacements of Mn^{3+} and Tb^{3+} ions are generally larger than those of O^{2-} ions and give a significant contribution to the polarization [67], an effect not predictable by the current theories. At the end of this section, it is worth noting that multiferroic systems with spiral spin order do show the intrinsic magnetoelectric coupling, as demonstrated by careful experiments. However, their ferromagnetism seems to be very weak since essentially no spontaneous magnetization is produced by helical or spiral spin order.

1.3.5 Ferroelectricity in charge-ordered systems

In parallel to the development of multiferroics of spiral (helical) spin order, another type of multiferroics, *i.e.* charge-ordered (CO) multiferroics, is also receiving considerable interest. For conventional ferroelectrics and all of the multiferroics addressed above, the ferroelectricity originates from the relative displacement of anions and cations as well as from the lattice distortion associated with the second-order Jahn-Teller effect. However, an alternative mechanism, electronic ferroelectricity [68], was proposed recently, in which the electric dipole originates from the electronic correlation rather than the covalency. This would offer an attractive possibility for novel ferroelectricity which could be controlled by the charge, spin and orbital degrees of freedom of the electrons.

In many oxides which present strong electronic correlations, charge carriers may become localized at low temperature and form a periodic structure (*i.e.* CO state). The often cited example is magnetite Fe_3O_4, which undergoes a metal-to-insulator transition at approximately 125K (the Verwey transition) with a rather complex iron charge order pattern [69]. One expects that such a non-symmetric charge order may induce electric polarization. Another of the well-studied CO materials are manganites [70]. When $LaMnO_3$ (or related compounds in which the charge of Mn ions is formally 3+) and $CaMnO_3$ (in which the Mn charge is formally 4+) are alloyed, the resulting arrangement of Mn^{3+} and Mn^{4+} ions can be ordered in a particular case, as shown in Fig.1.16. Moreover, a spontaneously ordered pattern of the occupied orbitals throughout the crystal lattice (*i.e.* orbital-ordered state, (CO-OO) is possible.

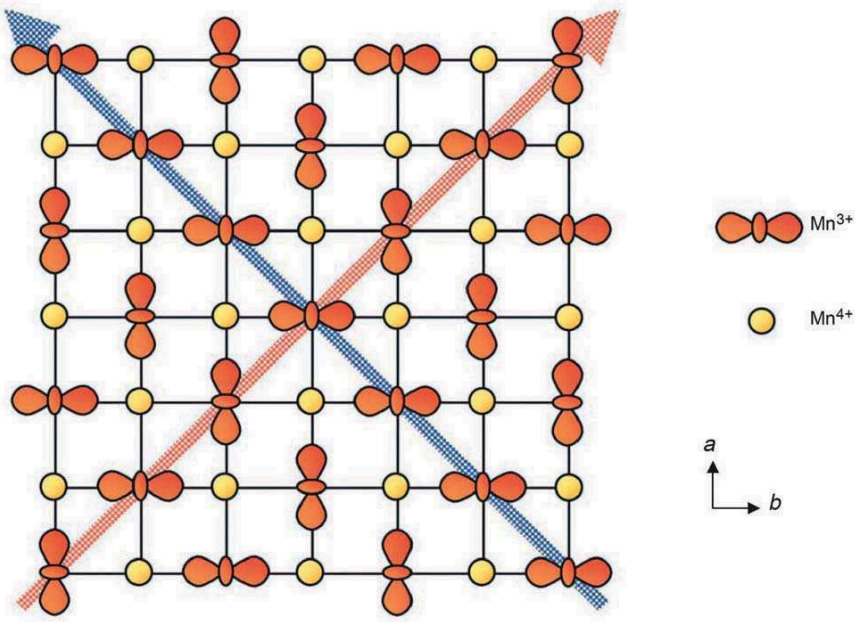

FIGURE 1.16 – CO-OO structure of $Pr_{0.5}Ca_{0.5}MnO_3$ at low temperature [70].

1.3.5.1 Charge frustration in $LuFe_2O_4$

$LuFe_2O_4$ is one of the systems investigated in this work ; thus we will describe in detail all the structural and magnetic properties of this compound later, giving in this section a brief description of the main features concerning unconventional ferroelectricity.

The ferroelectricity associated with a CO state was first demonstrated in this mixed-valence oxide : at room temperature, it has a hexagonal layered structure (space group $R\bar{3}m$, a = 3.44 , c = 25.28) in which all Fe sites are crystallographically equivalent. The crystal structure consists of an alternative stacking of triangular lattices of rare-earth elements, irons and oxygens. The Fe_2O_4 layers and Lu^{3+} ion layers stack alternatively with three Fe_2O_4 layers per unit cell. Each Fe_2O_4 layer is made up of two triangular sheets of corner-sharing FeO_5 trigonal bi-pyramids. An equal number of Fe^{2+} and Fe^{3+} ions coexists on the same site of the triangular lattice. With respect to the average $Fe^{2.5+}$ valence, Fe^{2+} and Fe^{3+} ions are considered to be facilitated with an excess and a deficient half electron, respectively. The Coulomb preference for pairing oppositely signed charges Fe^{2+} and Fe^{3+} causes the degeneracy in the lowest energy for charge configuration in the triangular lattice, and then the charge-ordered state. The charge order pattern of alternating Fe^{2+} :Fe^{3+} layers with ratios of 2 : 1 and 1 : 2, appearing at a temperature as high as $\simeq$ 370K, is shown in Fig.1.17(a). This postulated CO structure allows for the presence of a local electric polarization, because the centers of Fe^{2+} and Fe^{3+} ions do not coincide in the unit cell of the superstructure, as highlighted by the arrow in Fig.1.17(c). The high-resolution transmission electron microscopy image shown in Fig.1.17(b) is consistent with this pattern. An electric polarization as high as approximately 26μC cm^{-2} was measured using the

pyroelectric current method. In response to temperature variation, significant decaying of the polarization occurs at approximately 250 K, the magnetic transition point, and at approximately 330K where the CO superstructure of Fe^{2+} and Fe^{3+} disappears, as displayed in Fig.1.17(d).

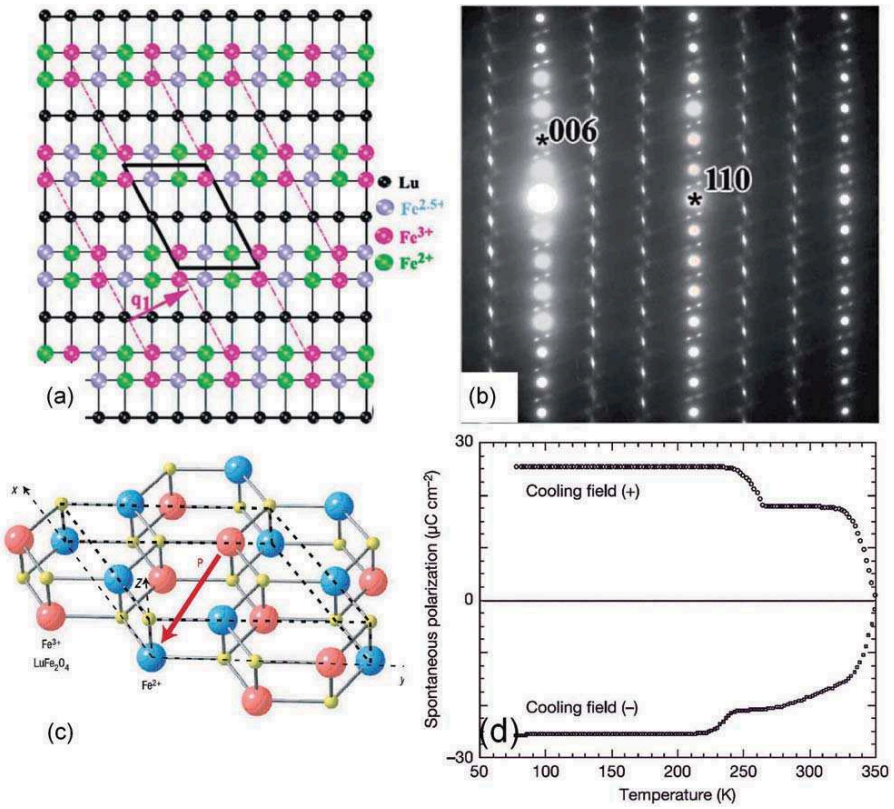

FIGURE 1.17 – Atomic configuration of the charge-order state of $LuFe_2O_4$ (a) on the ab-plane and (c) in 3D space (c). The red arrow in (c) indicates the direction of polarization. (b) Transmission electron diffraction pattern of $LuFe_2O_4$ along the $[1\bar{1}0]$ direction at T = 20 K. (d) Electric polarization of $LuFe_2O_4$ as a function of temperature under two different cooling field modes. (see Ref.[71] for (a) and (b), Ref.[32] for (c) and Ref.[72] for (d).

$LuFe_2O_4$ also exhibits remarkable magnetoelectric coupling effect. For example, a significant response of the dielectric constant to a small magnetic field at room temperature was given by a change of 25% upon a field of approximately 1 kOe [73]. Moreover, Fe^{2+} onsite crystal field excitations are sensitive to the monoclinic distortion which can be driven by temperature/magnetic field. The distortion further splits the three groups of Fe $3d$ level of D_{3d} symmetry, and then a large magneto-optical effect was observed [74].

First principle calculation, in combination with Monte Carlo simulation, reveals another CO state consisting of Fe^{2+} chains alternating with Fe^{3+} chains in each triangular sheet. This state has almost the same stability as the CO state discussed above, although it does not favor ferroelectricity and is not the ground state. The charge fluctuations associated

with the inter-conversion between the two different types of CO states could be important because of their similar energy. Under this respect, $LuFe_2O_4$ can be viewed as a phase-separated system, consisting of two types of CO domains separated by domain boundaries. The observed giant dielectric constant of Fe_2O_4 may be due to this CO state fluctuations. By applying an external magnetic field, the Zeeman energy may preferentially stabilize one of the two CO states because the two states most likely have different total spin moments. This explains why the dielectric response and polarization will be weakened by a magnetic field, which suppresses the charge fluctuations [75]. Experimental results also indicate that the charge fluctuations have an onset point well below the CO temperature [74]. This point is still discussed in the literature and further investigations on the proposed origin of multiferroism in $LuFe_2O_4$ are certainly required.

1.3.5.2 Charge/orbital order in manganites

A charge-ordered state is also often observed in manganites $R_xA_{1-x}MnO_3$. In addition, the CO-OO state is highly favored in Ruddlesden-Popper series manganites [70]. For example, $Pr(Sr_{0.1}Ca_{0.9})_2Mn_2O_7$ is composed of bilayers of MnO_6 octahedra, exhibiting two CO-OO phases : high temperature phase (CO1) and low-temperature phase (CO2). The space groups are *Amam* (with $a = 5.410$, $b = 5.462$, $c = 19.277$ at 405 K) for the charge-disordered phase ($T > T_{CO1}$), *Pbnm* (with $a = 5.412$, $b = 10.921$, $c = 19.234$ A at 330 K) for the CO1 phase ($T_{CO2} < T < T_{CO1}$) and *Am*2*m* (with $a = 10.812$, $b = 5.475$, $c = 19.203$ at 295 K) for the CO2 phase ($T < T_{CO2}$). The charge/orbital configurations for the three phases are shown in Fig.1.18.

From the synchrotron X-ray oscillation photography, it was found that with respect to the CO1 phase, the orbital stripes and zigzag chains rotate by 90°when T falls down to T_{CO2} [76]. Above T_{CO2}, each MnO_6 octahedron tilts towards the b-axis, as shown in Fig.1.18(a). Within a single bilayer unit, pairs of tilted MnO_6 octahedra on the upper and lower layers line up with the shared O^{2-} shifting towards the $+b$ and $-b$ directions. Such a situation causes the alternation of the Mn-O-Mn bond in the MnO plane along the *b*-axis. For the low-temperature phases, the structural modulation accompanied by the CO-OO is superimposed onto this structure.

For simplicity we describe the charge ordering processes in the assumed *Amam* orthorhombic lattice. For the charge order transition, as shown in Fig.1.18(b) (CO1) and Fig.1.18(c) (CO2) the charge polarization appears along the b-axis in each bilayer. In the CO1 phase, however, the CO pattern stacks along the c-axis shifting by (1/2,0,0) with respect to the next bilayer, as shown in Fig.1.18(b) facilitating the inter-bilayer coupling of the polarization which is antiferroelectrically in nature. At T_{CO2} the rotation of the orbital stripes is accompanied by the rearrangement of Mn^{3+} and Mn^{4+} ions and, thus, by the CO stacking pattern. In the CO2 phase, the charge-order sequence stacks along the c-axis with a shift by (0, 1/2, 0) with respect to the next bilayer, coinciding with the stacking of the bond alternation. Therefore, the polarization of each bilayer along the b-axis is excessive, forming a charge-polarized state below T_{CO2}.

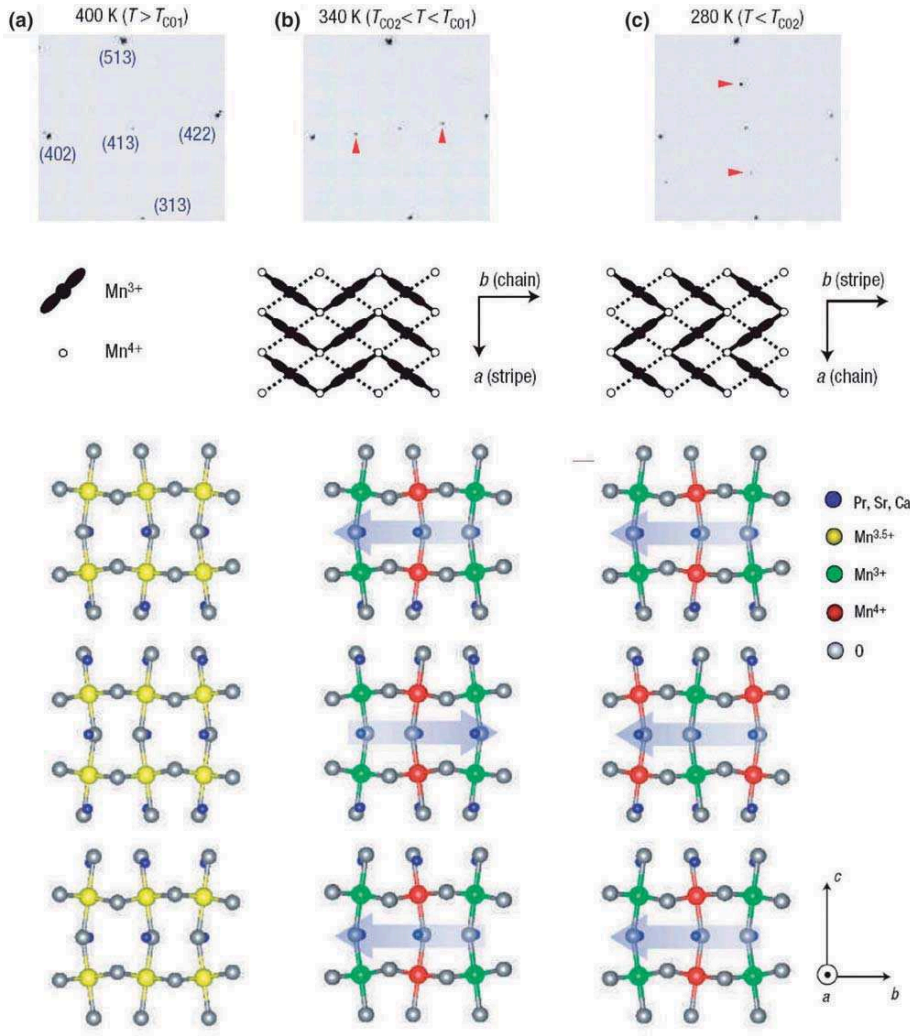

FIGURE 1.18 – Synchrotron X-ray oscillation photographs (upper row), and schematic CO-OO configurations (middle row) as well as lattice structures (lower row) of $Pr(Sr_{0.1}Ca_{0.9})_2Mn_2O_7$ at three different temperatures [76].

1.3.6 Ferrotoroidic systems

Ferromagnetism, ferroelectricity and ferroelasticity are widely utilized in modern technology. The three functions are always called fundamental ferroicity. One common character for these functions is the domain structure associated with the spontaneous magnetization, polarization and elastic transform, respectively. These domains are the key units for data memory. For example, ferromagnetic domains are memory units in computer hard disks and ferroelectric domains are found in FeRAMs. Recently, a fourth ferroicity, ferrotoroidicity, was proposed as being one of the fundamental ferroicities, and consequently a fourth kind of ferroics, ferrotoroidics, was addressed.

1.3.6.1 Ferrotoroidic order

It is well known that a vortex of a magnetic moment induces a toroidic magnetic moment. Atomic spins or orbital currents can be responsible for this particular magnetic moment which can be represented by a time-odd polar (or "axiopolar") vector $\mathbf{T} = 1/2\sum_i \mathbf{r}_i \times \mathbf{S}_i$, where $\mathbf{S}_i$ and $\mathbf{r}_i$ are the ith magnetic moment and its positional vector, respectively [77]. This toroidic vector $\mathbf{T}$ changes its sign upon both time-inversion and space-inversion operations and is generally associated with a "circular" or "ring-like" arrangement of spins. The concept of a magnetic toroidic moment can be sketched by a ring-shape torus : the magnetic toroidic moment T (the green arrow in Fig.1.19(a)) is perpendicular to the ring plane. In a magnetic toroidic system, it is possible to induce a

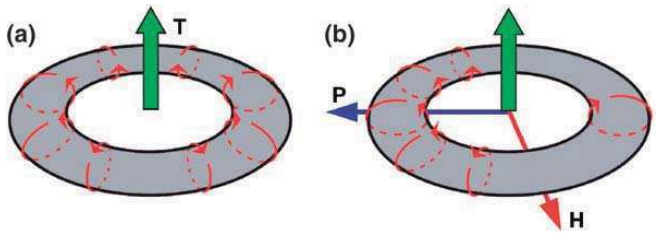

FIGURE 1.19 – Magnetic toroidic moment in a simple system : (a) a ring-shaped torus with an even number of current windings exhibits a toroidic moment T (the green arrow) ; (b) a magnetic field along the ring plane induces the current loops in one direction and eventually an electric polarization along this direction [78].

magnetization M by an electric field E and a polarization P by a magnetic filed H, which is one of the reasons why much attention has been paid to magnetic toroidic systems. For example, in the system shown in Fig.1.19(a), a magnetic field along the ring plane drives the current loops in one direction and an electric polarization could appear along this direction, as shown in Fig.1.19(b). Ferromagnetics and ferroelectrics correspond to the systems whose order parameters change their sign upon the temporal and spatial reversal ; for a ferroelastic system, no such change occurs under the two reversals (*i.e.* the order parameters are invariant), as shown in Fig.1.21. It is apparent that the three fundamental

ferroic orders correspond to three of the four parity-group representations and the residual should be assigned as the ferrotoroidic order which changes sign under both reversals. This is the reason why ferrotoroidics are named the fourth type of fundamental ferroics. The multiferroics are spatial and time asymmetric because of the coexistence of two order parameters : one violating the spatial-reversal symmetry and the other one breaking the temporal-reversal symmetry.

It is easy to derive that for the macroscopic vector "toroidic moment **T**" stands $\mathbf{T} \propto \mathbf{P} \times M$ for multiferroics of ferroelectric and ferromagnetic orders. However, it should be mentioned that a non-zero macroscopic **T** does not necessarily require the coexistence of **P** and **M**. For example, $GaFeO_3$ is a prototypical ferrotoroidic system, as shown in Fig.1.20. Also in this case, being this system subject of this thesis, we will describe in details the properties of this compound in Chapter 3. $GaFeO_3$ is pyroelectric in nature with the built-in electronic polarization along the *b*-axis in the orthorhombic cell, and its spontaneous magnetization arises from the ferromagnetic arrangement of Fe spins. However, the displacements of two Fe-ion sites are opposite, as if it were antiferroelectric. In this case, a macroscopic toroidal moment is present but its magnitude is larger than $P \times M$. This is also one of the reasons why antiferromagnetics or antiferroelectrics are categorized into the components of multiferroics.

1.3.6.2 Magnetoelectric effect in ferrotoroidic systems

The toroidic moment **T** can cause some interesting optical magnetoelectric effects. One of them originates from the polarization component induced by the optical magnetic field, which is an analogue of the magnetoelectric coupling in the optical frequency. The normal Faraday (or Kerr) rotation, as shown in Fig.1.20(c), arises from the dichroism or birefringence with respect to the right-hand or left-hand circularly polarized light. The optical magnetoelectric effect refers to the dichroism/birefringence with respect to the light propagation vector, being irrespective of the light polarization (Fig.1.20(c)). Another important feature of the optical magnetoelectric effect is the second-order non-linear optical activity. In presence of a toroidal moment **T**, in addition to the ordinary SH light polarized along the **P** direction, a second harmonic (SH) light with polarization parallel to **T** can be generated (1.20(c)). Moreover it is possible that an incident light polarized along the **T** direction can generate the SH components polarized along the **P** and **T** directions, respectively. This **T**-induced SH component may reverse its phase upon the magnetization reversal. Consequently, the polarization of the SH light can rotate depending on the magnetization direction or, equivalently, on the toroidic moment direction. This non-linear Kerr rotation can be used to sensitively probe the toroidic moment or the breaking of the inversion symmetry.

In addition to $GaFeO_3$, also $LiCoPO_4$ and $LiNiPO_4$ are typical ferrotoroidics [80] [78]. The importance of these compounds is that both of them exhibit very large magnetoelectric coupling [81] [82]. For example, in $LiNiPO_4$, the magnetoelectric tensor α has two non-zero components α_{xz} and α_{zx} [82] ; correspondingly for $LiCoPO_4$ subscript z should be replaced by y. Fig.1.22 shows the electric polarization along the z-axis under an external magnetic field along the x-axis below the magnetic transition point around 20K. It is evident that a relatively large magnetic field along the x-axis can induce a large polarization along the

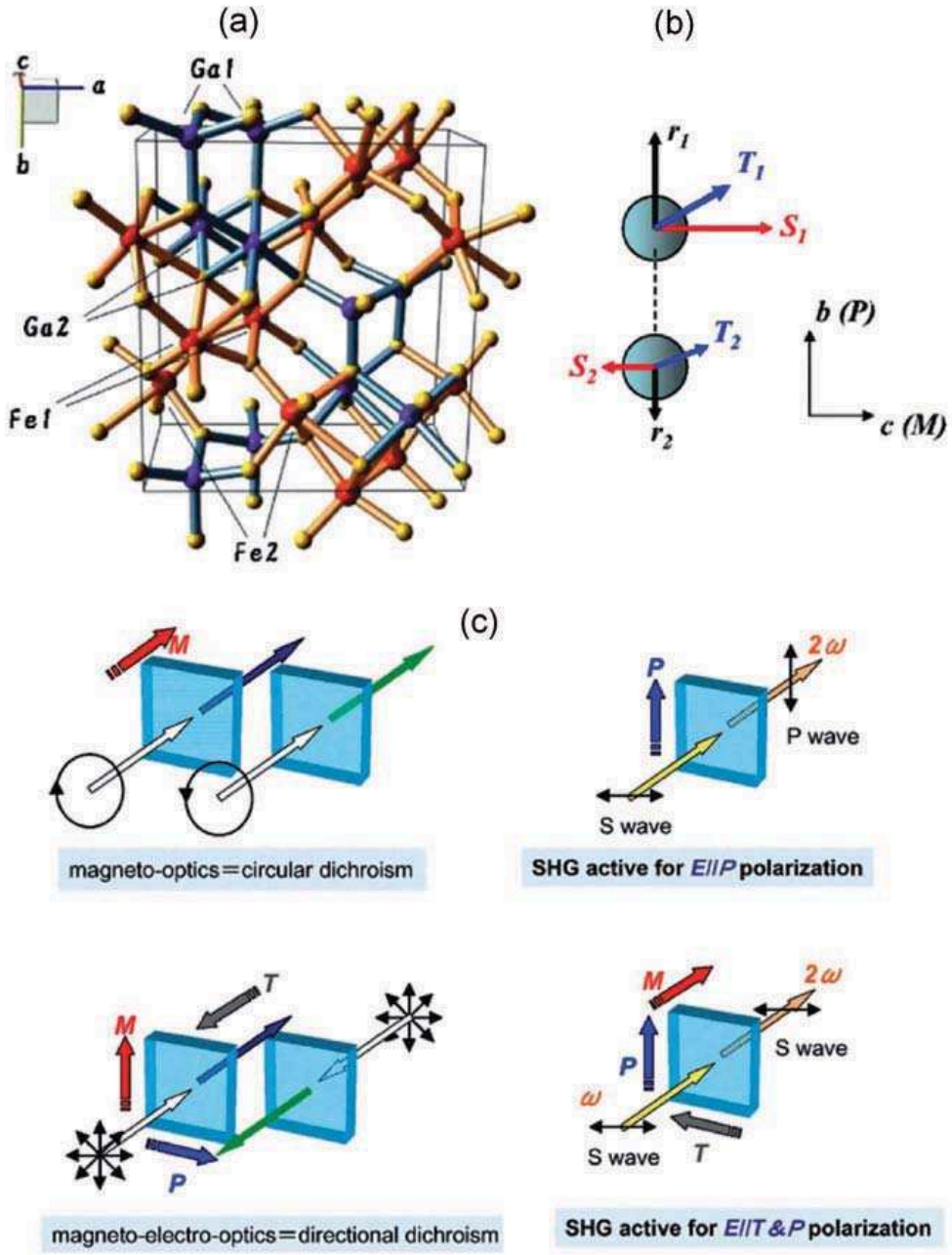

FIGURE 1.20 – Crystal lattice structure and (b) schematic magnetic toroidic moments of $GaFeO_3$; (c) four kinds of magneto- optical effects [79].

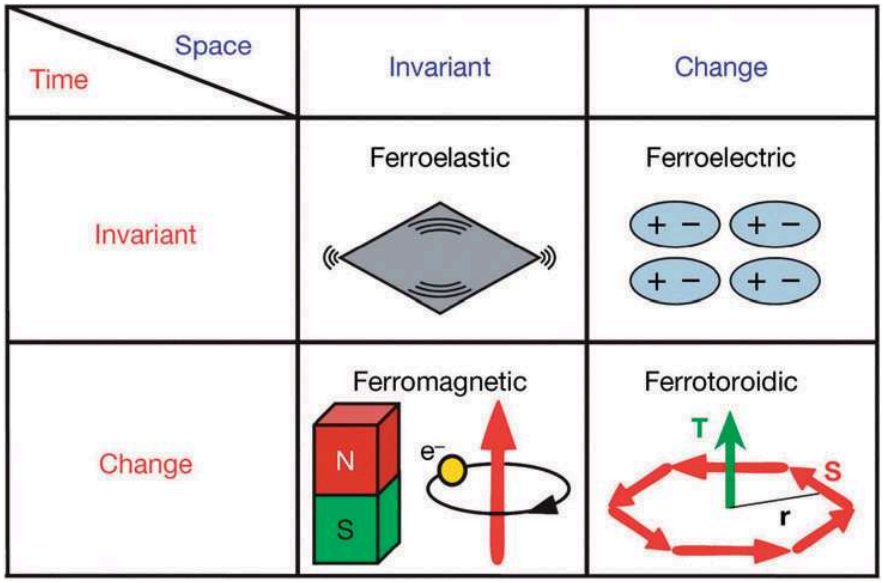

FIGURE 1.21 – Relations between the ferroic orders and the space-/time-reversal [78].

z-axis. More exciting is that the relationship between the polarization along the z-axis and the magnetic field along the x-axis exhibits a butterfly loop around the magnetic transition point and this loop disappears at a lower temperature. It is well known that the butterfly loop always corresponds to the appearance of spontaneous moments, as in ferromagnetics and ferroelectrics, and this phenomenon demonstrates the existence of the macroscopic and spontaneous toroidical moments.

1.4 Potential applications

We have largely mentioned that multiferroics, or ferrotoroidics, simultaneously exhibit ferroelectricity and magnetism and provide alternative ways to encode and store data using both electric polarization and magnetization. Moreover, the mutual control between the electric polarization and magnetization due to the strong magnetoelectric coupling gives even more potential to applications in the sensor industry, spintronics and so on.

1.4.1 Magnetic field sensors using multiferroics

One of the most direct application of multiferroics is to utilize the sensitivity of electric polarization (voltage) to an external magnetic field to develop a magnetic field sensor, as shown in Fig.1.23(a).

A prototype read-head using multiferroic materials is shown in Fig.1.23(b). The reversed process is also possible and even more interesting, *i.e.* the control of magnetization by an external electric field or electric polarization. For example, multiferroics can be used

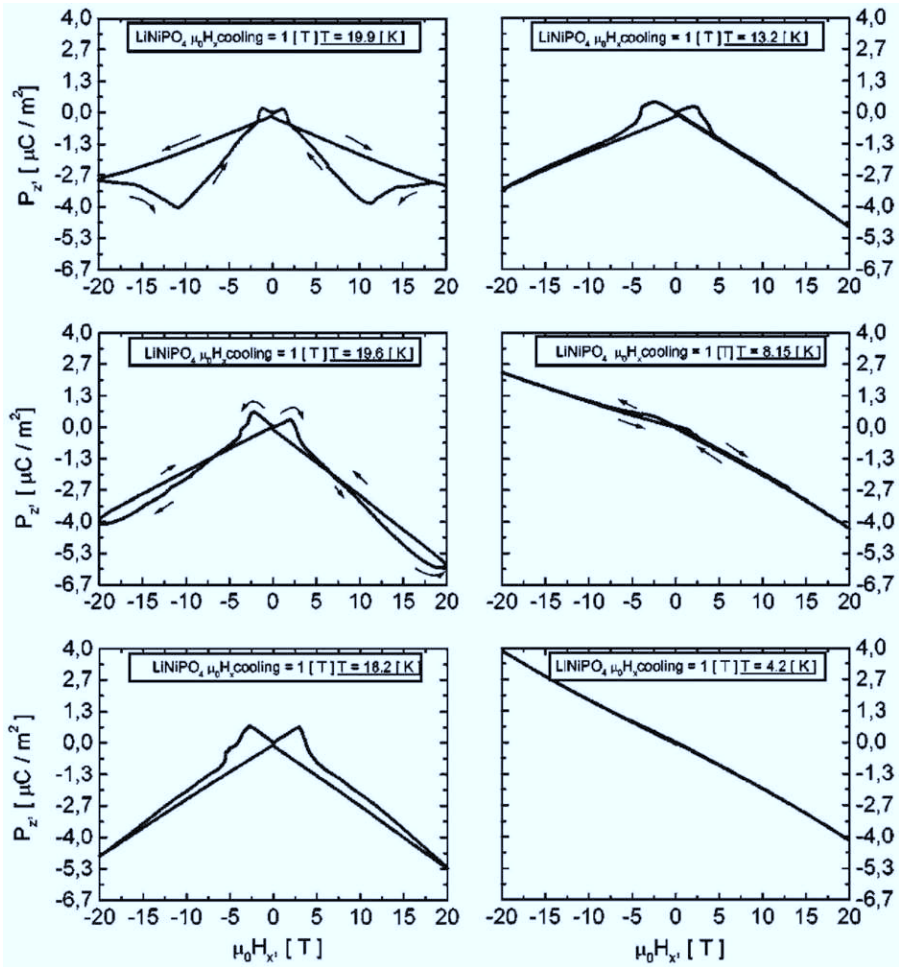

FIGURE 1.22 – Relations between electric polarization along the z-direction and magnetic field along the x-direction at different temperatures adjacent to the magnetic transition point of $LiNiPO_4$ [83].

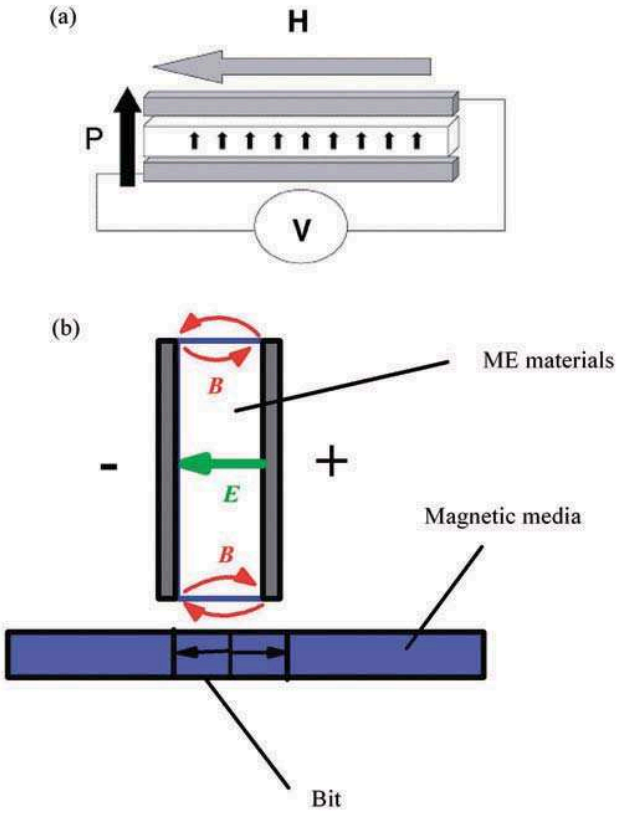

FIGURE 1.23 – (a) Multiferroic as a probe of the magnetic field. The middle (white) layer is multiferroic, while both the upper and lower layers (grey) are ferromagnetic metals. An external magnetic field H will induce an electric polarization perpendicular to the magnetic field direction, and then a voltage V. (b) The read-head device uses the probe in (a). The blue layer is the magnetic media (magnetic disk) and the black arrows in it indicate two opposite bits [35].

for modulating the phase and amplitude of millimeter wavelength by using a fin-line waveguide, while conventional devices for the control of magnetic parameters imply the use of electromagnets. A fin-line waveguide is a rectangular waveguide provided with a slab of dielectric material at the centre. Magnetoelectric materials allow for the possibility of tuning magnetic parameters by voltage. Indeed, applying a voltage across the slab results in a shift in the absorption line for the multiferroic material, thus inducing the modulation of the phase and amplitude of the propagating wave.

Unfortunately, however, most available multiferroic materials are antiferromagnetic and exhibit a small macroscopic magnetic moment. Therefore, it is difficult to detect the small influence of an external electric field on the magnetization and the associated change of electric polarization directly. Given this consideration, and the fact that a ferromagnetic layer can be pinned by its antiferromagnetic neighbor, it is possible to utilize this pinning

effect to monitor magnetization switching by electric field/polarization [84]. By depositing a soft ferromagnetic layer onto an antiferromagnetic multiferroic film, as shown in Fig.1.24, by applying an external electric field to modulate the magnetization of the multiferroic film one can eventually switch the magnetization of the soft ferromagnetic layer due to the magnetic pinning. In this way the magnetoelectric process can be used as a read out operation of information. Following this roadmap, a NiFe alloy film was deposited on a (001) epitaxial $YMnO3_3$ film, and the magnetic pinning effect as well as the exchange bias were confirmed [85].

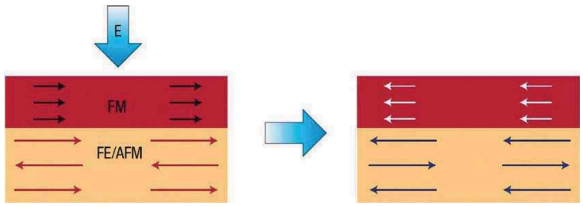

FIGURE 1.24 – Schematic view of a soft ferromagnetic layer deposited on multiferroic antiferromagnetic film. The external electric field induces a variation in the magnetization of the antiferromagnetic multiferroic film, and results in the reversal of magnetization in the soft ferromagnetic layer due to the magnetic pinning effect [84].

1.4.2 Electric field control of the exchange bias by multiferroics

Another potential application of multiferroicity is the control of transport in spin-valve structures ; the basis of this approach is the exchange bias effect. There are two general manifestations of exchange bias interactions that have been observed in the interface between a ferromagnetic layer and an antiferromagnetic (conventional spin-valve) layer. The first is an exchange bias of the magnetic hysteresis which manifests itself by a shift of the hysteresis, for the ferromagnetic layer, along the magnetic field axis [86]. It is a consequence of pinned uncompensated spins on the interface. The second is an enhancement of the coercivity of the ferromagnetic layer.

By replacing the antiferromagnetic layer with a multiferroic layer, such as $BiFeO_3$ where antiferromagnetic domains are cross-coupled with ferroelectric domains, a multiferroic spin-valve structure can be developed. As discussed above, an external electric field will drive motion and/or switching of the ferroelectric domains, thus modulating the coupled antiferromagnetic domains. In this case, the exchange bias effect can be controlled by means of an electric field instead of the magnetic field used in conventional spintronics. Some experiments have demonstrated the reliability of this approach. For example, in the $CoFeB/BiFeO_3$ spin-valve structure, hysteresis loops of different structures and significant exchange bias were observed (Fig.1.25)

In addition to the $CoFeB/BiFeO_3$ spin-valve structure reviewed above, a similar experiment on a Cr_2O_3/ferromagnetic alloy bilayer structure, where Cr_2O_3 is a magnetoelectric compound rather than a multiferroic compound, has been performed [88]. However, in this

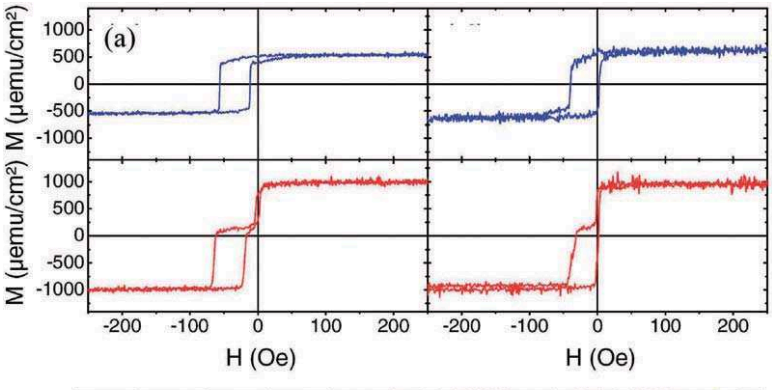

FIGURE 1.25 – Exchange bias in the $CoFe/BiFeO_3$ system. Magnetic field dependence of magnetization of $CoFeB/BiFeO_3/SrTiO_3(001)$ multilayer (upper left), $CoFeB/BiFeO_3/SrTiO_3(111)$ (upper right), $CoFeB/BiFeO_3/La_{0.7}Sr_{0.3}MnO_3/SrTiO_3(001)$ (lower left), and $CoFeB/BiFeO_3/La_{0.7}Sr_{0.3}MnO_3/SrTiO_3(111)$ (lower right) [87].

case the detected signal was tiny. Another experiment where a significant effect was observed, has been recently reported with the structure $Pt/YMnO_3/Py$. Therein, $YMnO_3$ is the pinning layer and Py is the soft ferromagnetic alloy [89]. In Fig.1.26(a) a plot of the magnetic hysteresis (M-H loops) of this structure, as measured under different electric fields at T = 2 K, is presented. The loop shifts from the origin point and indicates an exchange-bias field of approximately 60 Oe under zero electric field ($V_e = 0$) (note that the both the magnetization and the exchange-bias field depend on temperature). Upon applying an electric field across the $YMnO_3$ layer, the shift of the M-H loop gradually disappears, indicating suppression of the exchange-bias field and of coercitivity. Thus the electric-field-induced magnetization reversal is made evident by the decrease in magnetization with an increasing electric field from zero up to $V_e = 0.4V$, where the magnetization changes sign (Fig1.26(b)). Unfortunately, this process is irreversible and no back-switching of the magnetization was observed.

1.4.3 Multiferroic/semiconductor structures as spin filters

Much effort has also been directed towards multiferroic thin films as potential dielectric gates for semiconductor devices. The most widely studied system is a $YMnO_3/GaN$ heterostructure because $YMnO_3$ and GaN have the same hexagonal symmetry [90]. First principle calculations predict different band offsets at the interface between the two systems. This behavior is due to the interface-induced spin splitting of the valence band. The energy barrier depends on the relative orientation between the electric polarization and the polarization direction of the GaN substrate : this suggests an opportunity to create a magnetic tunnel junction in this heterostructure.

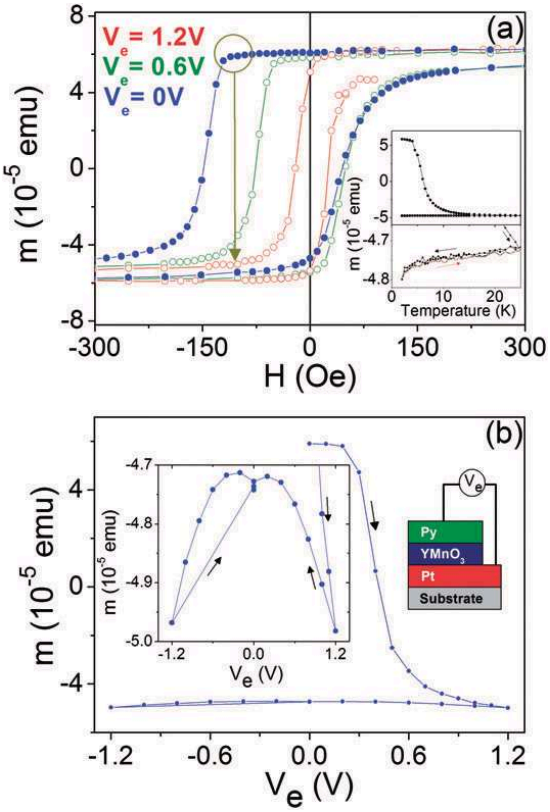

FIGURE 1.26 – Measured (a) M-H loops and (b) magnetization of the exchange-biased $Pt/YMnO_3/Py$ structure under different external electric fields V_e. The inset in (a) shows the relation between magnetization and temperature, and the inset in (b) is the multilayered structure [89].

1.4.4 Logical states in a tunneling junction by use of multiferroics

The novel devices based on multiferroic functions may offer particularly high performance for spintronics, for example, reading the spin states, and writing the polarization states by applying an electric field. This could allow to improve the performances of the devices actually in use as Ferroelectric Random-Access Memories (FeRAMs) and Magnetic Random-Access Memories (MRAMs). The main disadvantage of the FeRAMs based devices is the destructive read and reset operations [92], while MRAMs present slow and high-power read/ write operations[91]. Multiferroics now offer a possibility to combine the high speed performance of FeRAMs with the recoverable operation mode of the MRAMs.

Recently, a novel Magnetic tunneling Junction (MTJ) has been developed : the multiferroic compound $La_{0.1}Bi_{0.9}MnO_3$ (LBMO) was used as an insulating barrier, while the ferromagnetic half-metal $La_{2/3}Sr_{1/3}MnO_3$ (LSMO) and Au were used as the bottom and top electrodes, respectively [1]. The structure and energy level of this novel MTJ are sketched in Fig.1.27. The ferroelectricity and ferromagnetism of the ultra thin $La_{0.1}Bi_{0.9}MnO_3$

film of 2nm thick were verified. This MTJ exhibits the normal tunneling magnetoresistance (TMR) effect (*i.e.*, the resistance is low when the magnetization of the bottom electrode, $La_{2/3}Sr_{1/3}MnO_3$, is aligned with that of $La_{0.1}Bi_{0.9}MnO_3$, and higher when their magnetizations are antiparallel), as shown in Fig.1.28. In addition, a modulation of resistance

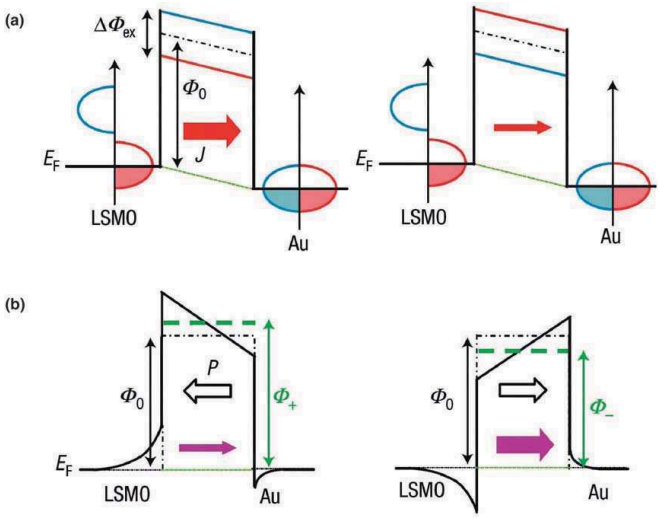

FIGURE 1.27 – Structure and energy scheme for a new magnetic tunneling junction (MTJ). Multiferroic $La_{0.1}Bi_{0.9}MnO_3$ (LBMO) was used as the insulating barrier and ferromagnetic half-metal $La_{2/3}Sr_{1/3}MnO_3$ (LSMO), while Au were used as the bottom and top electrodes, respectively [1].

by the ferroelectricity of the $La_{0.1}Bi_{0.9}MnO_3$ film (*i.e.* the electroresistance effect) can be expected. Indeed, as shown in Fig.1.29(a), when the voltage is swept from $+2V$ to $-2V$ the tunneling current is smaller, that means that the bias-voltage dependence exhibits a significant hysteresis. Consequently, it is possible to obtain four different resistance states at a low bias voltage in this TMR structure by combining the TMR and the electroresistance effect, as shown in Fig.1.29(d). This prototype device allows for an encoding of quaternary information by both ferromagnetic and ferroelectric order parameters.

1.4.5 Negative refractive-index materials

Materials which simultaneously display negative permittivity and permeability (often referred to as NIMs), have been received special attention in the last few years, because their interaction with electromagnetic radiations can be described by a negative index of refraction [93]. To date, this effect has only been implemented in metamaterials, made of arrays of metallic resonant circuits working in the microwave or Terahertz range of frequencies. Using an ideal model in which both ferromagnetic and ferroelectric resonances are available, a negative index of refraction, also working in the Terahertz region, was predicted [94]. These results point toward a possible control of the phase between the electric field E and magnetic field H by means of a multiferroic material. Moreover, this

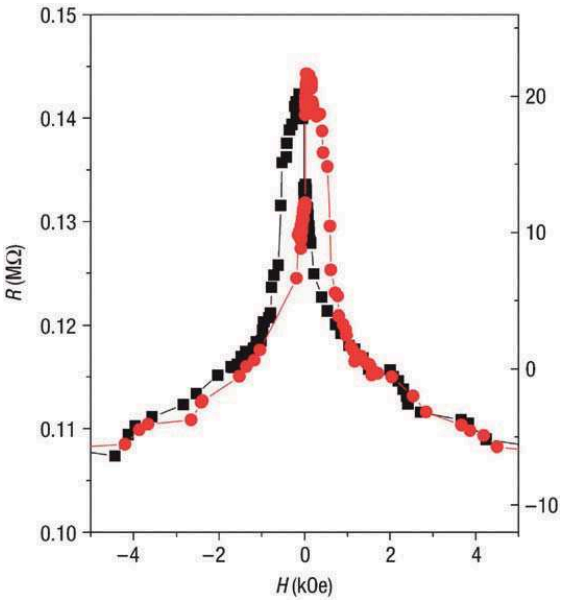

FIGURE 1.28 – Measured TMR effect in a $La_{2/3}Sr_{1/3}MnO_3/La_{0.1}Bi_{0.9}MnO_3/Au$ multilayer structure. The red curve represents the resistivity and the black curve the magnetoresistance ratio [1].

would allow one to manipulate the direction of the power propagation.

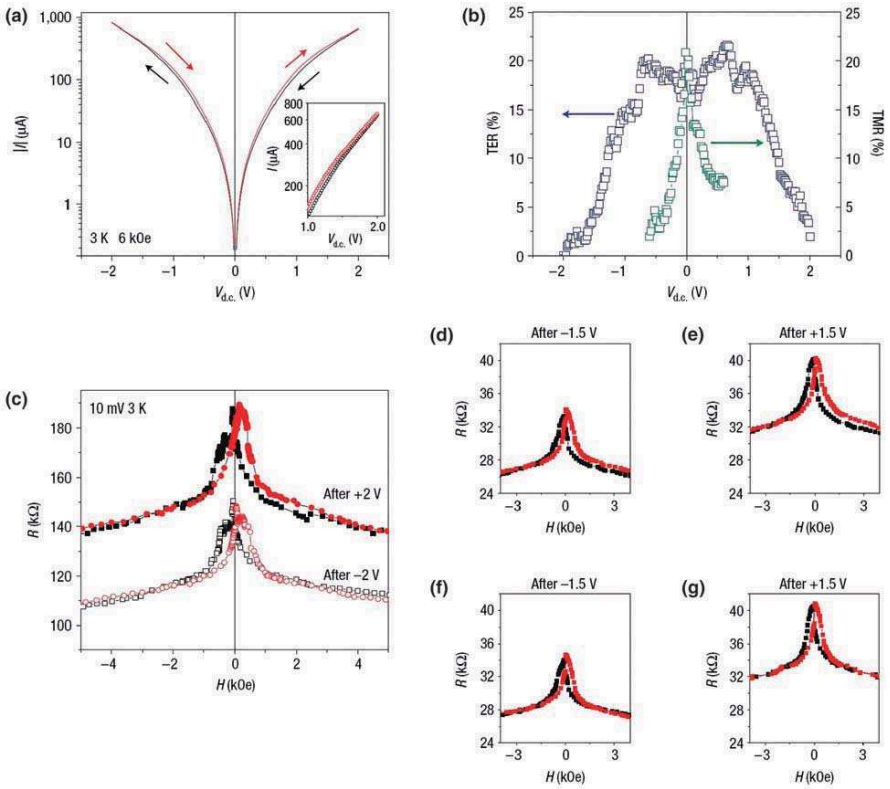

FIGURE 1.29 – Influence of the external electric field on the tunneling current in $La_{2/3}Sr_{1/3}MnO_3/La_{0.1}Bi_{0.9}MnO_3/Au$ junctions. The arrows denote the sequence for electric field application. (b) Dependence of the tunneling electroresistance effect (TER) and tunneling magnetoresistance (TMR) on the external electric field V_{dc}. (c) Measured TMR upon an electric bias of $+2V$ and $-2V$. (d)-(g) Four-state resistance in the junction [1].

Bibliographie

[1] M. Gajek, M. Bibes, S. Fusil, K. Bouzehouane, J. Fontcuberta, A. Barthelemy, and A. Fert, Nature Mater. **6**, 296 (2007).

[2] P. Curie, J. Physique **3**, p. 393 (1894).

[3] P. Debye, Z. Phys. **36**, p. 300 (1926).

[4] G.T. Rado and V.J. Folen, Phys. Rev. Lett. **7**, p. 310 (1961).

[5] M. Fiebig, J. Phys. D : Appl. Phys. **38** R123 (2005)

[6] A. V. Shubnikov *Symmetry and Antisymmetry of Finite Figures* (Moscow : USSR Academy of Sciences 1951)

[7] R. R. Birss *Symmetry and Magnetism* (Amsterdam : North-Holland 1966)

[8] T. H. O'Dell *The Electrodynamics of Magneto-Electric Media* (Amsterdam : North-Holland 1970)

[9] R.M. Hornreich and S. Shtrikman, Phys.Rev. **161**, 506 (1967)

[10] G. A. Gehring, Ferroelectrics **161**, 275 (1994)

[11] Rivera J. P., Ferroelectrics **161**, 165 (1994)

[12] Rivera J. P., Ferroelectrics **161**, 147 (1993)

[13] B. B. Krichevtsov, V. V. Pavlov and R.V. Pisarev JETP Lett. **49**, 535 (1989)

[14] G. T. Rado, J. M. Ferrari and W. G. Maisch, Phys. Rev. B **29**, 4041 (1984)

[15] W. F. Jr. Brown, R.M. Hornreich and S. Shtrikman, Phys. Rev. **168**, 574 (1968)

[16] H. Schmid, *Magnetoelectric Interaction Phenomena in Crystals* ed M Fiebig *et al* (Dordrecht : Kluwer) p1 (2004)

[17] F. Kubel and H. Schmid, Acta Crystallogr. B **46**, 698 (1990)

[18] Y. N. Venevtsev, V. V. Gagulin and I.D. Zhitomirsky, Ferroelectrics **73**, 221 (1987)

[19] J. F. Scott, Ferroelectrics **24**, 127 (1980)

[20] Eibschutz M and H. J. Guggenheim, Solid State Commun. **6**, 737 (1968)

[21] I. Bersuker, Chem. Rev. **101**, 1067 (2001).

[22] M. Rondinelli, A. S. Eidelson and N. A. Spaldin, Phys. Rev. B **79**, 205119 (2009)

[23] Y.N. Venevtsev and V.V. Gagulin, Ferroelectrics **162**, p. 23 (1994).

[24] V.A. Vokov, Sov. Phys. JETP. **15**, p. 447 (1962).

[25] R. Wongmaneerung, X. Tan, R.W. McCallum, S. Ananta, and R. Yimnirun, Appl. Phys. Lett. **90** (2007), p. 242905.

[26] G.W. Waston, S.C. Parker, and G. Kresse, Phys. Rev. B **59** (1999), p. 8481.

[27] G. Trinquier and J.R. Hoffmann, J. Phys. Chem. **88**, p. 6696 (1984).

[28] A. Moreira dos Santos, A.K. Cheetham, T. Atou, Y. Syono, Y. Yamaguchi, K. Ohoyama, H. Chiba, and C.N.R. Rao, Phys. Rev. **B** 66, p. 064425 (2002).

[29] T. Atou, H. Chiba, K. Ohoyama, Y. Yamaguchi, and Y. Syono, J. Solid State Chem. **145**, p. 639 (1999).

[30] F. Sugawara, S. Iida, Y. Syono, and S. Akimoto, J. Phys. Soc. Jpn. 25 (1968), p. 1553.

[31] T. Kimura, S. Kawamoto, I. Yamada, M. Azuma, M. Takano, and Y. Tokura, Phys. Rev. B 67 (2003), p. 180401.

[32] S-W. Cheong and M. Mostovoy, Nature Materials **6**, 13 - 20 (2007)

[33] R. Seshadri and N.A. Hill, Chem. Mater. **13** , p. 2892 (2001).

[34] D. Lebeugle, D. Colson, A. Forget, and M. Viret, Appl. Phys. Lett. **91**, 022907 (2007).

[35] K.F. Wangab, J.-M. Liuab and Z.F. Renc, Advances in Physics **58**, 4 (2009).

[36] M. Cazayous, Y. Gallais, and A. Sacuto, Phys. Rev. Lett. 101, p. 037601 (2008).

[37] J.D. Bucci, B.K. Robertson, and W.J. James, J. Appl. Crystallogr. **5** , p. 187 (1972).

[38] J. Wang, J.B. Neaton, H. Zheng, V. Nagarajan, S.B. Ogale, B. Liu, D. Viehland, V. Vaithyanathan, D.G. Schlom, U.V. Waghmare, N.A. Spaldin, K.M. Rabe, M. Wuttig, and R. Ramesh, Science **299**, p. 1719 (2003).

[39] H. Béa, M. Bibes, X.-H. Zhu, S. Fusil, K. Bouzehouane, S. Petit, J. Kreisel, and A. Barthélémy, Appl. Phys. Lett. **93**, p. 072901 (2008).

[40] S. Nakashima, O. Sakata, Y. Nakamura, T. Kanashima, H. Funakubo, and M. Okuyama, Appl. Phys. Lett. **93** (2008), p. 042907.

[41] H.W. Jang, S.H. Baek, D. Ortiz, C.M. Folkman, R.R. Das, Y.H. Chu, P. Shafer, J.X. Zhang, S. Choudhury, V. Vaithyanathan, Y.B. Chen, D.A. Felker, M.D. Biegalski, M.S. Rzchowski, X.Q. Pan, D.G. Schlom, L.Q. Chen, R. Ramesh, and C.B. Eom, Phys. Rev. Lett. **101**, p. 107602 (2008).

[42] R. Mazumder, P. Sujatha Devi, D. Bhattacharya, P. Choudhury, A. Sen, and M. Raja, Appl. Phys. Lett. **91**, p. 062510 (2007).

[43] B. van Aken, T.T.M. Palstra, A. Filippetti, and N.A. Spaldin, Nature Mater. **3**, p. 164 (2004).

[44] E.F. Bertaut, R. Pauthenet, and M. Mercier, Phys. Lett. **7**, p. 110 (1963).

[45] M. Fiebig, D. Frohlich, Th. Lottermoser, and M. Maat, Phys. Rev. B **66**, 144102 (2002).

[46] D.-Y. Cho, J.-Y. Kim, B.-G. Park, K.-J. Rho, J.-H. Park, H.-J. Noh, B.J. Kim, S.-J. Oh, H.-M. Park, J.-S. Ahn, H. Ishibashi, S.-W. Cheong, J.H. Lee, P. Murugavel, T.W. Noh, A. Tanaka, and T. Jo, Phys. Rev. Lett. **98**, 217601 (2007).

[47] H.D. Zhou, J.A. Janik, B.W. Vogt, Y.J. Jo, L. Balicas, M.J. Case, C.R. Wiebe, J.C. Denyszyn, J.B. Goodenough, and J.G. Cheng, Phys. Rev. B **74**, 094426 (2006).

[48] Th. Lottermoser, T. Lonkai, U. Amann, D. Hohlwein, J. Ihringer, and M. Fiebig, Nature **430**, 541 (2004).

[49] B. Lorenz, A.P. Litvinchuk, M.M. Gospodinov, and C.W. Chu, Phys. Rev. Lett. **92**, 087204 (2004).

[50] M. Mostovoy, Phys. Rev. Lett. **96**, 067601 (2006).

[51] J.J. Betouras, G. Giovannetti, and J. van den Brink, Phys. Rev. Lett. **98**, 257602 (2007).

[52] I.E. Dzyaloshinskii, Sov. Phys. JETP **19**, 960 (1964).

[53] I.A. Sergienko and E. Dagotto, Phys. Rev. B **73**, 094434 (2006).

[54] H. Katasura, N. Nagaosa, and A.V. Balatsky, Phys. Rev. Lett. **95**, 057205 (2005).

[55] J. Hu, Phys. Rev. Lett. **100**, 077202 (2008).

[56] S. Park, Y.J. Choi, C.L. Zhang, and S.-W. Cheong, Phys. Rev. Lett. **98**, 057601 (2007).

[57] G. Lawes, A.B. Harris, T. Kimura, N. Rogado, R.J. Cava, A. Aharony, O. Entin-Wohlman, T. Yildirim, M. Kenzelmann, C. Broholm, and A.P. Ramirez, Phys. Rev. Lett. **95**, 087205 (2005).

[58] M. Kenzelmann, G. Lawes, A.B. Harris, G. Gasparovic, C. Broholm, A.P. Ramirez, G.A. Jorge, M. Jaime, S. Park, Q. Huang, A. Ya. Shapiro, and L.A. Demianets, Phys. Rev. Lett. **98**, 267205 (2007).

[59] T. Kimura, T. Goto, H. Shintani, K. Ishizaka, T. Arima, and Y. Tokura, Nature **426**, 55 (2003).

[60] T. Goto, G. Lawes, A.P. Ramirez, and Y. Tokura, Phys. Rev. Lett. **92**, 257201 (2004).

[61] Y. Yamosoki, H. Sagayama, T. Goto, M. Matsuura, K. Hirota, T. Arima, and Y. Tokura, Phys. Rev. Lett. **98**, 147204 (2007).

[62] D. Lebeugle, D. Colson, A. Forget, M. Viret, A.M. Bataille, and A. Gukasov, Phys. Rev. Lett. **100**, 227602 (2008).

[63] F. Zavaliche, P. Shafer, R. Ramesh, M.P. Cruz, R.R. Das, D.M. Kim, and C.B. Eom, Appl. Phys. Lett. **87**, 252902 (2005).

[64] F. Zavaliche, R.R. Das, D.M. Kim, C.B. Eom, S.Y. Yang, P. Shafer, and R. Ramesh, Appl. Phys. Lett. **87**, 182912 (2005).

[65] A. Malashevich and D. Vanderbilt, Phys. Rev. Lett. **101**, 037210 (2008).

[66] H.J. Xiang and M.-H. Whangbo, Phys. Rev. Lett. **99**, 257203 (2007).

[67] H.J. Xiang, S.-H. Wei, M.-H. Whangbo, and J.L. Da Silva, Phys. Rev. Lett. **101**, 037209 (2008).

[68] T. Portengen, Th. Ostreich, and L.J. Sham, Phys. Rev. B **54**, 174521 (1996).

[69] E.J. Vervey and P.W. Haayman, Physica **8**, 979 (1941).

[70] Y. Tokura and N. Nagaosa, Science **288**, 462 (2000).

[71] Y. Zhang, H.X. Yang, H.F. Tian, and J.Q. Li, Phys. Rev. Lett. **98**, 247602 (2007).

[72] N. Ikeda, H. Ohsumi, K. Ohweda, K. Ishii, T. Inami, K. Kakurai, Y. Murakami, S. Mori, Y. Horibe, and H. Kilo, Nature **436**, 1136 (2005).

[73] M.A. Subramanian, T. He, and J.Z. Chen, Adv. Mater. **18**, 1737 (2006).

[74] X.S. Xu, M. Angst, T.V. Brinzari, R.P. Hermann, J.L. Musfeldt, A.D. Christianson, D. Mandrus, B.C. Sales, S. McGill, J.-W. Kim, and Z. Islam, Phys. Rev. Lett. **101**, 227602 (2008).

[75] H.J. Xiang and M.-H. Whangbo, Phys. Rev. Lett. **98**, 246403 (2007).

[76] Y. Tokunaga, T. Lottermoser, Y. Lee, R. Kumai, M. Uchida, T. Arima, and Y. Tokura, Nature Mater. **5**, 937 (2006).

[77] H. Schmid, Ferroelectrics **252**, 41 (2001).

[78] B.B. van Aken, J.-P. Rivera, H. Schmid, and M. Fiebig, Nature **449**, 702 (2007).

[79] Y. Tokura, Science 312 (2006), p. 1481 ; J. Magn. Magn. Mater. **310**, 1145 (2007).

[80] D. Vaknin, J.L. Zarestky, L.L. Miller, J.-P. Rivera, and H. Schmid, Phys. Rev. B **65**, 224414 (2002).

[81] D. Talbayev, S.A. Trugman, A.V. Balatsky, T. Kimura, A.J. Taylor, and D.A. Averitt, Phys. Rev. Lett. **101**, 097603 (2008).

[82] S. Kamba, D. Nuzhnyy, M. Savinov, J. Sebek, J. Petzelt, J. Prokleska, R. Haumont, and J. Kreisel, Phys. Rev. B **75**, 024403 (2007).

[83] I. Kornev, M. Bichurin, J.-P. Rivera, S. Gentil, H. Schmid, A.G.M. Jansen, and P. Wyder, Phys. Rev. B **62**, 12247 (2000).

[84] R. Ramesh and N.A. Spaldin, Nature Mater. **6**, 21 (2007).

[85] J. Dho and M.G. Blamire, Appl. Phys. Lett. **87**, 252504 (2005).

[86] J. Nogues and I.K. Schuller, J. Magn. Magn. Mater. **192**, 203 (1999).

[87] H. Bea, M. Bibes, F. Ott, B. Dupe, X.-H. Zhu, S. Petit, S. Fusil, C. Deranlot, K. Bouzehouane, and A. Barthelemy, Phys. Rev. Lett. **100**, 017204 (2008).

[88] P. Borisor, A. Hochstrat, X. Chen, W. Kleemann, and C. Binek, Phys. Rev. Lett. **94**, 117203 (2005).

[89] V. Lankhim, V. Skuimryev, X. Marti, D. Hrabovsky, F. Sanchev, M.V. Garcia-Guenca, C. Ferrater, M. Varela, U. Liiders, J.F. Bobo, and J. Foutiuberta, Phys. Rev. Lett.**97**, 227201 (2006).

[90] N. Fujimora, T. Ishida, T. Yoshimura, and T. Ito, Appl. Phys. Lett. **69**, 1011 (1996).

[91] M. Ziese and M.J. Thornton (eds.), *Spin Electronics* (Springer, Berlin, 2001).

[92] J.F. Scott, *Ferroelectric Memories*, Springer, Berlin, 2000.

[93] R.A. Shelby, D.R. Smith, and S. Schultz, Science **292**, 77 (2001).

[94] D.W. Ward, E. Statz, K.J. Webb and K.A. Nelson, Preprint cond-mat/0401046 (2004).

Chapitre 2

The experimental techniques

In this chapter we describe both experimental techniques which have been used in this work : Fourier-Transform Infrared Spectroscopy (FT-IR) and Electronic Paramagnetic Resonance (EPR) spectroscopy. Reflectivity measurements performed via FT-IR spectroscopy allow one to obtain the optical response functions of investigated systems in the linear response regime. In particular we focus on the optical conductivity function, obtained by using Kramers-Kronig transformations. We also describe the theoretical models used to analyze the data. A section is devoted to the reflectivity measurements with coherent synchrotron radiation and with an electric field applied.

In turn, EPR spectroscopy has been used to investigate the local magnetic response of multiferroic materials. Once coupled to magnetization measurements, it provides information on both the microscopic and macroscopic magnetic interactions.

2.1 Reflectivity measurements with FT-IR Spectroscopy

The aim of FT-IR spectroscopy is to obtain informations on the optical functions of the system, by investigating its response to electromagnetic radiation. In this work we performed reflectivity measurements by varying temperature and the applied electric field.

The reflectivity is defined by

$$R(\omega) = \frac{I_R(\omega)}{I_0(\omega)} \tag{2.1}$$

where $I_R(\omega)$ ($I_0(\omega)$) is the radiation intensity reflected by (incident on) the sample. To obtain a spectral analysis of reflectivity data it is necessary to use either a dispersive or an interferometric technique. We use FT-IR spectroscopy (Section 2.1.3) to have frequency-dependent reflectivity data R(ω).

Starting from R(ω) at quasi-normal incidence (angle of incidence $\approx$ 0) we use the following analysis to obtain all the optical functions which describe the systems. Let us introduce the reflectivity coefficient at normal incidence $\tilde{r}$ defined by

$$\tilde{r}(\omega) = \frac{\tilde{E}_r(\omega)}{\tilde{E}_0(\omega)} \tag{2.2}$$

where $\tilde{E}_r$ ($\tilde{E}_0$) is the complex electric field of the electromagnetic radiation reflected by (incident on) the sample. By applying continuity equation for the parallel-component of the EM radiation at the interface vacuum-sample we obtain

$$\tilde{r}(\omega) = \frac{\tilde{E}_r(\omega)}{\tilde{E}_0(\omega)} = \frac{n(\omega) + ik(\omega) - 1}{n(\omega) + ik(\omega) + 1} \tag{2.3}$$

where $\tilde{n}(\omega) = n(\omega) + ik(\omega)$ is the complex refractive index. By taking the square modulus we have

$$R(\omega) = \frac{(n(\omega) - 1)^2 + k^2(\omega)}{(n(\omega) + 1)^2 + k^2(\omega)} \tag{2.4}$$

To obtain the real and imaginary part of $\tilde{n}(\omega)$ we use the Kramers-Kronig (KK) transformations [1]. For a given a response function $\widetilde{\chi} = \chi' + i\chi''$, KK can be written as

$$\chi''(\omega) = -\frac{2\omega}{\pi} P \int_0^\infty \frac{\chi'(\omega)}{\omega'^2 - \omega^2} d\omega' \tag{2.5}$$

relating the real and the imaginary part of the response function. By writing $\tilde{r}(\omega)$ in the polar formalism

$\tilde{r}(\omega) = \rho(\omega) e^{i\theta(\omega)}$ and substituting in Eq.2.5

$$\tilde{\chi} = ln\tilde{r}(\omega) = \ln \rho(\omega) + i\theta(\omega) \tag{2.6}$$

(with $\rho = |\tilde{r}| = \sqrt{R}$) we obtain

$$\theta(\omega) = -\frac{2\omega}{\pi} P \int_0^\infty \frac{\ln \sqrt{R}}{\omega'^2 - \omega^2} d\omega' \tag{2.7}$$

where P indicates the principal value of the integral. These relations play a fundamental role, not only in the theory of response functions : they are of great practical importance as they allow for the evaluation of the components of the complex dielectric constant or conductivity when only one optical parameter such as reflected or absorbed power is measured. In fact, by writing Eq.2.3 as

$$\sqrt{R} e^{i\theta} = \frac{n + ik - 1}{n + ik + 1} \tag{2.8}$$

we can see that by means of KK transformations, we can obtain values for n(ω) and k(ω) by measuring only R(ω). Finally, by using the following relations

$$\varepsilon_1(\omega) = n^2(\omega) - k^2(\omega) = \varepsilon_\infty - \frac{4\pi}{\omega}\sigma_2(\omega) \tag{2.9}$$

$$\varepsilon_2(\omega) = 2n(\omega)k(\omega) = \frac{4\pi}{\omega}\sigma_1(\omega) \tag{2.10}$$

we can calculate the dielectric function $\tilde{\varepsilon}(\omega)$ and the conductivity $\tilde{\varepsilon}(\omega)$ that fully characterize a system. It has to be stressed that, according to Eq 2.7, $\theta(\omega)$ can be calculated only if the reflectivity data are collected over an infinite range of frequencies. Therefore, we will use standard extrapolation procedures for frequencies both lower and higher than the measured interval (see next sections). As we state before, we will focus this study on the optical conductivity $\sigma_1(\omega)$: in the next section we describe this optical function and the properties of solid systems which can be derived from it.

2.1.1 Optical conductivity function

Under a macroscopic approach, the optical conductivity $\tilde{\sigma}(\omega)$ is defined as the linear response function which relates the electrical current vector **J** to the electrical field vector **E** by the relation $\mathbf{J}(\omega, \mathbf{q}) = \tilde{\sigma}\ (\omega, \mathbf{q})\mathbf{E}(\omega, \mathbf{q})$. In optical experiments, only the transverse conductivity ($\mathbf{J} \perp \mathbf{q}$) is detected, due to the transverse component conservation of the EM electric field [1]. Furthermore, in optics one probes excitations of any available energy $\hbar\omega = \varepsilon_n$, but only at $|\mathbf{q}| \approx 0$. The latter condition is related to the conservation of energy and momentum in an absorption process, which requires $\mathbf{q} = \mathrm{v/c}\ \mathbf{k}$, where $\epsilon = \mathrm{v}|\mathbf{k}|$ is the excitation dispersion relation. In condensed matter, no velocity v higher than 10^6 cm/s (Fermi velocity in metals) is reached, while c $\approx 3{\cdot}10^{10}$ cm/s, which implies $|\mathbf{q}| \approx 0$ for any value of ω in the optical range. It is worth noting that the excitation of an electron of momentum **k** in a metal to an energy level ε_f - $\varepsilon_i = \hbar\omega$ implies the creation of a hole of momentum -**k**, so that the total momentum **q** of the electron-hole excitation is still zero and electron with any **k** can be excited.

Following another approach we can relate $\tilde{\sigma}(\omega)$ to the microscopic observables defined in a N-electron system. $\tilde{\sigma}(\omega)$ in fact, is related to the imaginary part of the electric susceptibility $\tilde{\chi} = \mathbf{P}/\mathbf{E}$ through the relation $\mathrm{i}\omega\tilde{\sigma}(\omega) = \tilde{\chi}(\omega)$. Here **P** is the polarization operator and $\mathbf{J} = \partial\mathbf{P}/\partial\mathbf{t} = \mathrm{i}\hbar[\mathcal{H},\mathbf{P}]$ is the current operator, which is defined microscopically as the sum over all particles of the particle-velocity operator at the particle position. The interaction Hamiltonian between a medium and the electromagnetic radiation of vector potential A can be written as

$$\mathcal{H}_{int} = -\frac{1}{c}\mathbf{J} \cdot \mathbf{A}, \tag{2.11}$$

Starting from the fluctuation-dissipation theorem, the following expression can be derived directly from the Fermi golden rule

$$\sigma_1(\omega) = \sum_n \frac{1}{\hbar\omega V} \int_0^\infty dt \langle n|[\mathbf{J}(0)\mathbf{J}(t)]|n\rangle e^{i\omega t} \tag{2.12}$$

where V is the unit volume. This is the so-called Kubo formula [1]. The right-hand side of Eq.2.12 can be also derived independently from the Fermi golden rule for the transition probability W_{mn} between two energy levels [1] :

$$W_{mn} = \frac{2\pi}{\hbar}|\langle n|\mathcal{H}_{int}|m\rangle|^2 f(\varepsilon_n)[1 - f(\varepsilon_n)]\delta(\hbar\omega - \varepsilon_n + \varepsilon_m) \tag{2.13}$$

1. Although the optical (transverse) conductivity in general is a tensor for arbitrary crystal symmetry, for crystals with orthorhombic and higher symmetry the conductivity tensor reduces to a vector, with different components in the different crystallographic orientations, this difference being determined by the (anisotropic) form factor.

where f(ε_n) is the Fermi function. Once summed over all the possible initial and final states, this equation states that $\sigma_1(\omega)$ is proportional to the total transition rate W. Thus, the optical conductivity is proportional to the sum over all the possible $\hbar\omega$ energy transitions in a given distribution of states ε_n whose ground state is ε_m, weighted by their dipole matrix element (Fig. 2.1) :

$$\sigma_1(\omega) = \frac{\pi}{V} \sum_n |\langle n|\mathbf{J}|m\rangle|^2 \frac{\delta(\hbar\omega - \varepsilon_n + \varepsilon_m)}{\varepsilon_n - \varepsilon_m} \tag{2.14}$$

Basing on this microscopical interpretation of $\sigma_1(\omega)$, we can now investigate the transitions

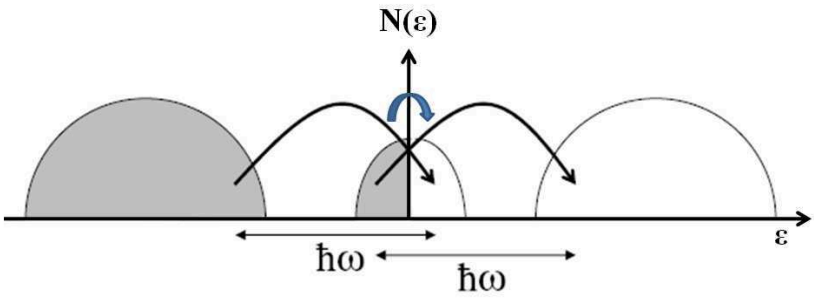

FIGURE 2.1 – Sketch of a density of states N(ε) (grey : occupied, white : unoccupied). The optical conductivity at a given frequency ω is the sum of all the transitions from an occupied to an empty state separated by an energy $\hbar\omega$.

taking place either in metals or insulators. In the next section we follow this approach in the framework of the Drude-Loretz model.

2.1.2 The Drude-Lorentz model

In the Drude-Lorentz model, a linear response function (in our case $\sigma_1(\omega)$ can be decomposed into a sum of several contributions related to different charge excitations. It describes the interaction of an electron gas with the electromagnetic radiation in a solid and allows one to describe the infrared spectra in terms of a sum of Lorentz oscillators. It is also possible to calculate the low-frequency behavior of R(ω), below the measurement range, in order to perform KK transformations.

2.1.2.1 Drude conductivity in metals

The Drude model considers metals as classical electron gases undergoing a diffusive motion. The central assumption of the model is the existence of an average relaxation time τ which governs the relaxation of the system towards the equilibrium. The equation of motion for the electron, when an external electric field $\mathbf{E}$ is applied, is

$$\frac{d\langle \mathbf{p}\rangle}{dt} = -\frac{\langle \mathbf{p}\rangle}{\tau} - e\mathbf{E} \tag{2.15}$$

The current density is given by $\mathbf{J} = -nep/m$ where n is the density of charge carriers, m the carrier mass, and $-e$ the electronic charge. For dc electric fields, the condition $d\langle\mathbf{p}\rangle/dt = 0$ leads to a dc conductivity $\sigma_{dc} = ne^2\tau/m$. If the electric field is an EM wave so that $\mathbf{E}(t) = \mathbf{E}_0 e^{-i\omega t}$, the solution of the equation of motion is

$$m\frac{d^2\mathbf{r}}{dt^2} + \frac{m}{\tau}\frac{d\mathbf{r}}{dt} = -e\mathbf{E}(t) \tag{2.16}$$

giving for the complex conductivity the expression

$$\tilde{\sigma}(\omega) = \frac{ne^2\tau}{m}\frac{1}{1 - i\omega\tau} \tag{2.17}$$

In the framework of this model, the electron mean free path is $\ell = \langle v\rangle_{th}\tau$ where $\langle v\rangle_{th}$ is the average thermal velocity of classical particles.

If we now consider electrons obeying to quantum statistics, the picture is fundamentally different : this problem has been investigated by Sommerfeld. The Fermi surface plays an essential role. The equation of motion for the average momentum is the same as given above but the scattering processes which establish the equilibrium in the presence of an electric field involve only electrons near to the Fermi surface. In the absence of an electric field, the Fermi sphere is centered around zero momentum [$\langle\mathbf{p}\rangle = \hbar\langle\mathbf{k}\rangle = 0$], while it is displaced in the presence of an applied field $\mathbf{E}$ by $-eE\tau/\hbar$, as shown in Fig. 2.2. Quantum states deep inside the Fermi sea are not affected by the electric field and the expression for the mean free path is $\ell = \mathrm{v}_F\tau$, with v_F the Fermi velocity. This expression differs dramatically from the mean free path given by the original Drude model. Such difference has important consequences for the temperature dependence, as well as for the non-linear response to large electric fields [2].

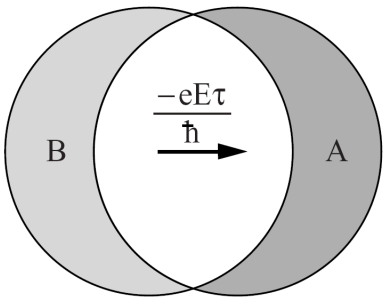

FIGURE 2.2 – Displaced Fermi sphere in the presence of an applied electric field E. Electrons are moved from region B to A. The Figure applies to a metal with a spherical Fermi surface of radius k_F, or to a circular Fermi surface in two dimensions.

2. Further corrections to these models take into account interactions with the lattice, electron-electron and electron-phonon interactions. These effects can be summarized assuming a frequency dependence for the scattering time τ and the effective mass m^* [21]

Using the complex conductivity in Eq.2.17, as obtained by the Drude-Sommerfeld model, various optical parameters can be easily evaluated. The dc limit of the conductivity is $\sigma_1(\omega \to 0) = \sigma_{dc} = ne^2\tau/m = \omega_p^2\tau/4\pi$ and the frequency dependence of $\sigma_1(\omega)$ can be written as :

$$\sigma_1(\omega) = \frac{\omega_p^2\tau}{4\pi}\frac{1}{1+\omega^2\tau^2} \tag{2.18}$$

It should be noted that the Drude expression for the conductivity can be easily recovered from the Kubo formula in Eq.2.12, assuming for all states the same current-current correlation time τ and $\mathbf{J}(t) = \mathbf{J}(0)e^{-t/\tau}$ as the time dependent correlation of the current density [1]. Therefore, in the Drude model, the complex conductivity, and consequently all the linear response functions, are fully characterized by two parameters : the plasma frequency ω_p and the relaxation rate $\gamma_D = 1/\tau$ (in general $\gamma_D \ll \omega_p$). The optical conductivity $\sigma_1(\omega)$ is shown at the bottom of Fig. 2.3 for a general metal. The reflectivity $R(\omega)$ for a bulk material is plotted at the top of Fig. 2.3. $R(\omega)$ is close to 1 up to the plasma frequency where it drops rapidly to almost zero ; this is called the plasma edge.

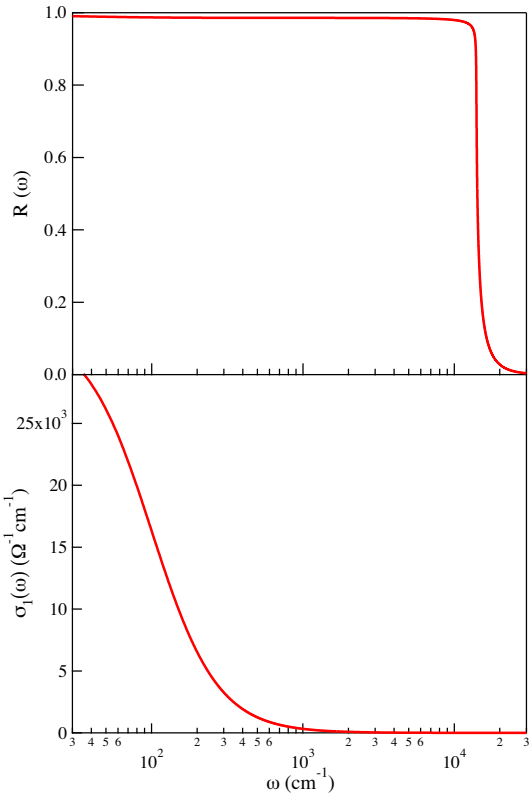

FIGURE 2.3 – Frequency-dependent reflectivity and optical conductivity calculated using the Drude model (see text) : values for plasma frequency ω_p and scattering rate γ_D are typical for metals ($\omega_p = 14000$ cm^{-1}, $\gamma_D = 100$ cm^{-1}).

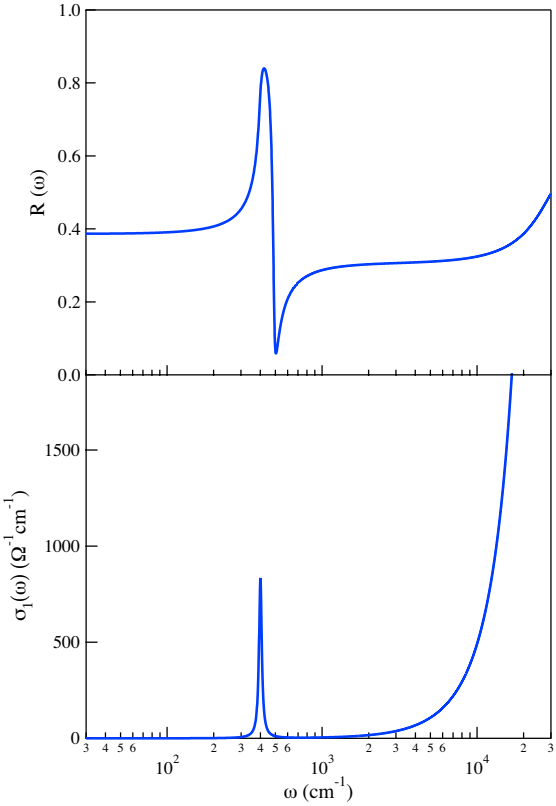

FIGURE 2.4 – Frequency dependent reflectivity and optical conductivity calculated using the Lorentz model (see text) with parameter values typical for an insulator. A phonon absorption in the far infrared (ω_0 = 400 cm^{-1}, S = 1000 cm^{-1}, γ = 20 cm^{-1}) and an optical electronic transition in the visible range (ω_0 = 30000 cm^{-1}, S = 100000 cm^{-1}, γ = 20000 cm^{-1}) are shown.

2.1.2.2 Lorentz atomic oscillator model for insulators

The main optical feature of an insulator is the presence of a single-particle gap in the excitation spectrum, separating the valence band from the conduction band. The former is full and the latter is empty at zero temperature. The Fermi energy lies between these bands leading to zero dc conduction at T = 0 and to a finite static dielectric constant. This situation can be reproduced assuming the response of a classic atomic oscillator, that provides a phenomenological description reproducing many of the optical characteristics of insulators and semiconductors. We keep the same terms that we included in the Drude description, inertial and relaxational response, introducing a new parameter, a restoring force K. This is the so-called Lorentz model for a harmonic oscillator. The equation of motion is

$$\frac{d^2\mathbf{r}}{dt^2} + \gamma\frac{d\mathbf{r}}{dt} + \omega_0^2\mathbf{r} = -\frac{e}{m}\mathbf{E}(t) \tag{2.19}$$

where $\omega_0 = \sqrt{K/m}$, m is the electron mass and $\gamma = 1/\tau$ takes into account the damping effects. Such a model obviously does not lead to a well-defined energy gap, but it is nevertheless fitting most of the features of non-conducting systems. It is thus widely used to describe the optical properties of insulating materials.

When a local electric field $\mathbf{E}$ has the form $\mathbf{E}$=$\mathbf{E}_0 e^{-i\omega t}$, the induced dipole moment is

$$\tilde{\mathbf{p}} = -e\tilde{\mathbf{r}}(\omega) = \frac{e^2}{m}\mathbf{E}\frac{1}{(\omega_0^2 - \omega^2) - i\gamma\omega} = \tilde{\alpha}_a(\omega)\mathbf{E} \tag{2.20}$$

where $\tilde{\alpha}_a(\omega)$ is the atomic polarizability. The macroscopic polarization is the sum over all the n atoms per unit volume involved in this excitation : $\mathbf{P} = n\langle\tilde{\mathbf{p}}\rangle = n\tilde{\alpha}_a\ \mathbf{E} = \tilde{\chi}_e\mathbf{E}$. Since the dielectric function is related to the dielectric susceptibility via $\tilde{\varepsilon}(\omega) = 1 + 4\pi\tilde{\chi}_e$, we obtain for the frequency-dependent complex dielectric function :

$$\tilde{\varepsilon}(\omega) = 1 + \frac{4\pi n e^2}{m}\frac{1}{(\omega_0^2 - \omega^2) - i\gamma\omega} \tag{2.21}$$

where ω_0 is the central frequency of the oscillator, γ denotes the broadening of the oscillator due to damping, and $4\pi ne^2/m$ describes the oscillator strength. Here we have assumed that each atom contributes with one electron to the absorption process. Using the relation $\tilde{\varepsilon} = 1 + 4\pi\tilde{\sigma}/\omega$ we can easily evaluate the Lorentz expression for the complex conductivity :

$$\tilde{\sigma}(\omega) = \frac{ne^2}{m}\frac{\omega}{i[(\omega_0^2 - \omega^2) - i\gamma\omega]} \tag{2.22}$$

A comparison between Eq.2.22 and Eq.2.17 shows that the Drude conductivity can be obtained from the Lorentz model by setting ω_0= 0. This is not surprising, as we have retained only the inertial and damping terms to describe the properties of the metallic state. In crystals, also the ions contribute to the polarizability : two atoms vibrating in a transverse-optical mode generate an electric dipole moment oscillating at the corresponding phonon frequency. One can describe the phonon contribution to the polarizability in the framework of Lorentz model : the energy associated to lattice vibrations is about $\hbar\omega \sim 10^2 \div 10^3$ cm^{-1} and is generally lower than the typical energies of interband electron transitions, thus strongly contributing to the conductivity in the far infrared. In Fig.2.4 the frequency-dependent reflectivity and optical conductivity calculated for a typical insulating material are shown. While no metallic Drude term is present, a phonon absorption in the far infrared and an optical electron transition in the visible range are both evident. It is worth remarking that in good conductors optical phonons are usually screened, and therefore not observed. Indeed the electronic plasma frequency ($\omega_p^2 = 4\pi ne_2/\mathrm{m}$) is much greater than the frequencies of the lattice vibrations.

The overall trend of the complex dielectric function in a crystal can thus be expressed as

$$\tilde{\epsilon}(\omega) = \epsilon_\infty - \frac{\omega_p^2}{\omega^2 + i\gamma_D\omega} + \sum_j \frac{S_{el,j}^2}{(\omega_{0,j}^2 - \omega^2) - i\gamma_j\omega} + \sum_k \frac{S_{ph,k}^2}{(\omega_{0,k}^2 - \omega^2) - i\gamma_k\omega} \tag{2.23}$$

which takes into account the contributions coming from free electrons (first term, Drude), electron transitions ("el" suffix) and phonons ("ph" suffix). Eq.2.23 represents the so-called Drude-Lorentz model and allows for the evaluation of the different contributions to

the conductivity. The second term in Eq.2.23 is also present in metals, in addition to the Drude term, in order to take into account the high-energy electronic interband transitions. Similarly to the case of the Drude model in metals, by fitting the experimental reflectivity acquired on an insulating sample with Lorentz oscillators, it is possible to extrapolate its low-frequency behavior in order to perform the KK analysis. As one can see in Fig. 2.4, in a typical insulator the reflectivity displays a constant trend of R(ω) in the low frequency region, below the phonon absorption.

In the next section we describe the FT-IR spectroscopy, the technique we used to perform the spectral analysis of the reflected radiation.

2.1.3 Fourier-Transform Infrared Spectroscopy

The Fourier-Transform Infrared Spectroscopy (FT-IR) is a widely used optical technique which allows one to obtain a rapid spectral analysis of the electromagnetic radiation with high spectral resolution. It is a non-dispersive method and can be used over a wide spectral range (TeraHertz - Uv e.g. 1meV - 5 eV). This technique employes the Michelson interferometer (shown in Fig. 2.5) as a spectrometer, first developed by Michelson and Morley in 1880. Therein, a beam of radiation from a point source (a black body or a synchrotron) is split into two beams, directed along two different paths. When the two beams are recombined, as a consequence of interference, the intensity becomes an oscillating function of the path difference x (the interferogram $I(x)$). $I(x)$ is sampled by the fringes of a monochromatic laser beam sent through the same optical path. The Fourier transform of $I(x)$ gives the power spectrum B(ω) of the radiation (Fig.2.6).

Here we summarize the FT-IR spectroscopy main advantages :
- broad band energy analysis (more than three order of magnitude) : most of the principal solid state physics ranges of interest ;
- high frequencies resolving power (proportional to the maximum value of x,) ;
- circular apertures instead of slits (as in monochromators : *Jaquinot advantage*) ;
- simultaneous measurement of the whole frequency range : this reduces the collecting time by a factor of n (where n is the number of points in the spectrum) and improves the signal-to-noise ratio by a factor $N^{1/2}$ (averaging N spectra), with respect to a single spectrum collected with dispersive techniques (*Fellget advantage*) ;

On the other hand, two main disadvantages of this technique are :
- the need for the K-K procedure or, alternatively, for another independent measurement (e.g., ellipsometry, transmittance) to determine both the real and imaginary part of the response functions ;
- the lack of high-flux broadband radiation sources.

A detailed formal discussion of FT-IR interferometry can be found in Ref.[2]

2.1.4 FT-IR Spectroscopy Experimental apparatus

In this section we describe the experimental setup used for FT-IR reflectivity measurements. The apparatus consists of a Michelson interferometer, model BOMEM DA- 3, a sample chamber mounted on it and several cryogenic and vacuum components. In what follow we report a brief description of the apparatus and a functional characterization of

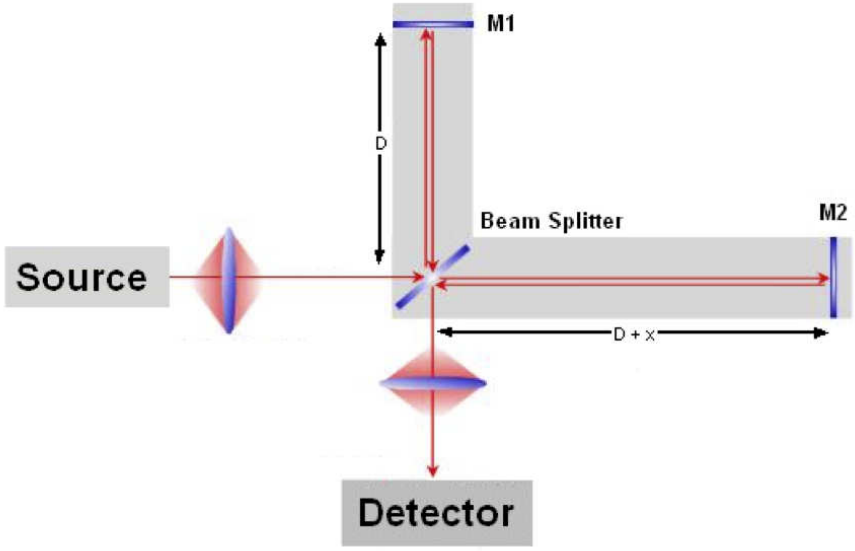

FIGURE 2.5 – Sketch of a Michelson interferometer. From a point source S, using collimating mirrors, electromagnetic radiation is sent to a beam splitter BS that separates it in two components. One of them is sent to a static mirror SM, while the other one to a moving mirror MM. Thereafter the signals are recombined and sent to the detector D.

the instruments.

2.1.4.1 BOMEM DA-3 Interferometer

The BOMEM DA-3 interferometer has a vertical structure : the main compartment contains the sources, the beamsplitter and the main optical components Fig.2.7. A sample compartment is connected to the main compartment and both of them can be independently evacuated down to a pressure of about 1 mbar. Different detectors can be connected to the modular sample compartment Fig. 2.9. One can see the radiation path through the reflectivity setup, made of a series of aluminum mirrors (Fig. 2.10). The central mirrors are both spherical, in order to focus the beam onto the sample and collect the reflected light sent to the detector. They are connected to remotely-controlled motors, which allow for an in-vacuum alignment. The beamsplitter is located in the main compartment of the interferometer and, as for detectors, can be changed depending on the investigated spectral range. The following standard commercial detectors have been employed :

- Ge Bolometers from InfraredLabs, contained in a Dewar flask and provided of low-passing filters ; the working temperature is 4.2 K and is used below 650 cm^{-1} ;
- photoconductive nitrogen-cooled HgCdTe detector from 500 to 10000 cm^{-1} ;

– a Si photodiode for frequencies higher than 9000 cm^{-1}.

In Fig.2.8 we report the optical configuration of the apparatus with the suitable components for each spectral range.

2.1.4.2 Closed-cycle cryostat and heating system

In order to perform reflectivity measurements at low temperature, we used a closed-cycle cryostat Leybold Coolpack 600 with minimum temperature T = 10 K on its cold finger. A thermometer and a heating coil are mounted on the cold finger allowing for temperature setting within 1 K. The sample is glued by silver paint to a brass cone screwed on the cold finger (see Fig.2.11). To avoid water or carbon dioxide condensation on the sample surface, a pressure of 10^{-6} mbar was kept within the cryostat, using a turbomolecular pump.

The heating system is under vacuum as the cryogenic setup. It contains two power resistors coupled to a metallic sample holder. Maximum temperature available is 500 K with stable thermal regulation. A sketch of the heating system is shown in Fig.2.12.

2.1.4.3 Measuring the reference : the overfilling technique

In order to obtain the absolute value of the reflectivity R(ω) in Eq.4.16 it is necessary to measure a reference signal. Usually, the intensity reflected by a pre-aligned reference (mirror) is measured at every temperature. However, in case of irregular single crystals, diffusion and/or diffraction effects become important because of surface defects. Such effects can be partially eliminated with the overfilling technique : by means of in-vacuum metal evaporation, the sample surface itself is covered by a gold (or silver) film and then used as a reference. The thickness of such film is maintained smaller than the surface-defect dimension. Therefore diffusion/diffraction effects could become negligible, as showed by Homes et al. [3].

In Fig.2.13 we show the evaporation device. A short wire of the metal (gold, silver or aluminum) to be evaporated is wounded around a tungsten filament. The filament is connected to a moving wand that can be placed in front of the sample. When a current

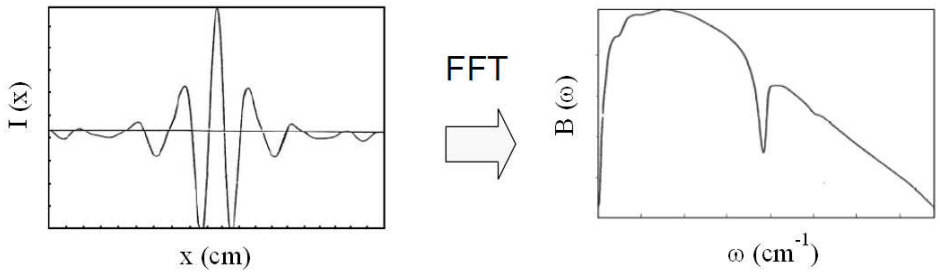

FIGURE 2.6 – Interferogram I(x) and the corresponding power spectrum B(ω), obtained through a Fast Fourier Transform (FFT) algorithm

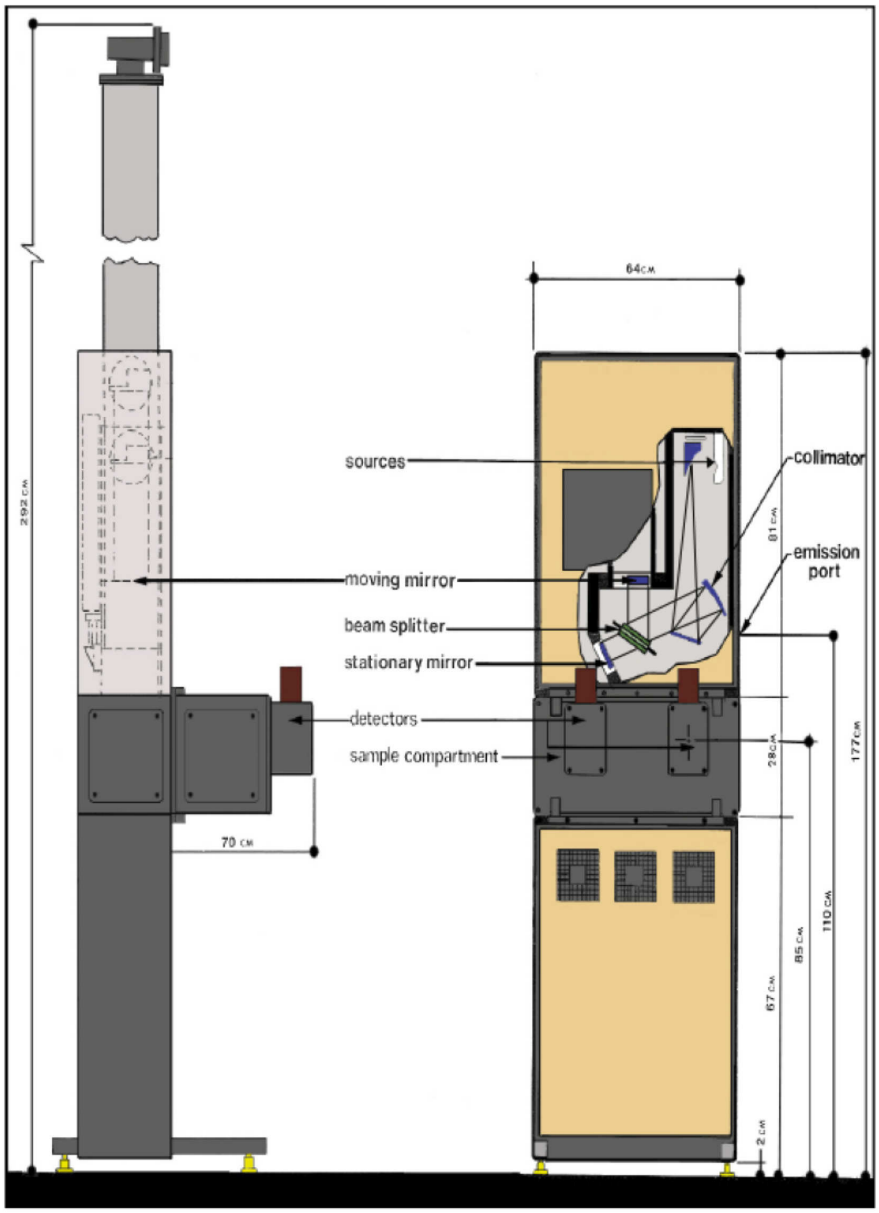

FIGURE 2.7 – Scheme of BOMEM DA-3 : side and front view. The source location and the beamsplitter are shown, as well as the moving mirror.

of about 3 A passes through the filament, the metal melts and a film is deposited on the sample surface. Another advantage of this technique is that the optical path doesn't change during the deposition and the interferometer is kept evacuated and free of any mechanical stress. It is common experience that the best deposition occurs when the sample is at room temperature therefore two thermal cycles are required with this procedure : during the first cycle we measure (the sample-reflected intensity), during the second one we measure

Spectral range	$\omega_L \div \omega_H$ (cm^{-1})	Source	Beamsplitter	Window	Detector (T)
far IR	20÷100	Hg arc	Mylar 25 μm	polyethilene	Bolometer (4.2 K)
	30÷220	Hg arc	Mylar 12 μm	polyethilene	Bolometer (4.2 K)
	190÷650	Globar	Mylar 3 μm	KRS5	Bolometer (4.2 K)
	30÷650	Hg arc	Si-covered Mylar 6 μm	polyethilene	Bolometer (4.2 K)
mid IR	500÷6000	Globar	Ge on KBr	KRS5	HgCdTe (77 K)
near IR	4000÷10000	Quartz-halogen	Quartz	Glass	HgCdTe (77 K)
visible	9000÷25000	Quartz-halogen	Quartz	Glass	Si (295 K)

FIGURE 2.8 – Experimental setup for different optical ranges. Note that many far-IR ranges overlap to get independent determinations of the IR reflectivity.

the reference intensity $I_0(\omega)$ after the metal deposition over the sample surface. Both the sample and the reference are measured at each temperature so that most of the thermal contractions of the sample holder can be recovered. High-T measurements (T > 300 K) allow us to deposit a metal film at each temperature by recovering all the thermal distortion.

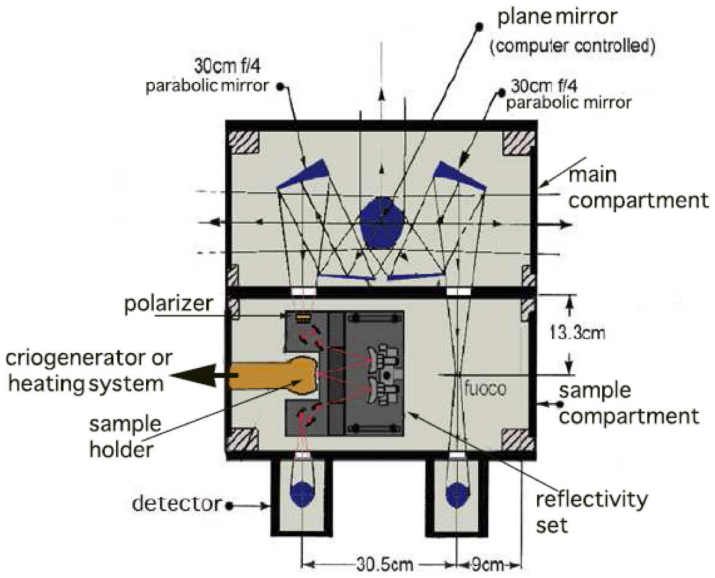

FIGURE 2.9 – Schematic top view of the interferometer BOMEM DA-3. The optical path within the reflectivity setup is indicated by a red line.

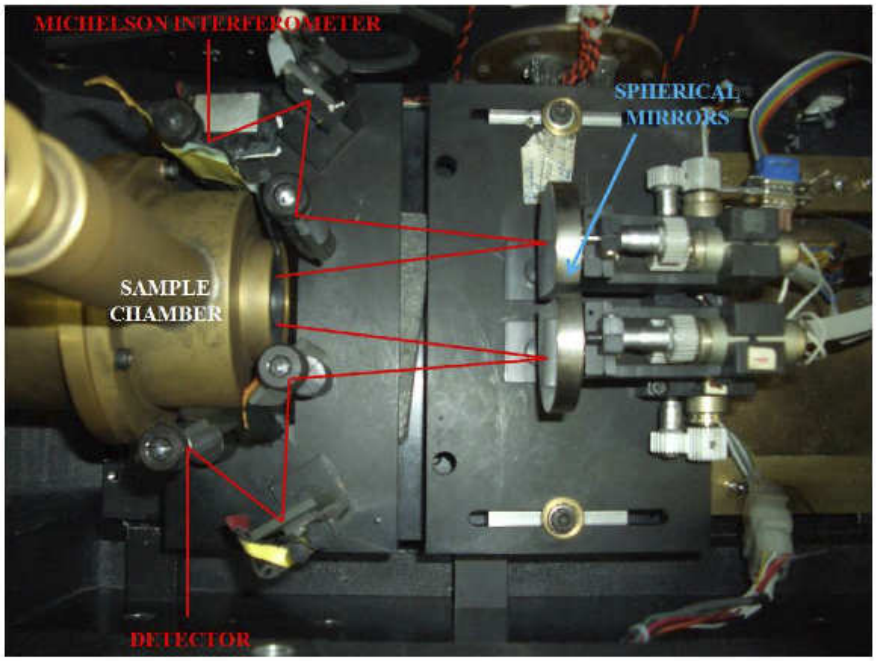

FIGURE 2.10 – Reflectivity setup in the sample compartment of BOMEM DA-3. The optical path from the Michelson interferometer to the detector is indicated by a red line.

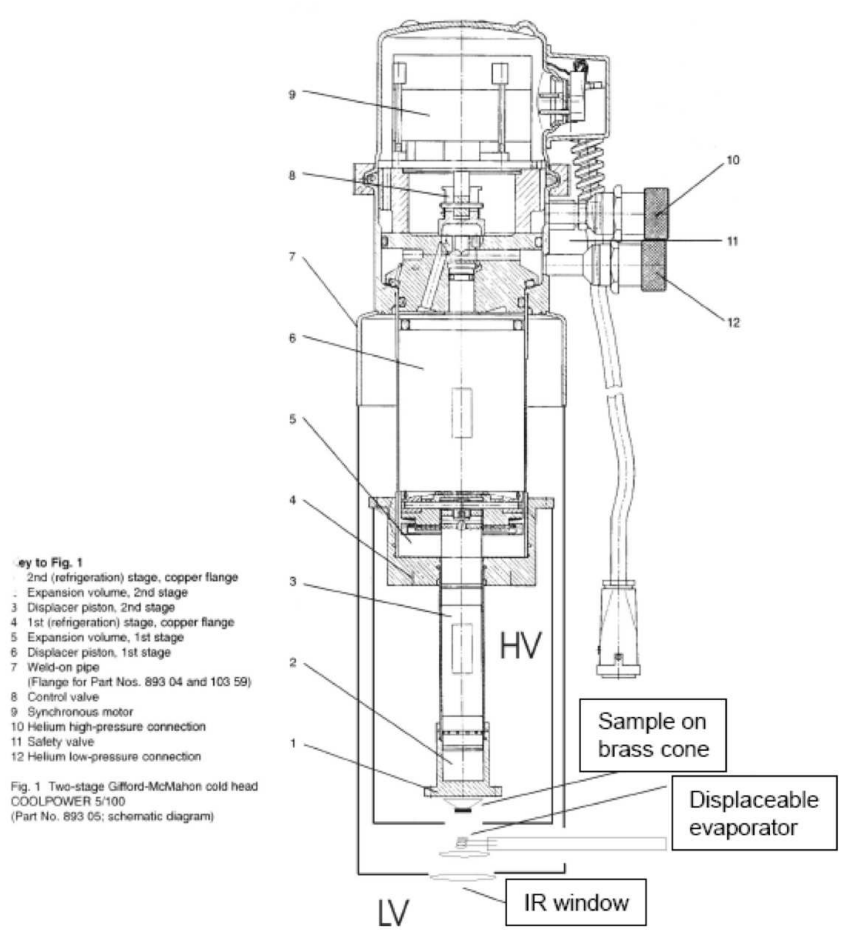

FIGURE 2.11 – Scheme of the Leybold cryopump with the sample holder on top. Two vacuum environments are present : LV (low vacuum, for the interferometer optics) and HV (high vacuum, in the cryostat). An IR window separates the two environments.

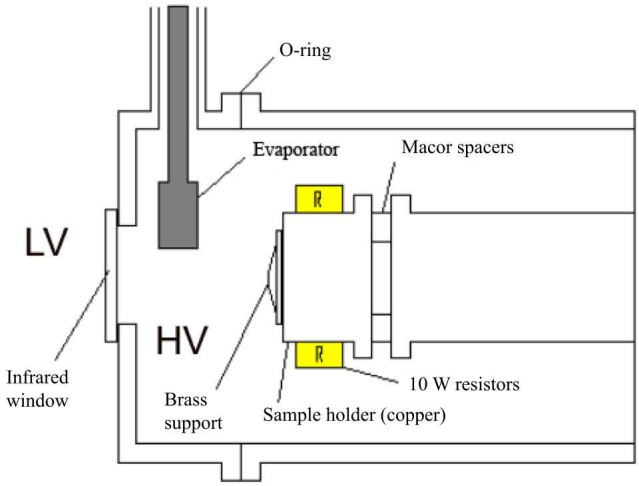

FIGURE 2.12 – Schematic representation of heating system. As for the closed-cycle cryogenerator there are two vacuum environments : LV (low vacuum, for the interferometer optics) and HV (high vacuum, for the cryostat). An IR window separates the two environments.

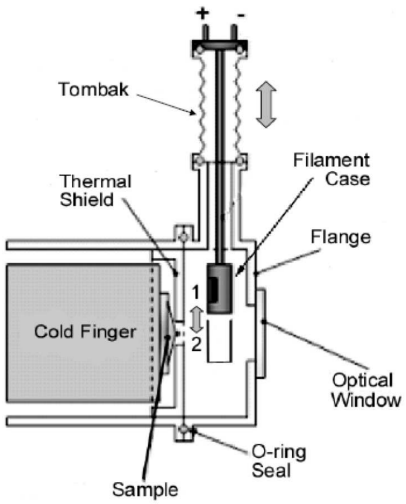

FIGURE 2.13 – Scheme of the evaporator. The filament is in position 1 while measuring, where it allows the passage of the light beam. When the spectra on the sample have been acquired at all temperatures, the sample is re-heated to room temperature ; the filament is displaced to position 2, a current of about 3 A is applied to evaporate metal. Filament is then moved back to position 1 to acquire reference spectra.

2.1.5 Terahertz spectroscopy with Coherent Synchrotron Radiation

In this section we explain how coherent synchrotron radiation has been used to extend the reflectivity measurements to the Terahertz region. Experiments with this technique have been performed at the BESSY II Storage Ring in Berlin at the IRIS Beamline.

The optical Terahertz (THz) and sub-THz range (1 THz = 33 cm^{-1}) is beyond the normal operation regime of optical and electronic experimental setup [4]. In the last decade these regions have become accessible in the time domain, by the use of ultra-fast laser pulses incident on biased semiconductors [5]. Recently, a brilliant but non-perturbative, broadband THz source has become available : the coherent synchrotron radiation (CSR) emitted by short relativistic electron bunches [6] [7] [9]. The high-average power of the CSR source thus allows one to extend the traditional infrared frequency range with respect either to thermal or conventional synchrotron sources. Using this high intensity pulsed THz source new opportunities for scientific applications are now available not only in condensed matter but also for medical, technological, manufacturing, space and defense applications. At present days, several storage rings worldwide try to establish coherent far-infrared radiation (e.g. ELETTRA at Trieste, ANKA at Karlsruhe) and even proposals for new dedicated CSR rings (CIRCE at the ALS, Berkeley) have been submitted. BESSY II has been working in CSR operation mode since 2002 for both THz and time-resolved experiments [10][11][12]

2.1.5.1 Coherent Synchrotron Radiation

The conventional synchrotron radiation emitted from an electron storage ring covers the EM spectra from the far-IR to the x-ray region. The radiation is provided by relativistic electrons experiencing a transverse acceleration and is usually emitted incoherently : EM waves are emitted with random phase relations by the individual N electrons in the bunch. In this case the radiation intensity is proportional to N. If, however, the electron bunches length is comparable with the long-wavelength part of the radiation, as displayed in Fig. 2.14, EM waves superimpose in phase and all the electric fields add up coherently [13]. Total radiation power is proportional to the square of the emitting electrons (Fig. 2.14(b)). As shown in Fig.2.14(c), coherent radiation lies in the far-IR range, where conventional thermal sources have quite low intensity. This spectral range at the boundary to the microwave region is commonly referred to as the THz gap, covering frequencies too high to be accessible to microwave sources and too low for photonic devices. Coherent far-IR synchrotron radiation was first detected at LINAC-based sources[14]. Recently, broadband coherent enhancement of far-IR synchrotron radiation was observed at the Jefferson Laboratory free electron laser for sub-picosecond electron bunches [7] [8]. At several electron storage rings, fluctuating bursts of coherent far-IR radiation have been observed, but they are not suitable for far-IR spectroscopy [15]. For the first time, steady state coherent far-IR radiation from an electron storage ring [6] was achieved at BESSY (Berliner Elektronenspeicherring-Gesellschaft f*ü*r Synchrotronstrahlung m.b.H., Berlin, Germany). For a given radiation wavelength, λ, the emitted power, P, can be derived from the *incoherent* single-particle power, $P_{1,incoh}$ [16] :

$$P = NP_{1,incoh}(1 + Nf_{\lambda}) \tag{2.24}$$

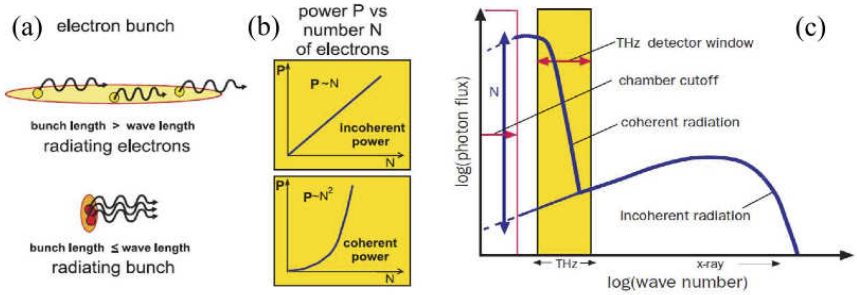

FIGURE 2.14 – (a) Long bunches emit incoherent waves with random phase relation. Short bunches behave as a macroparticle and emit coherent waves at equal phase. (b) The resulting power grows linearly with the number of electrons for the incoherent case, while the coherent intensity grows with the square of the charges involved. (c) The synchrotron radiation spectrum shows a dramatic increase of photon flux in the long-wavelength range, if the coherent radiation is no longer shielded by the vacuum chamber. This additional increase is proportional to the number N of electrons involved [13]

where f_λ is the form factor, derived from the Fourier transform of the longitudinal electron density in the bunch. For $Nf_\lambda \gg 1$ phase correlation is achieved and mostly coherent synchrotron radiation is emitted. In the case of a Gaussian bunch density distribution with the rms length σ, form factor is given by $f_\lambda = exp[-(2\pi\sigma/\lambda)^2]$. According to this relation short bunches support CSR emission at long wavelengths. Shielding effects of the dipole vacuum chamber suppresses coherent far-IR radiation using standard BESSY user optics [17]. To overcome this limitation bunch length and shape are adjusted tuning the storage ring optics as displayed in Fig. 2.17 : this ring operation is called low-α mode [6] (α is the *momentum compaction factor*, describing orbit length variation with respect to the beam energy). This operation mode produces shorter bunches, higher beam current and non-Gaussian beam shape.

Above a certain threshold current, bunch instabilities are involved in the emission process, often leading to periodic or even stochastic bursting [18]. These instabilities can limit spectroscopic applications but enhance the emitted CSR power. By changing α, fixing the rf-cavity voltage, zero-current bunch length, σ, can be tuned as follow

$$\sigma = \sigma_0 f_s / f_{s_0} \quad and \quad \alpha/\alpha_0 = f_s^2/f_{s_0}^2 \tag{2.25}$$

where "0" subscript refers to operating parameters of the regular-user optics and f_s is the synchrotron frequency. Values of regular-user optics are $\sigma_0 = 4.5$ mm, $\alpha_0 = 7.3{\cdot}10^{-4}$, f_{s_0}= 7.5 kHz at 1.3 MV rf voltage with 1.7 GeV beam energy. With the low-α optics, f_s can be reduced by more than one order of magnitude, corresponding to a 100 times smaller α. The electrons revolution time at Bessy is 800 ns and in low-α operation mode typical rms length of radiation pulse is about 1 mm (equivalent to 3 ps), defined by the electron bunch length. Depending on the fill pattern, there can be up to 400 bunches stored in the ring equally spaced by 2 ns (500 MHz repetition rate).

The radiation from bending dipoles has typical wavelength between few millimeters and , and mostly incoherently emitted. Coherent radiation is only reached in the long-wavelength limit, corresponding to an energy "transition region" that lies between few cm^{-1} ($\approx$ 2-3 cm^{-1}) and the shielding cutoff at $\approx$ 40 cm^{-1}. The coherence disappears at shorter wavelengths. The intensity in the transition region depends strongly on the coherent superposition of the emitted radiation from different electrons in the bunch, described by the form factor, f_λ, strongly related to bunch current, rf-voltage amplitude, beam energy, and α value. The bunch length is also sensitive to bunch current. A high current value leads to longer bunches but also to high CSR power. This indicates a bunch deformation away from a Gaussian shape, which results from an interaction of the bunch with its own CSR field. Above a threshold current, interaction of the CSR field with the bunch becomes strong, and emitted intensity is periodically modulated or changes into a chaotic bursting process. This unstable bunch dynamics and radiation process can be detected in the normal-user and the low-α optics, whereas the stable emission only occurs in low-α mode. Emitted power of incoherent radiation is proportional to the average current, independent of α, whereas the coherent power scales with the square of the bunch current. However, due to bunch deforming and lengthening effects, scaling is actually stronger than the square of current. This nonlinear dependence is a proof of coherent emission process [19]. In Fig.2.15 results of beam diagnostic at BESSY [6] are presented.

The maximum in the power spectrum lies between 10 and 20 cm^{-1} [0.5 to 1 mm wavelength Fig.2.15(a)]. The intensity at larger wave numbers depends on the current bunch. As shown in Fig.2.15(b), an additional current enhances the spectrum at larger wave numbers beyond 40 cm^{-1} producing instability in the emission process. The incoherent spectrum in this frequency range shows very low intensity [2.15(a)] (normal-user optics operation). The ratio between coherent and incoherent spectra at the same average beam current can be used to measure the power amplification due to the coherent emission process. The amplification factor displayed in Fig. 2.15(c) is about 10^5. Fig. 2.15(a) shows also the intensity of the spectra of an internal 80 W Hg arc lamp (representing a blackbody of about 4500 K) : CSR source flux is 10^3 times higher at 10 cm^{-1}.

2.1.5.2 The infrared experimental station at BESSY

The benefit of highly-brilliant synchrotron radiation source is presently exploited, also in the infrared, in many storage rings worldwide. BESSY II has been provided by a large-acceptance multipurpose infrared beamline (IRIS) since 2001. The beamline provides a highly-brilliant IR radiation with a photon energy covering about 4 orders of magnitude, from the THz region up to the near IR region [19]. The optical design of the IRIS beamline is schematically shown in Fig. 2.16. The excellent performance in the THz region is provided by a maximum horizontal and vertical acceptance of this beamline : $\pm$30 mrad horizontally and $\pm$20 mrad vertically acceptance angle. The first mirror M1, plane, is placed at a distance of 900 mm from the source, the shorter possible distance from dipole magnet. The mirror is split into two halves, leaving a gap in the middle, that permits the high energy fan of the beam to pass through a water-cooled absorber. This design minimizes mechanical vibrations arising from the cooling system. The second and third mirrors, M2 and M3, are cylindrical and focus the IR radiation into an intermediate focus, F1, just behind a wedged window of

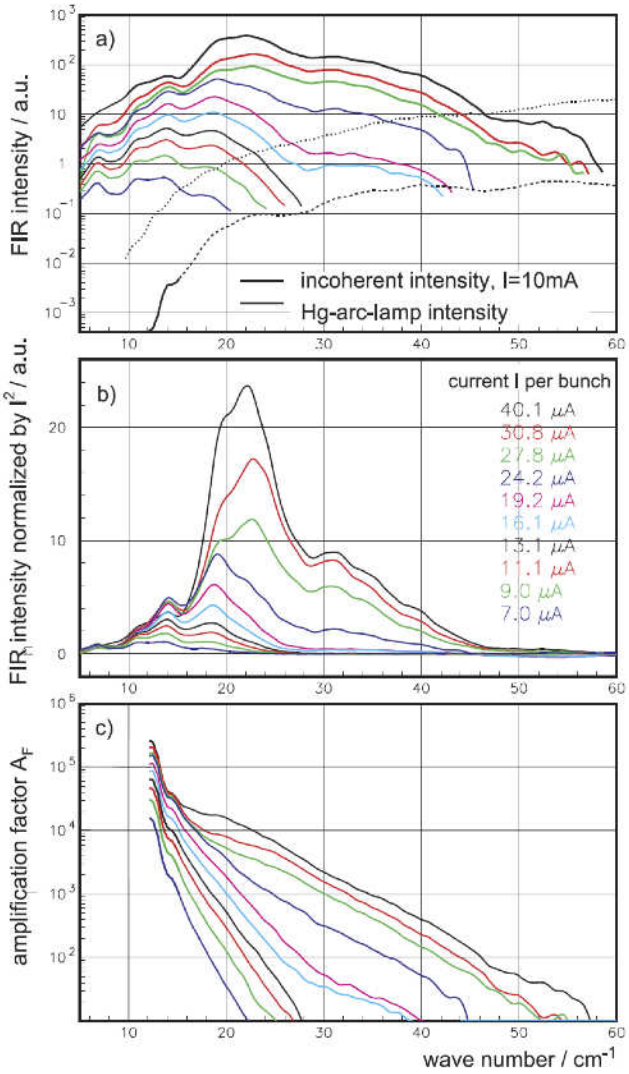

FIGURE 2.15 – (a) Radiation frequency spectra measured with a Fourier-transform spectrometer. (b) The intensity is normalized by the square of the bunch current : the intensity enhancement is more than square of the bunch current, indicating bunch deformation effects. (c) The amplification factor AF is the ratio between the coherent and the incoherent intensity. The amplification due to the coherent superposition of the waves becomes 10^5 times grater.

polycrystalline CVD diamond, which allows a broad transmission from the THz to visible. This window separates the ultra-highvacuum system from the fore-vacuum environment. The mirrors M4 and M5, both cylindrical, transfer and refocus the radiation into a second focus F2. The toroidal mirror M6 collimates the radiation, that is then transferred to the different experiments by a couple of plane mirrors. The beamline is equipped with several

experimental stations : two Fourier-transform infrared spectrometers (Bruker Optics), a mid-infrared microscope and an infrared ellipsometer. All the stations are suited for a wide range of spectroscopic applications in life science, material science, chemistry and solid state physics. The Fourier-transform spectrometer Bruker 66/v operates under vacuum and allows for broadband THz transmittance and reflectivity measurements.

The setup for low-temperature reflection and transmission measurements is shown in Fig. 2.18. The synchrotron radiation is fed into the evacuated Fourier-transform spectrometer with a Mylar beamsplitter. The modulated beam is then focused onto the sample by a first elliptical mirror with an incidence angle close to the normal. The reflected radiation is collected by a second elliptical mirror which focuses the radiation onto the detector. Geometrical factors, which strongly influence the diffraction pattern, are taken into account by successive insitu evaporation of a thick gold film on the sample surface as an optical reference (see section 2.1.4.3). The detector is a silicon bolometer operated at 1.4 K, with a modified optics entrance to reduce diffraction effects below 10 cm^{-1}. As will be described later, the above experimental setup has been used to extend the range of our reflectivity measurements to the sub-TeraHertz region.

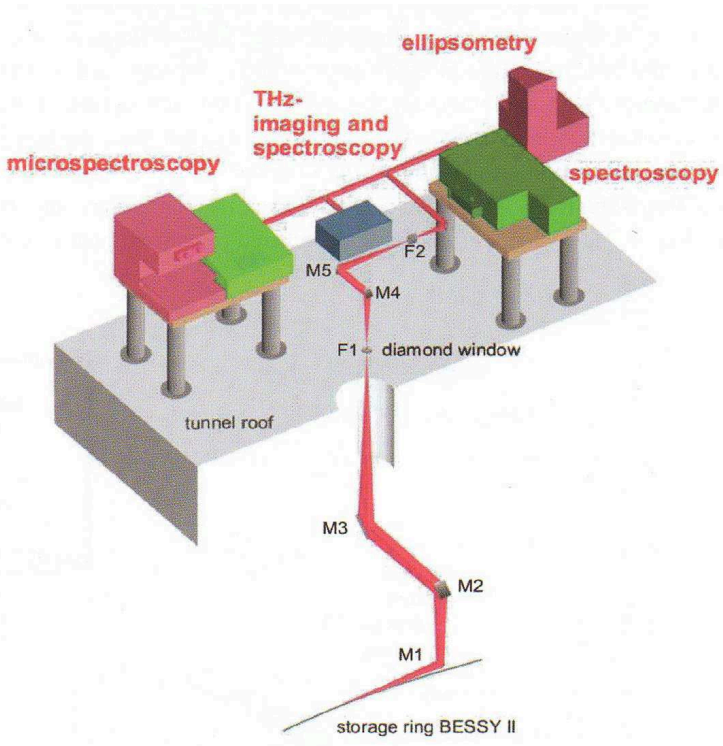

FIGURE 2.16 – Optical and mechanical draft of the BESSY II infrared beamline IRIS. The beamline provides highly-brilliant synchrotron radiation from the far-IR or THz up to the near-IR region. Experiments are mounted on the roof of the 0.7 m thick monolithic radiation shielding tunnel in the experimental hall, providing an almost vibration-free environment necessary for Fourier-transform spectroscopy [4].

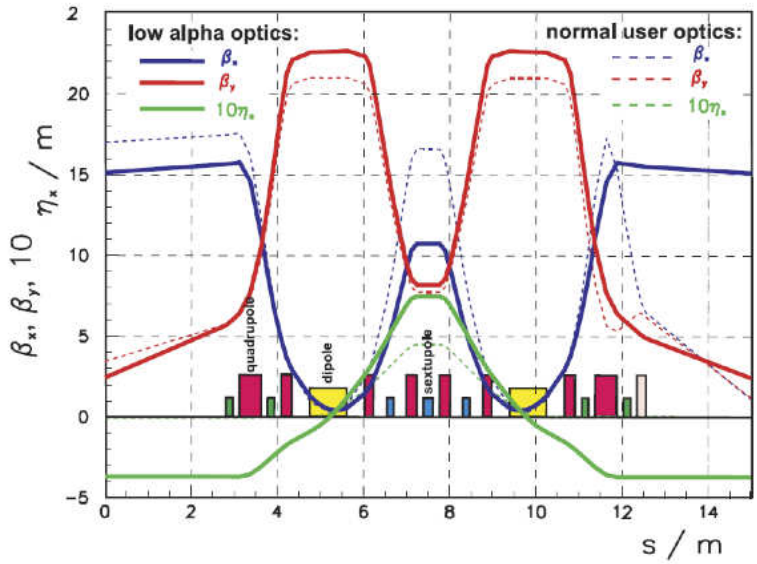

FIGURE 2.17 – Optical functions in low-α and normal operation mode. The low-α optics changes the dispersion function (green) inside the dipoles in an appropriate way. α is defined as the change of the orbit length L per momentum p change $\alpha = (\delta L/L)/(\delta p/p)$ [20]

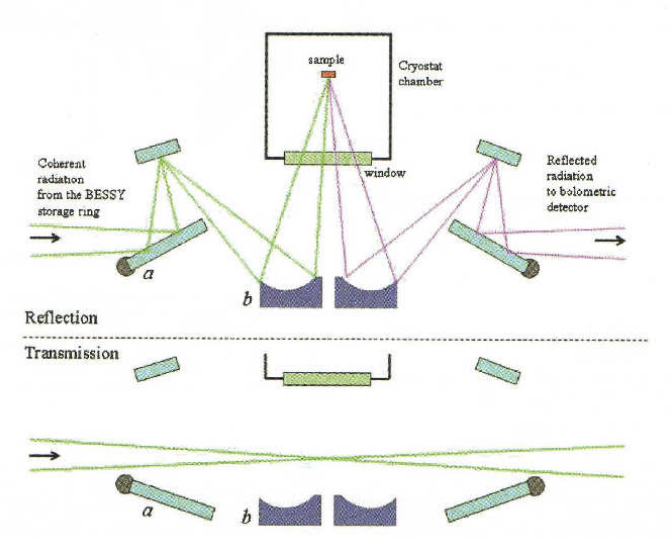

FIGURE 2.18 – Sketch of the optical setup for terahertz reflection spectroscopy with coherent synchrotron radiation at the storage ring BESSY. The optical setup is placed in the sample compartment of a Bruker 66/v interferometer. The sample is placed and oriented into a cryostat chamber. By using two remotely controlled mirrors (a), the beam can be either sent to the sample (upper panel) or directly transmitted to the detector (lower panel). A tight, diffraction-limited focusing of radiation is obtained through an ellipsoidal mirror (b). the specular reflection is collected by a symmetric mirror and sent to the detector [4].

2.1.6 Reflectivity measurements in electric field

As already stated, the FT-IR spectroscopy can provide information about the dynamics of the charge carriers in either metallic or insulating systems. Moreover, it provides important information on the fundamental energy scales involved in some phase transition. For this reason we investigate the recently reported intrinsic colossal electroresistace effect in LFO around room temperature, that leads to a metal-to-Insulator-transition (MIT). FT-IR is a powerful tool to investigate this kind of transitions because it shows whether the transition is purely bulk or affected by some other non intrinsic mechanisms (grain boundary, percolative paths, etc). To investigate this MIT we performed infrared reflectivity measurements under an applied electric field up to 10V/cm at several temperatures : Fig2.19 presents a scheme of the set up, which shows the conventional four-contact configuration. To avoid high-interface resistance we made electrical contacts (grey in the figure) by sputtering deposition of an aluminum film of 100nm. Three microwires for each contact were connected with the electrodes. In order to prevent damage on micro contacts we limited the current to 200 mA.

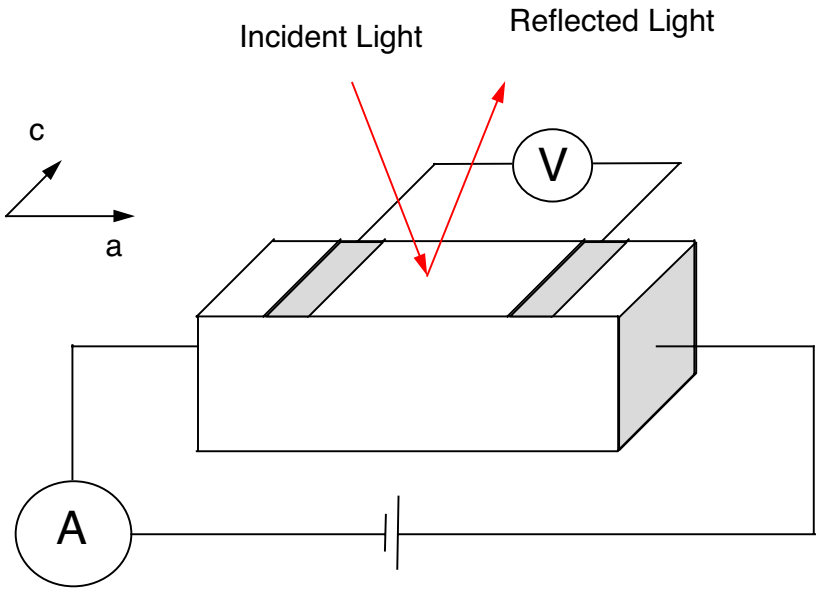

FIGURE 2.19 – Sketch of the geometry of the electrical contacts (grey in the figure) on the sample for electric field reflectivity measurements.

2.2 Electron Paramagnetic Resonance Spectroscopy

In this section we present the second technique we used for this work : the Electron Paramagnetic Resonance (EPR) spectroscopy. EPR is very similar in concept to the more familiar nuclear magnetic resonance (NMR) technique. Both exploit the interaction between electromagnetic radiation and magnetic moments but, in the case of EPR, they are those of electrons rather than those of nuclei. On the other hand, if in most spectroscopic studies the response arises from the the electrical component of the radiation , in EPR spectroscopy the signal comes from the interaction between the oscillating magnetic component of the electromagnetic radiation and the atomic magnetic dipole arising from one or more unpaired electrons. In almost all cases encountered in EPR spectroscopy, the electron magnetic dipole arises from the spin angular momentum with only a small contribution from orbital motion.

EPR spectroscopy is a suitable technique for any system in a paramagnetic state (or which can be brought to such a state), that is, a state having net electron angular momentum. Thus, in principle, all atoms and molecules are suitable for being studied by EPR. As we will focus on multiferroic oxides, we deal with transition ions that may have up to five or seven unpaired electrons. Although in any given molecule or atom there exists an infinite set of electronic states, in EPR spectroscopy the energy of the photons is very low ; hence one can ignore the multitude of electronic states except the ground state.

In the next section we will give a brief description of some magnetic properties of solids, necessary to understand the bases of the EPR technique and then we will present the experimental apparatus used in this work.

2.2.1 Bulk magnetic properties

The two magnetic-field quantities *magnetic induction* **B** and *magnetic field* **H** needed to describe all the magnetic properties of condensed matter systems are related to each other via

$$\mathbf{H} = \mathbf{B}/\mu_m \tag{2.26}$$

where the permeability

$$\mu_m = \kappa_m \mu_0 \tag{2.27}$$

is expressed in terms of the permeability of the vacuum μ_0 and of κ_m, a dimensionless parameter (unity for the vacuum) describing the (isotropic) medium considered. The subindex m labels the medium. Another important quantity is the magnetic-dipole moment $\boldsymbol{\mu}$. The macroscopic collection of N such dipoles in a given volume V produces a magnetization, or macroscopic moment per unit volume,

$$\mathbf{M} = \frac{1}{V}\sum_{i=1}^{N} \boldsymbol{\mu}_i \tag{2.28}$$

As all magnetic moments of nuclei, atoms and molecules are proportional to the angular momenta of these species,

$$\boldsymbol{\mu} = \alpha g \beta \mathbf{J} \tag{2.29}$$

Here β has the same units as $\boldsymbol{\mu}$, g is a pure number that depends on the relative contributions of the orbit and the spin to the total angular momentum [22], α depends on the charge sign of the species and $\mathbf{J}$ is the general angular-momentum vector. For free electrons in vacuum one has

$$\mu = -g_e \mu_B \mathbf{J} \tag{2.30}$$

where g_e is the free electron Landé factor and μ_B is the Bohr Magneton.

Another equivalent approach to understanding these quantities is via the vector relation

$$\mathbf{H} = \mu_0^{-1}\mathbf{B} - \mathbf{M} \tag{2.31}$$

where $\mathbf{M} = \mathbf{M}(\mathbf{H})$ is dependent on the laboratory medium, whereas $\mathbf{B}$ is based on the atom-free vacuum as the relevant medium.

The magnetization $\mathbf{M}$ is related to the applied field $\mathbf{H}$ by a dimensionless proportionality factor χ_m, the rationalized volume magnetic susceptibility. The contribution to χ_m of a set of non-interacting magnetic dipoles in the simplest (isotropic) case for electrons is

$$\chi_m = \frac{M}{H} = \frac{M}{B\kappa_m \mu_0} \tag{2.32}$$

With assumption of equilibrium (i.e. Boltzmann distribution) and independent behavior of the members of the electron spin ensemble, this becomes

$$\chi_m = \frac{N_V \mu^2}{3\kappa_B T}\mu_0 \equiv \frac{C}{T} \geq 0 \tag{2.33}$$

where $\mu^2 = g^2\mu_B^2 \mathrm{S(S+1)}$ and N_V is the number of magnetic species per unit volume. Here C is the Curie "constant". The quantity $\kappa_m = 1 + \chi_m$ is called the relative permeability (compared to free space). In the literature one most often finds the next-best approximation, the Curie-Weiss law :

$$\chi = \frac{C}{T - T_C} \tag{2.34}$$

Note that, by definition, paramagnetic samples have $\chi_m > 0$ whereas diamagnetic samples have $\chi_m < 0$ [23].

2.2.2 Interaction of magnetic dipoles with electromagnetic radiation : bases of EPR spectroscopy

To investigate interactions of magnetic dipoles with electromagnetic radiation we define the energy of an individual magnetic dipole of moment $\boldsymbol{\mu}$ in a field $\mathbf{B}$ as

$$U = -\mu^T \cdot \mathbf{B} = |\mu B| cos(\mu \mathbf{B}) \tag{2.35}$$

This expression shows that the single-particle magnetic energy U is proportional to the magnetic moment. Thus, the quantization of spin angular momentum in a specified direction leads to the quantization of the energy levels of a magnetic dipole in a magnetic field. If the direction z is chosen to be along B, Eq.2.30 leads to

$$\mu_z = -g_e \mu_B M_S \tag{2.36}$$

where M_S is the projection of angular momentum along the given direction (for a single unpaired electron M_S=± 1/2)

Eq.2.35 and Eq.2.36 describe a set of energies

$$U = g_e \mu_B B M_S \tag{2.37}$$

which are sometimes defined as the electronic Zeeman energies. Transitions between any two of such electronic Zeeman levels may be induced by an electromagnetic field **B** of the appropriate frequency ν such that the photon energy $h\nu$ matches the energy-level separation ΔU. Thus, considering the selection rules imposed by the conservation of angular momentum $|\Delta M_S| = 1$, the energy-level separation ΔU is (from Eq.2.37)

$$\Delta U = g_e \mu_B B \tag{2.38}$$

where B designates the magnetic field satisfying the *resonance condition* (Eq.2.38).

By considering the simplest energy-level diagram for a particle of spin 1/2 in a magnetic field, we can describe the energy levels of the system as in Fig. 2.20. The levels are labeled with the symbols α and β, or with the numbers **M**=±1/2 to be defined. In the absence of an applied magnetic field the two energy levels are degenerate. By varying the static field **B**, one may change the energy-level separation, as indicated in the figure. The resonant absorption occurs if the frequency of EM radiation is adjusted so that $\Delta U = h\nu$. Here ν is the center frequency of the source of incident radiant energy. The magnitude of the transition is the energy that must be absorbed from the oscillating magnetic field to move the system from the lower state to the upper state. We can note that, for many single unpaired-electron systems, resonance occurs with a magnetic field of about 0.3 T with $\nu \sim$ 9 GHz. In atomic and molecular systems, no more than two electrons can occupy a given spatial orbital. This is expressed by the Pauli exclusion principle, which arises from the fact that electrons act quantum-statistically as fermions. When two electrons occupy a given orbital, their spin components (M_S) always have opposite sign, and their magnetic moments cancel each other. Thus filled orbitals are ineffective with respect to spin magnetism. An EPR signal will be observed only when at least one orbital in a chemical species contains a single electron, that is a semioccupied atomic or molecular orbital.

From Eq.2.38 one may infer that there are two possible approaches for detection of resonant energy absorption. In the first case, the separation of the Zeeman levels is fixed by holding the magnetic field constant ; the microwave frequency is then varied until the resonant absorption is found. In the second case, the microwave frequency is kept fixed and the magnetic field is then varied. Until recently, the second method has been the one of choice, because experimentally it was relatively easy to vary the field B (i.e., the current in an electromagnet) but difficult and expensive to obtain microwave sources with wide frequency variability. Also in our EPR measurements we choose the latter solution.

2.2.2.1 The g factor

One of the most important quantity for EPR spectroscopy is the g factor that we have already described in the simplest case of free unpaired electrons. To go further it should be noted that the total field at each spin species is not necessarily only the magnetic field $\mathbf{B}_{ext}$

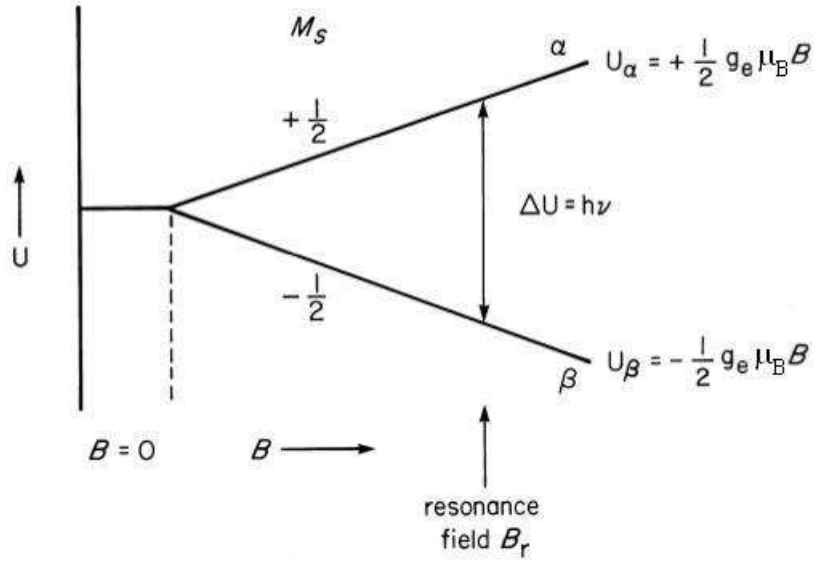

FIGURE 2.20 – Zeeman Energy-level scheme for a simple system (free electron) as a function of the applied magnetic field B, showing the EPR absorption. Uα and Uβ represent the energies of the M=$\pm$1/2 states. g and μ_B are defined in text.

applied externally to the sample. In addition, there may exist local fields $\mathbf{B}_{local}$ which add vectorially to the external field to produce the total field $\mathbf{B}_{eff}$ that electrons experience

$$\mathbf{B}_{eff} = \mathbf{B} + \mathbf{B}_{local} \tag{2.39}$$

where the subindex *ext* has been suppressed (as is the usual practice). There are two types of local field : (1) those induced by $\mathbf{B}$, and hence with a magnitude dependent on B ; (2) those permanent and independent of $\mathbf{B}$ except for their orientation. For the moment we can consider only the first type, that is, the induced contribution to $\mathbf{B}_{local}$. In principle the field $\mathbf{B}$ in Eq.2.38 should be replaced by $\mathbf{B}_{eff}$; in practice it is much more convenient to retain the external magnetic field $\mathbf{B}$. Then g_e must be replaced by a variable g factor that deviates from g_e (according to the strength of $\mathbf{B}_{local}$). Thus we can write Eq.2.39 as

$$\begin{aligned} \mathbf{B}_{eff} &= (1-\sigma)\mathbf{B} \\ &= (g/g_e)\mathbf{B} \end{aligned} \tag{2.40}$$

where σ is the EPR analog of the "chemical shift" parameter σ_n used in NMR spectroscopy ($0 \leq \sigma^2 \leq 1$) and g is the *effective Zeeman factor* used by EPR spectroscopists. Sometimes it is also convenient to write the effective g parameter g_{eff} (B) as

$$g_{eff} \equiv h\nu/\mu_B B \tag{2.41}$$

A lot of systems do have g $\approx$ g_e, but in many cases (e.g., for many transition ions) the experiments show marked deviations from this value. We can note that incorporation of

the generalized g factor into the magnetic moment allows for a variable g to take account of field-induced local magnetic fields. For example, these local fields often arise from the orbital motion of the unpaired electron. In practice, these factors cause all useful phenomena observable in EPR spectroscopy.

Moreover, in anisotropic systems, a variability of g with respect to the relative orientation of the crystal axes to $\mathbf{B}$ is expected. Thus in Eq.2.40 the magnetic field $\mathbf{B}_{eff}$ acting on the electrons generally differs in direction from$\mathbf{B}$, meaning that the resonant field value is a function of the field orientation relative to the crystal axes. For some purposes, it is convenient to use subscripts on g to specify the field orientation. If the principal axes of the paramagnetic entity are labeled X, Y and Z, g_X is to be interpreted for our simple case as $g_X = h\nu/\mu_B B_X$, that is, the g factor for $\mathbf{B}$ along the X axis of the magnetic system. A truly isotropic system is one where, of course,

$$g_X = g_Y = g_Z. \tag{2.42}$$

2.2.3 Interactions between magnetic moments

In addition to the interactions between magnetic moment and electromagnetic radiation, also mutual interactions between different magnetic moments are really important in defining the magnetic properties of physical systems. In this section we describe the different types of interaction between magnetic moments that are responsible for the principal magnetic characteristics of condensed matter systems.

2.2.3.1 Magnetic dipolar interaction

The first local interaction that has to be considered is the magnetic dipolar interaction ; a system consisting of two magnetic dipoles $\boldsymbol{\mu}_1$ and $\boldsymbol{\mu}_2$ separated by $\mathbf{r}$ has an energy

$$E = \frac{\mu_0}{4\pi r^3}\left[\boldsymbol{\mu}_1 \cdot \boldsymbol{\mu}_2 - \frac{3}{r^2}(\boldsymbol{\mu}_1 \cdot \mathbf{r})(\boldsymbol{\mu}_2 \cdot \mathbf{r})\right] \tag{2.43}$$

We can estimate the order of magnitude of this interaction by considering two magnetic dipoles each of $\boldsymbol{\mu} \approx 1\mu_B$ separated by $\mathbf{r} \approx 1$: the energy is approximately $\mu^2/4\pi \mathrm{r}^3 \sim 10^{-23}$ J, which is equivalent to about 1 K in temperature. Since many materials have ordering temperatures much higher than 1K, it is clear that the dipolar interaction is really weak, and other interactions should be considered to explain the magnetic ordering processes in solids.

2.2.3.2 Direct exchange interaction

The exchange interaction is one of the most useful examples to explain how quantum mechanics is the only way to describe phenomena that we can meet in the common experience. This interaction describes the simple phenomena in which charges of the same sign tend to stay apart to minimize the electrostatic energy of the system, but a detailed

treatment of this model needs a quantum-mechanical formalism. We can start by considering a simple model where two electrons have spatial coordinates $\mathbf{r}_1$ and $\mathbf{r}_2$, respectively. The wave function of the system can be written as a product of one-electron states but it must obey the exchange symmetry [24]. As for fermions the overall wave function must be antisymmetric, the spin part gives either the antisymmetric singlet state χ_S (S = 0) or the symmetric triplet state χ_T (S = 1), for a symmetric or an antisymmetric spatial state, respectively. The corresponding wavefunctions are

$$\Psi_S = \frac{1}{\sqrt{2}}\left[\psi_a(\mathbf{r}_1)\psi_b(\mathbf{r}_2) + \psi_a(\mathbf{r}_2)\psi_b(\mathbf{r}_1)\right]\chi_S \tag{2.44}$$
$$\Psi_T = \frac{1}{\sqrt{2}}\left[\psi_a(\mathbf{r}_1)\psi_b(\mathbf{r}_2) - \psi_a(\mathbf{r}_2)\psi_b(\mathbf{r}_1)\right]\chi_T$$

with energies

$$E_S = \int \Psi_S^* \hat{\mathcal{H}} \Psi_S d\mathbf{r}_1 d\mathbf{r}_2 \tag{2.45}$$
$$E_T = \int \Psi_T^* \hat{\mathcal{H}} \Psi_T d\mathbf{r}_1 d\mathbf{r}_2$$

The difference in energy between the two states is then

$$E_S - E_T = 2\int \psi_a^*(\mathbf{r}_1)\psi_b^*(\mathbf{r}_2)\hat{\mathcal{H}}\psi_a(\mathbf{r}_2)\psi_b(\mathbf{r}_1)d\mathbf{r}_1 d\mathbf{r}_2 \tag{2.46}$$

For a singlet state $\mathbf{S_1}\cdot\mathbf{S_2}$= -3/4 while for a triplet state $\mathbf{S_1}\cdot\mathbf{S_2}$= 1/4. We can thus write an "effective Hamiltonian" as

$$\hat{\mathcal{H}} = \frac{1}{4}(E_S + 3E_T) - (E_S - E_T)\mathbf{S}_1 \cdot \mathbf{S}_2 \tag{2.47}$$

The first term is constant and can be absorbed into other constant energy terms. The second term depends on the spin. We can define the ***exchange integral*** J as :

$$J = \frac{E_S - E_T}{2} = \int \psi_a^*(\mathbf{r}_1)\psi_b^*(\mathbf{r}_2)\hat{\mathcal{H}}\psi_a(\mathbf{r}_2)\psi_b(\mathbf{r}_1)d\mathbf{r}_1 d\mathbf{r}_2 \tag{2.48}$$

and, consequently, the spin-dependent term in Eq.2.47 as :

$$\hat{\mathcal{H}}^{spin} = -2J\mathbf{S}_1 \cdot \mathbf{S}_2 \tag{2.49}$$

If J>0, E_S>E_T and the triplet state S=1 is favored, if If J<0, E_S<E_T and the singlet state S=0 is favored. Eq.2.49 is valid for two electrons and its generalization to a many-body system is not trivial, but it was recognize that it applies for all neighboring atoms. This also motivates the Hamiltonian of ***Heisenberg model*** which can be expressed as $\mathcal{H} = -\sum_{ij} J_{ij}\mathbf{S}_i\mathbf{S}_j$.

The interactions between electrons on neighboring magnetic atoms via exchange interaction, without the need for an intermediary is called ***Direct Exchange,DE*** interaction.

In many cases this interaction cannot be important in controlling magnetic properties of solids due to the small overlap between neighboring magnetic orbitals. For example, in rare earths and even in transition metals, electrons in the outer shells are close to their nuclei and DE cannot be the leading process in magnetic ordering phenomena. It is thus necessary to consider some indirect exchange interaction.

2.2.3.3 Superexchange in ionic solids

A significant number of ionic solids (like oxides and some fluorides) have magnetic ground states which cannot be explained by DE. By considering a simple example like MnO, we can observe that there is no direct overlap between the electrons of the magnetic ions Mn^{2+}. The exchange mechanism in this long range order system appears to be in some sense "super" : the process which is operative in this kind of systems is in fact called ***superexchange*** interaction. It can be defined as an indirect exchange between magnetic ions separated by a non-magnetic ion, which mediates the interaction.

To describe this process we consider a simple system, similar to MnO, but with a single unpaired electron for each magnetic ion (more complicated cases can be treated in a similar way). In this example two magnetic (transition) ions are separated by an oxygen (non magnetic) ion with the assumption that the system is completely ionic.

The mechanism can be described by a general Hamiltonian (Hubbard Hamiltonian in second quantization) which consists of two terms, the kinetic term $\mathcal{H}'$ associated with the hopping of the d-electrons between two neighbors sites i and j, and the Hamiltonian $\mathcal{H}_0$ associated with the on site Coulomb repulsion :

$$\mathcal{H} = \mathcal{H}' + \mathcal{H}_0 = \sum_{ij} t_{ij} c^{\dagger}_{i\sigma} c_{i\sigma} + U \sum_{i} n_{i\uparrow} n_{i\downarrow} \tag{2.50}$$

In the above expression $c^{\dagger}_{i\sigma}$ ($c_{i\sigma}$) and $n_{i\sigma}$ have the usual meaning of creation (annihilation) operators and number operators in second quantization, respectively. t_{ij} is called hopping integral and is related to the gain in energy of the system when an electron is transferred from the i-site to the $j-$site. If the hopping is very important with respect to the on-site Coulomb repulsion U ($t_{ij} \gg U$), the system is in a metallic state (itinerant system). Conversely, if $t_{ij} \ll U$, the hopping matrix elements are small, the electrons are more localized, and the system is an insulator. Two magnetic ground states are possible : a ferromagnetic state F (spins parallel) or an antiferromagnetic state AF (spins antiparallel), as shown in Fig. 2.21. Virtual hopping, which can be considered as an excited state of the system, is allowed in the AF ground state configuration, and the system thus gains the associated kinetic energy (Heisenberg principle). For the F ground state the delocalization of one electron from the i-site to the j-site is forbidden by the Pauli's exclusion principle, and the gain in energy is zero. Thus the superexchange interaction is antiferromagnetic because the two lobes at either side of the O anion contain one electron each, which must have opposite spins to satisfy the exclusion principle.

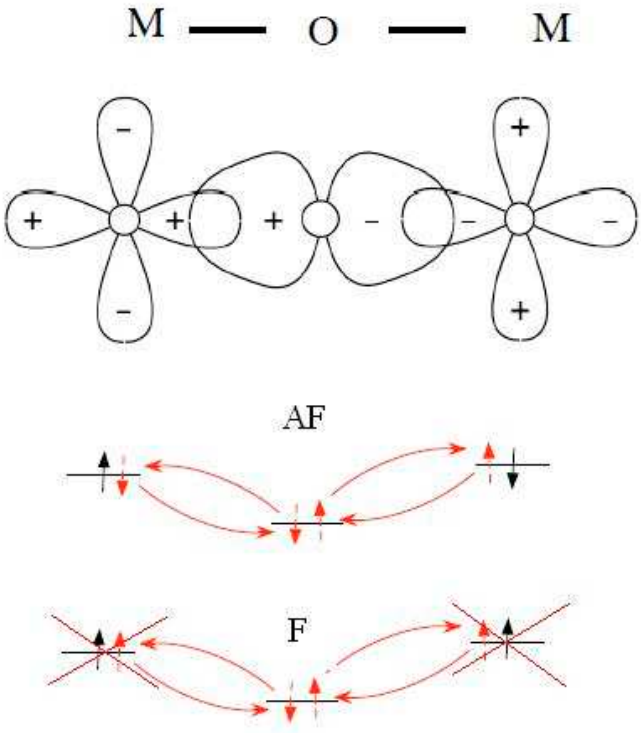

FIGURE 2.21 – Superexchange in magnetic oxides. Examples of superexchange interaction between the localized 3d electrons of a transition metal (M) and the p-orbitals of the oxygen (O). For simplicity, we consider only one electron at the magnetic ion site on a single orbital.

2.2.3.4 Anisotropic exchange : Dzyaloshinsky-Moriya interaction

In some systems the spin-orbit coupling plays an important role in the magnetic properties. The mechanism is similar to the superexchange interaction, but the excited state is created directly by the spin-orbit interaction in either magnetic ion. The exchange interaction is therefore between the excited state of one ion and the ground state of the other ion. This process is known as ***anisotropic exchange interaction*** or ***Dzyaloshinsky-Moriya interaction***. When acting between two spins $\mathbf{S}_1$ and $\mathbf{S}_2$ it can be described by an Hamiltonian

$$\hat{\mathcal{H}} = \mathbf{D} \cdot \mathbf{S}_1 \times \mathbf{S}_2 \tag{2.51}$$

where the vector $\mathbf{D}$ vanishes when the crystal field has an inversion symmetry with respect to the centre between the magnetic ions. The form of the interaction is such that it tends to force $\mathbf{S}_1$ and $\mathbf{S}_2$ to be at right angles, in order to minimize the energy of the system. The effect results in canting the spins by a small angle. It occurs very often in antiferromagnetic systems and is responsible for a small ferromagnetic component (*weak ferromagnetism*).

Microwave Band	Frequency (GHz)	B_{res} (G)
L	1.1	392
S	3.0	1070
X	9.75	3480
Q	34.0	12000
W	94.0	34000

FIGURE 2.22 – Resonance fields for a g = 2 signal at microwave frequencies commonly available in EPR spectrometers.

2.2.4 The EPR experimental apparatus : the spectrometer

Up to now, the EPR absorption has been detected from zero magnetic field to 100 T. At one extreme, a sensitive magnetometer used by geologists utilizes EPR absorption to measure the Earth's magnetic field, which is only $\sim$ 0.05 mT. On the other hand, pulsed electromagnets, designed to avoid destructive power dissipation, have been used at ultra-high fields. In this work we investigate magnetic excitations in solids, and the common X-Band configuration was adopted. In Fig.2.22 the various configurations of an EPR apparatus are shown.

In Fig.2.23 we show a typical setup for an EPR experiment : a microwave (approximately monochromatic) radiation coming from the source impinges on a sample located in an appropriate resonant cavity. The cavity is placed between the poles of an electromagnet which provides the static magnetic field. The detector placed at the end of the line measures the signal while the static magnetic field is varied.

In Fig.2.25 the general layout of the Bruker EPR spectrometer used in the present work is shown. The electromagnetic radiation source and the detector are in a box called "microwave bridge". The sample is in a microwave cavity, which is a metal box that helps to amplify weak signals from the sample. The magnet "tunes" the electronic energy levels producing the static magnetic field, as described below.

2.2.4.1 The Microwave Bridge

The microwave bridge houses the microwave source and the detector. There are more parts in a bridge than shown in Fig.2.26 but most of them are electrical components not necessary to understand the basic operations of the bridge. We shall now follow the path of the microwaves from the source to the detector starting from the point A, the microwave source. The next component, at point B, is a variable attenuator, a device which blocks the flow of microwave radiation. With the attenuator, we can precisely and accurately control the microwave power that is sent to the sample. The Bruker EPR spectrometers operates slightly differently than the simple spectrometer shown in the block diagram in Fig.2.23.

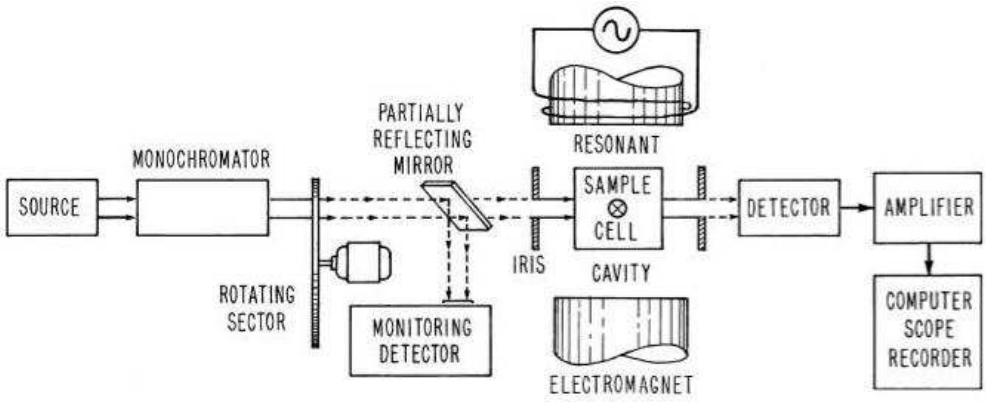

FIGURE 2.23 – Schematic view of an electron paramagnetic resonance (EPR) spectrometer (see text).

The diagram depicts a transmission spectrometer but the BRUKER Elaxsys EMX 6/1 is a reflection spectrometers : it measures the changes (due to spectroscopic transitions) in the amount of radiation reflected back from the microwave cavity containing the sample (point D in Fig.2.26). In order to detect only the microwave radiation coming back from the cavity, a circulator is positioned at point C. The microwaves coming in port 1 of the circulator only go to the cavity through port 2 and not directly to the detector. Reflected microwaves are directed only to the detector and not back to the microwave source through port 3. A Schottky barrier diode is placed at point E in the figure to detect the reflected microwaves. It converts the microwave power to an electrical current. At low power levels, (less than 1 μW) the diode current is proportional to the microwave power and the detector is called a square law detector. At higher power levels, (greater than 1 mW) the diode current is proportional to the square root of the microwave power and the detector is called a linear detector. The transition between the two regions is very gradual. For quantitative signal intensity measurements as well as optimal sensitivity, the diode should operate in the linear region. The best results are attained with a detector current of approximately 200 μA. To insure that the detector operates at that level, there is a reference arm (point F in the figure) which supplies the detector with some extra microwave power or "bias". Some of the source power is tapped off into the reference arm, where a second attenuator controls the power level (and consequently the diode current) for optimal performance. There is also a phase shifter to insure that the reference arm microwaves are in phase with the reflected signal microwaves when the two signals combine at the detector diode.

2.2.4.2 The EPR Cavity

In this section, we shall discuss the properties of microwave (EPR) cavities and how changes in these properties due to absorption result in an EPR signal. The principle is to use microwave cavities to amplify weak signals from the sample. A microwave cavity is simply a metal box with a rectangular or cylindrical shape which resonates with mi-



FIGURE 2.24 – The EPR experimental apparatus used in this work : on the left the BRUKER Elaxsys EMX 6/1 spectrometer, on the right the console for signal processing and electronic controls.

crowaves. Resonance means that the cavity stores the microwave energy ; therefore, at the resonance frequency of the cavity, no microwaves will be reflected back, but will remain inside the cavity. Cavities are characterized by their Q, the *quality factor*, which indicates how efficiently the cavity stores microwave energy. As Q increases, the sensitivity of the spectrometer increases. The Q factor is defined as the ratio between stored energy and dissipated energy per cycle (the amount of energy lost during one microwave period). Energy can be lost to the side walls of the cavity because the microwaves generate electrical currents in the side walls of the cavity which in turn generate heat. We can measure Q factors easily because there is another way of expressing Q :

$$Q = \frac{\nu_{res}}{\Delta\nu} \tag{2.52}$$

where ν_{res} is the resonant frequency of the cavity and $\Delta\nu$ is the width at half height of the resonance.

A consequence of the resonance is that there will be a standing wave inside the cavity. The standing electromagnetic waves have their electric and magnetic field components exactly out of phase, i.e. where the magnetic field is maximum, the electric field is minimum and vice versa. The spatial distribution of the amplitudes of the electric and magnetic fields in the most commonly used EPR cavity is shown in Fig.2.27. We can use the spatial separation of the electric and magnetic fields in a cavity to great advantage. Most samples

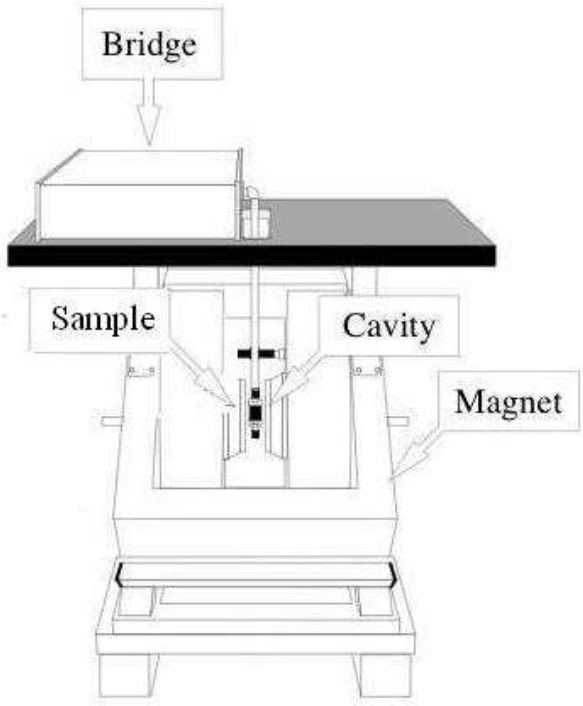

FIGURE 2.25 – Components of the EMX spectrometer.

have non-resonant absorption of the microwaves via the electric field and the Q will be degraded by an increase in the dissipated energy. It is the magnetic field that drives the absorption in EPR. Therefore, if we place our sample in the electric field minimum and the magnetic field maximum, we obtain the biggest signals and the highest sensitivity. The cavities are designed for optimal placement of the sample. Microwaves are coupled into the cavity via a hole called "iris". The size of the iris controls the amount of microwaves which will be reflected back from the cavity and how much will enter the cavity. The iris accomplishes this by carefully matching or transforming the impedances (the resistance to the waves) of the cavity and the waveguide (a rectangular pipe used to carry microwaves). There is an iris screw in front of the iris which allows one to adjust the matching. When the sample absorbs the microwave energy, the Q is lowered because of the increased losses and the coupling changes because the absorbing sample changes the impedance of the cavity. The cavity is therefore no longer critically coupled and microwave will be reflected back to the bridge, resulting in an EPR signal.

2.2.4.3 The Magnetic Field Controller

The magnetic field controller allows to sweep the magnetic field in a really precise manner. It consists of two parts : the first one sets the field values and the timing of the field sweep and the second one regulates the current in the windings of the magnet to attain the requested magnetic field value. The magnetic field values and the timing of

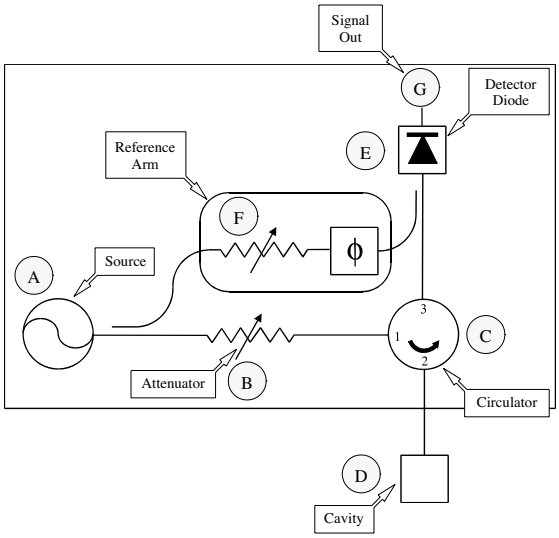

FIGURE 2.26 – Block diagram of a microwave bridge.

the magnetic field sweep are controlled by a microprocessor in the controller (Fig.2.28). A field sweep is divided into a maximum of 4096 discrete steps called sweep addresses. At each step, a reference voltage corresponding to the magnetic field value is sent to the part of the controller that regulates the magnetic field. The sweep rate is controlled by varying the waiting time between each individual step. The magnetic field regulation occurs via a Hall probe placed in the gap of the magnet. It produces a voltage which is dependent on the magnetic field perpendicular to the probe. The relationship is not linear and the voltage changes with temperature ; however, this is easily compensated for by keeping the probe at a constant temperature slightly above room temperature and characterizing the nonlinearities so that the microprocessor in the controller can make the appropriate corrections. Regulation is accomplished by comparing the voltage from the Hall probe with the reference voltage given by the other part of the controller. When there is a difference between the two voltages, a correction voltage is sent to the magnet power supply which changes the amount of current flowing through the magnet windings and hence the magnetic field.

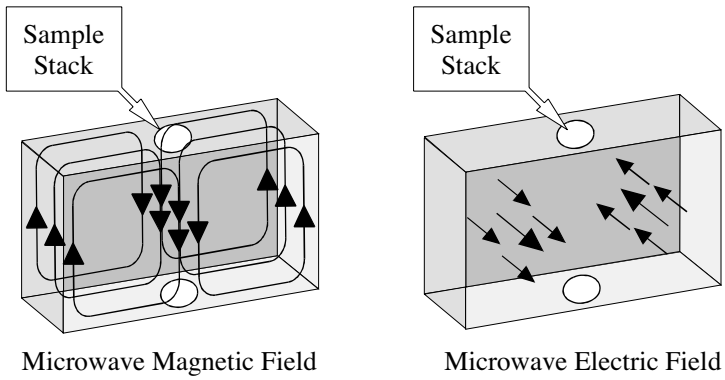

FIGURE 2.27 – Magnetic and electric field patterns in a standard EPR cavity.

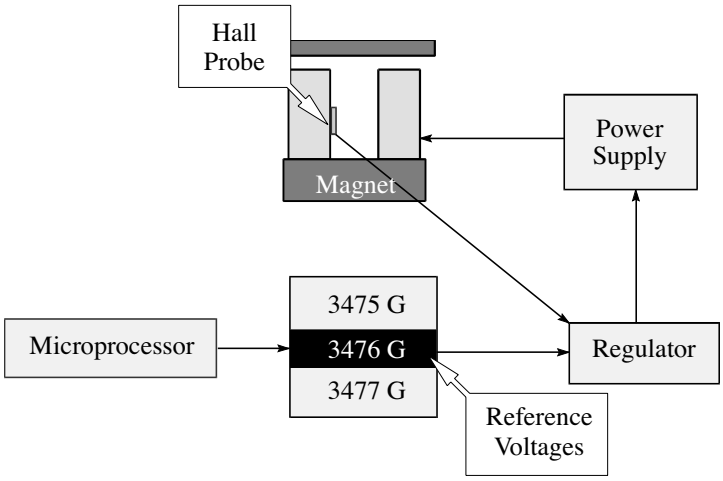

FIGURE 2.28 – A block diagram of the field controller and associated components.

Bibliographie

[1] M. Dressel and G. Grüner, *Electrodynamics of solids*, (Cambridge University Press, 2002).

[2] P. R. Griffiths and J. A. De Haseth, *Fourier Transform Infrared Spectroscopy*, (John Wiley and sons, 1986).

[3] C. C. Homes, M. Reedik, D. A. Cradles, and T. Timusk, Applied Optics **32**, 2976 (1993)

[4] U. Schade, M. Ortolani, and J. Lee, Synchrotron Radiation News **20**, 17 (2007)

[5] D. H. Auston, K. P. Cheung, J. A. Valdmanis, and D. A. Kleinman, Phys- ical Review Letters **53**, 1555 (1984) ; B. Ferguson and X. C. Zhang, Nature Materials **1**, 26 (2002).

[6] M. Abo-Bakr, J. Feikes, K. Holldack, G. Wustefeld, and H.-W. Hubers, Physi- cal Rewiew Letters **90**, 254801 (2003) ; M. Abo-Bakr, J. Feikes, K. Holldack, P. Kuske, W. B. Peatman, U. Schade, G. Wustefeld, and H.-W. Hubers, Physical Review Letters **90**, 094801 (2003).

[7] G. L. Carr, M. C. Martin, W. R. McKinney, K. Jordan, G. R. Neil, and G. P. Williams, Nature (London) **420**, 153 (2002).

[8] G. P. Williams, Review of Scientific Instruments **73**, 1461 (2002).

[9] Y. Shen, T. Watanabe, D. A. Arena, C.-C. Kao, J. B. Murphy, T. Y. Tsang, X. J. Wang, and G. L. Carr, Physical Review Letters **99**, 043901 (2007).

[10] U. Schade, K. Holldack, P. Kuske, G. Wustefeld, and H.-W. Hubers, Applied Physics Letters **84**, 1422 (2004).

[11] M. Ortolani, P. Calvani, S. Lupi, U. Schade, A. Perla, M. Fujita, and K. Ya- mada, Physical Review B **73**, 184508 (2006).

[12] M. Ortolani, S. Lupi, L. Baldassarre, U. Schade, P. Calvani, Y. Takano, M. Nagao, T. Takenouchi, and H. Kawarada, Physical Review B **97**, 097002 (2006).

[13] BESSY - Highlights 2002 - Special : New Light at BESSY !

[14] T. Nakazato, M. Oyamada, N. Niimura, S. Urasawa, O. Konno, A. Kagaya, R. Kato, T. Kamiyama, Y. Torizuka, T. Nanba, Y. Kondo, Y. Shibata, K. Ishi, T. Ohsaka, and M. Ikezawa, Physical Review Letters **63**, 1245 (1989) ; E. B. Blum, U. Happek, and A. J. Sievers, Nuclear Instrumuments and Methods in Physics Research, Section A **307**, 568 (1991).

[15] G. L. Carr, S. L. Kramer, J. B. Murphy, R. P. S. M. Lobo, and D. B. Tanner, Nuclear Instruments and Methods in Physics Research, Section A **463**, 387 (2001) ; J. M.

Byrd, W. P. Leemans, A. Loftsdottir, B. Marcelis, M. C. Martin, W. R. McKinney, F. Sannibale, T. Scarvie, and C. Steier, Physical Review Letters **89**, 224801 (2002).

[16] J. S. Nodvick and D. S. Saxon, Physical Review **96**, 180 (1954).

[17] R. L. Warnock and P. Morton, Particle Accelerators 25, 113 (1990) ; J. B. Murphy, S. Krinsky, and R. L. Gluckstern, Particle Accelerators **57**, 9 (1997).

[18] M. Venturini and R. Warnock, Physical Review Letters **89**, 224802 (2002).

[19] U. Schade, A. Roseler, E. H. Korte, F. Bartl, K. P. Hofmann, T. Noll and W. B. Peatman, Review of Scientific Instruments **73**, 1568 (2002).

[20] M. Abo-Bakr, J. Feikes, K. Holldack, U. Schade, G. Wustefeld, and H.-W. Hubers, Proceedings of EPAC 2002 (Paris, France).

[21] D. Pines and P. Nozieres, *The theory of Quantum Liquids, Vol. 1* (Addison- Wedsley, Reading, MA, 1966).

[22] A. Abragam and B. Bleaney, *Electron paramagnetic resonance of transition atoms* (Dover Publications, Inc. New York)

[23] J. A. Weil J. R. Bolton, *Electron Paramagnetic Resonance. Elementary Theory and Practical Applications.* John Wiley & Sons, Inc., Hoboken, New Jersey (2007)

[24] Stephen Blundell, *Magnetism in condensed matter*, Oxford University Press (2001)

Chapitre 3

Structural, electronic and ferroic properties of the investigated systems

In this work we analyze two multiferroic systems included in the category of improper ferroelectrics : $LuFe_2O_4$ and $GaFeO_3$. The former system presents a CO induced ferroelectricity and in the latter one multiferroicity is induced by the ferrotoroidic moment. We measured the optical and magnetic properties of this two compounds by means of FT-IR and EPR spectroscopy. In this chapter we present a summary of experiments on both $LuFe_2O_4$ and $GaFeO_3$ describing the most interesting features of these systems.

3.1 $LuFe_2O_4$

3.1.1 Sample characterization

$LuFe_2O_4$ belongs to a class of materials generally expressed by RFe_2O_4 (R indicates rare-earth metals), which present a rhombohedral structure (space group $R\bar{3}m$). The crystals of these materials have two common characteristics : Fe ions form hexagonal double layers and stack in the sequence of (AB),(CA),(BC),... along the rhombohedral axis (Fig.3.1 (a)). Moreover, the average valence of Fe ions is $Fe^{2.5+}$, which implies that Fe^{2+} and Fe^{3+} are equally distributed in the equivalent Fe sites on the hexagonal net plane. Compared with the average iron valence of $Fe^{2.5}$, Fe^{2+} and Fe^{3+} are considered as having an excess and a deficiency of half an electron, respectively. The Coulomb interaction tends to pair the "opposite" signed charges (Fe^{2+} and Fe^{3+}) and this produces a degeneracy in the lowest energy for the charge configuration in the triangular lattice, similarly to the triangular antiferromagnetic Ising spins. The formal similarity of spin and charge frustration is explained in Fig.3.1(b). When trying to arrange an equal number of Fe^{2+} (black site) and Fe^{3+} (white site) on the hexagonal lattice, one finds that the common nearest-neighbor site adjacent to a black and white pair is frustrated, which means that the ground state of the system tends to be degenerate. Thus, $LuFe_2O_4$ is considered to be a spin-charge frustrated system of triangular lattices.

By means of x-ray diffraction, it has been shown that $LuFe_2O_4$ undergoes two phase transitions ; both of them have been reported to be of CO type. The transition temperatures

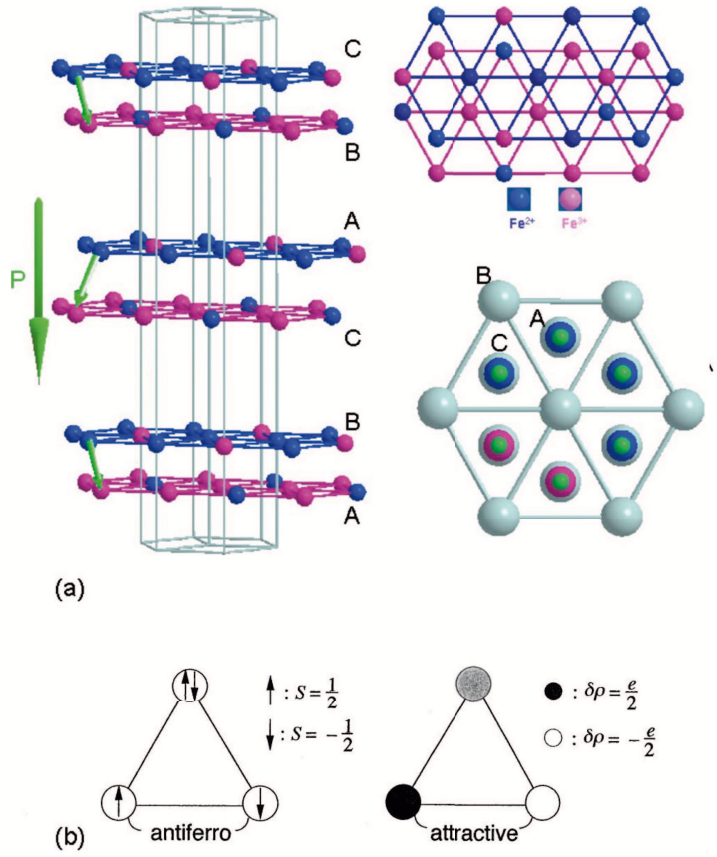

FIGURE 3.1 – Schematic description of the crystal structure of $LuFe_2O_4$. Fe ions form the hexagonal double layers (A,B) which are packed between (Lu, O) blocks and stacked along the rhombohedral axis in (AB), (CA), (BC).... [9] (b) Spin frustration and charge frustration on a 2D hexagonal lattice. The common nearest-neighbor site for the $(\uparrow - \downarrow)$ pair (black and white pair) has no preference for $\uparrow$ or $\downarrow$ (black or white) since the energy is completely degenerate. This situation is expressed by the gray site in the case of charge frustration [1].

are $T_{C1} = 320K$ and $T_{C2} = 500K$ [1] . The low temperature phase ($T < T_{C1}$) consists in a three-dimensional incommensurate charge density wave (3D CDW). In the temperature range $320K < T < 500K$, only a short-range order of the charge density develops. Since the intra-layer correlation length is largely bigger compared with the inter-layer correlation length, the state in this temperature range can be addressed as a 2D ordered state in hexagonal basal plane. The ordering disappears completely above T_{C2}. The nature of the CO sequence remains still controversy.

A possible model of the superstructure of Fe^{2+} and Fe^{3+} has been proposed by Yamada *et al.*, and is depicted in Fig.3.2 [1]. By analogy with the robust long-range order of Ising

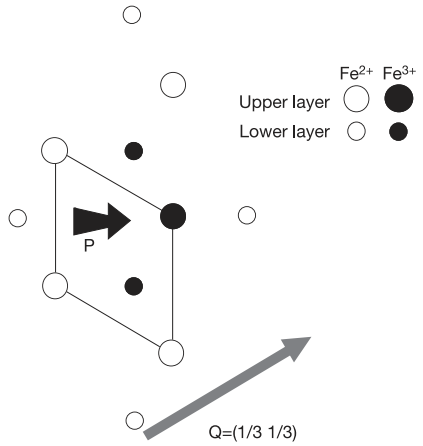

FIGURE 3.2 – Scheme of the superstructure of the CO phase of $LuFe_2O_4$. The solid lines show the chemical unit cell. The dotted lines show the charge superlattice cell. The Fe ions in the upper and lower layers are indicated by large and small circles, respectively. Fe^{2+} and Fe^{3+} are represented by open and filled circles, respectively. The polarization P is represented with a short, black arrow. A charge density wave vector Q is drawn as a long, grey arrow [1].

spins in a triangular lattice antiferromagnet, a model CO structure in which the two triangular sheets of a W layer (*e.g.*, Fe_2O_4 layer) do not have the same number of Fe^{2+} and Fe^{3+} ions, *i.e.*, $[Fe^{2+}]:[Fe^{3+}] = 1:2$ in one triangular sheet, and 2 :1 in another triangular sheet. The supercell, defined by $\sqrt{3} \times \sqrt{3}$ structure, is enlarged by three times in the ab plane along the (1 1 0) direction. Such a charge charge structure allows for the presence of a local electrical polarization, since the centers of Fe^{2+} (excess electron) and Fe^{3+} (electron deficiency) do not coincide in the unit cell of the superstructure. This indicates the possibility of ferroelectricity originating from the electron density modulation without a dipole of a cation and anion pair. Subramanian *et al.* proposed a different CO structure in which one triangular sheet of a W layer has only Fe^{2+} ions and the other triangular sheet has only Fe^{3+} ions, on the basis of the fact that the closest Fe-Fe distances in $LuFe_2O_4$ occur between adjacent triangular sheets of a W layer rather than within each triangular sheet. If all the Fe double layers had the lower-charged Fe^{2+} in the upper layer, the structure would be polarized along the c-axis [5]. Thus the exact CO configuration of this system is still under debate.

The charge-ordering transition at $\sim$ 320 K can be further confirmed by resistivity measurements (ρ *vs.* T) [8]. Data within T = 200 - 400 K are shown in Fig.3.3. While a semiconductor-like behavior ($d\rho/dT < 0$) is observed over the whole T-range, the high-T data (T = 320 - 400 K) and low-T data (T = 220 - 320 K) allow for different activation energies. The charge-ordered state has reasonably higher activation energy for electron transport than the charge-disordered state. Nevertheless, no significant change of the transport behavior across the 2D ferrimagnetic transition at T $\sim$ 240 K is observed.

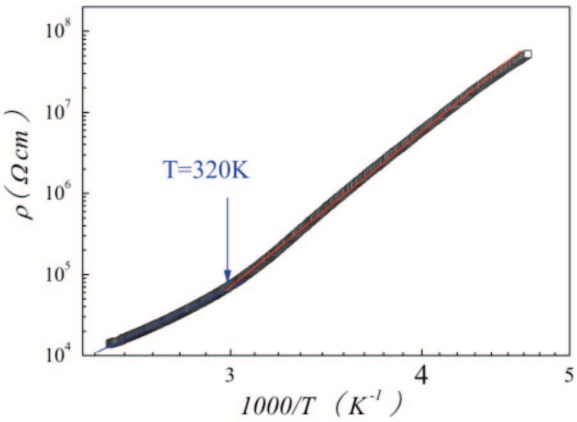

FIGURE 3.3 – Measured ρ *vs* T curve in $LuFe_2O_4$. Two different activation energies for the CO (T<320 K) and the disordered phase (T>320 K) are detected [8].

$LuFe_2O_4$ also shows a ferrimagnetic (FIM) order below $T_N \sim 240$ K, as revealed by neutron scattering [6] (it has to be noted that in literature different values of T_N are reported between 220 K and 240 K, suggesting that the transition temperature in $LuFe_2O_4$ may be slightly sample dependent).

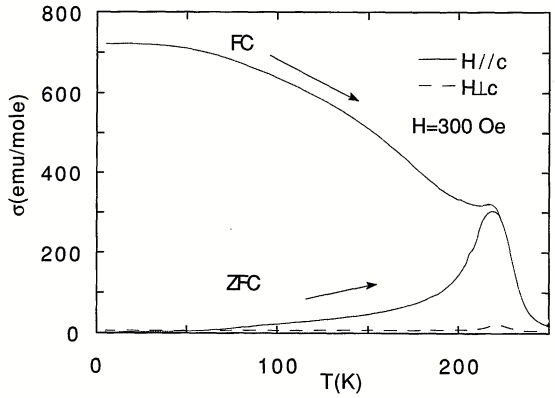

FIGURE 3.4 – Thermo-magnetization curves of $LuFe_2O_4$ in 300 Oe. The solid and dotted lines show the $H \parallel c$ and $H \perp c$ configuration, respectively.

The thermo-magnetic curves of a single crystal of $LuFe_2O_4$ are shown in Fig.3.4. The experiments have been performed at 300 Oe with the magnetic field either parallel ($\parallel c$) or perpendicular ($\perp c$) to the c-axis [6]. In the $H \perp c$ configuration the magnetization is much lower compared with the $H \parallel c$ measurements. In the field-cooling curve with $H \parallel c$, magnetization shows a peaks below ∼220 K. High field magnetization curves in the parallel configuration ($H \parallel c$) at 4.2 K are presented in Fig.3.5(a) [6] . The FC curve

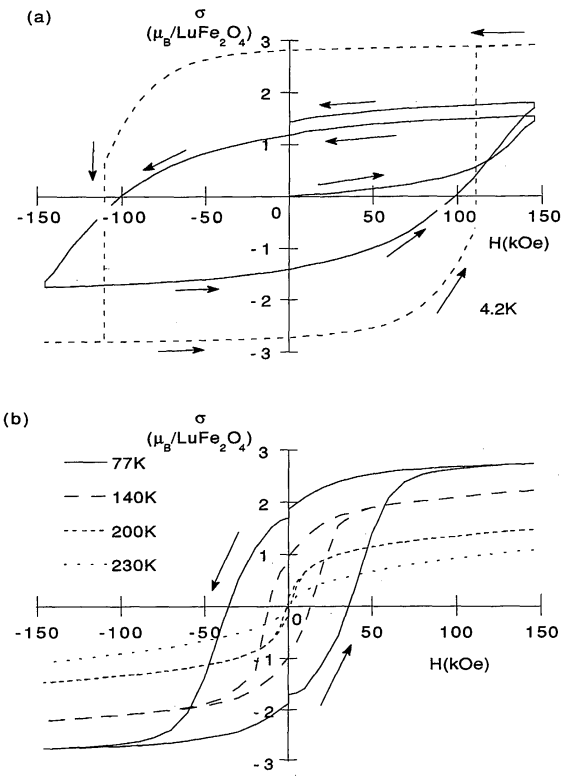

FIGURE 3.5 – High field magnetization curves in the parallel configuration $H \parallel c$ of $LuFe_2O_4$. (a) Solid and broken lines refer to ZFC and FC data at 4.2 K, respectively . (b) Isothermal magnetization curves above 77 K.

(dotted line) is obtained after a field cooling from above 220 K to 4.2 K under 145 KOe and shows a larger hysteresis with respect to the ZFC curve. In the FC curves a large moment of $2.84\mu_B$ per formula unit is reached. Figure 3.5(b) shows instead the ZFC curves at several temperatures with $H \parallel c$. The data exhibit reversible curves above 220 K, and the magnetization above room temperature is almost proportional to the magnetic field. In contrast, in the perpendicular configuration, the magnetization is proportional to the magnetic field at all temperatures. By coupling these results with neutron diffraction measurement [6], it has been suggested that $LuFe_2O_4$ exhibits a 2D ferrimagnetic order on triangular nets of W-layer below $T_N \sim 220$ K. Recently, a new model for the magnetic structure of $LuFe_2O_4$ has been extracted from neutron diffraction measurements [2]. The results show two magnetic transitions below 300 K, at $T_N = 240K$ and $T_L = 175K$, both involving a 3D magnetically correlated structure with a finite correlation length along the c-axis. The 3D magnetic correlations persist below T_L, but show a shorter correlation length. The proposed magnetic structure shown in Fig.3.6 is ferrimagnetic with an excess 1/3 of the spins pointing along the c-axis. This results in a saturation ordered moment of $3\mu_B/FU$. This value is very close to the saturation magnetization in high fields reported in Ref. [6].

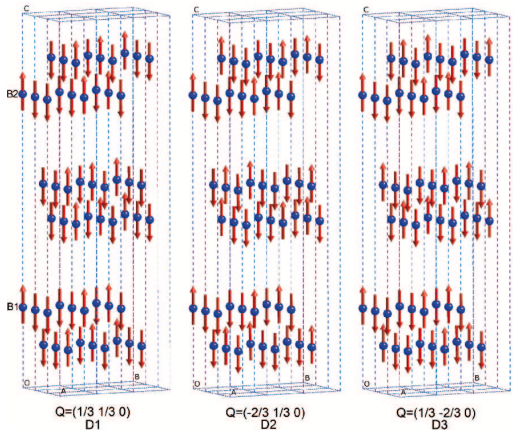

FIGURE 3.6 – Magnetic structure of $LuFe_2O_4$ at T = 220 K. The three magnetic domains correspond to the three symmetry equivalent magnetic propagation vectors [2].

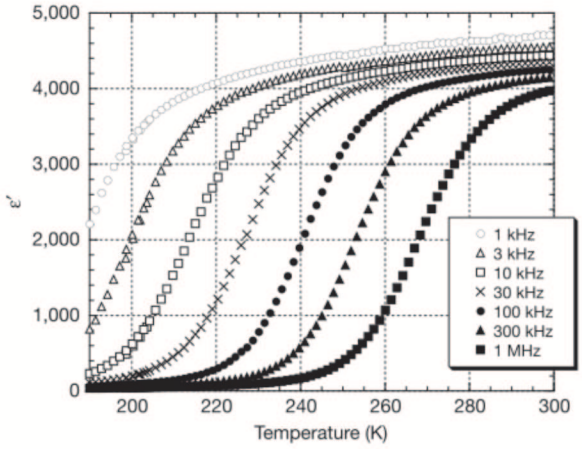

FIGURE 3.7 – The a.c. dielectric dispersion in $LuFe_2O_4$ polycrystalline samples. The in-phase component of the a.c. dielectric constant has been measured in the frequency range from 1 kHz to 1 MHz [4].

As already mentioned, $LuFe_2O_4$ has attracted much attention as a novel ferroelectric material where ferroelectricity is driven by the electronic process of charge ordering of Fe^{2+} and Fe^{3+} ions. A characteristic large dispersion for the dielectric constant measured by low frequency alternating voltage (a.c.) has been indeed observed (Fig.3.7) [4]. The dielectric dispersion is a common feature with the order-disorder type of ferroelectric transitions, where it is caused by the motion of the ferroelectric domain boundary. Also a polarization switching in accordance with the external electric field has been reported Fig.3.8 [4].

In the experiment, the sample was cooled down to 77 K under an electric field of ± 10 kV cm^{-1} along the *c*-axis, and then the current flow from the sample was recorded upon

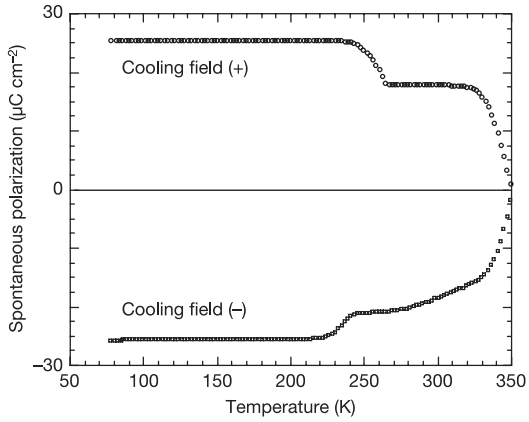

FIGURE 3.8 – Integration of a pyroelectric current measurement. The current flow from the sample was recorded on heating after electric field cooling along the *c*-axis. The direction of the electric polarization depends on the direction of electric field, which indicates the macroscopic electric polarization [4].

heating without the electric field. The direction of current flow depends on the sign of the cooling electric field below 350 K. The spontaneous polarization was estimated by the integral of the current in the sample. Both the switching of electric polarization and the large dielectric constant dispersion are consistent with the existence of ferroelectricity. A large decrease occurs as the temperature is increased around 250 K, which is roughly the magnetic transition temperature, and at 330 K where the superstructure of Fe^{2+} and Fe^{3+} appears. This shows that $LuFe_2O_4$ is a polar substance and suggests that the ferroelectricity is related to the polar arrangement of Fe^{2+} and Fe^{3+}. Moreover, the shoulder of the electric polarization at the magnetic transition temperature can indicate a coupling between magnetization and electric polarization.

Other experimental results outline the complexity of the ferroelectric order in $LuFe_2O_4$. Angst *et al.* have proposed an *anti*ferroelectric polar arrangement as the ground state of the system. In such a model the CO structure exhibits a $\sqrt{3} \times \sqrt{3} \times 2$ supercell [7] and the configuration in each individual double layer is polar as proposed by Yamada *et al.* [1]. However, the stacking of the polarization of the six double layers of the supercell is antiferroelectric with no net polarization. In contrast, short-range charge correlations above the CO temperature were found to correspond to a ferroelectric CO configuration. From DFT calculations they obtained that within a $\sqrt{3}\times\sqrt{3}\times 2$ supercell the antiferroelectric CO configuration is more stable than the ferroelectric one and hence corresponds to the ground state. Given the small energy differences between antiferro- and ferroelectric configurations it seems likely that cooling with an electric field applied may stabilize the long-range order of the ferroelectric CO configuration, which would explain the remanent polarization observed (only) after cooling in an electric field.

In addition, from terahertz time-domain spectroscopy (THz-TDS) measurements, Li *et al.* have proposed a displacing type of ferroelectric transition superimposed to the order-

disorder ferroelectric transition [8]. They analyzed the response of the low-frequency phonon modes in order to reveal the possible soft mode (SM) and central mode (CM) which are characteristic of such transition. Data in Fig.3.9 show the soft mode identified below ∼240

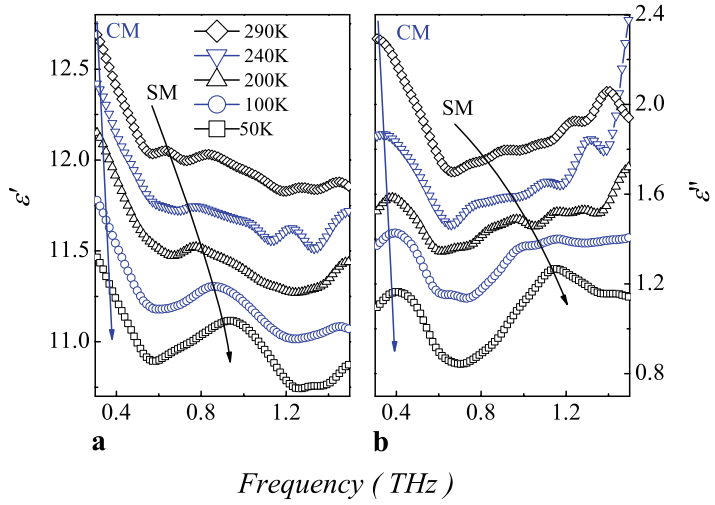

FIGURE 3.9 – Frequency dependence of (a) real part ε' and (b) imaginary part ε'' of the dielectric constant of $LuFe_2O_4$ at various T by THz-TDS [8]

K, which indicates the existence of displacing ferroelectricity, in addition to the charge-ordering-induced ferroelectricity below 320 K.

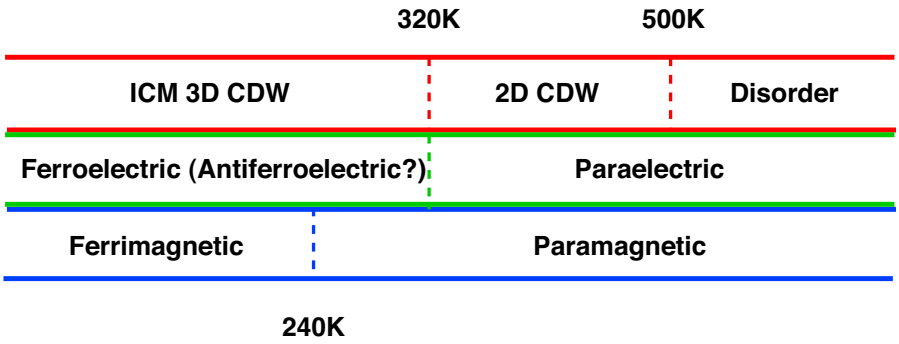

FIGURE 3.10 – Scheme of main phase transitions of $LuFe_2O_4$. Inspired by [1].

In conclusion, the phase transitions in $LuFe_2O_4$ can be summarized as in Fig. 3.10 which shows clearly that this system is a really good candidate for high-temperature multiferroicity.

3.1.2 Magnetoelectric coupling : Magnetic-field control of the dielectric properties and of the charge structure

3.1.2.1 Giant room-temperature Magnetocapacitance

$LuFe_2O_4$ has attracted much interest also for indications of coupling between electronic and magnetic degrees of freedom (magnetoelectric coupling). One of these findings is the giant-room temperature magnetocapacitance reported by Subramanian *et al.*. Figure 3.11 shows the dielectric constant of $LuFe_2O_4$ as a function of temperature under zero external magnetic field. As already remarked, a large dielectric dispersion and a large room-temperature dielectric constant are found. The coupling between the dielectric constant and the applied magnetic field is presented in the inset. The dielectric response is reduced

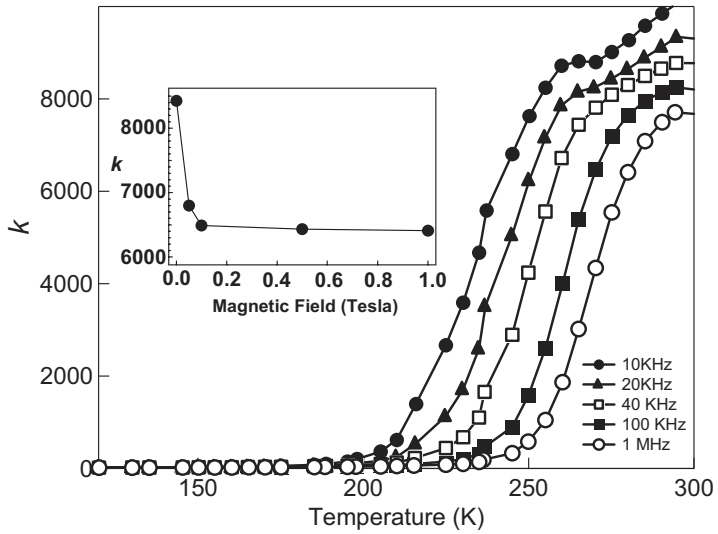

FIGURE 3.11 – Real part of the dielectric constant (k) versus temperature measured at various frequencies for $LuFe_2O_4$ under zero magnetic field. The inset shows the variation of k with magnetic field at room temperature at 20 kHz [5].

by almost 25% by the external magnetic field at room temperature. This behavior can be explained as follows. The dielectric constant of a system is directly related to its polarizability, which decreases as the system becomes polarized. On cooling through a ferroelectric transition, fluctuating dipoles are frozen in a particular orientation, polarizability is lost, and the dielectric constant decreases. The application of a magnetic field can be expected to polarize the system because Fe^{3+} is more strongly attracted to the field than Fe^{2+}, and it is the charge fluctuations on the Fe sites that is the main contributor to polarizability at higher temperatures (when there is no charge ordering). The need of low magnetic field make the magnetocapacitance effect in $LuFe_2O_4$ really promising for device applications.

3.1.2.2 Magnetic-field control of charge structures

Another interesting result arose from a neutron-scattering work by Wen *et al.* [9]. They found that the static charge structure in $LuFe_2O_4$ can be affected by the application of an external magnetic field in the non-magnetic phase, which is extremely unusual.

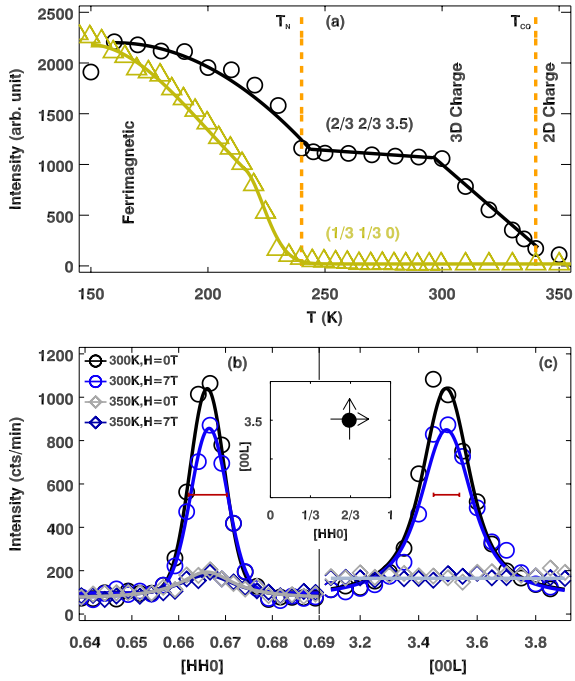

FIGURE 3.12 – Magnetic and charge order in $LuFe_2O_4$. (a) The magnetic and charge Bragg-peak intensities as a function of temperature. (b) (c) Linear intensity profiles of the charge superlattice peak (2/3,2/3,3.5) along the (110) and (001) directions, respectively. The horizontal bars indicate the instrument resolution along the measured directions. The lines are fits to the data using a Lorentzian function. The inset denotes the direction of the performed scans [9].

In Fig.3.12(a), the intensity measured at (1/3,1/3,0) (magnetic peak), together with the intensity measured at (2/3,2/3,3.5) (charge-order peak) are plotted as magnetic and charge order parameters, respectively. The former one correctly starts to rise only around $T_N \sim 240$ K. Charge order starts instead to appear at higher temperature, ∼340 K when Fe^{2+} and Fe^{3+} are believed to form the superstructure. In Fig.3.12(b and (c), the charge superlattice peaks (2/3,2/3,3.5) along the (110) and (001) directions are shown, respectively. Upon cooling below 340 K, the system enters a 3D charge-ordered phase, evidenced by the arising intensity of the peak, which appears to become saturated below 300 K. The sudden intensity increase at T_N corresponds to a superimposed magnetic scattering intensity at this wave vector due to the magnetic order. By applying a magnetic field H=7 T (field cooling condition) perpendicular to the scattering plane in the 2D charge-ordered phase (T >

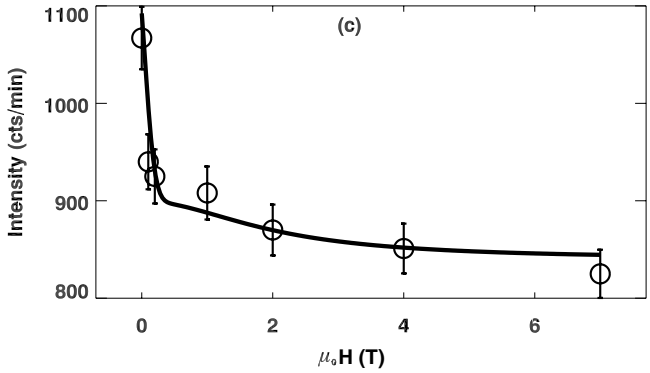

FIGURE 3.13 – Magnetic-field response on the charge superlattice peak (2/3,2/3,3.5). Charge peak intensity measured at 300 K with FC from 350 K at different magnetic-field strengths. The lines are guides to the eyes [9].

340 K) no changes have been observed (see Fig.3.12(b)and Fig.3.12(c)) compared to the measurements under zero-field cooling (ZFC). With further cooling under field, at T = 300 K a partial reduction in the charge peak intensity is clearly evident. The temperature dependence of the magnetic-field effect is given in Fig.3.13 : at 300 K, the charge peak intensity is reduced by about 25% with FC (H=7 T).

What has been observed in this non-magnetic charge-ordered phase of $LuFe_2O_4$ is extremely unusual. As (static) charges do not respond directly to an external magnetic field, one generally does not expect charge order to be affected by a magnetic field. Some exceptions are colossal magnetoresistance manganites and charge/spin stripe ordered high-temperature superconducting cuprates. However, even in these few examples, it has been shown that charge order can be affected by an external magnetic field through another order (magnetic/superconducting). In $LuFe_2O_4$, no such intermediate order is present between T_N and T_{CO}, and the magnetic field appears to directly affect the charge structure. One possible explanation of this effect could be that the Zeeman splitting of different spin states caused by an external magnetic field affects the stability of charge structures in the CO phase, and therefore the dielectric response.

These results can also explain the giant magnetoelectric response at room temperature, that has been originally attributed to the field affecting charge fluctuations. The authors suggest that the room-temperature magnetoelectric effect in this multiferroic system is a direct result of the field affecting the static charge order. When charge order is reduced, the magnitude of the resulting local electric dipole moments becomes smaller, and therefore the dielectric response is smaller. Furthermore, the fact that the magnetic field can directly affect the charge structure without any intermediate (magnetic) order suggests that a different magnetoelectric coupling mechanism has to be considered for this charge-ordered multiferroic system.

3.1.3 Magnetoelectric coupling : electric-field control of dielectric and magnetic properties

3.1.3.1 Room-temperature giant dielectric tunability effect

The magnetoelectric coupling is a change in the physical properties when an electric field is applied and it has been also reported to exist in $LuFe_2O_4$. In a recent work, Li *et al.* have studied the dielectric tunability of $LuFe_2O_4$ as a function of both temperature and ac field frequency.

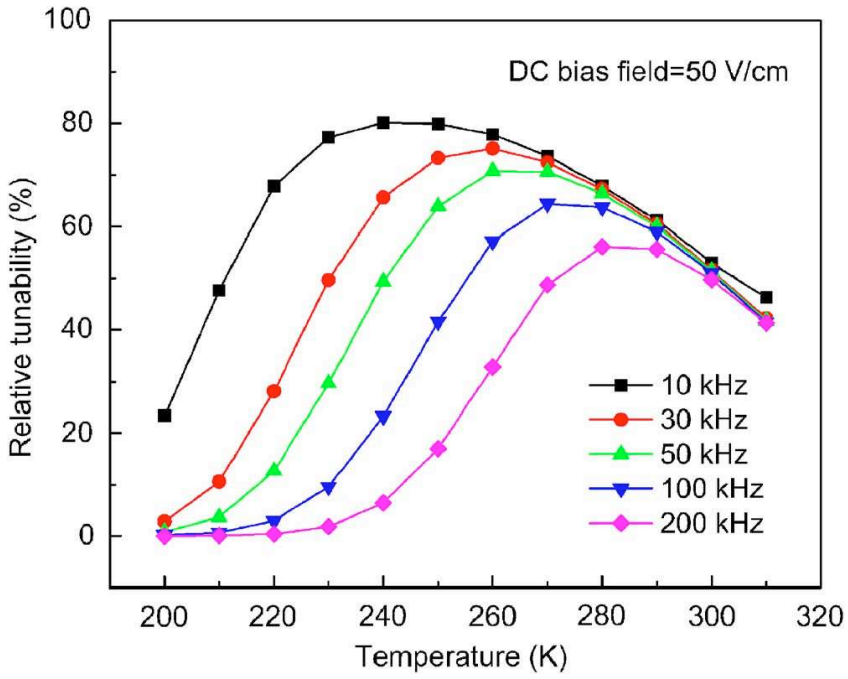

FIGURE 3.14 – Temperature dependence of relative tunability n_r under a 50 V/cm dc bias field at various frequencies between 10 and 200 kHz [10].

The relative electric tunability is defined by

$$n_r = \frac{\varepsilon_0 - \varepsilon_E}{\varepsilon_0} \tag{3.1}$$

and in Fig.3.14 is shown as a function of temperature at different frequencies under a 50 V/cm bias field. Unlike conventional ferroelectric materials where the tunability shows a sharp peak in a narrow temperature range, in $LuFe_2O_4$ it exhibits a broad peak vs. T, so that it may be exploited in a broad temperature interval around room temperature. This feature is very promising for applications.

The physical origin of the giant dielectric tunability effect in bulk $LuFe_2O_4$ is still a puzzle. In general, the reduction of dielectric permittivity under a dc bias field is mainly due to the suppression of polarization fluctuations. In conventional ferroelectrics where the

polarization arises from cation and anion pairs, tunability involves the displacement of ions and therefore usually requires a high electric field. In contrast, the electronic ferroelectricity in $LuFe_2O_4$ arises from a polar arrangement of the ordered Fe-3d charges. The energy required for the motion of 3d electrons is much lower than in case of ion displacement and a small electric field is needed to modulate the permittivity.

3.1.3.2 Electric field induced phase transition in charge-ordered $LuFe_2O_4$

In many systems the CO state can be melted by external forces such as magnetic field, electric field, and pressure, and an insulator-to-metal transition (IMT) is observed. Considering the high T_{CO} in $LuFe_2O_4$, one may expect a similar phase transition induced by electric field at relatively high temperatures. Li *et al.* found highly nonlinear current-voltage characteristics under various applied voltages. They interpret this effect as an electric field induced IMT, due to the breakdown of the charge-ordered state [10].

The relative change in resistance (R/R_0) as a function of the applied voltage at various temperatures is shown in Fig.3.15. At the threshold voltages the resistance changes by several orders, which denotes a colossal electroresistance effect. The measurements were performed on a bulk sample with a 3.8 mm length ; consequently the threshold voltage ∼22 V at room temperature corresponds to a small electric field, of the order of 50 V/cm.

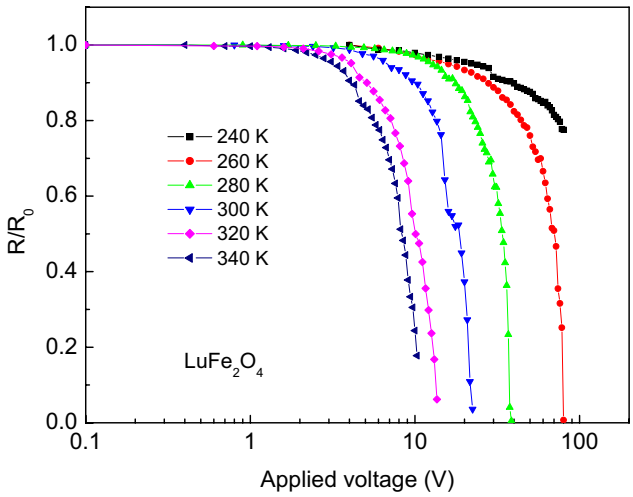

FIGURE 3.15 – Temperature dependence of the relative tunability n_r under a 50 V/cm dc bias field at various frequencies between 10 and 200 kHz [10].

The electrically-driven phase transition observed in $LuFe_2O_4$ has some features in common with that in the CO phase of $Pr_{1-x}Ca_xMnO_3$ manganites and in the magnetite (Fe_3O_4), but occurs at much higher temperatures and requires much smaller electric fields, features which are both interesting for the applications.

3.1.3.3 Electric-field control of the magnetization

The results shown in the last section suggest that the CO phase in $LuFe_2O_4$ can be broken down by an external stimulus such as the electric field. Moreover, given the magnetoelectric coupling observed in $LuFe_2O_4$, the electric-field induced breakdown of CO could induce a remarkable change also in magnetism.

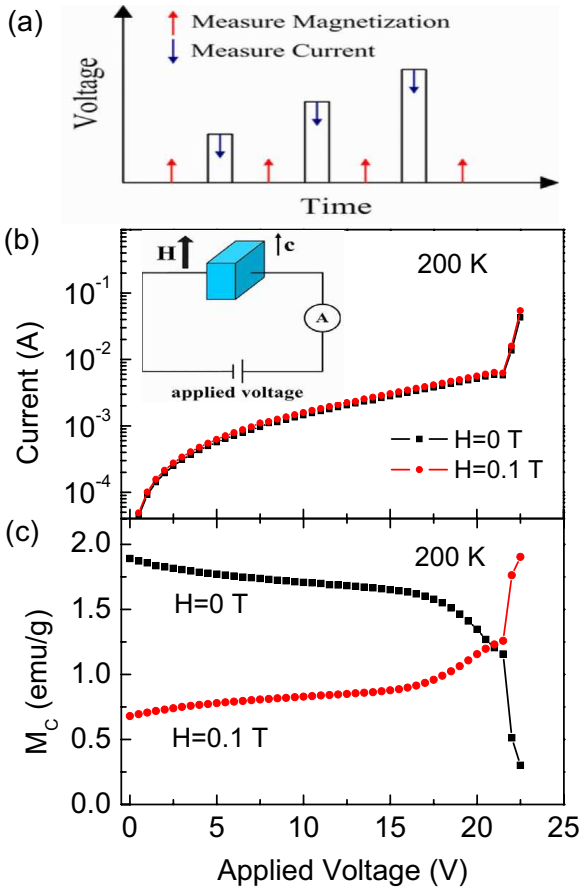

FIGURE 3.16 – (a)Current and magnetization measurements vs. time. (b) I-V curves in the *ab* plane at 200 K. The inset shows the simple experimental setup. (c) The c-axis magnetization as a function of applied voltage. The curve marked with 0 T is the remanent magnetization measured after cooling in a field of 5 T and removing the field at 200 K. The curve marked with 0.1 T was measured in a constant 0.1 T field after a ZFC process[11].

Figure 3.16 shows the magnetization of $LuFe_2O_4$ as a function of the applied voltage at 200 K, along with the I-V curves measured in the same scanning round. The magnetic field is applied along the c axis while the voltage pulse is applied in the ab plane where the CO can be more easily destroyed. The current limit is set to 0.1 A to avoid damages to the contacts. The I-V curves measured in 0 and 0.1 T are nearly the same and exhibit a big jump of current at a critical voltage $\sim$ 22 V, which indicates the suggested breakdown

of CO by the applied electric field. The magnetization as a function of applied voltage is shown in Fig.3.16(c). The curve marked with H = 0 T was measured as follows : a 5 T magnetic field was applied along the c axis to magnetize the sample, then the field was removed and the remanent magnetization was measured. The curve marked with H = 0.1 T was measured in a constant 0.1 T field. With the increase in applied voltage, the magnetization changes smoothly when the voltage is below 17 V. Above this value, the magnetization changes much faster and exhibits a sharp increase at the critical voltage. In zero magnetic field, the behavior of the remanent magnetization is inverted and it drops at the critical voltage. In contrast, the magnetization jumps up in a constant 0.1 T magnetic field. The magnetization change is independent of the polarity of the voltage : both positive and negative voltages have the same effect. The authors stress that the above results imply that the breakdown of CO is able to trigger remarkable changes in the magnetization of $LuFe_2O_4$.

Completely different interpretations have been proposed for the IMT and the electric-field control of the magnetization. Wen *et al.* performed neutron scattering measurements under electric field and suggested that no real effect is observable in the CO phase as a consequence of the electric field if one takes out the internal heating effect [12]. They pointed out that the resistivity in $LuFe_2O_4$ is low in the temperature range where most measurements are carried out, so a small voltage is able to drive a large current through the sample and heat the sample significantly. Consequently the resistance is lowered, which in turn increases the current further, which again raises the sample temperature. Eventually an avalanche occurs, which caused the breakdown of the charge order.

3.2 $GaFeO_3$

The magnetic and ME properties of $GaFeO_3$ were a topic of intensive research in 1960 since Remeika *et al.* discovered the room temperature piezoelectricity (above the magnetic transition temperature) [13]. Soon after, Rado *et al.* [14] observed the ME effect and showed that it is larger by an order of magnitude than in the previously known ME material, Cr_2O_2. A new research line has been developed in the last years following the revival of the study of magnetoelectric system, focused on the recently reported optical magnetoelectric effect.

3.2.1 Sample characterization

The crystal structure of $GaFeO_3$ is orthorhombic with four different cation sublattices, the tetrahedral (T_d) Ga1, and the three octahedral (O_h) Ga2, Fe1, and Fe2 sublattices (Fig.3.17). It has to be noted that each oxygen octahedron is significantly distorted. Since the ionic sizes of Ga and Fe are similar to each other, Fe and Ga can be distributed in the four sublattices although the Fe (Ga) ions are expected to occupy mainly Fe1 (Ga1) and Fe2 (Ga2) sublattices.

The lattice constants are $a \sim 8.75$, $b \sim 9.40$, $c \sim 5.08$ and the space group is $Pc2_1n$ or, equivalently, $Pna2_1$. All the Ga ions have a formal valence 3+ with a d^{10} nonmagnetic configuration. The Fe ions are expected to have the same valence 3+ as Ga ions but with a d^5 magnetic configuration. Ga2, Fe1 and Fe2 sites are surrounded by oxygen octahedra

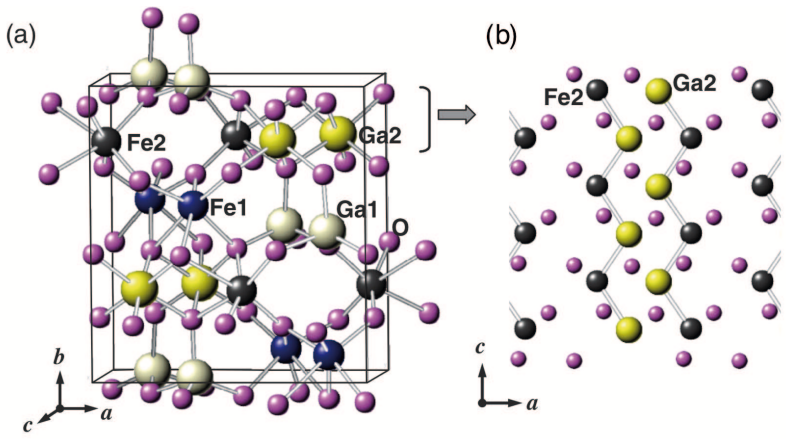

FIGURE 3.17 – (a) Crystal structure of $GaFeO_3$. Ga1, Ga2, Fe1, and Fe2 sublattices and O atoms are presented in different colors. (b) The Ga2 and Fe2 sublattice layer structure [15].

in contrast to the tetrahedral Ga1 site. The space group is $Pc2_1n$, which indicates the spontaneous polarization along the b axis. The distorted network of oxygens leads to the displacement in the Fe positions and to the noncentrosymmetric structure of each octahedron, which is considered to be responsible for the electric polarization. However, due to the complex nature of the coupling between structural and electronic degrees of freedom, its origin and its coupling to the local magnetic ordering are not fully understood yet.

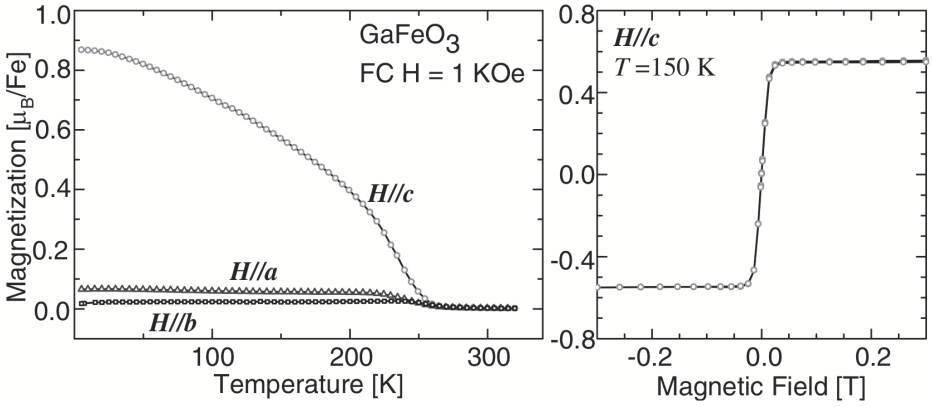

FIGURE 3.18 – Magnetization curves as functions of temperature (M vs T) and an applied magnetic field (M vs H)[15].

Several scenarios have been proposed to explain the magnetism in $GaFeO_3$, namely ferromagnetic, ferrimagnetic, or canted antiferromagnetic ordering. The magnetization curves M *vs* T and M *vs* H at constant T are presented in Fig.3.18. A net ordered moment $\mu \sim =$

0.87 μ_B/Fe is obtained at 4 K and the Néel temperature is T_N ∼260 K. It is worth noting that the preparation method has been found to influence T_N. Neutron diffraction measurements, in fact, suggest that the difference in T_N is likely to be caused by the change in the Ga / Fe occupation at the four types of cation sites [20]. The system shows strong magnetic anisotropy with the easy axis along the c axis and the hardest axis along the b axis. An experiment by Arima *et al.* [20] supports the idea that Fe substituted at the Ga site may be at the origin of the observed magnetic signal. In the magnetic ordered phase, the spin moments of Fe1 and Fe2 are directed nearly along c and antiferromagnetically coupled. Thus the compound behaves as a ferrimagnet since the Fe occupations at the Fe1 and Fe2 sites are slightly different from each other. Some results of first-principle calculations show that $GaFeO_3$ in its ideal structure has an AF order with no net moment [16]. The Fe substitution into the Ga2 site, appears to be the origin of the observed net magnetic moment, because both sites are ferromagnetically aligned thereby contributing to the net magnetic moment. This is an extraordinary case where the net moment is derived from the site disorder.

The temperature dependence of the resistivity $\rho(T)$ of $GaFeO_3$ from 360 K down to 260 K is presented in Fig.3.19. It shows a semiconducting-like behavior ($d\rho/dT < 0$) with lowering temperature. The resistivity increases from 50 kΩ m at 360 K to 60 MΩ m at 265 K. The inset in Fig.3.19 shows the plot of ln$\rho(T)$ versus 1/T which indicates that the Arrhenius law $\rho(T) = \rho_0 exp(E_a/k_BT)$ for thermally activated transport is followed in this compound with an activation energy of E_a=0.675 eV.

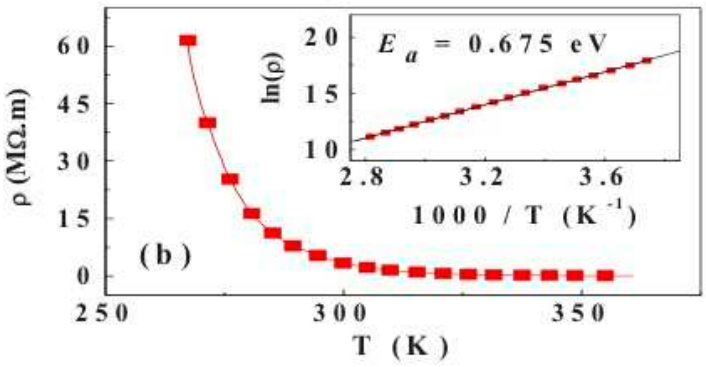

FIGURE 3.19 – Temperature dependence of the resistivity ρ of $GaFeO_3$ in the temperature interval 265-360 K. The inset shows the linear behavior of the logarithm of the resistivity vs $1/T$ [17].

3.2.2 Magnetoelectric coupling

Recently, an indication on the magnetoelectric coupling in $GaFeO_3$ has been found by Naik *et al.* by dielectric constant measurements [17]. The temperature dependence of the dielectric constant $\varepsilon(T)$ and the dissipation factor (D = $tan\ \delta$) in zero field for three different frequencies, 100 kHz, 500 kHz, and 1 MHz, is shown in the main panels of the

Fig.3.20. The $\varepsilon(T)$ presents an anomaly near the ferrimagnetic transition temperature, T_N∼228 K, but D does not show any clear anomaly close to T_N. Interestingly, a small magnetic field $B = 60$ mT suppresses the dielectric anomaly found near T_N, which is shown in the inset of the Fig.3.20(a) for $f = 1$ MHz (left scale). The magneto-dielectric (MD) coefficient calculated from the equation MD = $[\varepsilon(H)$ - $\varepsilon(0)]/\ \varepsilon(0)$ is plotted as a function of temperature in the inset of the Fig.3.20(a) (right scale) and is found to be -1.8% close to T_N. The temperature dependence of the dissipation factor is insensitive to the change from $B = 0$ to 60 mT for f=1 MHz, as shown in the inset of the Fig.3.20(b). The appearance of a dielectric anomaly around T_N and its suppression in a small $B = 60$ mT suggest an active ME coupling in $GaFeO_3$. A similar weak anomaly has been found in $\varepsilon(T)$ in the hexagonal $YMnO_3$ [18], while Kimura *et al.* [19] detected a pronounced anomaly at the paramagnetic to spiral antiferromagnetic transition in CuO.

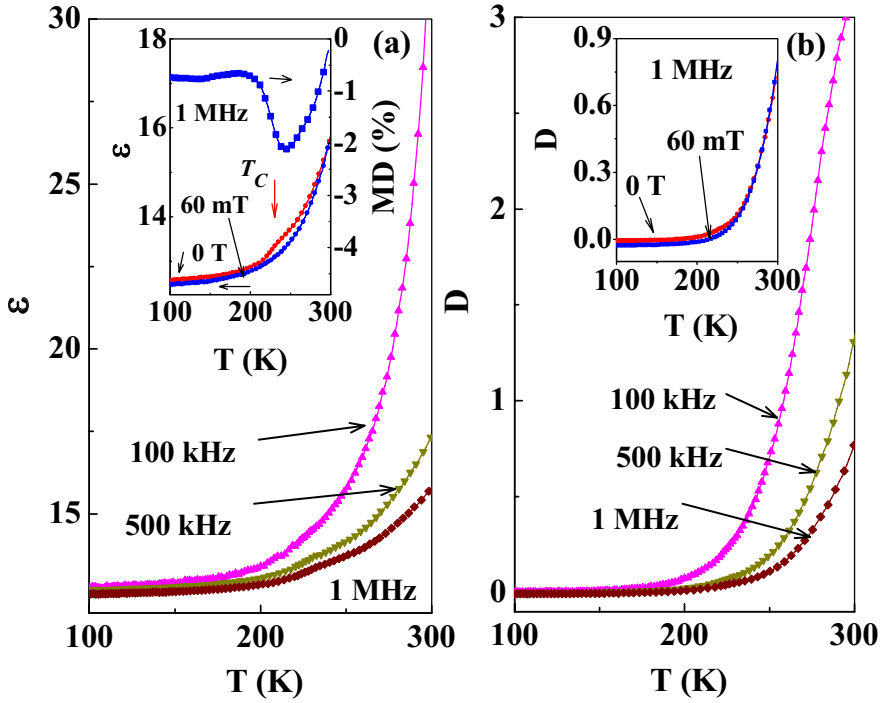

FIGURE 3.20 – Temperature dependence of (a) the dielectric constant (ε) and (b) the dissipation factor (D = $tan\ \delta$) for $f = 100$ kHz, 500 kHz, and 1 MHz. The insets show the temperature dependences of ε and D (left scale) in μ_0H=0 and 60 mT for f =1 MHz. The inset in the figure (a) shows the MD coefficient (right scale) as a function of temperature for f =1 MHz. [17].

3.2.2.1 Magnetoelectric effect

Since the magnetic easy axis is c, as shown above, $GaFeO_3$ belongs to $m'2'm$ in the Schubnikov group and one can expect two nonzero elements in the magnetoelectric tensor

($\boldsymbol{\alpha}$), α_{bc} and α_{cb}. Arima *et al.* [20] have obtained the values of this two parameters for a series of $Ga_{2-x}Fe_xO_3$ samples by measuring the induced electric current by the sweeping of a magnetic field, as shown in Fig.3.21. The Induced polarization (ΔP) was calculated by integration of the induced current. The butterfly-shape behavior was clearly observed in all the $\Delta P_b - H_c$ curves as shown in Fig.3.21, while little polarization along the c axis has been detected by application of a magnetic field along the b axis. The value of α_{bc} was obtained from the linear part of a $\Delta P_b - H_c$ curve. In a magnetic field parallel to the

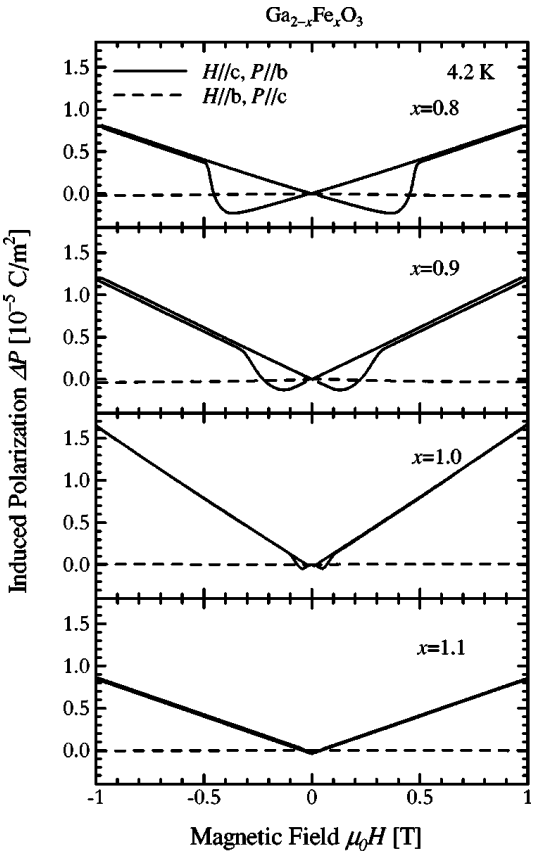

FIGURE 3.21 – Dependence of magnetoelectric polarization on magnetic field, δP_b versus H_c (solid lines) and δP_c versus H_b (dashed lines). Measurements were performed for the crystals immersed in liquid helium, i.e., at 4.2 K. [20].

b-axis, electric polarization along the *c*-axis was hardly induced as shown by broken lines in Fig.3.21.

A possible microscopic origin of the sharp contrast in the linear ME effects between the two configurations (α_{bc} and α_{cb}) was proposed by the authors [20]. When $H \parallel c$, the magnetic field is parallel to the Fe spin moments, thus the Fe2 moment increases while the Fe1 moment decreases. Therefore the displacement along the b axis of Fe2 is enlarged , that of Fe1 is reduced. Since the displacements of Fe1 and Fe2 are opposite with each other but

both toward an enhancement of the polarization, the magnetic-field-induced modulation of the displacement results in the bulk polarization P_b of Fig.3.22). In the $H \parallel b$ case, a magnetic field makes the Fe2 moment canted toward the +b direction, while the Fe1 moment is canted toward the -b direction. If Fe2 would be shifted to the +c direction by the rotation of the spin moment, the shift of Fe1 would be directed to the -c direction. The shifts of Fe1 and Fe2 along the c axis should be opposite in direction and hence partially cancelled in the bulk polarization.

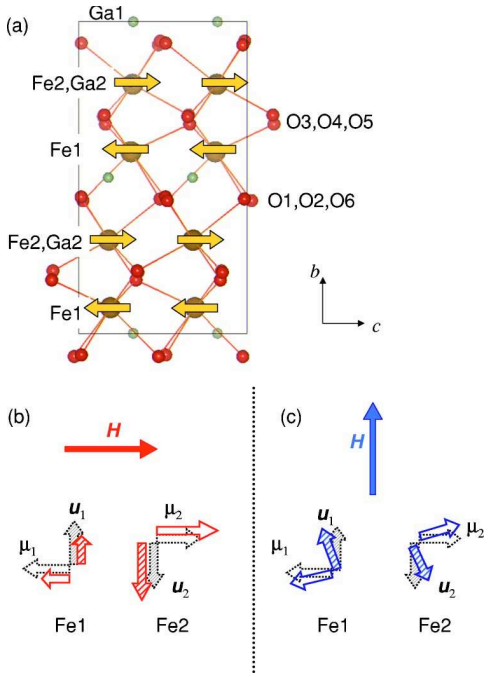

FIGURE 3.22 – (a) Magnetic structure of $GaFeO_3$. Arrows indicate Fe moments. Note that the positions of Fe1 and Fe2 are shifted to +b and -b, respectively, from the center of the two adjacent oxygen layers. (b), (c) Qualitative explanation of a large difference between the α_{bc} and α_{cb} values. $\mathbf{u}_i$ is the local displacement from the center of the octahedron and $\boldsymbol{\mu}_i$ the magnetic moments on Fe_i site (i=1,2) in zero (black lines) and strong (red and blue) magnetic fields H (see text). [20].

3.2.2.2 Optical magnetoelectric effect

Jung *et al.* have reported an interesting observation of the *optical ME effect* in $GaFeO_3$ [21]. In the conventional magneto-optical activity (see also Section 1.3.6) a change in refractive index of materials is induced by switching the incident light polarization. The optical ME effect results in the change of refractive index or absorption coefficient upon the reversal of light propagation direction (light propagation vector) relative to either the applied magnetic field (or spontaneous magnetization vector) or the applied electric field

(or spontaneous electric polarization vector), being irrespective of the light polarization. For multiferroic materials, the ME anisotropy can be realized by a change of the optical constants depending on the orientation of the light propagation vector k relative to the outer product of spontaneous polarization (P) and magnetization (M) vectors, $P \times M$.

The optical ME effect was measured for the energy region of 1.0-2.5 eV as a change in the transmittance T. In Fig.3.23 the absorption spectra $\alpha(\omega)t$ of $GaFeO_3$ for $E \parallel b$ (a solid line) and $E \parallel c$ (a dashed line) at 10 K are shown.

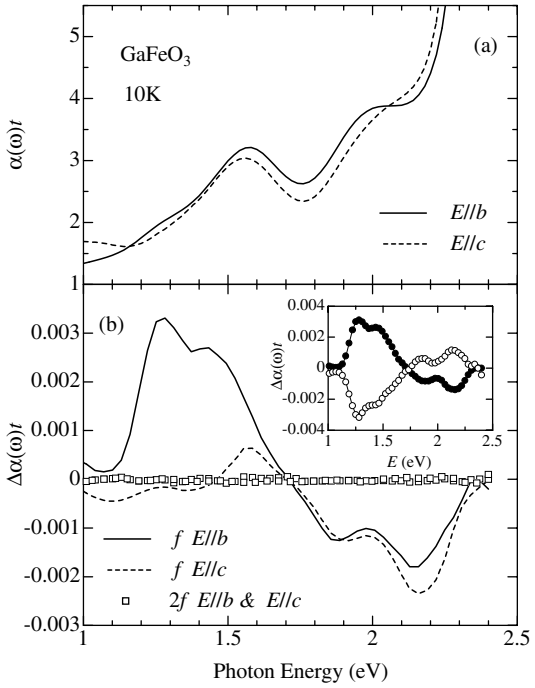

FIGURE 3.23 – (a) Absorption spectra, $\alpha(\omega)t$, and (b) magnetoelectric effect spectra, $\Delta\alpha(\omega)t$ for $E \parallel b$ (solid lines) and $E \parallel c$ (dashed lines) in $GaFeO_3$ (t $\sim$ 50 μm) at 10 K. In (b), open squares represent the second harmonic signal. Solid and open circles in the inset of (b) represent the $\Delta\alpha(\omega)t$ for the light propagation vector (k) being parallel and antiparallel to the outer product of spontaneous polarization and magnetization ($P \times M$), respectively, through the reversal of P, namely, the 180°rotation of the b axis of the sample [21].

Below the Néel temperature, the optical ME effect has been successfully detected with a high signal intensity in a small magnetic field. In the measured energy region, $\alpha(\omega)t$ spectra show anisotropy between $E \parallel b$ and $E \parallel c$ Fig.3.23(a). Fig.3.23(b) shows the magnetic field modulation spectra $\alpha(\omega)t$. These results imply also that use of polar ferrimagnets or ferromagnets may lead to enhanced ME anisotropy in other optical properties as well, such as luminescence, refraction, and diffraction.

Bibliographie

[1] Y. Yamada, K. Kitsuda, S. Nohdo, N. Ikeda, Phys. Rev. B 62, 12167 (2000)

[2] A.D. Christianson *et al.*., Phys. Rev. Lett. **100**, 107601 (2008).

[3] N. Ikeda, K. Kohn, N. Myouga, E. Takahashi, H. Kitoh, S. Takekawa, J. Phys. Soc. Jpn. **69**, 1526 (2000)

[4] N. Ikeda, H. Ohsumi, K. Ohwada, K. Ishi, T. Inami, K. Kakurai, Y. Murakami, K. Yoshii, S. Mori, Y. Horibe, and H. Kito, Nature 436, 1136 (2005).

[5] M. A. Subramanian, T. He, J. Chen, N.S. Rogado, T.G. Calvarese, A.W. Sleight, Adv. Mat. **18**, 1737 (2006)

[6] J. Iida *et al.*., J. Phys. Soc. Jpn. **62**, 1723 (1993).

[7] M. Angst, R.P. Hermann, A.D. Christianson, M.D. Lumsden, C. Lee, M.-H. Whangbo, J.-W. Kim, P.J. Ryan, S.E. Nagler, W. Tian, R. Jin, B.C. Sales, D. Mandrus, Phys. Rev. Lett. **101**, 227601 (2008)

[8] S. Z. Li, S. J. Luo, R. Fu, B. B. Jin, K. F. Wang, J.-M. Liu, J. F. Ding, X. G. Li, Appl. Phys. A : Mater. Sci. Process. **96**, 893 (2009).

[9] J. Wen, G. Xu, G. Gu, and S. M. Shapiro, Phys. Rev. B **80**, 020403(R) (2009).

[10] C.-H. Li, X.-Q. Zhang, Z.-H. Cheng, and Y. Sun, Appl. Phys. Lett. **92**, 182903 (2008).

[11] C. H. Li, F. Wang, Y. Liu, X. Q. Zhang, Z. H. Cheng, and Y. Sun, Phys. Rev. B **79**, 172412 (2009).

[12] Jinsheng Wen, Guangyong Xu, Genda Gu, and S. M. Shapiro, Phys. Rev. B **81**, 144121 (2010)

[13] J. P. Remeika, J. Appl. Phys. **31**, S263 (1960).

[14] G. T. Rado, Phys. Rev. Lett. **13**, 335 (1964).

[15] J.-Y. Kim, T. Y. Koo, and J.-H. Park, Phys. Rev. Lett. **96**, 047205 (2006).

[16] M. J. Han, T. Ozaki, and J. Yu, Phys. Rev. B **75**, 060404(R) (2007).

[17] V. B. Naik and R. Mahendiran, J. Appl. Phys. **106**, 123910 (2009).

[18] Y. Aikawa, T. Katsufuji, T. Arima, and K. Kato, Phys. Rev. B **71**, 184418 (2005).

[19] T. Kimura, Y. Sekio, H. Nakamura, T. Siegrist, and A. P. Ramirez, Nature Mater. **7**, 291 (2008).

[20] T. Arima, D. Higashiyama, Y. Kaneko, J. P. He, T. Goto, S. Miyasaka, T. Kimura, K. Oikawa, T. Kamiyama, R. Kumai, and Y. Tokura, Phys. Rev. B **70**, 064426 (2004).

[21] J. H. Jung, M. Matubara, T. Arima, J. P. He, Y. Kaneko, and Y. Tokura, Phys. Rev. Lett. **93**, 037403 (2004).

Chapitre 4

Experimental results and discussion : magnetic and optical properties of $LuFe_2O_4$ and $GaFeO_3$

In this Chapter the results of our study on $LuFe_2O_4$ and $GaFeO_3$ by infrared spectroscopy, magnetic measurements, and electron paramagnetic resonance (EPR), will be reported. The magnetic susceptibility of both samples has been measured between 5 K and 300 K and the paramagnetic phase as well as the ferrimagnetic phase has been investigated. A detailed study of the temperature and magnetic field dependence of the magnetization will be described for $GaFeO_3$. EPR measurements for $GaFeO_3$ have been performed in the X-band between 20 K and 300 K and allow us to locally investigate the magnetic properties in the proximity of the ferrimagnetic transition. For the single crystal $LuFe_2O_4$ we did not detect any EPR signal in all the investigated temperature range (20 K - 400 K) ; we suggest a relation of this behavior to the coupling of the charge ordering with the magnetic degrees of freedom already reported in the literature.

The reflectivity and optical conductivity spectra in the infrared range will be presented for both samples. For the single crystal $LuFe_2O_4$ the data have been collected between 10 K and 500 K, covering both the 2D and 3D CO phase as well as the paramagnetic and ferrimagnetic phase. For $GaFeO_3$ we extended the temperature range up to 1000 K. The phonon spectrum of both samples will be investigated and we will show that for $LuFe_2O_4$ an abrupt change in the number of observed phonons is related with the 2D - 3D CO transition. For $GaFeO_3$ we did not observe large changes in the phonon modes in the whole temperature range. Finally, we will present infrared reflectivity measurements as a function of the electric field applied to $LuFe_2O_4$ in order to investigate the metal-to-insulator transition recently reported to be driven by the electric field.

The polycrystalline $GaFeO_3$ sample has been synthesized in the Laboratoire d'Electrodynamique des Matériaux Avancés (LEMA) of the University of Tours (France). The single crystal of $LuFe_2O_4$ has been prepared in the Beijing National Laboratory for Condensed Matter Physics, Beijing (China). The infrared measurements in the FIR MIR and NIR range have been performed both in the Infrared Spectroscopy Lab. (IRS) ("La Sapienza" University of Rome) and in the LEMA laboratory. The sub-THz measurements on $LuFe_2O_4$

have been performed at the BESSY-II storage ring (Berlin) and the high temperature (300 $< T <$ 1000 K) reflectivity data on $GaFeO_3$ have been collected at the CEMHTI-CNRS in Orleans (France).

4.1 Sample preparation

Polycrystalline samples of $GaFeO_3$ were prepared by an organic gel-assisted citrate process [3]. Gallium and iron nitrates were mixed in a stoichiometric ratio and chelated by adding triammonium citrate. A polyacrylamide network was formed in situ by the organic monomers consisting of acrylamide and N,N'-methylene-bis-acrylamide which were co-polymerised by heating at about 100 °C . The gel was calcined at 700 °C for 5 hours. The powder was slightly crushed and pressed into pellets under 4000 bar/cm^2. The compound was sintered at 1350 °C during 15 hrs in air ; its structure and phase purity were checked by X-ray powder diffraction (XRD) by using a Bruker D8 diffractometer with a Cu K radiation (λ = 1.5418). $GaFeO_3$ crystallizes into orthorhombic structure with the space group $Pc2_1n$ with lattice constants a = 8.74 , b = 9.39 and c = 5.08 , according to the literature [1].

A large (8x3x2 mm^3) $LuFe_2O_4$ single crystal has been grown by optical floating zone melting method in a flowing argon atmosphere [2], and characterized by X-ray diffraction and Laue imaging at room temperature. The largest crystal surface contained the axes c and a (or b,as they cannot be distinguished).

4.2 Magnetic measurements and Electron Paramagnetic Resonance.

4.2.1 Magnetic susceptibility and magnetization of $GaFeO_3$

We performed ac susceptibility and dc magnetization measurements using a Quantum Design-Physical Properties Measurement System (QD-PPMS) magnetometer. The low frequency AC susceptibility $\chi(T)$ has been determined with an ac field modulation up to 1.7 mT at a frequency of 1 kHz superimposed to a constant field B. The magnetization measurements were performed between 5 K and 300 K at several magnetic fields between 500 Oe and 90 kOe, either in *field-cooling* (FC) and in *zero-field cooling* (ZFC) on a $GaFeO_3$ sample of 11.3 mg.

The temperature dependence of the magnetic susceptibility is shown in Fig.4.1(a). The value of $\chi(T)$ tends to diverge at $T\sim$ 207 K suggesting the onset of a magnetic phase transition. The inverse of the magnetic susceptibility $\chi^{-1}(T)$ (Fig.4.1(b)) at high temperature shows a quasilinear behavior with a small negative curvature. It drops down at T= 207 K and presents a shoulder around 180 K. At lower temperature it slightly increases with decreasing temperature down to 5 K. Fig.4.2 shows the temperature dependence of the magnetization under different magnetic fields, from 500 Oe to 90 kOe in both ZFC and FC procedures. At low fields and high temperatures the magnetization is almost zero and shows a rapid increase at $T \sim$ 210 K. By decreasing further the temperature, the

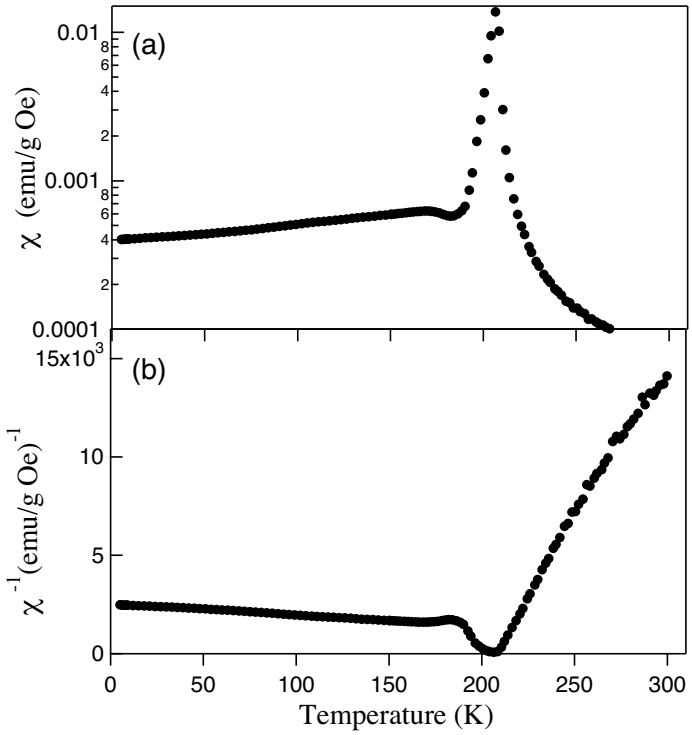

FIGURE 4.1 – (a) Temperature dependence of the ac magnetic susceptibility of polycrystalline $GaFeO_3$ measured by Quantum Design-Physical Properties Measurement System (QD-PPMS) with an ac field modulation up to 1.7 mT. The divergence at 207 K suggest the onset of a magnetic transition. (b) Temperature dependence of the inverse susceptibility.

FC magnetization increases down to 5 K while the ZFC one decreases under 100 K and tends to zero at the lowest temperature. Only the curves collected at 500 Oe and 1 kOe show ZFC and FC curves differing from each other under 100 K. Above 5 kOe there is no difference between the ZFC and FC curves. By increasing the magnetic field, the sharp increase at T $\sim$ 210 K starts to broaden and the curve at 9 kOe shows a smooth increase of magnetization by decreasing temperature. In Fig.4.3 we show the magnetic field dependence of the magnetization at 2 K up to 9 kOe after ZFC. Starting from the low fields the curve shows a rapid increase from zero to $\sim$ 0.4 μ_B/Fe at about 200 Oe. At higher field the slope decreases and the magnetization tends to the saturation reaching the value of $M_S = 0.77\mu_B/Fe$.

$GaFeO_3$ has been reported to have a ferrimagnetic ground state [4]. As mentioned in Chapter 3, different transition temperatures are reported in the literature either for different single crystals or for polycrystalline samples [4] [6] [7]. The highest temperature transition $T_C = 260$ K has been reported by Kim *et al.* [5] in single crystals. Our results are in good agreement with those reported by Kaneko *et al.* [8]. Thus, the T_C of $GaFeO_3$ significantly depends on the preparation technique : it has been suggested that this dependence is related

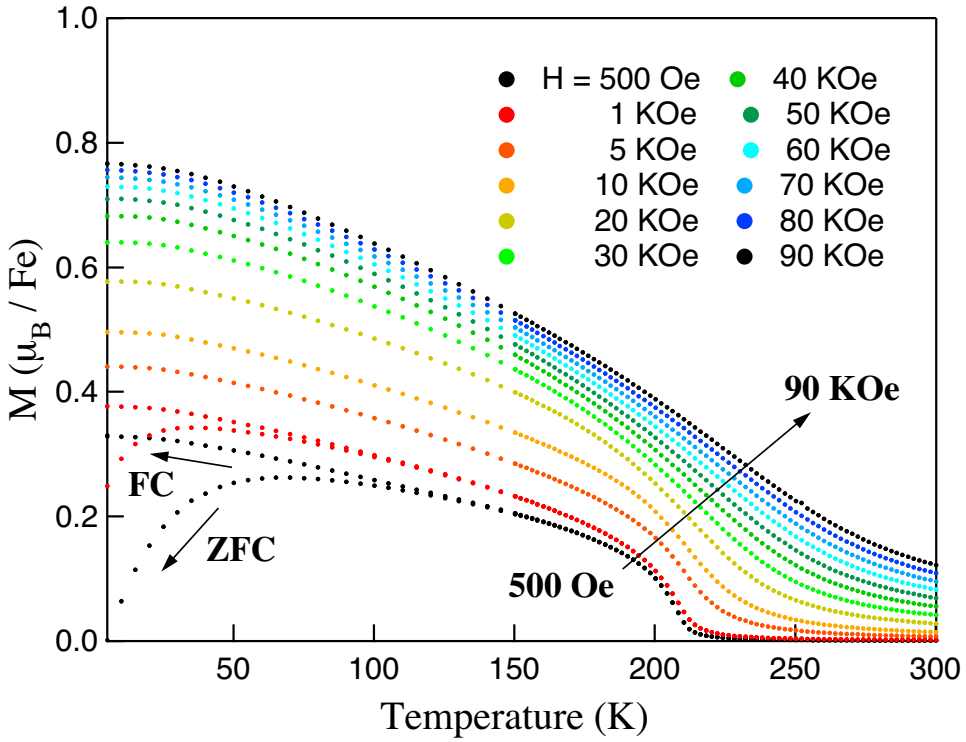

FIGURE 4.2 – Temperature dependence of the magnetization under different magnetic fields, from 500 Oe to 90 kOe in both ZFC and FC for polycrystalline $GaFeO_3$. No difference between the ZFC and FC curve is detected above 5 kOe.

to the different Ga / Fe occupations at the four types of cation sites [4].

In Fig.4.1(a) the susceptibility suggests the onset of a magnetic transition at $T = 207$ K. The temperature dependence of $\chi^{-1}(T)$ shows some anomalies. At high temperature ($T > 207$ K) the T-dependence of $\chi^{-1}(T)$ cannot be described by a simple paramagnetic law, because of the small negative curvature still present at room temperature. Moreover the shoulder at 180 K may indicate another singularity in the magnetic susceptibility.

We have also calculated the onset of the ferrimagnetic transition from the maximum change in slope at 500 Oe from the data shown in Fig.4.2. This value is in good agreement with the susceptibility measurements and gives $T_C = 206$ K. The Fig.4.2 shows that the transition broadens in temperature when the magnetic field is increased and the maximum of the magnetization at 5 K is 0.77 μ_B/Fe atom, under the applied field of 90 kOe. It has been shown that in single crystals the saturation is reached at about $0.7\mu_B$/Fe at 5 K [4] with an applied magnetic field of 10 mT at 5 K along the easy magnetic axis c. In our polycrystalline sample the saturation is reached only in high magnetic fields (see Fig.4.3) but the maximum magnetic moment (0.77 μ_B/Fe) has almost the same value as that reported for a single crystal. However, unsaturated hysteresis loop is commonly seen in the polycrystalline ferrites. Thus, to check if the maximum value of magnetization at 2

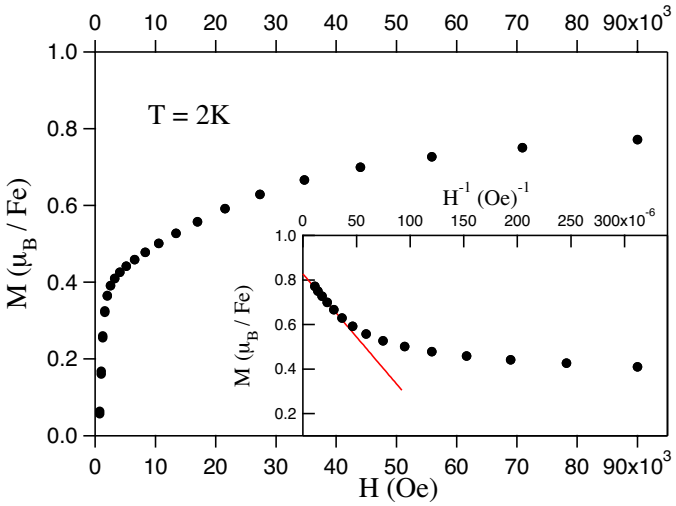

FIGURE 4.3 – Magnetic field dependence of the magnetization at 2 K up to 9 kOe in ZFC for polycrystalline $GaFeO_3$. In the inset, the magnetization is plotted vs, the reciprocal of the magnetic field applied.

K and 90 kOe is the saturation magnetization value of our sample, we applied the law of approach to saturation [9] $M = M_S(1-A/H)$, where M_S is the saturation magnetization, A is a coefficient related to the magnetic hardness and H is the applied magnetic field. In the inset of Fig.4.3, the magnetization at 2 K as a function of the inverse magnetic applied field (M vs $1/H$) is shown. The red line is the linear fit for the high field part. The extrapolation to the origin ($H \to \infty$) leads to the saturation value of the magnetization, which results M_S = 0.82 μ_B/Fe. With the same procedure Naik *et al.* [7] have obtained M_S = 0.764 μ_B/Fe by measuring the magnetization up to 5 T. It seems, therefore, that for $GaFeO_3$ also the value of M_S is slightly sample-dependent (as for the T_C). It could be understood as a consequence of the specific origin of the magnetization in this compound. In fact, different Ga/Fe occupation in the Ga2 sites can induce different values of the macroscopic magnetic moment (the same argument is used to explain the sample dependent T_C). Therefore, an increase in the Fe occupation at the Ga2 sites may lead to an enhancement of the saturation magnetization. The strong dependence of M_S and T_C from the preparation method could be a very useful feature for possible applications. In fact, a suitable control of the site occupation could lead to an enhancement either of the T_C and of the magnetization in $GaFeO_3$. Moreover, as it has been already shown that in $Ga_{2-x}Fe_xO_3$ (with $x > 1$) T_C linearly increases with doping [4], one can propose $GaFeO_3$ as a very good candidate for room temperature multiferroicity.

In Fig.4.4 we show the magnetic field dependence of the magnetization in FC procedure at selected temperatures down to 5 K, deduced from Fig.4.2. At room temperature a paramagnetic behavior is evident from the linear dependence of the magnetization. At 5 K a branch of hysteresis is observed but the magnetization does not seem to reach a complete saturation even at high magnetic fields. By lowering the temperature from 300 K, the

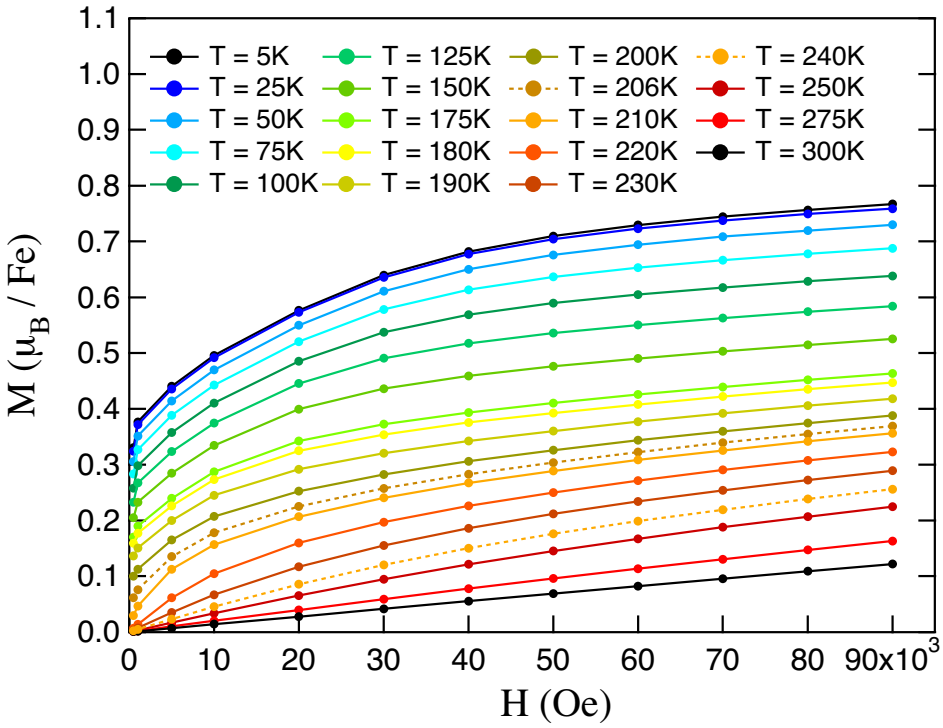

FIGURE 4.4 – Magnetic field dependence of the magnetization in FC procedure at selected temperatures down to 5 K, as calculated from data in Fig.4.2.

curves show a non-linear dependence starting from 240 K, well above $T_C = 207$ K. This behavior can be considered as the appearance of *short-range-order* magnetic interactions above T_C. In what follows we will try to investigate this possible scenario adding new observations that can confirm our claim. First we will introduce a useful analysis method aimed at determining certain physical quantities associated with magnetism, and actually defined in zero field - as the critical temperature T_C or the susceptibility χ. This is the Arrott plot method [10] in which the square of the magnetization M in a magnetic field H is plotted as a function of H/M for fixed temperatures. For ferromagnetic (or ferrimagnetic) systems, each of these plots is a straight line with a negative y-intercept which vanishes when T approaches T_C. Moreover, the x-intercept represents the value of $1/\chi$.

In Fig.4.5 we report the Arrott plots for $T > T_C$ for the magnetization data in Fig.4.4 at selected temperatures. At $T = 300$ K, for high values of H, M^2 shows a linear behavior. The data collected at low magnetic field, *i.e.* small M^2, are not aligned with the high magnetic field data, and roughly lie on the x-axis. At $T = 206$ K the x-intercept vanishes, indicating a $T_{C,Arrott}$ very close to the critical temperature deduced from susceptibility measurements ($T_C = 207$ K). One of the most useful characteristics of the Arrott plot is that one can obtain the values for χ in the zero field limit form the x-intercept of the linear parts of the plots. It has to be noted, that in the low field magnetization region

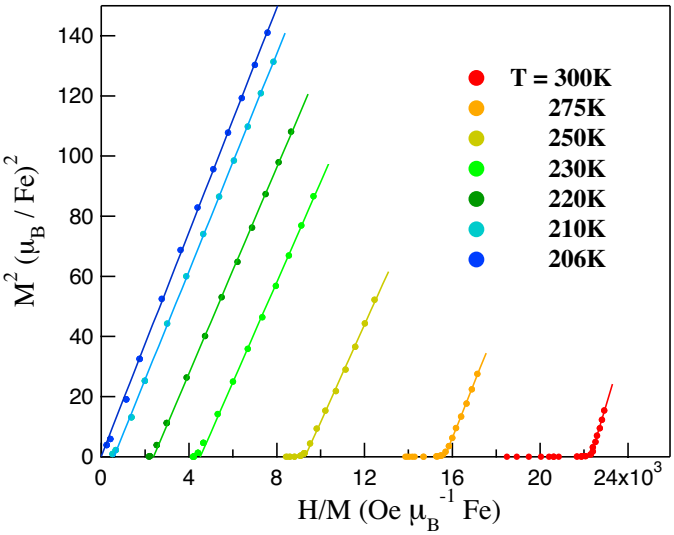

FIGURE 4.5 – Arrott plot at selected temperatures calculated from data in Fig.4.2 for polycrystalline $GaFeO_3$.

the value of H/M does not coincide with the value of χ. This discrepancy is more evident in the high-temperature measurements. This difference is not due to low experimental sensitivity or systematic errors ; it demonstrates that, in order to obtain the real value of $\chi(T)$ (*i.e.* in the zero magnetic field limit), it is not enough to perform susceptibility measurements or magnetization measurements at low magnetic fields. By collecting the x-intercept of all the fits of the linear part of the plots, we can now evaluate the zero field limit of the susceptibility. The calculated χ_{Arrott} is plotted in Fig.4.6 together with the data of the AC magnetic susceptibility. As we can see, there is a big discrepancy between the two curves which increases with temperature. By plotting χ^{-1}_{Arrott} *vs* T, we can estimate some parameters which characterize the paramagnetic phase of $GaFeO_3$. At high temperatures, $\chi^{-1}_{Arrott}(T)$ follows a Curie-Weiss law $\chi(T) = C/(T-\theta)$ (inset Fig.4.6), meanwhile, for temperatures below $\sim 240\ K$, the curve shows a positive curvature. From the linear behavior for $T > 240\ K$ we have determined the Curie constant C and the Curie-Weiss temperature θ, which are $C_{CW} = 0.6(6)\ mol\ K\ /\ emu$ and $\theta = 214\ K$. Moreover, as we can see from the inset of Fig.4.6, the deviation from the paramagnetic linear regime is observed at $240\ K$, well above the transition temperature T_C. We interpret this as the signature of the onset of short range antiferromagnetic interactions arising at $T = 240\ K$. This hypothesis can be verified also by analyzing the slope m of the linear part of the Arrott plots. In a typical Arrott plot for a paramagnetic system, the product $m \times T$ (temperature) in the paramagnetic phase decreases with decreasing temperatures, while in an antiferromagnetic or ferromagnetic phase, the value of $m \times T$ is constant in temperature. In Fig.4.7 we present the temperature dependence of $m \times T$ for $GaFeO_3$. As we can see the curve is not monotonic : at high temperature $m \times T$ decreases, while under $\sim 240\ K$ it remains almost constant. This behavior can be therefore considered as the signature of

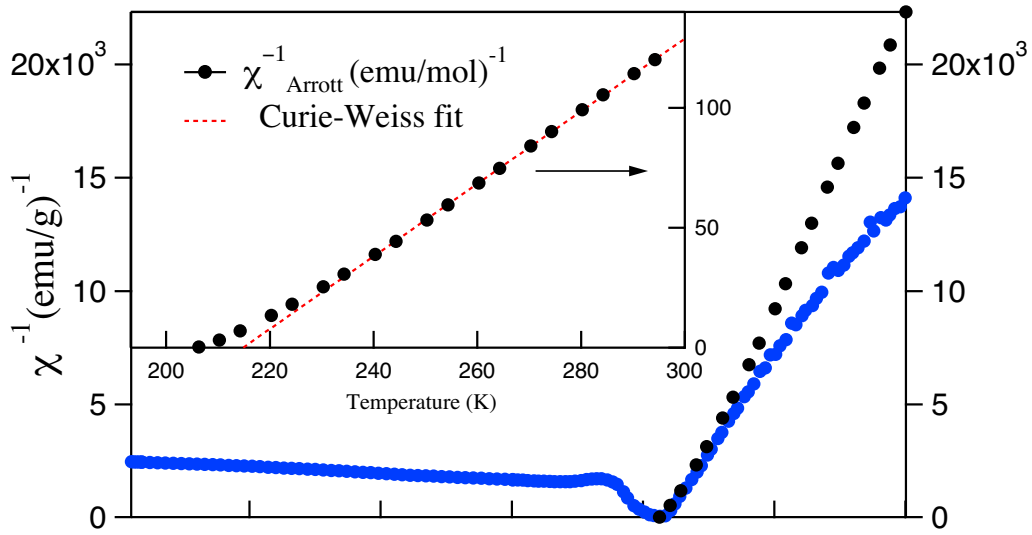

FIGURE 4.6 – Comparison between the magnetic susceptibility data reported in Fig.4.1 (blu circles) and the magnetic susceptibility calculated from the Arrott plots (black circles) χ_{Arrott} (see text). In the inset the temperature dependence of χ_{Arrott} is plotted in the paramagnetic region. The red dashed line is the Curie-Weiss fit.

a crossover from a simple paramagnetic phase to an antiferromagnetic one. Therefore, we define $T_{SR} = 240\ K$ as the onset temperature of short range antiferromagnetic interactions. We will corroborate this interpretation with the temperature evolution of the EPR signal in the next section.

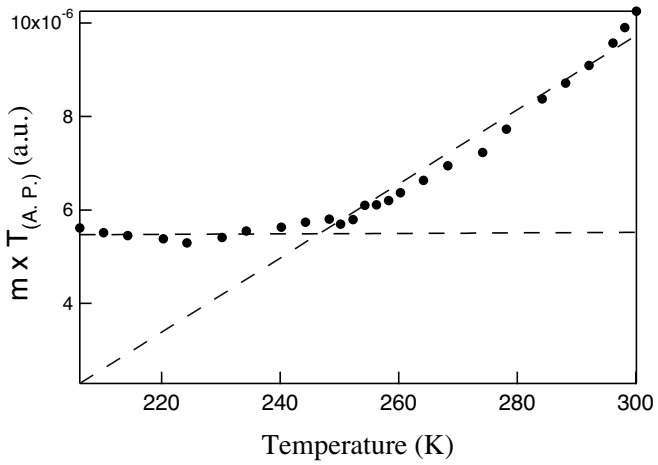

FIGURE 4.7 – Temperature dependence of the product $m \times T$ deduced from the Arrott plot : it suggests a crossover from a simple paramagnetic to a ferrimagnetic phase occurring at 240 K. The dashed lines are only a guide for the eyes.

4.2.2 Electron Paramagnetic Resonance on $GaFeO_3$

To investigate the dynamic local response of $GaFeO_3$, we performed EPR measurements as a function of temperature between 20 K and 300 K. The experiments were performed in the X-band at 9.4 GHz with a Bruker *Elaxsys EMX 6/1* spectrometer, equipped with a continuous flow cryostat. The sweeping dc applied magnetic field could be varied from 0 to 7000 G and all the experiments were collected under high vacuum. The Fig.4.8 reports the X-Band EPR spectra on the same sample of polycrystalline $GaFeO_3$ used for the magnetization measurements. The spectra show the temperature dependence of dP/dH, where P and H are the microwave powers absorbed by the sample and the external dc magnetic field, respectively. Starting from $T = 300$ K a single large contribution, centered around 3300 G, is detected.

By lowering the temperature the intensity of the signal shows an enhancement down to $T = 240$ K ; then the signal starts to be distorted and another contribution superimposes to the original one. Approaching T_C=207 K, the intensity of the signal is strongly suppressed. In the ferrimagnetic phase (inset Fig. 4.8) the spectra consist in a single contribution centered at about 2300 G. At temperature lower than 80 K the intensity of the signal is too weak to be detected. The Fig.4.8 shows that in PM state, far from the $T_C = 207$ K, the EPR spectra consist in a single Lorentzian-like resonance line, proper of free electron absorption processes. The low field shifted EPR line appearing at about $T\sim$ 240 K, is an evidence of spin-spin interactions and suggest the presence of a net magnetization due to ferro- or ferrimagnetic correlations. It is worth noting that the second absorption line appears at $T = T_{SR} = 240$ K.

For an accurate determination of the various line shape parameters of the EPR spectra we have fitted the curves with a Lorentzian function. From 300 K to 240 K (the paramagnetic phase) the fit has been performed using a single Lorentzian contribution, while a fit with two Lorentzian functions has been performed between 235 K and 215 K. At lower temperatures the line is too distorted to perform reliable fits. The results of the fit procedure are shown in Fig.4.9. Between 300 K and 240 K the fit well corresponds to the experimental lines, being slightly different only for $T = 240$ K, under 3000 G. When the second line appears the two-component fit is appropriate, even if at $T = 215$ K the experimental line is strongly distorted because the temperature is approaching T_C. Below 215 K the absorption presents line shapes so distorted that they do not allow for reliable fits.

The parameters of primary interest for the EPR analysis are :

– the Landé factor g, which is related to the center of the absorption line H_C through

$$g = h\nu/(\mu_B H_C) \tag{4.1}$$

where $h\nu$ is the energy of the microwave radiation and H_C is the center of the absorption line. It provides information about the electronic structure of the ground state ;

– the *line width* ΔH, the half width half maximum (HWHM) of the absorption line, which probes the spin dynamics ;

– the DIN, the doubly integrated intensity of the signal which, in suitable conditions, is related to the magnetic susceptibility.

In Fig.4.10 we report the values of the parameters obtained from the fit of the EPR signal as a function of temperature. In the paramagnetic phase the spectrum consists of a single line with a g factor almost temperature independent. Its value is $g \simeq 2.0$, which corresponds to the free-electron value $g = 2.0023$. Below 240 K, the second contribution appears (hereafter we will refer to this absorption with the subscript $'2'$). The center of the first and the second absorption shows a different temperature dependence : if the first contribution shifts to higher fields, the other absorption is shifted towards the low-field region. The g_1 value slightly decreases down to 1.8 at 215 K ; g_2 appears around 2.9 and at 240 K, and increases up to 3.8. The linewidth between 300 K and 240 K slightly narrows with decreasing temperature, and below 240 K ΔH for both contributions shows a strong enhancement when the temperature is lowered. The intensity of the EPR signal is softly increasing between 300 K and 240 K showing a large enhancement below 240 K for both lines.

The appearance of the second spectral line and the temperature dependence of g_2 can be interpreted as the consequence of a phase transition from a paramagnetic to an ordered phase (in our case ferrimagnetic, as shown by the magnetization measurements). It is usual, in fact, that in the presence of an internal magnetic field, a new line splits from the principal one and shifts to lower field. In a simple paramagnetic to ferromagnetic transition, the intensity is progressively transferred from one contribution to the other, and below the Curie temperature a single line at low field is again obtained [13] [12]. On the other hand, the T dependence of g_1 is unusual, because neither in a ferromagnetic nor in an antiferromagnetic (or ferrimagnetic) phase a decrease of the g factor is expected. To explain this unattended result we propose an argument related to the unique, disorder-related, origin of the net magnetization in this compound. As we pointed out in the Chapter 3, the ferrimagnetism in $GaFeO_3$ arises from Fe substitution at the Ga site. Moreover, it has been reported that the Fe occupation at the Ga1 T_d site is negligible [4]. Therefore, in the ordered phase the net magnetization is related with the Fe occupation of the Ga2 sites. The decreasing value of the g_1 factor with decreasing temperature can be interpreted as an indication that the free electrons of the magnetic Fe ions are experiencing an internal magnetic field directed in the opposite direction with respect of the external magnetic field applied. By considering that when the magnetic order appears, the spin moments of Fe1 are antiparallel to those at the Fe2 and Ga2 sites (see Fig.3.22), it is likely that some Fe ions at the Fe1 site, having their magnetic moment parallel to the external magnetic field, locally experience an internal field in the opposite direction , which arises from the alignment of the next neighbor Fe ions in Fe2 and Ga2 sites. Thus, in this scenario, the decrease of g_1 is possible only because the Fe occupation between Ga1 and Ga2 sites is unbalanced (the Fe occupation of Ga1 sites being probably structurally suppressed). A study presented by Gilleo *et al.* [14] supports this hypothesis. They proposed a simple model in which the fraction of the Fe ion occupation was suggested to be 0, 0.35, 0.825, and 0.825 at the Ga1, Ga2, Fe1, and Fe2 sites, respectively. This model, in addition, predicts a net saturated magnetic moment of $0.86\mu_B/Fe$, which is both in good agreement with the 0.82 μ_B/Fe value calculated in this work (the result of the extrapolation in the inset of Fig.4.3) and almost coincident with the value reported for single crystal [5].

The temperature evolution of ΔH can be easily understood in the above scenario, in fact the strong enhancement between 240 K and 215 K is found usually in antiferromagnetic

materials. The weak absorption line observed under T_C, corresponding to $g \approx 2.80$, can be interpreted as a weak remnant ferromagnetic signal, which decreases with decreasing temperature as the long range antiferromagnetic phase becomes stable. As we can see from Fig.4.10, all the EPR parameters show significant changes at 240 K, the T_{SR} temperature defined above, confirming that at this temperature there is a clear evidence of short range antiferromagnetic interactions, locally experienced as a net magnetization.

By means of EPR measurements we can also obtain informations about the formal valence of the Fe ions. Our room-temperature spectra show that the Landé factor g corresponds to the free electron value $g = 2.0$, clearly identifying a spin-only ground state. This resonance is related to the $3d^5$ Fe^{3+} ions, because the Fe^{2+} ions have a triplet ground state, and in octahedral environment (Fe1 Fe2 and Ga2 sites have O_h coordination) they are expected to have $g \simeq 3.4$, which is far from our measured value. Moreover, the Fe^{2+}-Fe^{3+} coupling would induce a g-shift providing an additional temperature-dependent broadening to the Fe^{3+} EPR line [15]. We observed that g remains constant in the whole pure PM phase (300 K-240 K) allowing us to consider the Fe ion in the system as nominal Fe^{3+}.

The double integrated intensity (DIN) of the EPR signal, under certain conditions, is related to the magnetic susceptibility χ. It appears, in fact, that in far PM range, where g is T-independent, the DIN may be considered to be proportional to the susceptibility obtained from magnetization measurements. The as obtained $\chi^{-1}_{EPR}(T)$ vs T, calculated in the paramagnetic region 300 K - 220 K, and normalized to the value at 300 K, is presented in Fig.4.11, compared with the susceptibility measurements and the χ_{Arrott}, both normalized in the same way. As we can see, the accordance of the three methods is very good. The inset of Fig.4.11 shows that the approximation of $\chi^{-1}_{EPR}(T)$ with the Curie-Weiss law is good between 300 K and 240 K. At 240 K the curve shows a positive curvature as for the magnetic susceptibility calculated by means of the Arrott plots (see Fig.4.6). From the Curie-Weiss fit we found $\theta_{EPR} = 209$ K, slightly lower than $\theta_{Arrott} = 214$ K.

Let us now summarize the results obtained from magnetization measurements combined with the EPR technique. We have found from the ac susceptibility measurements that $GaFeO_3$ experiences a magnetic phase transition around 207 K. By means of magnetization measurements performed between 300 K and 2 K with a magnetic field up to 90 kOe we have determined the $T_C = 206$ K. The remnant magnetic moment below T_C in the M vs T curve measured at several H shows that our sample presents a ferrimagnetic-like transition as reported from other groups. The saturation magnetization is reached only at high magnetic field and the maximum magnetic moment $M_S = 0.77$ μ_B/Fe is comparable with the value reported for single crystals. Moreover, we have calculated the magnetic susceptibility in the zero magnetic field limit by means of the Arrott plots of the magnetization data. The temperature dependence of the parameters calculated from this analysis (χ_{Arrott} and $m \times T$) suggests that short range antiferromagnetic interactions appear at $T_{SR} = 240$ K. This is confirmed by the presence of two lines below $T = 240$ K in the EPR spectra (Fig.4.8) and by the temperature evolution of the EPR parameters g and ΔH. In Table 4.1 we report all the physical quantities we have deduced from this experimental investigation of $GaFeO_3$.

Transition temperature calculated from ac susceptibility measurements	T_C	$T = 207\ K$
Transition temperature calculated from dc magnetization measurements	T_C	$T = 206\ K$
Saturation magnetization at 2 K and 90 kOe	M_S	M=0.77μ_B/Fe
Transition temperature calculated from Arrott Plots	$T_{C,Arrott}$	$T = 207\ K$
Short range magnetic interaction transition temperature calculated from Arrott Plots	$T_{SR,Arrott}$	$T = 240\ K$
Short range magnetic interaction transition temperature calculated from EPR	$T_{SR,EPR}$	$T = 235\ K$

TABLE 4.1 – Physical quantities for $GaFeO_3$ deduced from magnetization and EPR measurements.

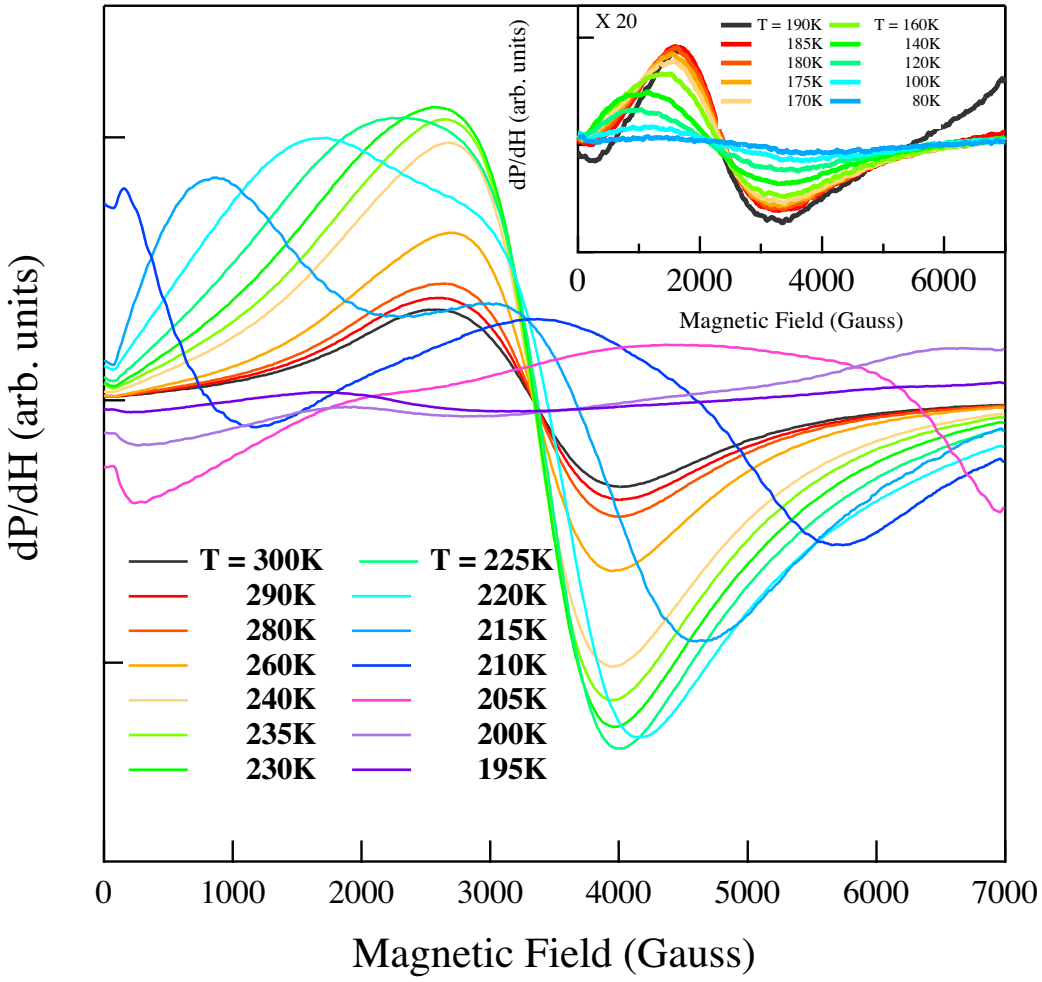

FIGURE 4.8 – Temperature dependence of the EPR spectra for polycrystalline $GaFeO_3$. In the inset the intensity of the signal is enlarged 20 times.

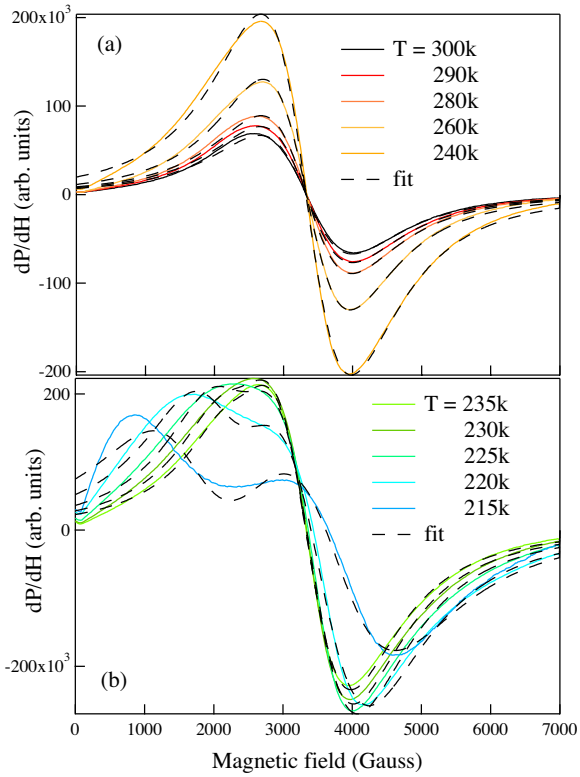

FIGURE 4.9 – Comparison between EPR experimental data (solid lines) and Lorentzian fit (dashed lines) for $T > T_C$. The fit has been performed with one and two Lorentzian contributions in (a) and (b), respectively.

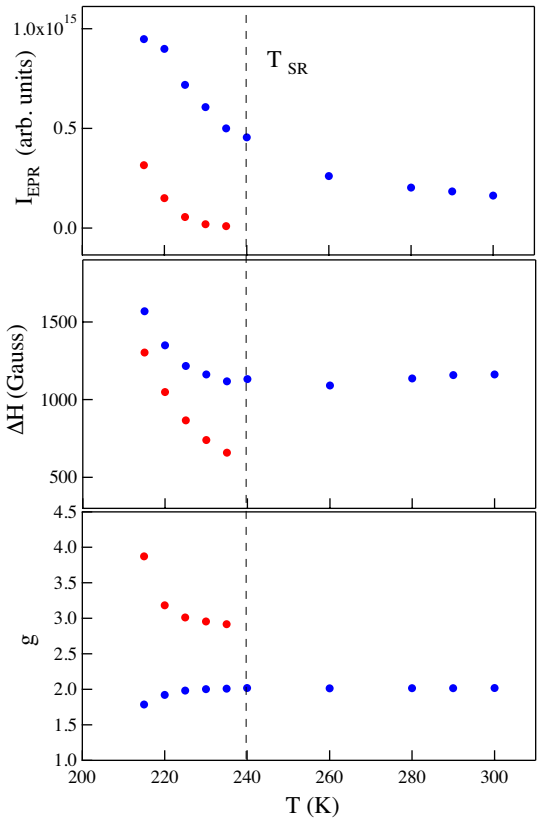

FIGURE 4.10 – Temperature dependence of EPR spectra parameters calculated from Lorentzian fit shown in Fig.4.9. g is the Landé factor related to the center of the absorption line through the Eq.4.1, ΔH and I_{EPR} are the HWHM and the Intensity of the Lorentzian functions, respectively.

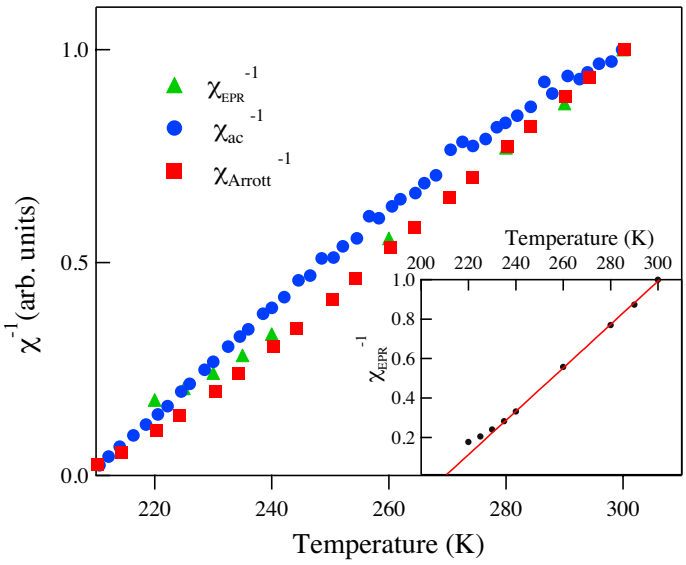

FIGURE 4.11 – Temperature dependence for $T > T_C$ of the inverse magnetic susceptibility $\chi^{-1}_{EPR}(T)$ calculated from the double integration (DIN) of EPR spectra, compared with the susceptibility measurements and χ_{Arrott}. In the inset, $\chi^{-1}_{EPR}(T)$ is plotted with a Curie-Weiss fit (red solid line).

4.2.3 Magnetic measurements and EPR on $LuFe_2O_4$

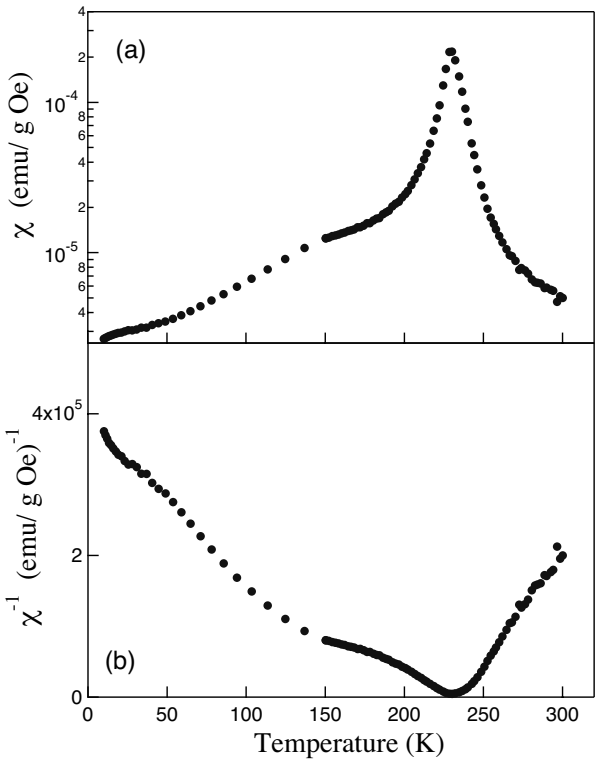

FIGURE 4.12 – Magnetic susceptibility of the single crystal of $LuFe_2O_4$, as measured in zero-field cooling.

In order to investigate the magnetic properties of $LuFe_2O_4$, we performed ac magnetic susceptibility measurements on a single crystal between 5 K and 300 K with the same apparatus used for $GaFeO_3$. The magnetic field $H = 1.7$ mT was directed along the c axis and modulated at 1 kHz. As we have reported in Chapter 3, magnetic measurements and neutron diffraction experiments show that $LuFe_2O_4$ exhibits a ferrimagnetic order at low temperature. It has to be noted, however, that the origin of the ferrimagnetism is completely different from that in the $GaFeO_3$ system, as here it arises from the frustrated antiferromagnetism in triangular nets.

The magnetic susceptibility of the sample, as measured in zero-fied cooling, is shown in Fig. 4.12(a) : at high temperature it is almost zero and increases rapidly toward a sharp peak at the onset of the ferrimagnetic transition at $T_N = 230$ K, also reported elsewhere [17]. This behavior is consistent with the predicted ferrimagnetic transition from the paramagnetic charge-order state at $T > 240$ K. By lowering the temperature we observe a change of slope at about 150 K. In Fig.4.12(b) we plot the inverse magnetic susceptibility $vs.$ T. At high T $\chi^{-1}(T)$ is paramagnetic, drops to zero at 240 K and then softly increase. An increase in the slope is observed at 150 K and the value continues to increase down to

5 K.

The feature observed at 150 K has been reported in other works, but it is strongly sample dependent. Christianson *et al.* [16], from neutron diffraction measurements, found two magnetic transitions at $T_N = 240\ K$ and $T_L = 175\ K$. They proposed that the observed singularity at T_L is related to a change in the magnetic correlation length. Our measurements can be interpreted in this scenario, even if we have to remark the different temperature $T = 150\ K$ at which we observed the anomaly.

To investigate further the local magnetic properties of $LuFe_2O_4$, we performed EPR measurements between 20 K and 400 K as for $GaFeO_3$. We have not detected any signal in the whole range of temperature. This behavior is generally encountered when the spin correlations are strong, so that the short correlation time make the linewidth very large and the signal intensity extremely low. However, it has to be stressed that the signal does not appear neither in the ferrimagnetic ($T < 240\ K$) nor in the paramagnetic phase. In the former case the magnetic interactions can be the origin of the large line-shape. but we cannot explain why the signal is absent in the paramagnetic phase . We can just remark that the charge ordering and the magnetization degrees of freedom are related with each other in $LuFe_2O_4$: this is one of the most interesting results on this compound. As we explained in Section 3.1.2, the peak revealed by neutron scattering and related to the charge-order superstructure is affected by the application of a magnetic field under 320 K, in the 3D charge-ordered phase. We can thus infer that on a local scale (EPR is a local probe) the spins are correlated via the charge ordering process. Moreover, from the fact that we do not detect any signal also in the temperature range 320 K-400 K, it is likely that the magnetic interactions are coupled with the charge superstructure also in the 2D CO phase. However, to support quantitatively this explanation we plan to measure the EPR response at $T > 500\ K$, where also the charge order is broken and the EPR signal should appear as a consequence of the vanishing of all the magnetic interactions.

4.3 Infrared spectroscopy of $GaFeO_3$ and $LuFe_2O_4$

The aim of the IR measurements is to investigate the phonon spectrum of both samples. The study of the temperature evolution of the phonon lines allows us to understand if and how the structural properties are modified by the different magnetic and charge orders.

4.3.1 Reflectivity measurements on $GaFeO_3$

The reflectivity R(ω) of polycrystalline $GaFeO_3$ has been measured at near-normal incidence in the rangeω = 50 - 7000 cm^{-1}. The sample had a disk shape of 7 mm in diameter, while its thickness was about 1 mm. The measurements have been performed by means of the experimental setup described in Chapter 2 between 10 K and 1000 K. The reference was a gold film evaporated in situ onto the sample.

Figure 4.13 shows the reflectivity of $GaFeO_3$ in the whole measured frequency range at selected temperatures between 10 K and 1000 K. In the far infrared (FIR) range , between 50 and 1000 cm^{-1} the curves show a strong temperature dependence, while in the mid infrared range (MIR) (1000 - 7000 cm^{-1}) the spectra are almost temperature

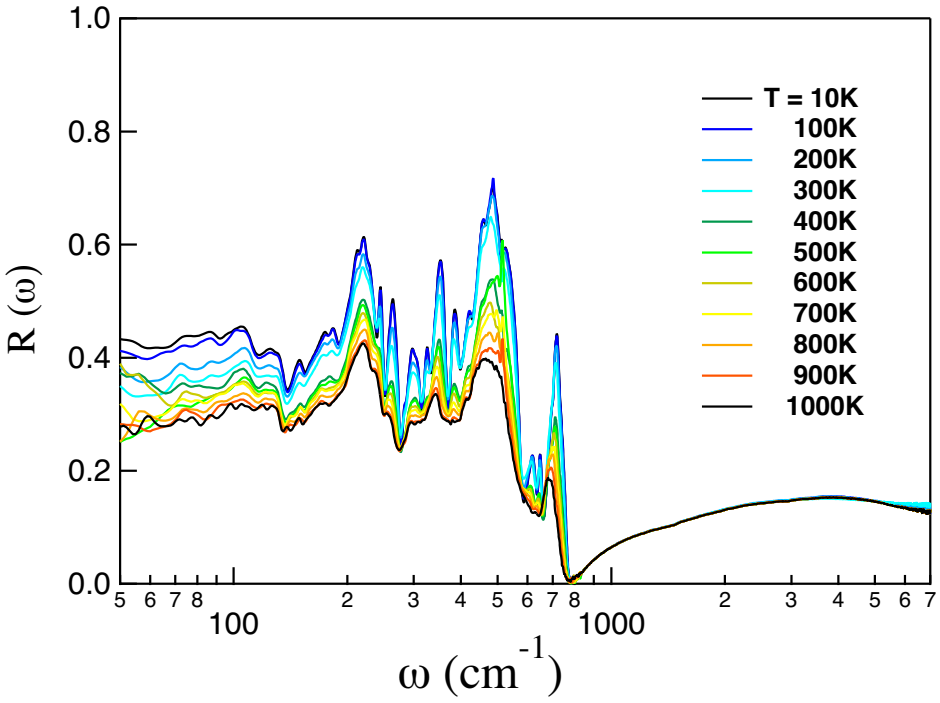

FIGURE 4.13 – Reflectivity of $GaFeO_3$ between 10 K and 1000 K in the MIR and FIR ranges (6 meV - 1 eV) in logarithmic scale.

independent. In the FIR range several narrow contributions arise, related to the normal modes of the crystal (phonon modes). In the MIR range the reflectivity presents a single broad contribution. It has to be noted that the reflectivity at a given frequency depends on both the dispersive and the absorptive part of the response. We then extracted the real part $\sigma(\omega)$ of the optical conductivity via Kramers-Kronig transformations, as explained in Section 2.1. An extrapolation commonly adopted for insulating compounds has been used for the low frequency range ($R = const.$ for $\omega \to 0$). For the high frequency range, the standard $R \sim \omega^{-4}$ for $\omega \to \infty$ extrapolation was used. In Fig.4.14 we show $\sigma(\omega)$ in the FIR range. It shows the phonon contributions superimposed to each other and strongly dependent on temperature. At low T the lines appear narrower, while new modes seem to appear. In fact, the fits (see below) show that they are just better resolved.

4.3.1.1 Drude-Lorentz analysis of the Infrared-active phonon modes

Infrared spectroscopy is sensitive to the optical phonon modes at q = 0 which generate a dipole moment in the ionic displacement, as then the first-order matrix element $\mathcal{M}_{if}^2$ of the interaction Hamiltonian ($\mathcal{H}_{int}$) between the electromagnetic field and the matter is

$$\mathcal{M}_{if}^2 \propto |\langle i|\varepsilon_\alpha \varepsilon_{phon} \mathcal{H}_{int}^1|f\rangle|^2 \neq 0 \tag{4.2}$$

Here, the scalar product between the polarization vector of the radiation ε_α and the polarization vector of the phonon ε_{phon} selects the transverse phonons, while the first-order term $\mathcal{H}_{int}$ is proportional to the ionic dipole operator. In our measurements we use a polycrystalline $GaFeO_3$ sample, so that we are able to detect all the normal modes related to the three crystal axes. On the other hand, this will allow us to identify neither the symmetry nor the degeneration of the modes. As we can see from Fig.4.14(a) the number of detected phonon modes is large, and their frequencies fall between 100 and 700 cm^{-1}. To perform a quantitative analysis, the phonon dielectric function (see Section 2.1.2) can be fitted to a sum of Lorentzian functions peaked at finite frequencies ω_j, with strength S_j and width γ_j. Therefore,

$$\tilde{\sigma}(\omega) = \frac{\omega}{4\pi i} \sum_j \frac{S_j^2 \omega_j^2}{(\omega_j^2 - \omega^2) - i\omega\gamma_j} \tag{4.3}$$

We used 22 contributions to fit the curve at 10 K. At higher temperature some contributions are strongly damped but keeping them for all the temperatures improves the fit quality. The comparison between the fit and the experimental results is reported in Fig.4.14(b) for three selected temperatures. As we can see the agreement is very good in the whole explored temperature and frequency range.

In Fig.4.15 we reported the temperature dependence of the phonon frequencies of the most intense contributions between 10 and 1000 K. We labelled the phonons with an increasing number accordingly with their increasing central frequency. We can see that there are essentially two behaviors : contributions 7, 10 and 14 present a central frequency slightly temperature dependent, while 19, 20 and 21 present a typical hardening at low T. The other contributions follow an intermediate behavior between those two.

The important point here is that the number of the most intense phonon modes does not vary between 10 K and 1000 K. The most evident effect, in fact, is the phonon hardening with decreasing temperature, and no splitting of the phonon modes is evident as a function of temperature. From this we can conclude that in the wide temperature range measured (10 - 1000 K) the symmetry of the crystal does not change. Moreover, given the fact that we explored both the paramagnetic and the ferrimagnetic phases, we have indications that the phonon modes are not affected by the magnetic transitions at $T_N = 207$ K.

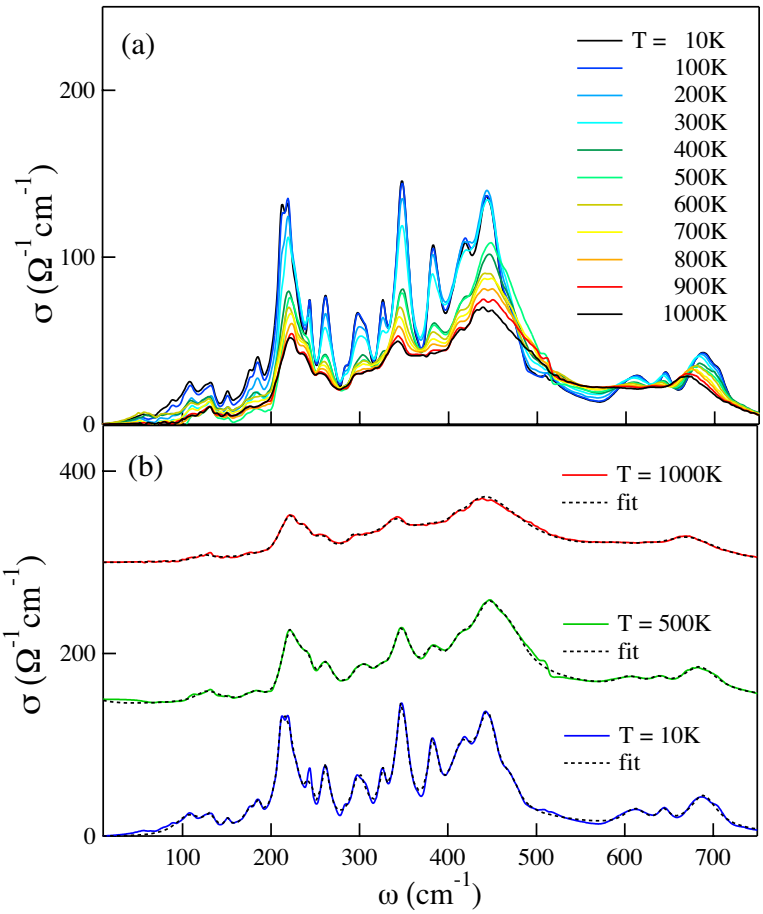

FIGURE 4.14 – (a) Optical conductivity of $GaFeO_3$ between 10 K and 1000 K in the phonon region. (b) Comparison of experimental (line) data with the fitting function (dashed lines). The zero of the curves measured at 500 K and 1000 K has been shifted by 150 and 300 $\Omega^{-1}\text{cm}^{-1}$ respectively, for sake of clarity.

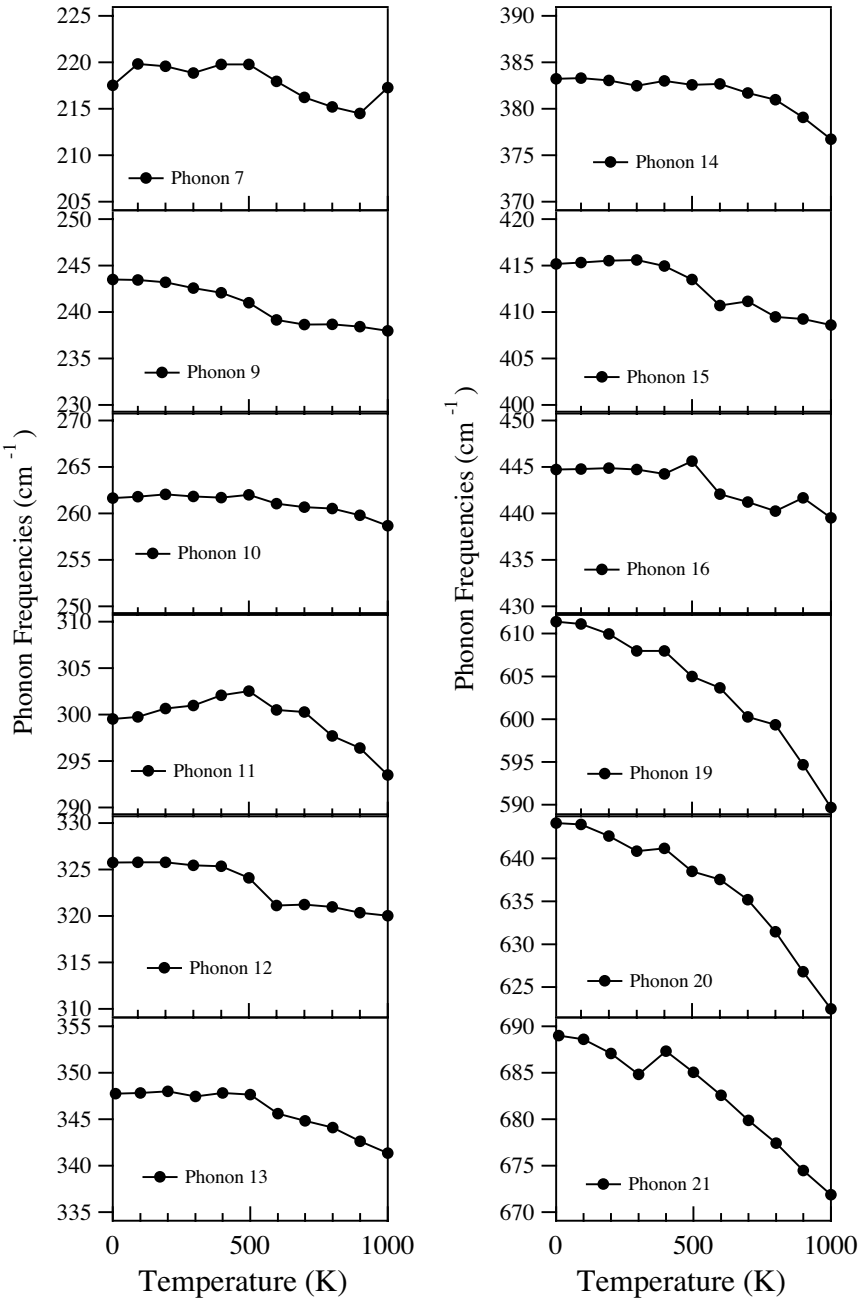

FIGURE 4.15 – Temperature dependence of the phonon frequencies for polycrystalline $GaFeO_3$.

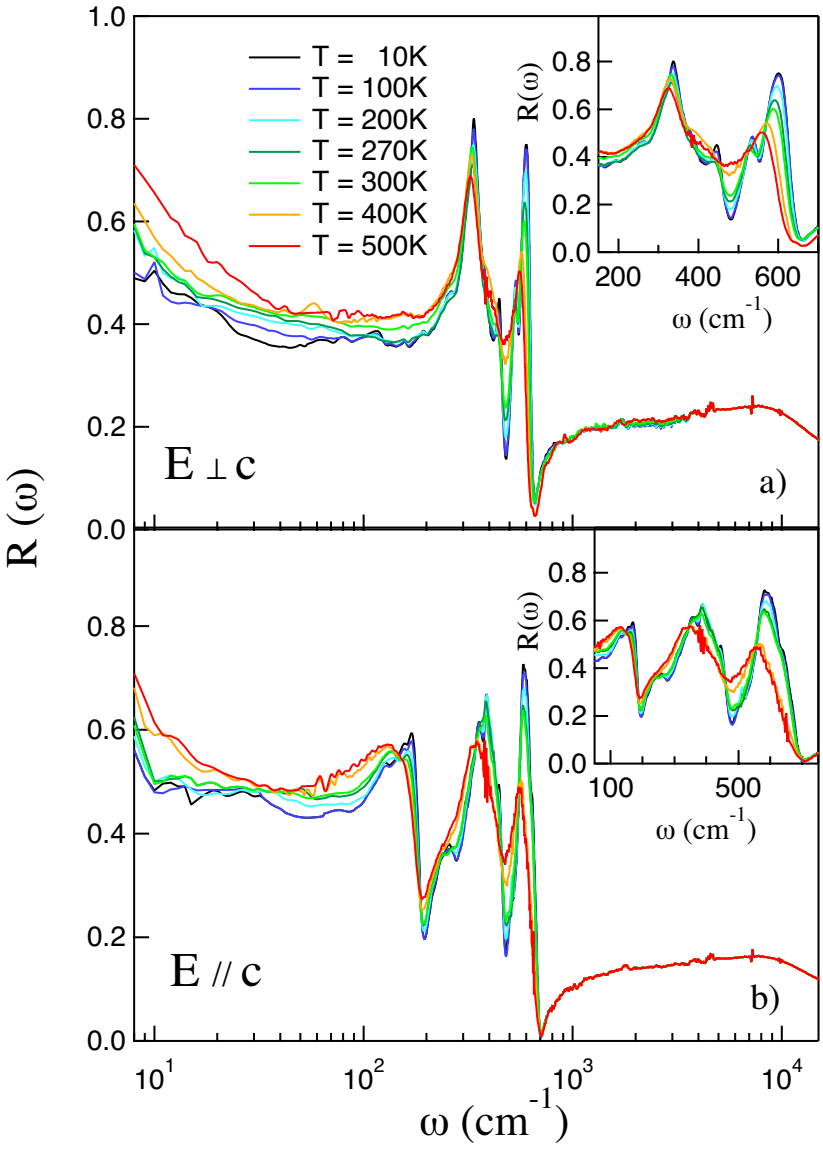

FIGURE 4.16 – Reflectivity of $LuFe_2O_4$ between 10 K and 500 K, as measured with the radiation field polarized along the $a(b)$-axis (above) and along the c-axis (below). The phonon region is reported in the inset on a linear frequency scale.

4.3.2 Reflectivity measurements on $LuFe_2O_4$

We have investigated both the sub-THz and the infrared optical conductivity of $LuFe_2O_4$ by performing reflectivity measurements on a large (8x3x2 mm^3) single crystal, grown by optical floating zone melting method. The largest crystal surface contained the axes c and a (or b,as they cannot be distinguished) and its reflectivity R(ω) has been measured from

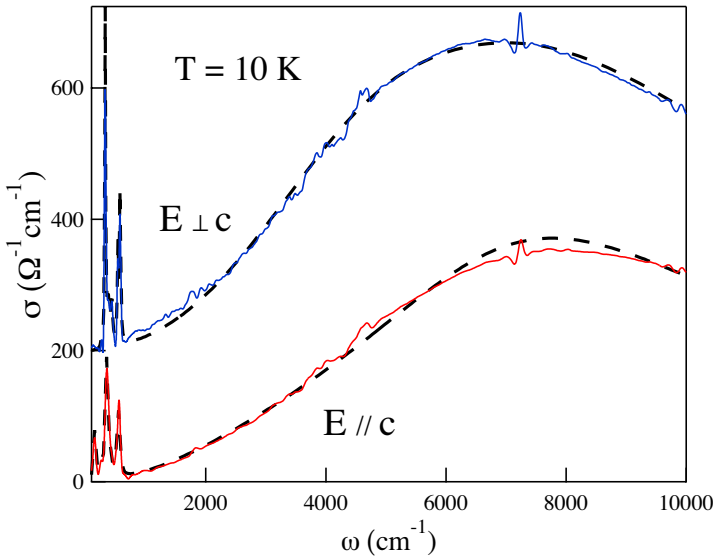

FIGURE 4.17 – Optical conductivity of $LuFe_2O_4$ at 10 K in the whole energy range, as measured with the radiation field $\mathbf{E} \perp \mathbf{c}$ or $\mathbf{E} \parallel \mathbf{c}$. The fitting curves are reported by dashed lines. The zero of the upper curves has been shifted by 200 $\Omega^{-1}\text{cm}^{-1}$ for sake of clarity.

7 to 16000 cm^{-1} (i. e., from about 1 meV to 2 eV), in the temperature range 10 - 500 K, with the radiation field $\mathbf{E}$ polarized both $\perp \mathbf{c}$ and $\parallel \mathbf{c}$. Also these measurements have been performed by using a Michelson interferometer, as described in Chapter 2.The sub-THz measurements were performed using the coherent synchrotron radiation extracted from a bending magnet of the BESSY-II storage ring when working in its low-α mode [18].

The reflectivity of the $LuFe_2O_4$ is reported in Fig.4.16 for $\mathbf{E} \perp \mathbf{c}$ (a) and $\mathbf{E} \parallel \mathbf{c}$ (b). The high frequency region (the mid- and the near-infrared ranges, between 1000 and 160000 cm^{-1}) presents a broad band with a maximum around 8000 cm^{-1} (1 eV). This large peak is practically temperature independent. The FIR region in both panels shows a rich and detailed optical-phonon spectrum that strongly depends on the temperature. In the inset the phonon region is reported in the linear scale. $R(\omega)$ shows a rich and detailed optical-phonon spectrum, also reported on a linear scale in the insets, which changes drastically at T_{CO}. In the $\mathbf{E} \perp \mathbf{c}$ configuration, at the lowest frequency and high T, the non-zero slope of $R(\omega)$ reveals a small and narrow Drude-like term, thermally activated. In the sub-THz region one instead detects a weak but well defined peak at about 10 cm^{-1}.

Figure 4.17 shows the real part of the optical conductivity, as extracted from $R(\omega)$ by the Kramers-Kronig transformations. To analyze the optical conductivity we performed the same fitting procedure used for $GaFeO_3$, by means of Eq.4.3. The broad peak detected in the MIR and NIR ranges is better seen here in a linear scale. The figure reports the data at 10 K, but the high-frequency conductivity is virtually independent of temperature. The best fit, also plotted in the Figure, requires a strong oscillator peaked at 7200 cm^{-1} (0.9 eV)

for $\mathbf{E} \perp \mathbf{c}$ and at 8400 cm^{-1} (1.05 eV) for $\mathbf{E} \parallel \mathbf{c}$. The former one is in fair agreement with the contribution at 1.1 eV reported in Ref. [22] and assigned to the lowest-energy allowed electronic transition, [23] namely the $Fe^{2+} \rightarrow Fe^{3+}$ charge transfer. This may occur between one of the doubly degenerate E levels, which slightly differ in energy from each other, and the A-symmetry singlet at higher energy [24]. The authors of Ref. [22] also report a much weaker contribution at 0.3 eV, detected in transmission measurements on thin samples. They assign it to on-site Fe^{3+} excitations, but it might also be due to the photoionization of the polaronic charges in the CO state [25]. Indeed, the mobility of the charges in the CO regime is treated in Ref. [22] in terms of small-polaron hopping. In the present reflectivity spectra we do observe a weak, lower-energy sideband of the main peak, that however the fit places (at 10 K) at 4000 cm^{-1} (0.5 eV) for $\mathbf{E} \perp \mathbf{c}$ and at 4500 cm^{-1} (0.55 eV) for $\mathbf{E} \parallel \mathbf{c}$.

In Fig.4.18 we show the optical conductivity in the FIR range for both polarization configurations. The phonons are evident and well defined. By decreasing the temperature, the two contributions at about 350 and 450 cm^{-1} become narrower and increase their intensity. In the high frequency part of the phonon spectrum, a major evolution in the shape of the $\sigma(\omega)$ is detected crossing the CO temperature $T_C = 320\ K$. Below T_C, the broad contribution at 530 cm^{-1} splits into two components separated by about 40 cm^{-1}. For $\mathbf{E} \parallel \mathbf{c}$ the difference between spectra above and below T_C is even more evident : by decreasing the temperature, all the lines shift abruptly to higher frequencies and new components do appear.

4.3.2.1 Analysis of the Infrared-active phonon modes

For the FIR range, the accuracy of the fitting procedure can be evaluated from Fig. 4.19, where the fitting curves are compared with the experimental $\sigma(\omega)$ at both extreme temperatures. The fitting procedure for the phonon region shows that at high T, in the rhombohedral $R\bar{3}m$ symmetry, it is necessary to use 5 contributions in the ab plane, 3 along the c axis. At low T, in the monoclinic symmetry $C2/m$, the best fit requires 6 modes for $\mathbf{E} \perp \mathbf{c}$ and 6 for $\mathbf{E} \parallel \mathbf{c}$. A shoulder which appears at 316 cm^{-1} both for $\mathbf{E} \perp \mathbf{c}$ and $\mathbf{E} \parallel \mathbf{c}$ is unlikely to be due to a normal mode of the crystal. The parameters obtained for 10 K and 500 K are listed in Table 4.2. The temperature evolution of the main phonon frequencies is shown in Fig.4.20 for both the ab plane and the c axis. Therein one may clearly see the branching at T_{CO} of the highest-energy mode of the ab plane and of two modes of the c axis. In all these cases, a narrower line originates from the high-T absorption at a moderately higher frequency, while a new mode springs up at a much higher frequency.

The high-temperature, rhombohedral $R\bar{3}m$, unit cell of $LuFe_2O_4$ contains 3 formula units, rotated by 120^0 around $\mathbf{c}$ with respect to one another, having the same 3 acoustic and 18 optical modes. The authors of Ref. [26] assumed, for the high temperature phase, 3 E_u and 3 E_g (doubly degenerate) optical phonons in the ab plane, 3 A_{2u} and 3 A_{1g} (non-degenerate) optical modes for the c axis, and calculated their frequencies as indicated in Table 4.2. It has to be noted that only the u modes are infrared active, meanwhile the g's are Raman active. As we can see from Fig.4.20, the experimental data do not match this prediction, in fact to fit the $\sigma(\omega)$ for the ab plane we need at least 5 oscillators. This results can be explained taking into account further symmetry reduction. We then

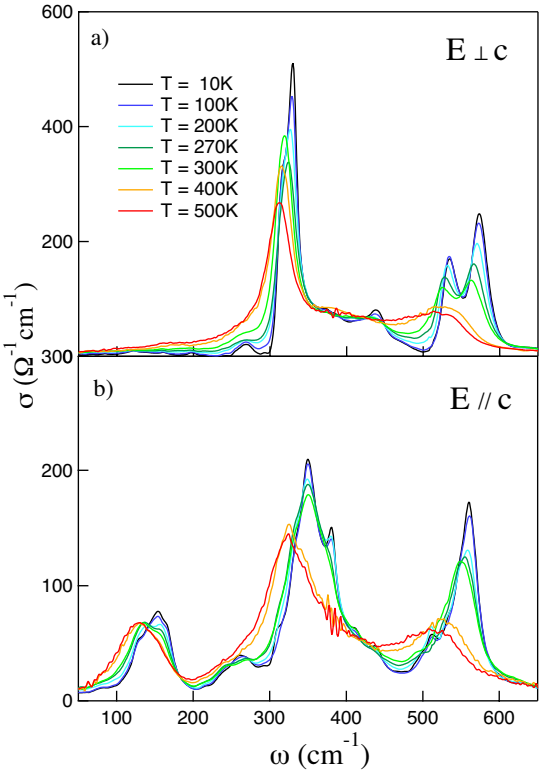

FIGURE 4.18 – Optical conductivity of $LuFe_2O_4$ between 10 K and 500 K in the phonon region, as measured with the radiation field $\mathbf{E} \perp \mathbf{c}$ and $\mathbf{E} \parallel \mathbf{c}$.

tentatively tried an alternative factor group analysis, considering a lower point symmetry for the Fe sites [20]. This leads us to a more complex phonon scenario for both the high and low temperature phases : in the high-T $R\bar{3}m$ symmetry, 5 E_u infrared-active modes are predicted in the ab plane, 4 A_{2u} along the c axis, to be compared with the 5 and 4 infrared modes, respectively, observed in Fig.4.18 and described in Table 4.2. At low temperature, the CO reduces the crystal symmetry to the monoclinic $C2/m$, [21] and our analysis predicts 12 infrared-active, non-degenerate, modes, in good agreement with the best fit in Fig4.19, which requires 6 modes for $\mathbf{E} \perp \mathbf{c}$ and 6 for $\mathbf{E} \parallel \mathbf{c}$. The aim of this calculation is to show how a reduction of symmetry is necessary to explain the experimental results.

4.3.2.2 Optical response in the sub-THz region

As already mentioned, we have extended our investigation well below the phonon region, in the sub-THz range, by use of coherent synchrotron radiation. We could thus greatly enhance the signal-to-noise ratio on the reflectivity, while maintaining a low perturbation on the system. The $R(\omega)$ thus obtained can be seen in Fig. 4.16 thanks to its logarithmic frequency scale. Therein, at 100 and 10 K a well defined peak appears at $\omega_0 = 10$ cm^{-1}.

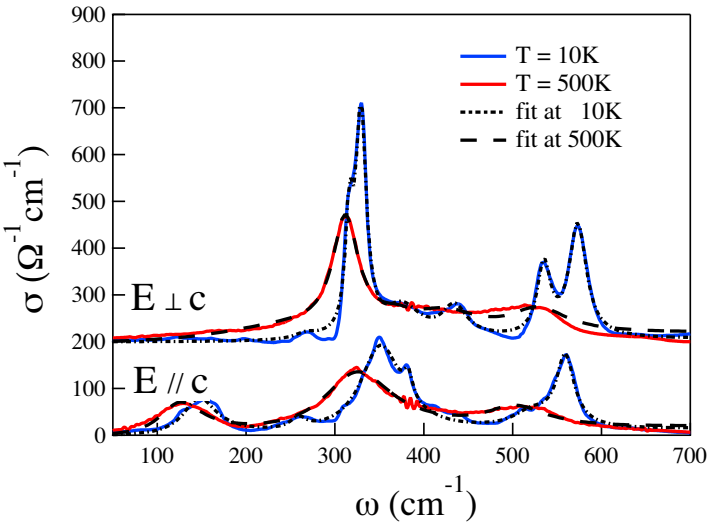

FIGURE 4.19 – Optical conductivity at 10 K and 500 K, for both $\mathbf{E} \perp \mathbf{c}$ and $\mathbf{E} \parallel \mathbf{c}$, with the fitting curves which provide the parameters listed in Table 4.2. The zero of the upper curves has been shifted by 200 $\Omega^{-1}\text{cm}^{-1}$ for sake of clarity.

This extremely low-frequency feature is then associated with the three-dimensional charge order, further reinforced by the ferrimagnetic transition at 240 K. The resulting sub-THz optical conductivity is reported in Fig. 4.21, with the feature at ω_0 again evident at low temperature. In Ref. [17], a peak was detected in the imaginary part of the dielectric function ϵ_2 (proportional to the optical conductivity) extracted from time-resolved sub-THz spectroscopy. [17] At 50 K it was reported at 13 cm^{-1} (left arrow in Fig. 4.21), in agreement within errors with the present ω_0. The authors of Ref. [17] attributed their peak to a central mode of the ferroelectric $LuFe_2O_4$ phase. They observed a further, broad contribution around 40 cm^{-1} (right arrow in Fig. 4.21), which was assigned to a soft mode. In Fig. 4.21, at 10 K, a second absorption possibly appears between 20 and 30 cm^{-1}.

The present observations may be consistent with those of time-resolved spectroscopy, if one considers that in polycrystalline samples, as is the case of Ref. [17] , the soft mode stiffens with respect to that observed in single crystals [29]. However, if one considers that $LuFe_2O_4$, as already mentioned, does not exhibit bulk ferroelectricity at zero field, there are alternative explanations for the present peak at 10 cm^{-1} (and for the broad band at higher frequency, if confirmed by further experiments). Indeed, similar features have been observed in several systems where the charge order can be described in terms of charge density waves (CDW) and this is also the case of $LuFe_2O_4$ [30]. For example, in the manganite $La_{0.25}Ca_{0.75}MnO_3$, below the charge ordering temperature T_{CO} a narrow peak at 7.5 cm^{-1} is observed, followed by a broad absorption at $\sim$ 30 cm^{-1}. [34] The former feature has been interpreted as a collective excitation (phason) of the CDW, which displaces from zero to a finite frequency when either it is pinned to lattice impurities or the charge order is commensurate with the lattice. The broader band was ascribed to a combination band of the phason with the amplitudon, another excitation which is present in a CDW.

Mode	Ω_{TO}	γ	A	Ω_{calc}	Ω_{TO}	γ	A
				$\mathbf{E} \perp \mathbf{c}$			
		10 K				500 K	
				92			
a1	268	30	150		264	34	190
	316						
a2	329	14	642	332	312	35	700
a3	376	50	441		370	43	215
a4	435	34	361		425	85	441
a5	535	18	408	474	530	75	473
a6	573	23	579				
				$\mathbf{E} \parallel \mathbf{c}$			
		10 K				500 K	
c1	148	46	461	161	127	59	493
c2	259	22	175				
	316						
c3	352	56	787	310	326	95	856
c4	383	12	196				
c5	523	55	341	465	504	83	466
c6	559	24	467				

TABLE 4.2 – Parameters obtained by fitting Eq. 4.3 to the phonon spectrum of $LuFe_2O_4$, as measured with the radiation field polarized in the *ab*-plane and along the *c*-axis. The calculated values are those reported in Ref. [26]. All figures are in cm^{-1}.

[34] According to other authors, the highest-frequency feature is instead due to an acoustic phonon, which becomes infrared active at zero wavevector due to the folding of the Brillouin zone determined by the CO [35]. Further sub-THz experiments are probably needed, before reaching a common interpretation of the elusive excitations which are detected at those low frequencies in the charge-ordered systems.

4.3.3 Infrared response of $LuFe_2O_4$ under an electric field

An abrupt drop in the dc resistivity under an electric field, at various temperatures below T_{CO}, has been recently reported in polycrystalline $LuFe_2O_4$ [36]. Here we report combined measurements of the reflectivity of our single crystal and of its current I vs. voltage ΔV characteristic. Infrared spectroscopy is a powerful tool to investigate this kind of transitions because it can detect if the transition is purely bulk or affected by some other non intrinsic mechanisms (grain boundary, percolative paths, etc). We performed infrared

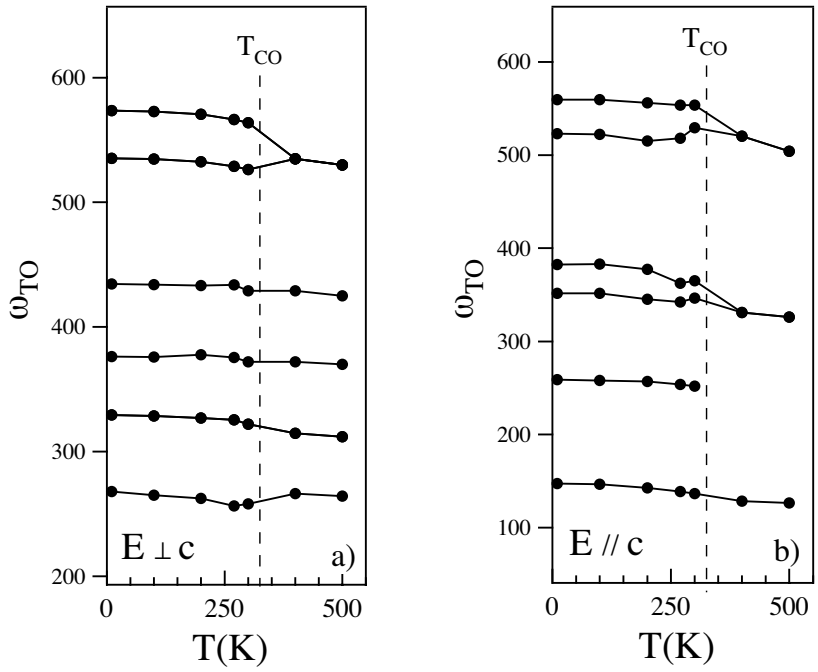

FIGURE 4.20 – Temperature dependence of the phonon frequencies for **E** $\perp$ **c** (left) and **E** $\parallel$ **c** (right) in $LuFe_2O_4$.

reflectivity measurements under applied electric field up to 10 V/cm using the set up shown in the inset of Fig.4.22 (b),which shows the conventional four-probe configuration. As it will be shown, we reached the non linear region of voltage/current curves at smaller values of the electric field than reported by other groups.

We created four contact areas on the crystal by sputtering on it a 100-nm thick aluminum film, after surface cleaning in Argon atmosphere in the same chamber. The sample was then glued to a quartz plate and microwire-bonded to dc lines fabricated on a PC board. Two contacts on the $a(b) - c$ surface allowed us to measure the current, and two others at opposite sides perpendicular to that surface were used to apply the voltage. The reflectivity was then measured in between the current contacts, for different applied voltages ΔV, and with the radiation field polarized both along the a (b) and the c axis. By use of a single crystal and of sputtered contacts, we could decrease the threshold field $E_0(T)$ - where the resistivity drop is observed - to values considerably lower than those reported previously [36]

In Fig. 4.22(a) we show the results of voltage-current loop at room temperature. When a small voltage is applied (<1 V) the current increases according to an insulating behavior with an almost constant slope (see the inset). By increasing the applied field, at $V_C = 3.27$ V we detect a jump in the current which reaches the limit set by us at 50 mA to protect the contacts. When the applied voltage is switched back the current remains over the limit down to 2.83 V, where the current drops down abruptly giving rise to a large hysteresis.

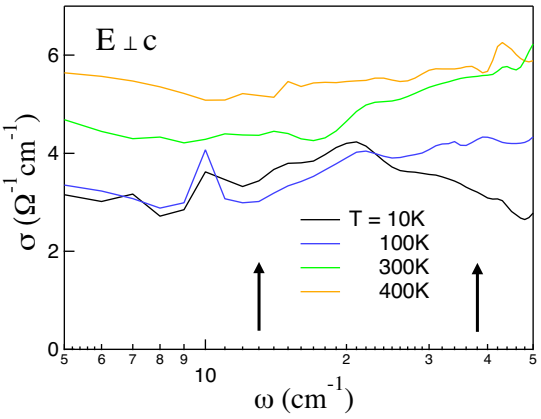

FIGURE 4.21 – Optical conductivity for $\mathbf{E} \perp \mathbf{c}$ of $LuFe_2O_4$ in the sub-THz region at different temperatures. The arrows mark the frequencies of the peaks in ϵ_2 extracted from a time-domain experiment [17].

With respect to the results of Ref. [36] we found a much smaller value of the the critical voltage V_C (3.27 V instead of 22 V). As we suggested before, this difference should be due to the different procedure used to make the electrical contacts : sputtering deposition, in fact, prevents the formation of a large contact resistance. Such a small value of V_C makes the system $LuFe_2O_4$ even more interesting for applications.

In Fig. 4.23(a) we finally show the reflectivity measurements performed under an electric field at 300 K. Both the incident light and electric field are parallel to the a axis. In this case the current has been limited to 100 mA. In the linear zone of the current-voltage curve (V $<$ 1 V) no changes are detected in the spectra. When the voltage approaches V_C and the current suddenly increases up to the set limiter, the intensity of the spectra starts to decrease while the temperature increases. As each spectrum collects data for 30 seconds, we report the temperature read on the controller at the end of the acquisition. The evolution of the spectra ends when the temperature remains constant (in this case at 330 K), at least 150 seconds after the current has reached the current limit. When the voltage is switched back to zero, the intensity comes back to the initial value (not shown).

In order to investigate the temperature dependence of the IR spectra in applied electric field, we lowered the temperature until 270 K. In Fig.4.23(b) we show the spectra at zero voltage at four temperatures : as the temperature decreases the intensity of the spectra increases. The evolution of the spectra at each temperature when the current is 100 mA is shown in Fig.4.23(c). For all temperatures we detected a decrease of the spectral intensity when the current reaches 50 mA. From these results we can notice that increasing the temperature of the sample has the same effect as the application of the electric field : the intensity of the spectra decreases in both cases.

To investigate if the current intensity affects the transport properties of the system we also performed measurements with different values of the current limiter. We used the same procedure as before below 100 mA and, leaving fixed the voltage, we increase the value

of the current limiter. For this experiment we polarized the incident radiation along both the a and c axis, and we applied alternatively the electric field along the two axes. This procedure allows us also to investigate if an electric field/current effect has a polarization dependence. In Fig.4.24 we show only the configuration with the field applied along the a axis and the light polarized in the same direction (a -a configuration). In the inset we plot the integrated signal between 20 and 700 cm^{-1} for all configurations. For all of them, we obtain a decrease of the intensity. We performed also reflectivity measurements under electric field at room temperature in the mid-Infrared range (from 700 cm^{-1} to 4000 cm^{-1}) and in the TeraHertz range (from 20 cm^{-1} to 50 cm^{-1}) with the same procedure : in this frequency ranges we do not detected any changes in the intensity.

The data collected in this study suggest that the changes in the reflectivity spectra due to the application of an electric field are related to the increasing temperature of the sample rather then a direct effect of the electric field. This is probably due to the fact the change in dc conductivity is not strong enough as to produce detectable changes in the reflectivity. This however exclude that the effect of the electric field on LuFeO may be that of triggering a real bulk transition, namely a metallization of the crystal.

In conclusion, the reflectivity measurements in the FIR range performed on polycrystalline $GaFeO_3$ and on a single crystal of $LuFe_2O_4$ allowed us to investigate the phonon spectrum of both systems. For $GaFeO_3$ in the wide temperature range explored (10 K - 1000 K) we did not detect any significant variation of the number of the phonon modes, but we could resolve 22 modes at low T. In turn, we could observe in detail the optical phonon spectrum of $LuFe_2O_4$, and the striking modifications that it undergoes when crossing T_{CO}. Indeed, the transition between the two-dimensional and the three-dimensional charge order at $T_{CO} = 320\ K$ is found to change dramatically the phonon spectrum in both polarizations : in the plane, and along the c axis. In the sub-THz spectral range of $LuFe_2O_4$ we detected at low T a peak at 10 cm^{-1}, which corresponds approximately to the central mode reported in Ref. [17]. We propose for that spectral feature an alternative interpretation which is related to charge order rather than to ferroelectricity. Moreover, by performing reflectivity measurements with an electric field applied on $LuFe_2O_4$, it turns out that some metallization of the single crystal may occur at a much lower field than previously reported for polycrystalline samples, but the optical measurements show it does not involve the bulk material. It instead probably opens percolative paths to the carriers, which reduce the resistivity without causing a real phase transition.

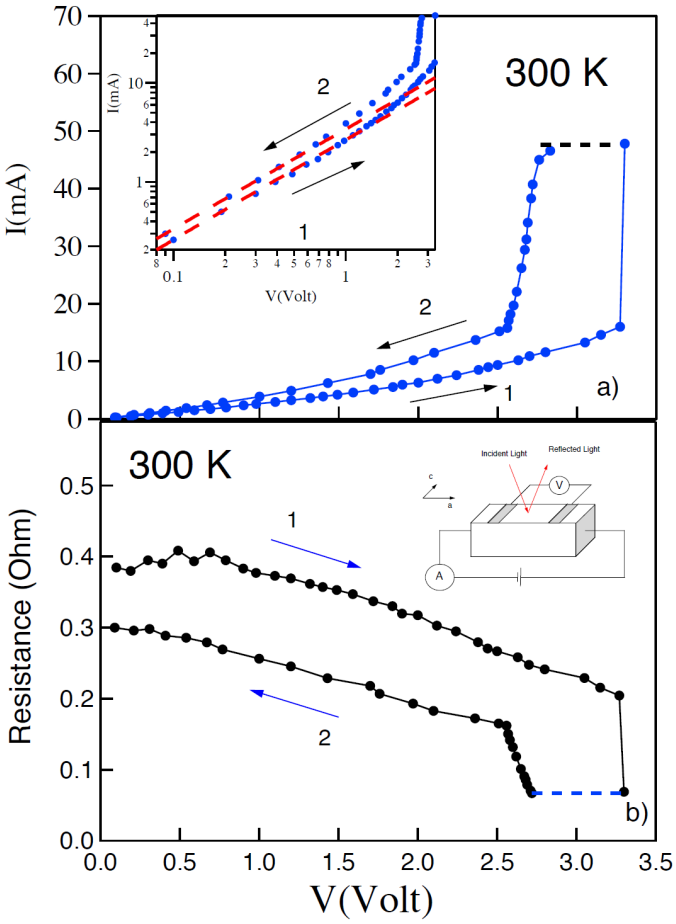

FIGURE 4.22 – Current vs. voltage (above) and resistance vs. voltage (below) of the $LuFe_2O_4$ crystal, showing the transition to a more conducting state at a threshold voltage which is higher for increasing field than for decreasing field. The contact geometry is also shown. The light impinges on the *ac* plane of the crystal.

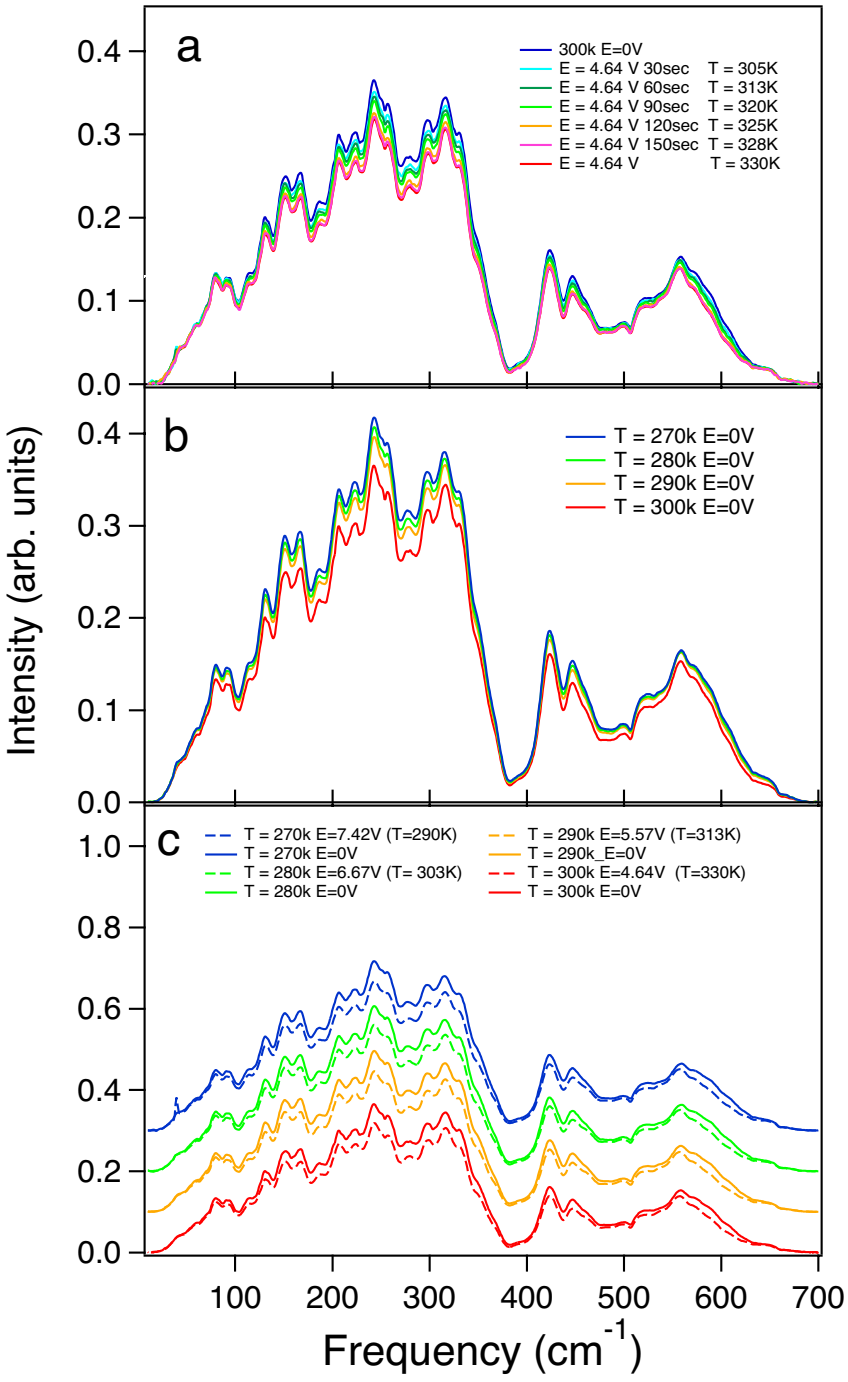

FIGURE 4.23 – a) Infrared spectra at 300 K with applied electric field. The current limiter was set at 100 mA. At the value of 4.64 V the current reaches the limit of 100m A, the intensity starts to decrease and the temperature start to increase. b) Spectra as a function of temperature when no electric field is applied. c) Infrared spectra with no electric field (solid lines) and after transition (dashed lines) spectra are shifted for clarity.

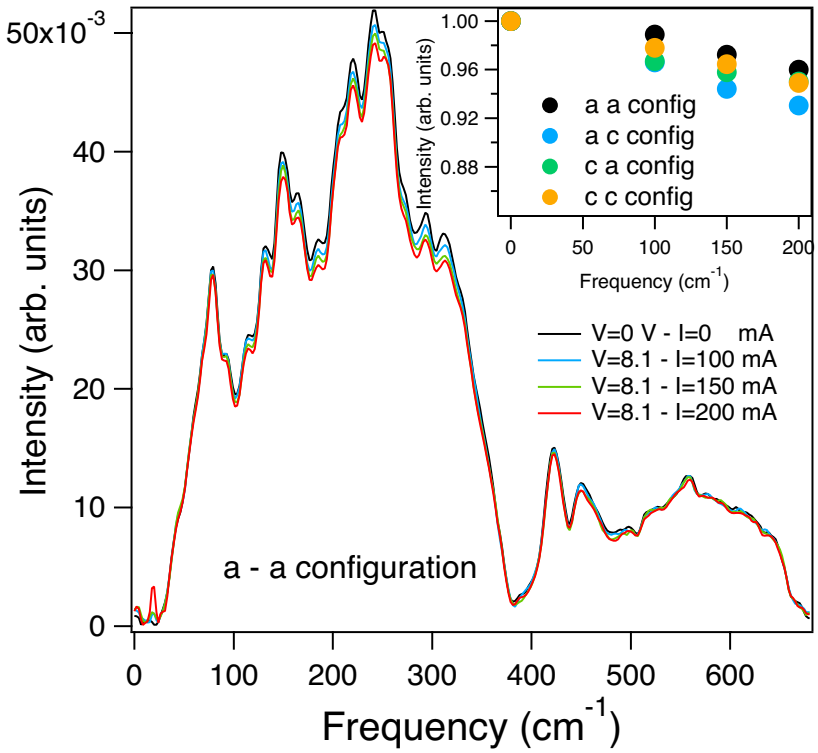

FIGURE 4.24 – Evolution of infrared spectra as a function of current in the a- a configuration (both light polarization and electric field are parallel to a axis respectively). In the inset in shown integration of intensity for all configurations.

Bibliographie

[1] Ferretti, Shanon, Mater. Res. Bull. 9, (1973) 379.

[2] C. H. Li, F. Wang, Y. Liu, X. Q. Zhang, Z. H. Cheng, and Y. Sun, Phys. Rev. B **79**, 172412 (2009).

[3] A. Douy, International Journal of Inorganic Materials 3 (2001) 699-707

[4] T. Arima, D. Higashiyama, Y. Kaneko, J. P. He, T. Goto, S. Miyasaka, T. Kimura, K. Oikawa, T. Kamiyama, R. Kumai, and Y. Tokura, Phys. Rev. B **70**, 064426 (2004).

[5] J.-Y. Kim, T. Y. Koo, and J.-H. Park, Phys. Rev. Lett. **96**, 047205 (2006).

[6] Z. H. Sun, B. L. Cheng, S. Dai, L. Z. Cao, Y. L. Zhou, K. J. Jin, Z. H. Chen, and G. Z. Yang, J. Phys. D : Appl. Phys. **39**, 2481 (2006).

[7] V. B. Naik and R. Mahendiran, J. Appl. Phys. **106**, 123910 (2009).

[8] Y. Kaneko, T. Arima, J. P. He, R. Kumai, Y. Tokura, Journal of Magnetism and Magnetic Materials, **272**, 555 (2004)

[9] R. M. Bozorth, Ferromagnetism, 6th ed. (Van Nostrand, New York, 1961), Chap. 11, p. 484.

[10] A. Arrott, Phys. Rev. **108**, 1394 (1957).

[11] Magnétisme I - Fondements, Sous la direction d'Etienne du Trémolet de Lacheisserie (2000), Collection Grenoble Sciences

[12] Blinc R, Cevc P, Zorko A, Holc J, Kosec M, Trontelj Z, Pintar J, Dalal N, Ramachandran V and Krzystek J, J. Appl. Phys. **101**, 033901 (2007).

[13] M. T. Causa, M. Tovar, A. Caneiro, F. Prado, G. Ibanez, C. Ramos, A. Butera, B. Alascio, X. Obradors, S. Pinol, F. Rivadulla, C. Vazquez-Vazquez, M. A. Lopez-Quintela, J. Rivas, Y. Tokura, and S. B. Oseroff, Phys. Rev. B **58**, 3233 (1998).

[14] M. A. Gilleo, J. Phys. Chem. Solids **13**, 33 (1960).

[15] J.E. Gulley, V. Jaccarino, Phys. Rev. B **6**, 58 (1972) .

[16] A.D. Christianson et al.., Phys. Rev. Lett. **100**, 107601 (2008).

[17] S.Z. Li, S.J. Luo, R. Fu, B.B. Jin, K.F. Wang, J.-M. Liu, J.F. Ding, X.G. Li, Appl. Phys. A **96**, 893 (2009).

[18] M. Abo-Bakr, J. Feikes, K. Holldack, P. Kuske, W. B. Peatman, U. Schade, G. Wüstefeld, and H. W. Hübers, Phys. Rev. Lett. **90**, 094801 (2003).

[19] Naoshi Ikeda, Hiroyuki Ohsumi, Kenji Ohwada, Kenji Ishii, Toshiya Inami, Kazuhisa Kakurai, Youichi Murakami, Kenji Yoshii, Shigeo Mori, Yoichi Horibe, and H. Kito, Nature **436**, 1136 (2005).

[20] F. M. Vitucci, A. Nucara, D. Nicoletti, Y. Sun, C. H. Li, J. C. Soret, U. Schade, and P. Calvani, Phys. Rev. B **81**, 195121 (2010)

[21] M. Angst, R.P. Hermann, A.D. Christianson, M.D. Lumsden, C. Lee, M.-H. Whangbo, J.-W. Kim, P.J. Ryan, S.E. Nagler, W. Tian, R. Jin, B.C. Sales, D. Mandrus, Phys. Rev. Lett. **101**, 227601 (2008).

[22] X. S. Xu, M. Angst, T. V. Brinzari, R. P. Hermann, J. L. Musfeldt, A. D. Christianson, D. Mandrus, B. C. Sales, S. McGill, J.-W. Kim, and Z. Islam, Phys. Rev. Lett. **101**, 227602 (2008).

[23] H. J. Xiang and M.-H. Whangbo, Phys. Rev. Lett. **98**, 246403 (2007).

[24] A. Nagano, M. Naka, J. Nasu, and S. Ishihara, Phys. Rev. Lett. **99**, 217202 (2007).

[25] P. Calvani, Riv. Nuovo Cimento Soc. Ital. Fis. **24**, 1 (2001).

[26] A. B. Harris and T. Yildirim, Phys. Rev. B **81**, 134417 (2010).

[27] G. W. Hateley, F. R. Dollish, N. T. McDevitt, and F. F. Bentley, *Infrared and Raman selection rules for molecular and lattice vibrations*, John Wiley & Sons, New York 1972.

[28] S. Lupi, M. Capizzi, P. Calvani, B. Ruzicka, P. Maselli, P. Dore, and A. Paolone, Phys. Rev. B **57**, 1248 (1998).

[29] J. Petzelt, J. Hlinka,, S. Kamba, T. Ostapchuk, D. Nouijni, and I. Rythchetsky, Ferroelectrics **334**, 199 (2006).

[30] Y. Yamada, S. Nohdo, and N. Ikeda, J. Phys. Soc. Japan **66** 3733 (1997) ; Y. Yamada, K. Kitsuda, S. Nohdo, and N. Ikeda, Phys. Rev. B **62** 12167 (2000).

[31] A. D. Christianson, M. D. Lumsden, M. Angst, Z. Yamani, W. Tian, R. Jin, E. A. Payzant, S. E. Nagler, B. C. Sales, and D. Mandrus, Phys. Rev. Lett., **100**, 107601 (2008).

[32] M. A. Subramanian, T. He, J. Chen, N.S. Rogado, T.G. Calvarese, and A.W. Sleight, Adv. Mater. **18**, 1737 (2006).

[33] C. Li, X.-Q. Zhang, Z.-H. Cheng, and Y. Sun, Appl. Phys. Lett. **92**, 182903 (2008).

[34] A. Nucara, P. Maselli, P. Calvani, R. Sopracase, M. Ortolani, G. Gruener, M. Cestelli Guidi, U. Schade, and J. García, Phys. Rev. Lett. **101**, 066407 (2008).

[35] T. Zhang, E. Zhukova, B. Gorshunov, D. Wu, A.S. Prokhorov, V.I. Torgashev, E.G. Maksimov, M. Dressel, Phys. Rev. B **81** 125132 (2010).

[36] C. Li, X.-Q. Zhang, Z.-H. Cheng, and Y. Sun, Appl. Phys. Lett. **92**, 152103 (2008).

Conclusions

In this work we have investigated two multiferroic compounds of iron : $LuFe_2O_4$ and $GaFeO_3$. For both systems we have studied the structural, electronic and magnetic properties by combining mainly two experimental techniques, Infrared Spectroscopy from the FIR to the visible range and Electronic Paramagnetic Resonance in the X-band configuration, with a microwave frequency of 9.4 GHz and a switching magnetic field up to 7000 G. Until now, these techniques have been only scarcely applied to the investigation of multiferroicity in the iron oxides. However, the present study should have shown that they can usefully concur, with other techniques, to investigate the interplay among magnetism, charge order, and electric polarizability in these promising materials. Extensive magnetization measurements were also used to characterize the materials and to better understand the EPR results on $GaFeO_3$. Finally, sub-Terahertz spectroscopy by Coherent Synchrotron Radiation was used to detect charge-order collective excitations in $LuFe_2O_4$ at low temperature.

In $GaFeO_3$ we investigated the magnetic transition that occurs between a high temperature disordered phase and a magnetically ordered, low-temperature phase. In the literature several scenarios have been proposed for the magnetic structure and different transition temperatures have been reported either for polycrystalline and single crystals. We performed ac susceptibility measurements on polycrystalline $GaFeO_3$ between 5 K and 300 K with an ac field modulation up to 1.7 mT. Our results show a magnetic phase transition around 207 K, in agreement with results reported in other studies on ceramic samples. Moreover, the temperature dependence of the susceptibility shows some anomalies in both phases. At high T, $\chi(T)$ cannot be described by a simple paramagnetic law, while a shoulder at 180 K may indicate another singularity in the magnetic susceptibility. In order to investigate the magnetic field dependence of the magnetization we performed measurements between 300 K and 2 K with a magnetic field up to 90 kOe. For all the values of H we detected a remnant magnetic moment at low temperature, showing that our sample presents a ferrimagnetic-like behavior. We have determined the transition temperature from the maximum change in slope at 500 Oe and, in optimum accordance with the susceptibility measurements, we found $T_C = 206\ K$. By analyzing the saturation magnetization at the lowest temperature and the highest magnetic field we found that the maximum magnetic moment is $M_S = 0.77\ \mu_B/Fe$, which is comparable with the value reported for single crystals. This result shows that the magnetic ordering of our polycrystalline sample has a strength comparable with that of the single crystals, but the maximum macroscopic moment is reached only by applying an intense magnetic field.

We also analyzed the magnetization data by means of the Arrott plots, to obtain the

temperature dependence of the zero-field susceptibility $\chi_{Arrott}(T)$: we thus found that the susceptibility follows a paramagnetic behavior between 300 K and 240 K, and then starts to deviate from a linear dependence at $T < 240K$, well above the $T_C = 206$ K. By analyzing the slope of the curves calculated with the Arrott plots, we could carefully investigate the origin of the anomalous behavior of $\chi_{Arrott}(T)$ between 240 K and T_C. The results suggest the appearance of short range antiferromagnetic interactions at $T = T_{SR} = 240$ K.

The EPR measurements allowed us to investigate the local magnetic response of $GaFeO_3$. By analyzing the temperature evolution of the EPR signal we found that the system exhibits a paramagnetic behavior between 300 K and 240 K, as it presents a single absorption line, proper of free electron absorption processes. Below T_{SR} the EPR spectra show instead two absorption lines with opposite temperature evolution. We interpret this as a confirmation of the proposed scenario in which T_{SR} corresponds to the onset of short range antiferromagnetic interactions. A relation of this process with the unique origin of the ferrimagnetic order in $GaFeO_3$ has been also presented.

In order to investigate the optical response of $GaFeO_3$ across the magnetic transition we performed reflectivity measurements in the FIR range in between 10 K and 1000 K. By means of the Kramers-Kronig transformations, we calculated the temperature dependence of the real part of the optical conductivity $\sigma(\omega)$. The phonon spectrum arising from the absorption in the $\sigma(\omega)$ does not show significant variations in the investigated temperature range. This provides evidence that the structural properties of $GaFeO_3$ are not affected by the magnetic transition.

This is not the case of $LuFe_2O_4$, where, conversely, the most interesting results have been provided by infrared spectroscopy. Its magnetic susceptibility has been preliminarily measured between 5 K and 300 K. The results show the onset of a ferrimagnetic transition at $T_N = 230$ K, in accordance with neutron diffraction experiments. Moreover, we observe a change of slope in $\chi(T)$ at about 150 K. A similar feature has been reported in other works, and has been attributed to a second magnetic transition related to a change in the magnetic correlation length. To investigate further the local magnetic properties, we performed EPR measurements also in $LuFe_2O_4$, between 20 K and 400 K. In the whole range we have not detected any signal for this compound. We related this behavior to the proposed coupling between the charge ordering and the magnetization degrees of freedom.

The reflectivity measurements on $LuFe_2O_4$ were performed in a wide frequency range, from the sub-THz to the visible (*i.e.* from 7 to 16000 cm^{-1}) and between 10 K and 500 K. The radiation was also polarized both perpendicular and parallel to the c axis. In both directions we could observe at the transition between the two-dimensional and the three-dimensional charge order at $T_{CO} = 320$ K a dramatical change in the phonon absorption, with characteristic phonon splittings and new modes resolved. The number of phonon modes deduced from the $\sigma(\omega)$, however, is not in agreement with the results of group-theory calculations proposed in the literature so that, possibly, a symmetry for the iron sites lower than usually accepted should be assumed.

In the sub-THz spectral range of $LuFe_2O_4$ we detected a peak at 10 cm^{-1}, associated with the three-dimensional charge order, further reinforced by the ferrimagnetic transition. This absorption corresponds approximately to the central mode reported in a previous

time-domain experiment. On the basis of an analogy with other charge-ordered oxides investigated in the same frequency range, we propose for that spectral feature an alternative interpretation which is related to charge order rather than to ferroelectricity.

Finally, dc transport measurements on $LuFe_2O_4$ show that some field-induced metallization occurs, and in our single crystal they are observed at a much lower field than previously reported for polycrystalline samples. However, the infrared reflectivity measured under the same fields does not show any effect - except for some heating of the sample - which may indicate an insultator-to-metal transition in the bulk material. The electric field probably opens percolative paths to the carriers in the charge-ordered phase, which reduce the dc resistivity without causing a real metallization of the bulk.

The results of the present work are the subject of the following papers :

- F. M. Vitucci, A. Nucara, D. Nicoletti, Y. Sun, C. H. Li, J. C. Soret, U. Schade, and P. Calvani,
  Infrared study of the charge-ordered multiferroic $\mathbf{LuFe_2O_4}$, Phys. Rev. B **81**, 195121 (2010)
- F. M. Vitucci, G. Gruner and J.C. Soret,
  Temperature-dependent electron paramagnetic resonance and magnetization of multiferroic $\mathbf{GaFeO_3}$, in preparation.

Contributions to papers on different topics :

- P. Maselli, D. Nicoletti, A. Nucara, F. M. Vitucci, A. Irizawa, K. Shoji, T. Nanba, and P. Calvani,
  Pressure-temperature phase diagram of charge-ordered $\mathbf{Nd_{1/2}Sr_{1/2}MnO_3}$
  EPL **92**, 47001 (2010).
- A. Nucara, F.M. Vitucci and P. Calvani,
  Optical investigation of $\mathbf{LaMnO_3}$ film : fine structure of the band at 2 eV, submitted to EPJ.

Résumé :

Nous présentons une contribution à l'étude des propriétés structurales, électroniques et magnétiques de composés multiferroïques – c'est à dire de matériaux dans lesquels coexistent ordre magnétique et ordre ferroélectrique ; les deux aspects étant couplés via des interactions et mécanismes microscopiques qui ne sont pas encore compris. C'est dans ce contexte que nous avons étudié les deux composés $GaFeO_3$ et $LuFe_2O_4$. L'étude a nécessité l'utilisation de plusieurs techniques expérimentales : les mesures magnétiques locales par résonance paramagnétique électronique (RPE) et macroscopiques par magnétométrie , et la spectroscopie infrarouge (IR). Du point de vue du magnétisme de $GaFeO_3$, les mesures locales et macroscopiques révèlent un comportement inusuel sur un large intervalle de température au-dessus de la température d'ordre, que nous attribuons à l'existence de corrélations magnétiques de courte portée dans la phase paramagnétique. D'autre part, l'analyse des spectres de phonon IR en fonction de la température montre que la mise en ordre des moments magnétiques n'affecte pas les propriétés structurales de $GaFeO_3$. Le cas de $LuFe_2O_4$ est très différent puisque les degrés de liberté magnétiques semblent couplés aux propriétés structurales au travers de l'ordre de charge des ions Fe^{3+}/Fe^{2+} comme le suggèrent les mesures RPE et de spectroscopie IR dans le domaine sub-terahertz.

Mots clés :

Multiferroïques, RPE, Spectroscopie Infrarouge, Magnétisme

Abstract :

We present a contribution to the study of structural, electronic and magnetic properties of multiferroic compounds. These materials – characterized by the coexistence and coupling of different types of long-range orders, such as magnetic and ferroelectic – have recently become a subject of great importance because of their academic interest and their significance for potential applications. In this context we have studied the two compounds $GaFeO_3$ and $LuFe_2O_4$. The study involved the use of several techniques : electronic spin resonance (ESR), magnetic measurements by magnetometry and infrared spectroscopy (IR). Local and macroscopic magnetic measurements reveal an anomalous paramagnetic phase in $GaFeO_3$. This is attributed to the existence of short-range magnetic correlations in a wide temperature range above the ordering temperature. On the other hand, the analysis of IR phonon spectra recorded at different temperatures ($10 \leq T \leq 1000$ K) shows that the ordering of magnetic moments does not affect the structural properties of GaFeO3. For $LuFe_2O_4$, conversely, the magnetic degrees of freedom are coupled to the structural properties via the charge ordering of Fe^{3+}/Fe^{2+} ions, as suggested by ESR and IR spectroscopy.

Keywords :

Multiferroics, EPR, Infrared spectroscopy, Magnetism